AD-A032 182 INSTITUTE FOR DEFENSE ANALYSES ARLINGTON VA SCIENCE A--ETC F/G 17/8
EFFECT OF WEATHER AT HANNOVER, FEDERAL REPUBLIC OF GERMANY, ON --ETC(U)
AUG 76 L M BIBERMAN

UNCLASSIFIED P-1123 IDA/HQ-76-18660 NL

1 OF 3
AD A032182



AD A032182

PAPER P-1123

EFFECT OF WEATHER AT HANNOVER, FEDERAL REPUBLIC OF GERMANY, ON PERFORMANCE OF ELECTROOPTICAL IMAGING SYSTEMS

Part 1. Theory, Methodology, and Data Base

August 1976

Lucien M. Biberman

DDC
RECEIVED
NOV 15 1976
C

INSTITUTE FOR DEFENSE ANALYSES
SCIENCE AND TECHNOLOGY DIVISION

DISTRIBUTION STATEMENT A
Approved for public release;
Distribution Unlimited

IDA Log No. HQ 76-18660
Copy 317 of 350 copies

Classified Defense Page H-16. Document should remain for public release per Mr. Hanley, IDA.

JEC
11/18/76

The work reported in this publication was conducted under IDA's Independent Research Program. Its publication does not imply endorsement by the Department of Defense or any other government agency, nor should the contents be construed as reflecting the official position of any government agency.

This document is unclassified and suitable for public release.

PAPER P-1123

EFFECT OF WEATHER AT HANNOVER, FEDERAL REPUBLIC OF GERMANY, ON PERFORMANCE OF ELECTROOPTICAL IMAGING SYSTEMS

Part 1. Theory, Methodology, and Data Base

August 1976

Lucien M. Biberman

with contributions by

George A. du Mais and Beverley F. Roberts, Institute for Defense Analyses

Frederick A. Rosell, Robert H. Willson, Kenneth C. Leonard, Jr., L. B. Sowell, and D. A. Waller, Defense & Electronic Systems Center, Westinghouse Electric Corporation

John E. A. Selby, Eric P. Shettle, Robert W. Fenn, Robert A. McClatchey, and Frederic E. Volz, Air Force Geophysics Laboratory

Major Thomas E. Stanton and Clarence B. Elam, Air Force Environmental Technical Applications Center



INSTITUTE FOR DEFENSE ANALYSES
SCIENCE AND TECHNOLOGY DIVISION
400 Army-Navy Drive, Arlington, Virginia 22202

IDA Independent Research



UNCLASSIFIED

SECURITY CLASSIFICATION OF THIS PAGE (When Data Entered)

REPORT DOCUMENTATION PAGE	READ INSTRUCTIONS BEFORE COMPLETING FORM
1. REPORT NUMBER: Paper P-1123 ✓	2. GOVT ACCESSION NO.
3. RECIPIENT'S CATALOG NUMBER (9)	
4. TITLE (and Subtitle): Effect of Weather at Hannover, Federal Republic of Germany, on Performance of Electro-optical Imaging Systems. Part I: Theory, Methodology, and Data Base. (6)	5. TYPE OF REPORT & PERIOD COVERED: FINAL Rept. July 1974 — July 1976
6. PERFORMING ORG. REPORT NUMBER: (14) P-1123	
7. AUTHOR(s): (10) Lucien M. Biberman	8. CONTRACT OR GRANT NUMBER(s): N/A
9. PERFORMING ORGANIZATION NAME AND ADDRESS: INSTITUTE FOR DEFENSE ANALYSES, 400 Army-Navy Drive, Arlington, Virginia 22202	10. PROGRAM ELEMENT, PROJECT, TASK AREA & WORK UNIT NUMBERS: IDA Independent Research
11. CONTROLLING OFFICE NAME AND ADDRESS: N/A	12. REPORT DATE: (11) August 1976
	13. NUMBER OF PAGES: 286
14. MONITORING AGENCY NAME & ADDRESS (if different from Controlling Office): N/A (12) 263p.	15. SECURITY CLASS. (of this report): UNCLASSIFIED
	15a. DECLASSIFICATION DOWNGRADING SCHEDULE: N/A
16. DISTRIBUTION STATEMENT (of this Report): This document is unclassified and suitable for public release.	
17. DISTRIBUTION STATEMENT (of the abstract entered in Block 20, if different from Report): N/A (18) IDA/HQ	
18. SUPPLEMENTARY NOTES: N/A (19) 76-18660	
19. KEY WORDS (Continue on reverse side if necessary and identify by block number): electrooptical sensors, forward-looking infrared (FLIR), active television, passive television, weather effects, performance modeling	
20. ABSTRACT (Continue on reverse side if necessary and identify by block number): This paper examines the effect of weather on the probability of electrooptical detection of tanks at various ranges. The paper employs actual weather data recorded hourly at Hannover, Federal Republic of Germany, for a full year (1970) and a mathematical model of the electro-optical detection/recognition process developed by R.L. Sendall and L.M. Biberman from the perceived signal-to-noise concept of F.A. Rosell. The mathematical model makes use of a slightly modified version of the	

DD FORM 1 JAN 73 1473 EDITION OF 1 NOV 65 IS OBSOLETE

UNCLASSIFIED

SECURITY CLASSIFICATION OF THIS PAGE (When Data Entered)

D D C
RECEIVED
NOV 15 1976
C

403108

20. cont fr p 1473A

LOWTRAN 3 atmospheric transmittance model developed by the Air Force Geophysics Laboratory. The results show a wide variability in the probability of detection caused by wide and frequent variations in the weather.

(1473B)

ACCESSION for
NTIS White Section
DDC Buff Section
UNANNOUNCED
JUSTIFICATION
BY
DISTRIBUTION/AVAILABILITY CODES
Dist. AVAIL. and/or SPECIAL
A

ACKNOWLEDGMENTS

The mathematical model used in this study was created cooperatively by a number of people with the support of their various parent organizations.

The basic model of the forward-looking infrared (FLIR) device was developed by Robert L. Sendall* of the Electro-Optical Systems Division, Xerox Corporation, and by Lucien M. Biberman of the Institute for Defense Analyses (IDA).

The low-light-level passive television model and the active television model were developed by Frederick A. Rosell of the Defense and Electronic Systems Center, Westinghouse Electric Corporation, Baltimore, Maryland.

The weather data were selected and assembled by the Air Force Environmental Technical Applications Center (ETAC) through the efforts of Major Thomas E. Stanton and Clarence B. Elam. The data were further processed by the Defense and Electronic Systems Center, Westinghouse Electric Corporation, Baltimore, under the supervision of Kenneth C. Leonard, Jr.

The need for data on cloud-free lines of sight, long unforeseen, lead to the cooperation of Colonel John T. McCabe of ETAC and Biberman of IDA to produce the work, Estimating Mean Cloud and Climatological Probability of Cloud-Free Lines of Sight (Ref. 1), in 1965. To extend this work, Norman Sissenwine, then of the Air Force Cambridge Research Laboratories (AFCRL),

*Now with the Hughes Aircraft Company.

proposed a global program to collect such data from routine observations by commercial aircrews. The program was implemented, and Ivar Lund of AFCRL published three papers on the subject (Refs. 2-4). The data on cloud-free lines of sight used in this study were prepared by ETAC on the basis of Lund's papers.

The atmospheric transmittance model used for this study is a modification of the LOWTRAN 3 Program of John E. A. Selby and Robert A. McClatchey of the Air Force Geophysics Laboratory (AFGL) (formerly AFCRL). The modification to the water vapor continuum part of that program was accomplished principally by Robert E. Roberts of IDA.

Overall program design for this study was accomplished by George du Mais of IDA, who is primarily responsible for the final numerical analysis reported herein.

The overall base of the sensor performance models grew from a long-range program of system analysis and system synthesis by Frederick A. Rosell, Robert L. Sendall, Lucien M. Biberman, and Alvin D. Schnitzler (IDA).

This report was edited by B. F. Roberts of IDA.

Part 1 of this study, which establishes the methodology and data base, and Part 2, which applies this to the FLIR technology, were done as part of the Central Research Program of IDA. The work reported in Parts 3, 4, and 5 was done under IDA Task T-36 for the Office of Research and Technology, Director of Defense Research and Engineering (ODDR&E).

PREFACE

In 1973, the Aerospace Applications Studies Committee (AASC) of the Advisory Group for Aerospace Research and Development (AGARD), North Atlantic Treaty Organization (NATO), sponsored a study on the application of night vision devices to fast combat aircraft. During the study it became apparent that the assumed weather conditions--highly smoothed 10-year averages--were far too uniform to give realistic results. Curiosity about the variations of unsmoothed weather data led to a proposal to the AASC by L. M. Biberman of the Institute for Defense Analyses (IDA) and M. H. A. Deller of the Royal Aircraft Establishment (RAE), Farnborough, that the problem be investigated in some detail to learn the effects of terrain masking, cloud obscuration, and hour-by-hour weather variations at a number of European locations.

This study, published in five parts, contains estimates of the hourly, daily, and seasonal effects of the actual weather at Hannover, Federal Republic of Germany, in 1970 on the performance of electrooptical imaging sensors. The questions we hope to answer are how great these effects are and when and how often they occur.

Part 1 of the study, in this unclassified volume, discusses methodology and samples the results of calculations. Part 2, in another, classified volume (IDA Paper P-1124), presents complete results for a forward-looking infrared (FLIR) device in the 8.5-11 μm band and analyzes the impact of weather on operations and operational planning. Part 3 (IDA Paper P-1128) compares FLIR performance in the 3.4-4.2 μm and 8.5-11 μm bands. Part 4

(IDA Paper P-1202) reports on calculations for active and passive television. Part 5 (IDA Paper P-1203) compares the performance of active television and several different FLIRs.

CONTENTS

Acknowledgments		iii
Preface		v
SUMMARY		1
I.	INTRODUCTION	5
	A. Purpose	5
	B. Choice of Targets	6
	C. Caveats	7
	1. Data	7
	2. Geographical Area	9
	3. Computation Model	9
	4. Masking Effects	10
II.	WEATHER DATA	11
	A. The Fallacy of Averaged Data	11
	B. Data Source	11
	C. Truncation of "Infinite" Visibilities at 10 Kilometers	12
	D. Hourly Values of Visibility, Dew Point, and Air Temperature in 1970 and the Corresponding Computed Transmittance Values	12
	E. Visibility as a Measure of Aerosol Attenuation	25
	F. Some Statistics on Hourly Visibility in 1970	25
	G. Some Statistics on Hourly Dew Point in 1970	36
	H. Cloud Obscuration of the Line of Sight	36
	I. Monthly Weather Patterns and Persistence of Weather Conditions	42
III.	MODELING OF SENSOR PERFORMANCE IN THE ATMOSPHERE	43
	A. Forward-Looking Infrared	44
	B. Active Television	45
	C. Passive Television	47
IV.	PROBABILITY OF DETECTION OR RECOGNITION	49
	A. General Foundations	49
	B. Forward-Looking Infrared	54
	1. Minimum Resolvable Temperature	54
	2. FLIR Characteristics	54

3. First-Order Corrections to Bar-Pattern Data 56
4. The Calculation Procedure 60
5. Probability of Detection of Tank in Frontal Aspect at Hannover, Germany, January and August 1970 61
6. Probability of Recognition of Tank in Frontal Aspect at Hannover, Germany, January and August 1970 68
C. Active Television 78
D. Passive Television 85

V. COMPUTER PROGRAMMING 89

A. Forward-Looking Infrared 89
1. LOWTRAN 3 89
2. Inputs 89
3. Output Tables 90
4. Hour-by-Hour Calculations 90
5. Machine Dependence 91
B. Active and Passive Television 91

VI. CONCLUSIONS 93

References 97

Appendix A--Principles of the LOWTRAN 3 & 3a Models A-1

Appendix B--Monthly Average Percentage Probabilities of Cloud-Free Lines of Sight Between the Ground and Altitudes of 984, 3280, and 4920 Feet above Ground Level Along Indicated Viewing Angles, Station 10338, Hannover, Federal Republic of Germany B-1

Appendix C--Weather Patterns at Hannover, Federal Republic of Germany, in 1970 C-1

Appendix D--First-Order Corrections to Bar-Pattern Data D-1

Appendix E--Calculation of Probability of Recognition of Tank in Frontal Aspect, Active Television E-1

Appendix F--Calculation of Probability of Recognition of Tank in Frontal Aspect, Passive Television F-1

Appendix G--Approximate Relationship of Photometric and Radiometric Quantities G-1

Appendix H--Effects of Flight Vibration, Air Turbulence, Acceleration, Viewing Distance, and Image Size on the Performance of Airborne Observers and thus on the Required Threshold Signal-to-Noise Ratio at the Display H-1

SUMMARY

This paper examines the effect of weather on the probability of electrooptical detection of tanks at various ranges. The paper employs actual weather data recorded hourly at Hannover, Federal Republic of Germany, for a full year (1970) and a mathematical model of the electrooptical detection/recognition process developed by Robert L. Sendall and Lucien M. Biberman from the perceived signal-to-noise concept of Frederick A. Rosell. The mathematical model makes use of a slightly modified version of the LOWTRAN 3 atmospheric transmittance model*† developed by the Air Force Geophysics Laboratory (AFGL) [formerly the Air Force Cambridge Research Laboratories (AFCRL)]. The results show a wide variability in the probability of detection caused by wide and frequent variations in the weather.

The prime conclusion of this paper is that extinction by aerosols often seriously limits the utility of electrooptical imaging devices. This effect is most frequent and serious during the winter months.

---

*The aerosol models used in LOWTRAN 3 are based on measurements of aerosol properties such as size and vertical distribution and have been found to be in reasonable agreement (typically ±20% to ±30%) with optical measurements. However, they have not been completely validated by a comprehensive program of simultaneous measurements of the spectral dependence of atmospheric transmission, the properties of the atmospheric aerosols, and the concentrations of the significant molecular absorbers.

†Use of the unmodified water vapor continuum component of the model seemed to underpredict the transmission and sensor ranges when the path length was long or when the water vapor content of the path was high. We have addressed and corrected the discrepancy.

SUMMARY

This paper examines the effect of weather on the probability of electrooptical detection of tanks at various ranges. The paper employs actual weather data recorded hourly at Hannover, Federal Republic of Germany, for a full year (1970) and a mathematical model of the electrooptical detection/recognition process developed by Robert L. Sendall and Lucien M. Biberman from the perceived signal-to-noise concept of Frederick A. Rosell. The mathematical model makes use of a slightly modified version of the LOWTRAN 3 atmospheric transmittance model*† developed by the Air Force Geophysics Laboratory (AFGL) [formerly the Air Force Cambridge Research Laboratories (AFCRL)]. The results show a wide variability in the probability of detection caused by wide and frequent variations in the weather.

The prime conclusion of this paper is that extinction by aerosols often seriously limits the utility of electrooptical imaging devices. This effect is most frequent and serious during the winter months.

---

*The aerosol models used in LOWTRAN 3 are based on measurements of aerosol properties such as size and vertical distribution and have been found to be in reasonable agreement (typically ±20% to ±30%) with optical measurements. However, they have not been completely validated by a comprehensive program of simultaneous measurements of the spectral dependence of atmospheric transmission, the properties of the atmospheric aerosols, and the concentrations of the significant molecular absorbers.

†Use of the unmodified water vapor continuum component of the model seemed to underpredict the transmission and sensor ranges when the path length was long or when the water vapor content of the path was high. We have addressed and corrected the discrepancy.

As is shown herein, aerosols can severely reduce FLIR performance about 10% of the time in winter, 5% of the time in spring and fall, and 3% of the time in summer. This finding points up the need for serious thinking about tactics and operational plans for the use of FLIRs in what might be called predictably bad weather. The operational limitations of FLIRs in bad weather are treated in Parts 2 and 5 of this series of reports.

This paper shows that calculations based on long-term averages of weather conditions do not help one to know the probable utility of imaging devices in target detection. Weather changes quickly, and infrared propagation through the atmosphere changes drastically in a single day--even within a few hours--and often cyclically from day to day to day.

Calculations based on present atmospheric models show that aerosol effects are far more important than molecular effects in determining the performance to be expected at the ranges studied. For the ranges of interest in this study, up to 10 km, present information indicates that the utility of optical image-forming devices for looking along essentially horizontal paths at sea level can be severely reduced by aerosols but is only moderately reduced by water vapor even in summer.

In several aerosol conditions, including fog, the LOWTRAN 3 model seems slightly more than justifiably optimistic about performance at visibilities below 1 or 2 km. We have not corrected this optimism because doing so would merely reduce the predicted performance from nearly zero to very nearly zero.

The LOWTRAN 3 model yielded transmittances that were consistently too low in the 8.5-11 μm region when there was appreciable water vapor in the path. We have traced this to the values used in the model for the extinction coefficient for the water vapor continuum. We have addressed and corrected this problem, and we discuss the matter in Appendix A. Examination of measured

data has led us to believe that a simple correction factor brings the model into close agreement with experience. This correction has a sound theoretical foundation, and we have therefore incorporated it into our calculations of atmospheric transmittance of infrared. The updated model is called LOWTRAN 3a.

Aerosol effects seem very important, but there have been few experimental field measurements to verify the extensive laboratory and theoretical work on the effects of aerosols on infrared propagation.*

Our detailed computations, the derived statistics, and the conclusions as to the comparative operational utility of the sensors considered are covered in Parts 2 through 5 of this series of reports.

*Experiments have been conducted at Grafenwöhr, Germany, to gather data to permit verification or correction of the model. Final reporting of the data analysis will be done separately by the Army Night Vision Laboratory, the Army Atmospheric Sciences Laboratory, and the Institute for Defense Analyses. Preliminary results of these trials and similar ones in Great Britain appear to corroborate predictions made for FLIRs on the basis of the model.

I. INTRODUCTION

A. PURPOSE

This is the first of five parts of a study of the effects of the weather at Hannover, Federal Republic of Germany (FRG), on the performance of three kinds of state-of-the-art electro-optical imaging sensors--forward-looking infrared (FLIR), active television, and passive television--in detecting and recognizing tactical military targets. The main objectives of this study are fourfold:

1. To obtain a full year's detailed statistics on the weather in a representative area of Central Europe.
2. To compute from those statistics the corresponding basic data on atmospheric transmission over different path lengths, and to show the sensitivity of atmospheric transmission to varying weather conditions, with particular regard to attenuation by aerosols and water vapor in the atmosphere.
3. To estimate the corresponding ranges at which each kind of sensor could detect and recognize selected targets at specific levels of probability.
4. To use the above data to show how often and how long the performance of each of the sensors is below useful levels, assuming different fields of view and display sizes.

This volume, Part 1 of the five-part study, discusses data and methodology and gives a sampling of the results of calculations.

PRECEDING PAGE BLANK-NOT FILMED

B. CHOICE OF TARGETS

The target type selected for this study was determined by the availability of characteristic thermal signatures of ground vehicles and by the fact that preliminary calculations had been made for typical forward-looking (FLIR) sensors with an M-60 tank as the target, as explained in AGARD Advisory Report 73 (Ref. 5).

We decided to confine our calculations to the tank target seen from the front and side only. We consider the tank to represent one of the most difficult ground targets for fixed-wing aircraft to attack, particularly when viewed from the front with its low thermal signature. It should be noted in this respect that, in the absence of discernible motion, differentiation between active and recently disabled tanks might prove very difficult.

The larger area presented by the side of a tank provides a better target for detection/recognition for all three kinds of sensors considered in this study and a much stronger thermal signature for FLIRs. The frontal and side aspects could thus be expected to bracket approximately the expected performance of all sensors considered for use against small targets. In addition, these two aspects can provide a guide to the performance of electrooptical sensors against other targets, particularly if they contain elements of a size comparable to that of tanks.

The rear aspect of a tank was not considered a suitable target for the sensors, not only because the strong thermal signature would generally be a much better target for detection by FLIR than by television, but also because the signature would be difficult to recognize without foreknowledge of its characteristics.

C. CAVEATS

1. Data

The data presented in this study are necessary but insufficient for assessing the overall effectiveness of electrooptical imaging sensors aboard attack aircraft used against ground targets. It must be recognized, however, that the data will almost always represent an upper bound of performance, since the computed probabilities of detection and recognition at given ranges assume that the observer is already looking at the area of the display that coincides with the position of the target within the field of view. Realistic assessments of the observer's capabilities will require better data than are currently available on his display search time, on his dynamic task performance (including his target recognition and weapon aiming time), and on the degradations to be expected from both the airborne environment and the actual operational environment.

No matter how good the viewing conditions and equipment, a drowsy or disinterested observer will not do very well. It was not within the province or competence of this study to ascertain motivation or interest on the part of the observer. Our calculations are based on more than 200,000 data points for the performance of serious observers looking at a variety of targets displayed against various noisy backgrounds. We do not know how much to degrade our results to cover various tactical situations or observers who are not very attentive.

We have also excluded degradations due to exposure of airborne observers to buffeting or g-loading. Preliminary experiments completed in May 1975,* for which we arranged, showed that both buffeting and g-loading degrade observer performance, but no analysis of the frequency and severity of these effects suitable for use in modifying our results is yet available.

*Discussed in Appendix H.

Arguments about the modeling of recognition range and about how to define "identification" remain unresolved. Semantics gain in importance as the tactical problem shifts from detection to identification. In military operations, recognition of an electrooptical image of a target is very closely related to circumstances. Given the appropriate background intelligence, a sensor operator can positively translate 30 unresolved specks moving along a road into a column of trucks or tanks, poor optical quality notwithstanding.

For detection of tactical vehicular targets, we use the criterion of two lines* across the minor dimension of the target, on which there is generally good agreement. For recognition, we use the best mean criterion we know: four resolvable line pairs across the minor dimension of the target. In undemanding situations, some people elect to use three line pairs as a criterion for recognition. In bad clutter, some use a criterion of four and a half or five line pairs, but we prefer to stay with four line pairs and to increase the signal-to-noise threshold (Refs. 6, 7).

In this study we treat in depth only data on FLIR and active television. The problem of atmospheric scatter in the visible spectrum is so complex, and the relevant data are so sparse, that definitive work on passive sensors in the visible must await inputs that will allow us to calculate the reduction of contrast at the sensor, which is the major limiting factor in television systems. Until then, we offer preliminary data.

Visibility is known, but this alone is not enough. We must also know how much luminance is scattered into our optical path from the sky and how much from the ground. The sky and ground

*Two lines, one line pair, and one cycle are synonymous.

brightnesses and their ratio yield a first-order approximation by use of the method outlined by Duntley (Refs. 8, 9) and Middleton (Ref. 10).* The method applies only for a cloud-free sky.

Path luminance can readily be seen to be a function not only of the sky and the ground but also of the skew ray of the optical path. Looking away from the sun is better than looking into it. Conditions between these two extremes vary nonlinearly. Rules of thumb do not justify extensive computation. We must await some of the results of the NATO Defense Research Group (DRG) Project OPAQUE (Optical Properties of Atmospheric Quantities in Europe)** and of the current program being conducted in the Federal Republic of Germany near the Czechoslovakian and East German borders by the U. S. Army Night Vision Laboratory.

2. Geographical Area

It must be remembered that the data presented in this study are pertinent only to the particular geographical area considered, North Central Europe. To provide comparable data for other theaters of operation, recomputation using relevant weather data and the same basic methodology will be necessary.

3. Computation Model

In our computations we were bothered by four problems:

1. The overly pessimistic predictions of LOWTRAN 3 for the water vapor continuum. We have solved this, bringing calculated results into line with measured values, by correcting the LOWTRAN predictions for the continuum

---

* The limitations of this approximation are discussed in Ref. 11.

** AFGL can provide reliable path radiance or contrast transmission models. The statistical significance or representativeness of the models must be learned from Project OPAQUE.

and its temperature coefficient. The details are given in Appendix A and are the subject of a separate paper (Ref. 12).

2. The necessity to change the aerosol model as the visibility drops below about 2 km. This has not been corrected, but it scarcely affects our results since it simply makes a very bad probability a little worse--it has almost no effect on the performance statistics.

3. The lapse rate for mists and fogs. The conditions on which we have based our calculations are valid for ground-to-ground observations. If an airborne sensor is looking down from 200 ft above ground, however, and if there is a fog layer 100 ft thick, the path through fog is only half what we have used in our computations. At present, we have almost no data on the layering of fog and haze at Hannover or anywhere else.

4. By international convention, visibility exceeding 10 km is reported as infinite in aviation weather data. We have examined the effect of truncating visibility at 10 km by recomputing for 20 km. Almost no change in the statistics could be found, since visibility dominates only when its values are small.

4. Masking Effects

The effects of cloud masking and terrain masking are not included in our models of probability of detection or recognition but must be considered in operations.

II. WEATHER DATA

A. THE FALLACY OF AVERAGED DATA

The performance of electrooptical imaging sensors is strongly affected by the actual weather of the moment, not by the average weather nor by averages of weather parameters. It is fallacious to say that the weather is very pleasant on the average because it is very hot in summer and very cold in winter. Similarly, the product of average temperature and average relative humidity does not yield average absolute humidity, nor can the average value of infrared transmittance through the atmosphere be computed from the average humidity.

One can easily obtain the 10-year average of weather over Germany and get values for temperature and relative humidity at 3-hour intervals averaged over every day in a month and over every like month in a 10-year span. From that, one can compute transmittances to four significant figures, but having done so, one had better not place any credence in the results.

That is why we have used hour-by-hour weather data for a full year in our calculations.

B. DATA SOURCE

The data were taken from the files of the USAF Environmental Technical Applications Center by K. C. Leonard, Jr., L. G. Sowell, and D. A. Waller of the Defense and Electronic Systems Center, Westinghouse Electric Corporation, from aviation routine weather reports and synoptic weather observations at Hannover, Federal Republic of Germany, for the year 1970. Hannover data were chosen as probably representative of the North German Plain, and 1970 data were chosen as the most complete available.

C. TRUNCATION OF "INFINITE" VISIBILITIES AT 10 KILOMETERS

Because visibilities greater than 10 km are reported as "infinite" in aviation weather data, they have been truncated at 10 km in this study. A sensitivity analysis of this artifical truncation shows its effect on our estimates of sensor performance is negligible, since visibilities dominate only when they are short.

D. HOURLY VALUES OF VISIBILITY, DEW POINT, AND AIR TEMPERATURE IN 1970 AND THE CORRESPONDING COMPUTED TRANSMITTANCE VALUES

The hourly visibility, dew point, and air temperature readings at Hannover in each of the 12 months of 1970 are shown graphically in Figs. 1-12, along with the corresponding values of atmospheric transmittance of radiation at wavelengths at 8.5-11 μm computed for ranges of 5 and 8 km.

Whenever the air temperature drops nearly to the dew point, atmospheric conditions favor the formation of mists and fogs. As a result, visibility drops, as does transmission of radiation in all spectral bands of interest in this study. Note the sharp drops in visibility and transmittance in Figs. 5-9 where air temperature and dew point tend to coincide.

Because of this relationship, poor visibility occurs frequently in winter but tends to occur in May or June to September only when the night air cools to predawn temperatures. Poor visibility in May or June to September is thus cyclical, predictable,* and of relatively short duration.

---

*The vertical extent of mists and fogs above ground level, which can be an important factor in the visibility of ground targets from the air, cannot be predicted from the data available to us.

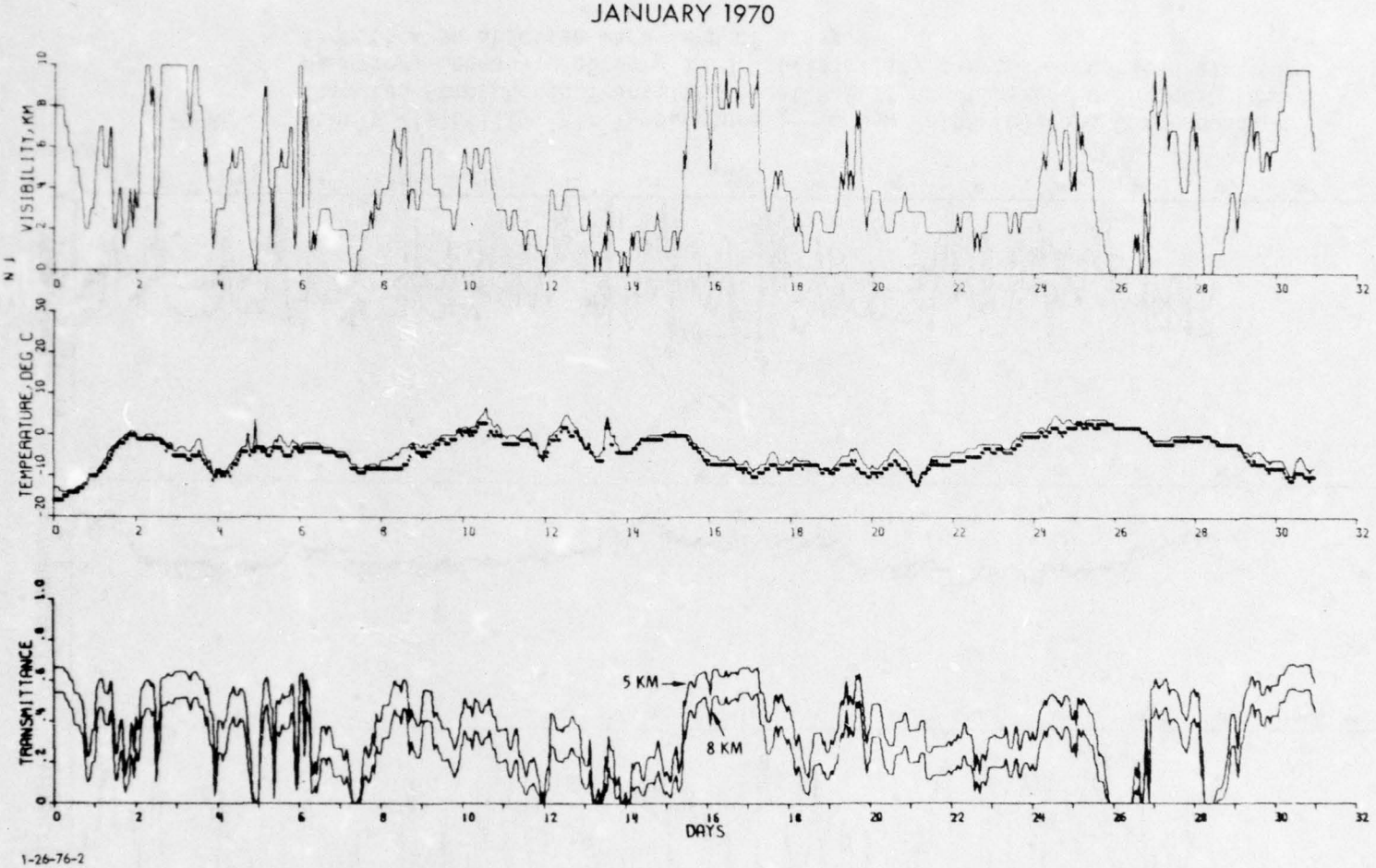


FIGURE 1. Hourly Visibility, Air Temperature (—), Dew Point (o), and Corresponding Computed Atmospheric Transmittance at 8.5-11 μm for Ranges of 5 and 8 km; Hannover, Germany; January 1970. (Visibility curve is truncated at 10 km. Each tick on abscissa marks end of a day.)

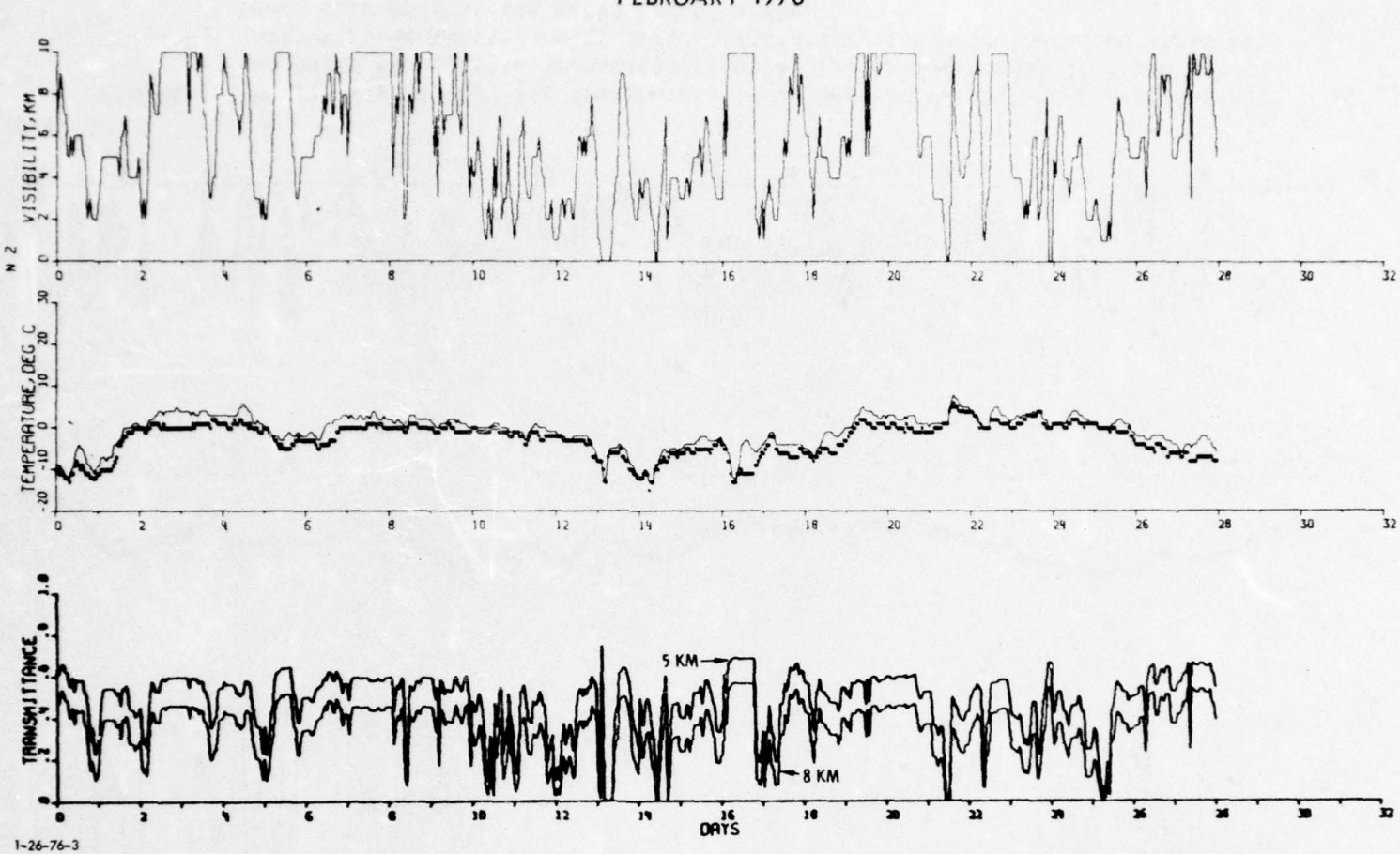


FIGURE 2. Hourly Visibility, Air Temperature (—), Dew Point (o), and Corresponding Computed Atmospheric Transmittance at 8.5-11 μm at Ranges of 5 and 8 km; Hannover, Germany; February 1970. (Visibility curve is truncated at 10 km. Each tick on abscissa marks end of a day.)

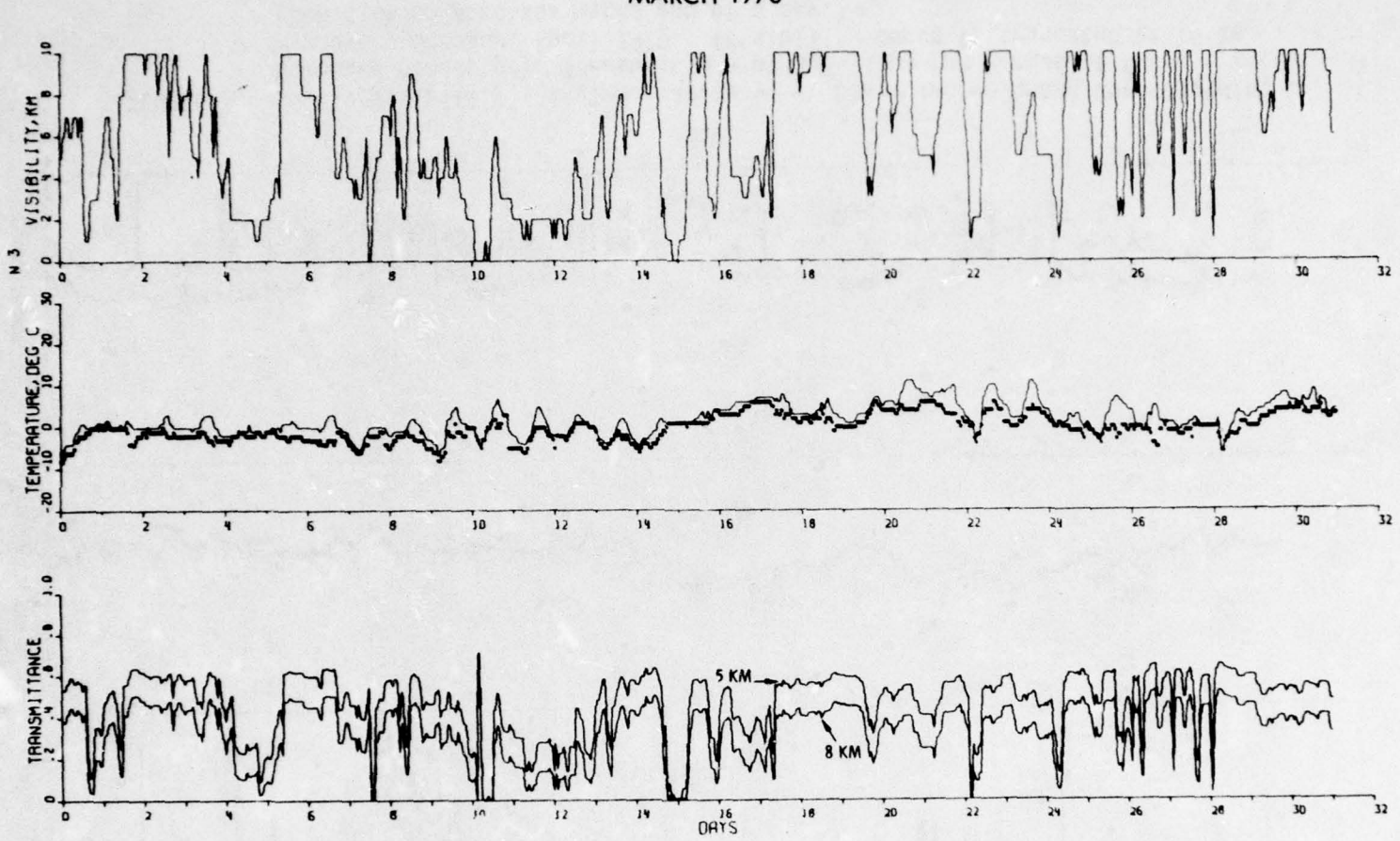


FIGURE 3. *Hourly Visibility, Air Temperature (—), Dew Point (o), and Corresponding Computed Atmospheric Transmittance at 8.5-11 μm for Ranges of 5 and 8 km; Hannover, Germany; March 1970.* (Visibility curve is truncated at 10 km. Each tick on abscissa marks end of a day.)

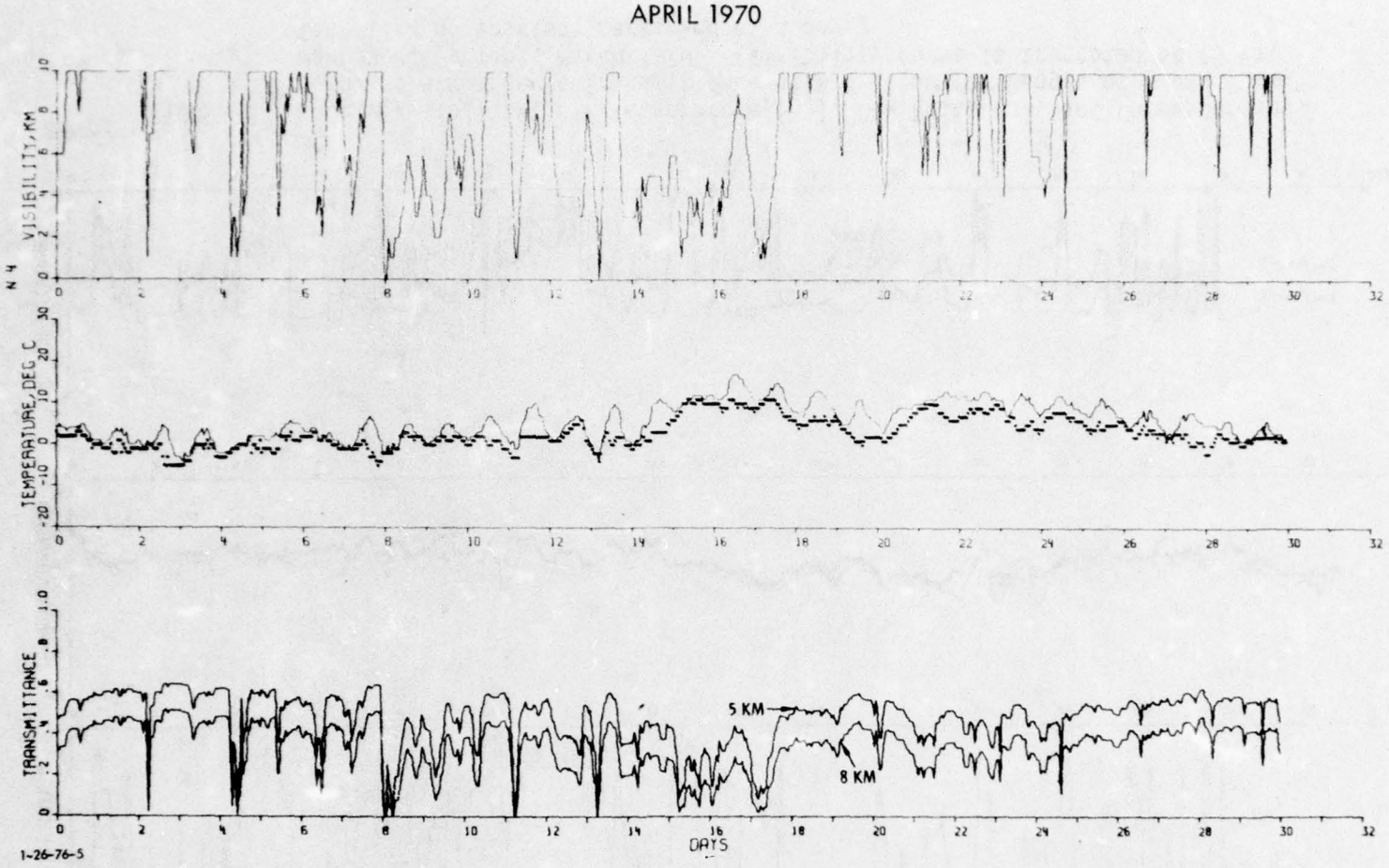


FIGURE 4. Hourly Visibility, Air Temperature (—), Dew Point (o), and Corresponding Computed Atmospheric Transmittance at 8.5-11 μm for Ranges of 5 and 8 km; Hannover, Germany; April 1970. (Visibility curve is truncated at 10 km. Each tick on abscissa marks end of a day.)

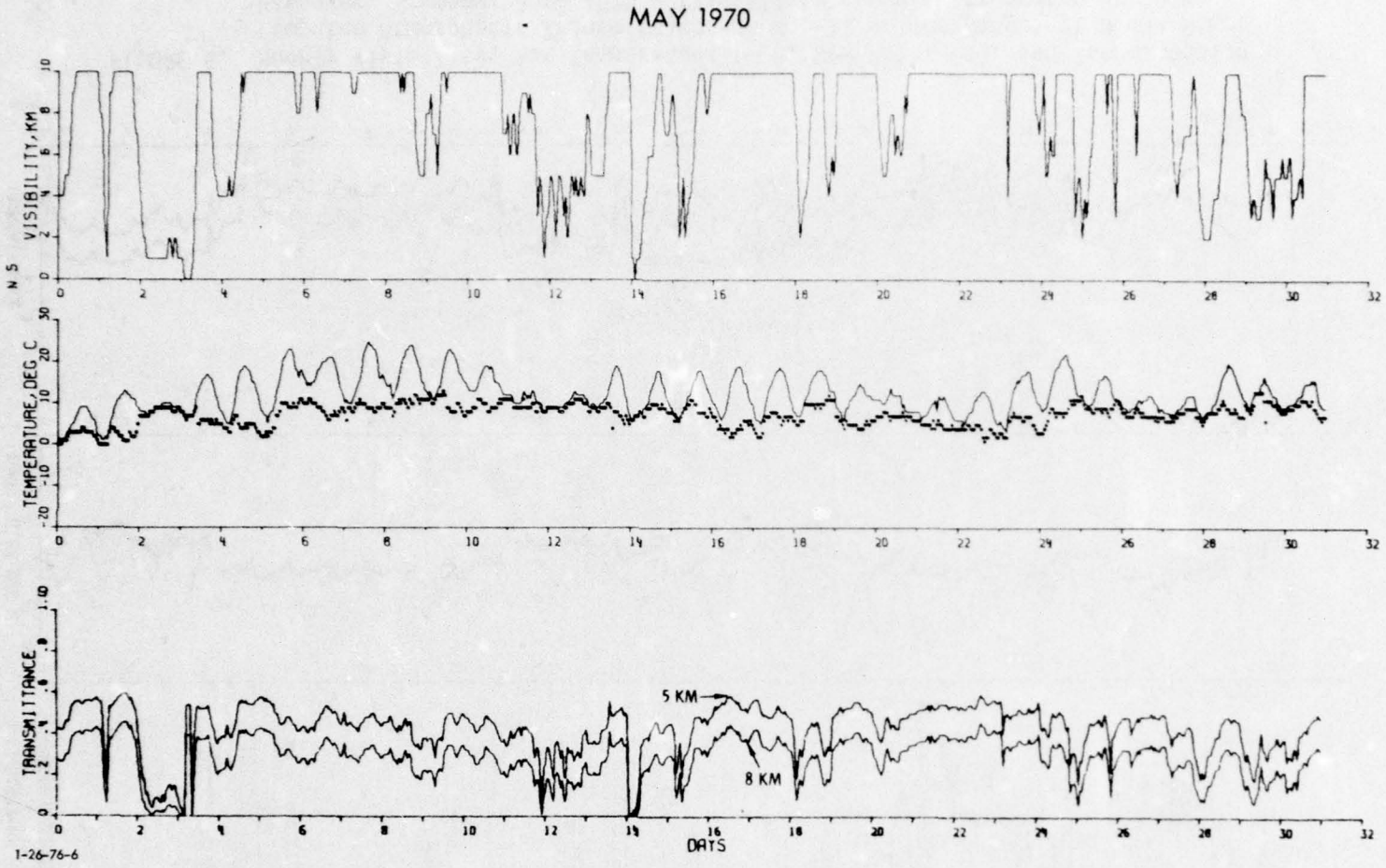


FIGURE 5. Hourly Visibility, Air Temperature (—), Dew Point (o), and Corresponding Computed Atmospheric Transmittance at 8.5-11 μm for Ranges of 5 and 8 km; Hannover, Germany; May 1970. (Visibility curve is truncated at 10 km. Each tick on abscissa marks end of a day.)

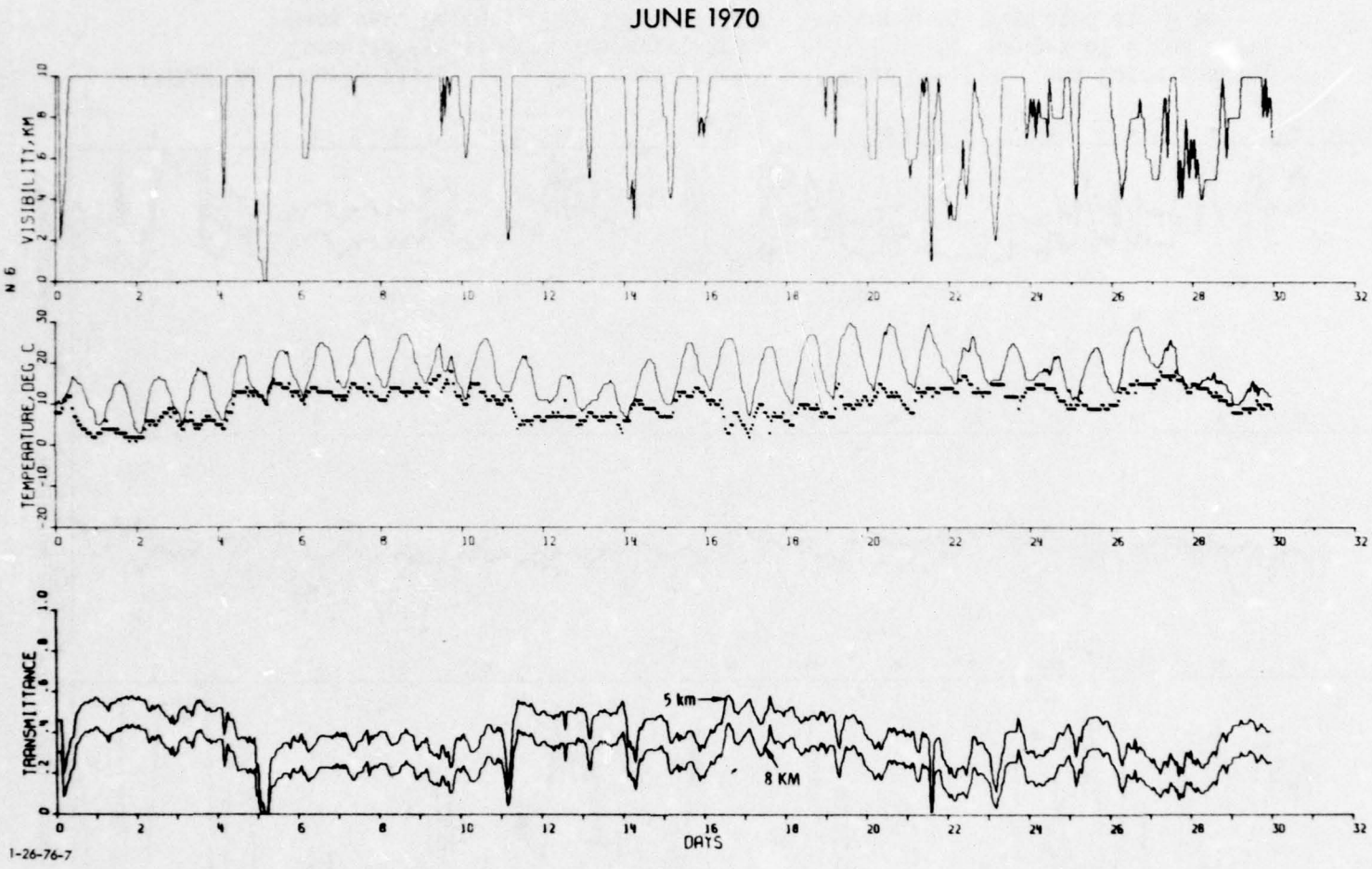


FIGURE 6. Hourly Visibility, Air Temperature (—), Dew Point (o), and Corresponding Computed Atmospheric Transmittance at 8.5-11 μm for Ranges of 5 and 8 km; Hannover, Germany; June 1970. (Visibility curve is truncated at 10 km. Each tick on abscissa marks end of a day.)

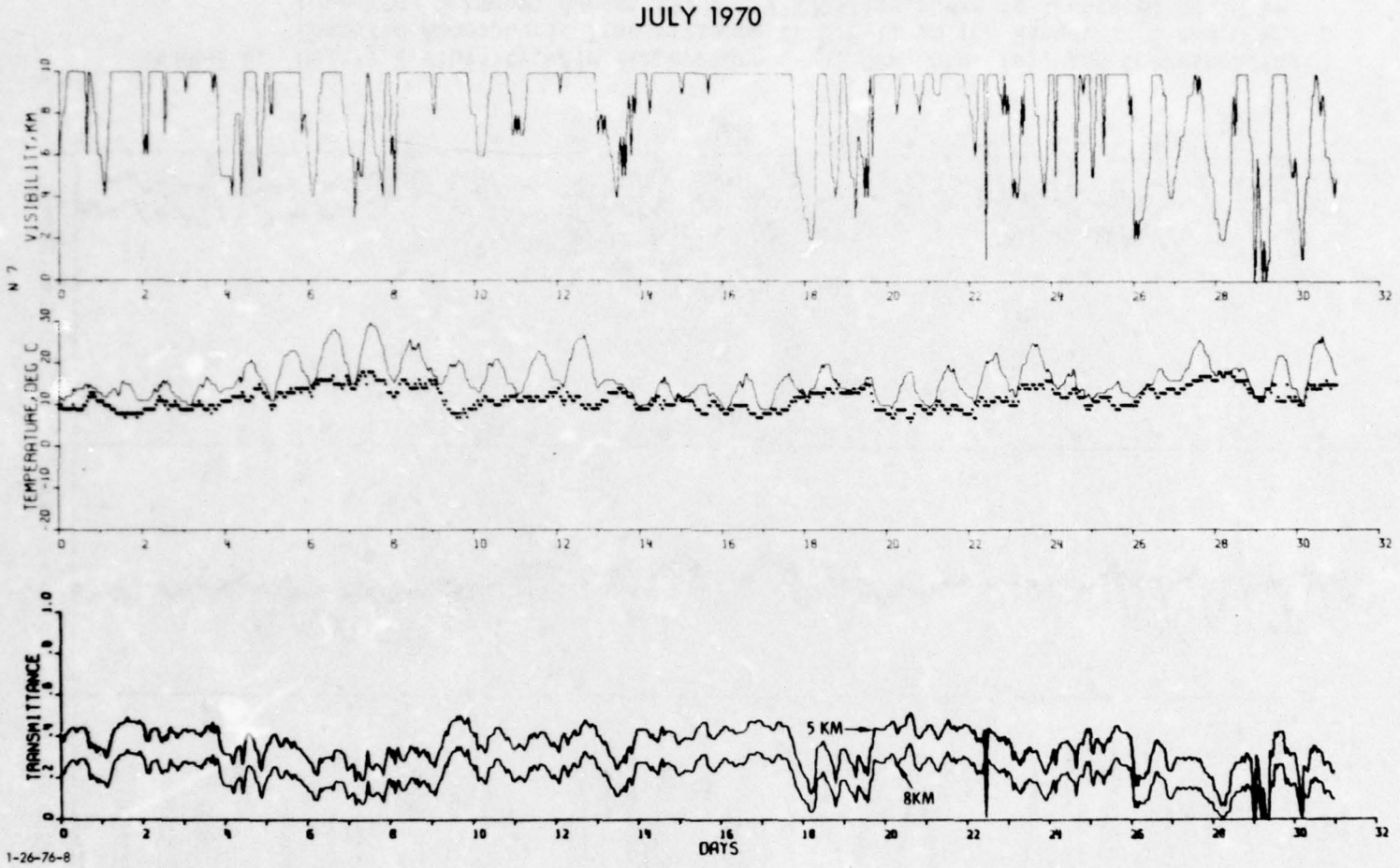


FIGURE 7. Hourly Visibility, Air Temperature (—), Dew Point (o), and Corresponding Computed Atmospheric Transmittance at 8.5-11 μm for Ranges of 5 and 8 km; Hannover, Germany; July 1970. (Visibility curve is truncated at 10 km. Each tick on abscissa marks end of a day.)

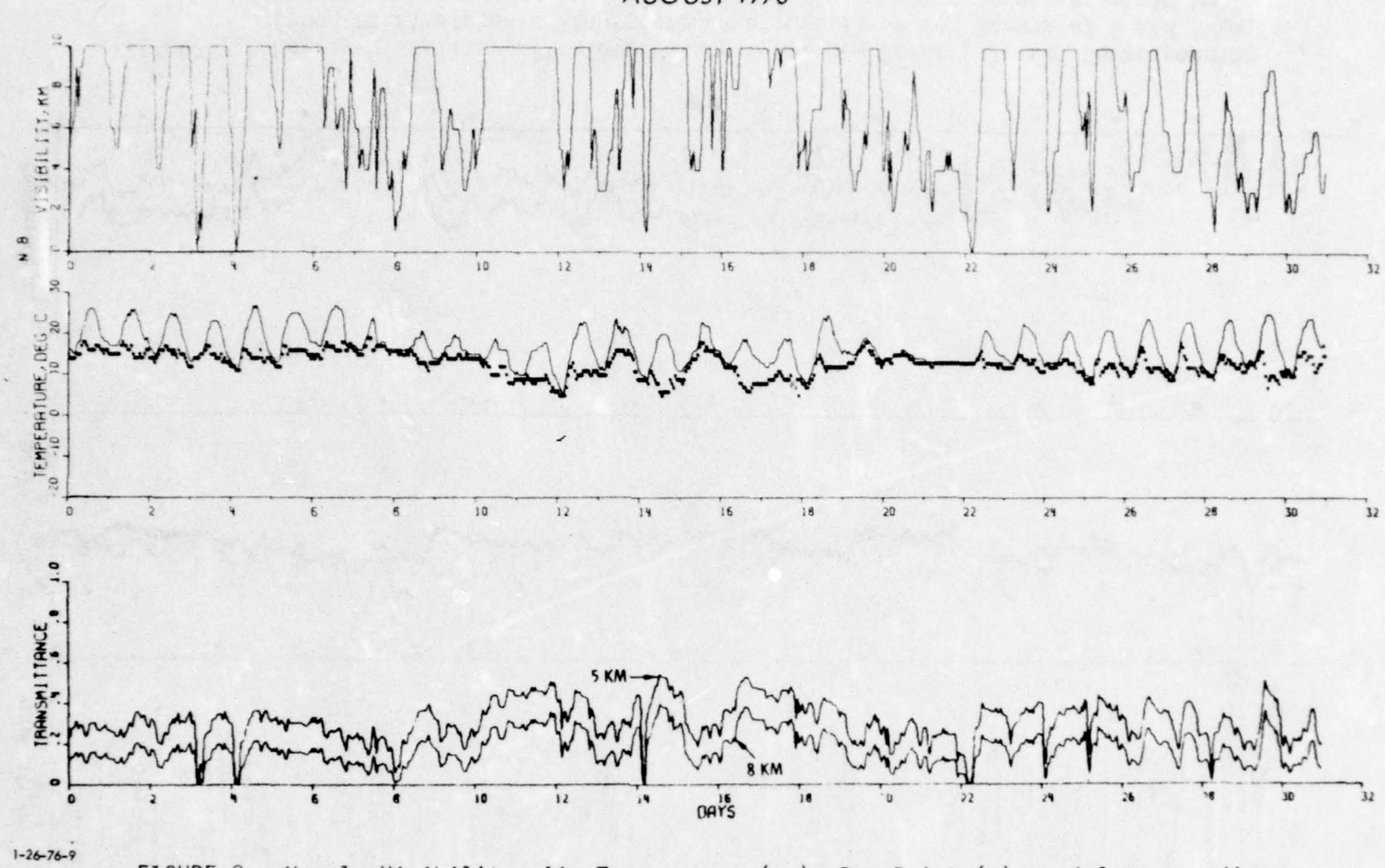


FIGURE 8. Hourly Visibility, Air Temperature (—), Dew Point (o), and Corresponding Computed Atmospheric Transmittance at 8.5-11 μm for Ranges of 5 and 8 km; Hannover, Germany; August 1970. (Visibility curve is truncated at 10 km. Each tick on abscissa marks end of a day.)

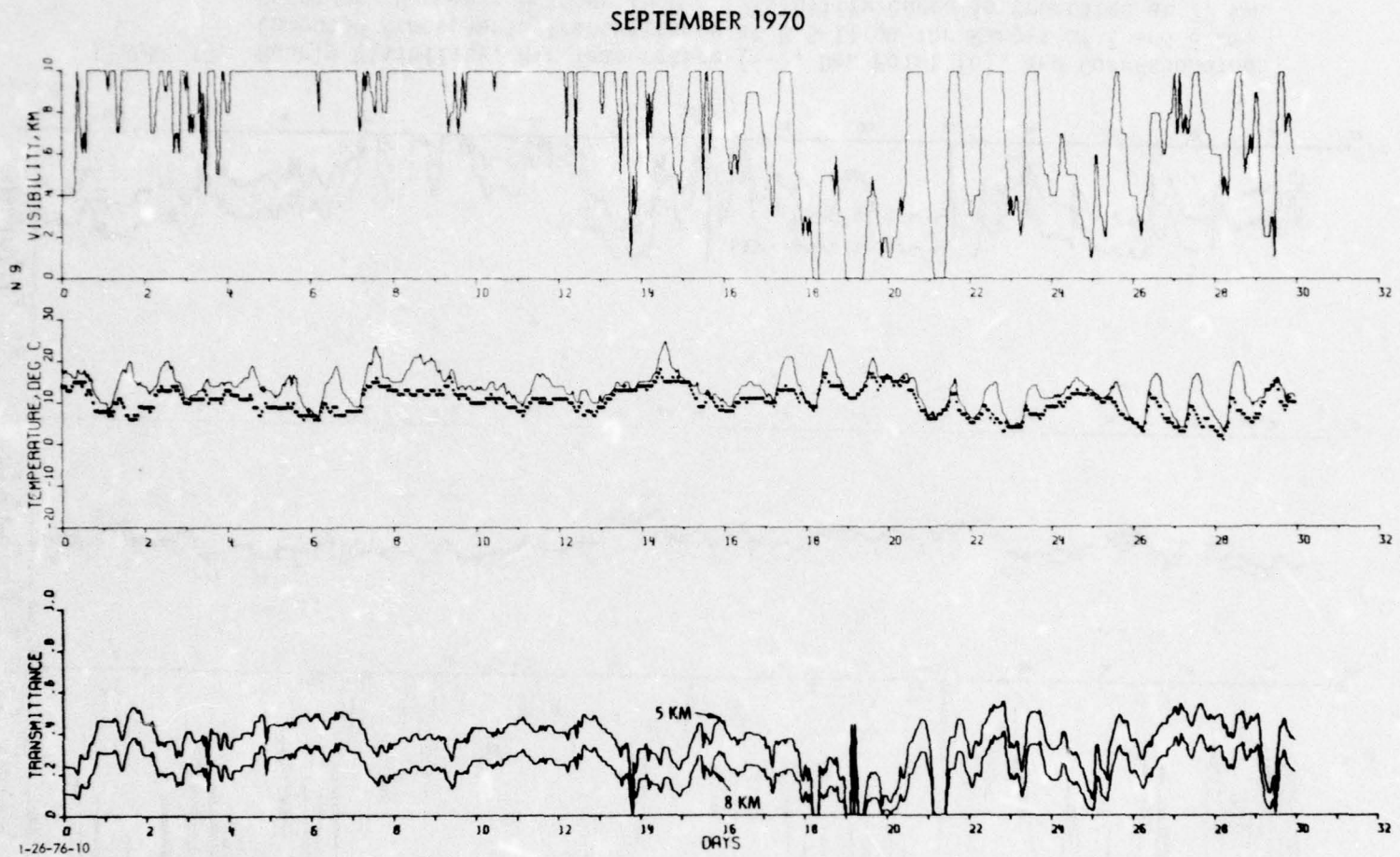


FIGURE 9. Hourly Visibility, Air Temperature (—), Dew Point (o), and Corresponding Computed Atmospheric Transmittance at 8.5-11 μm for Ranges of 5 and 8 km; Hannover, Germany; September 1970. (Visibility curve is truncated at 10 km. Each tick on abscissa marks end of a day.)

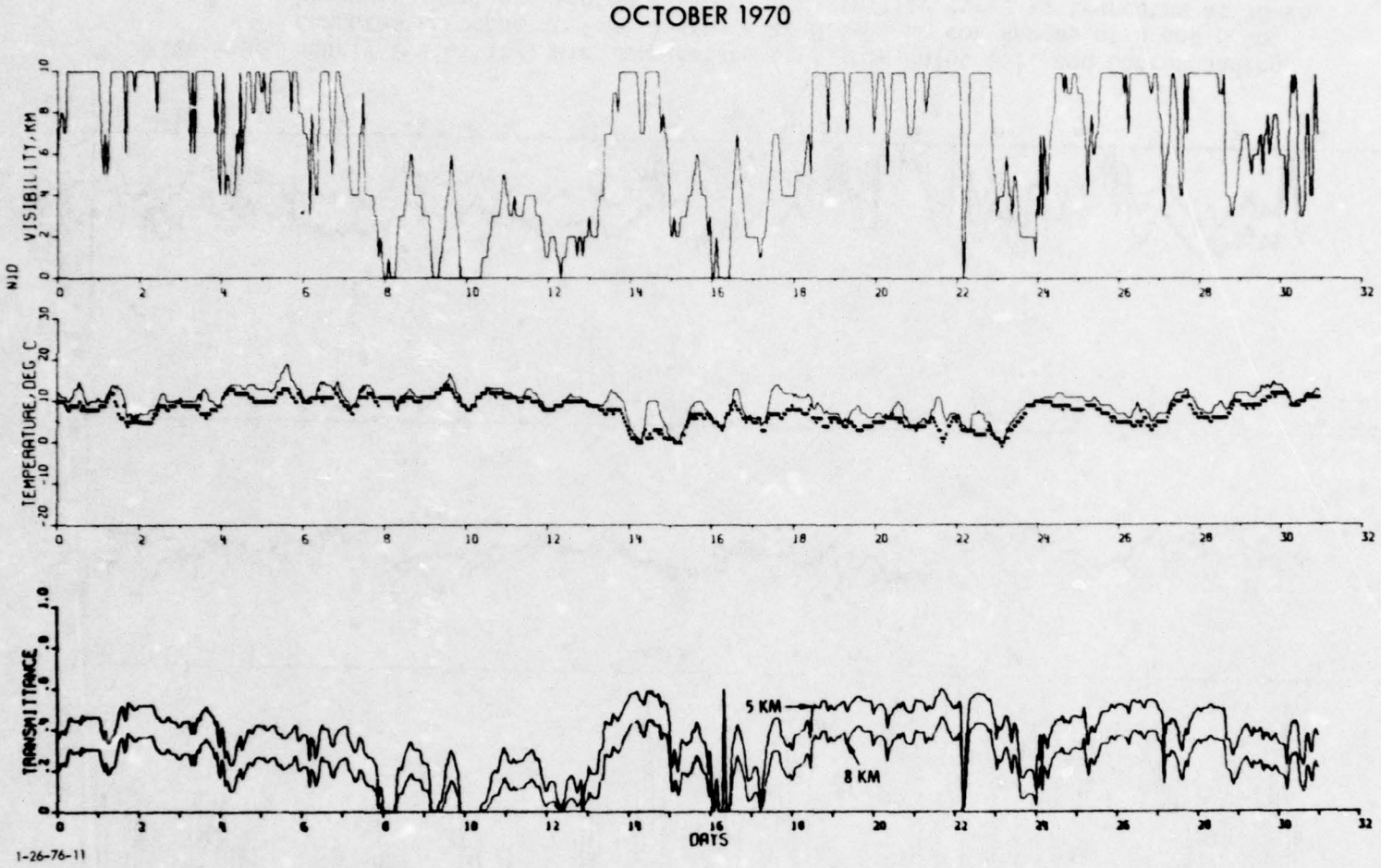


FIGURE 10. Hourly Visibility, Air Temperature (—), Dew Point (o), and Corresponding Computed Atmospheric Transmittance at 8.5-11 μm for Ranges of 5 and 8 km; Hannover, Germany; October 1970. (Visibility curve is truncated at 10 km. Each tick on abscissa marks end of a day.)

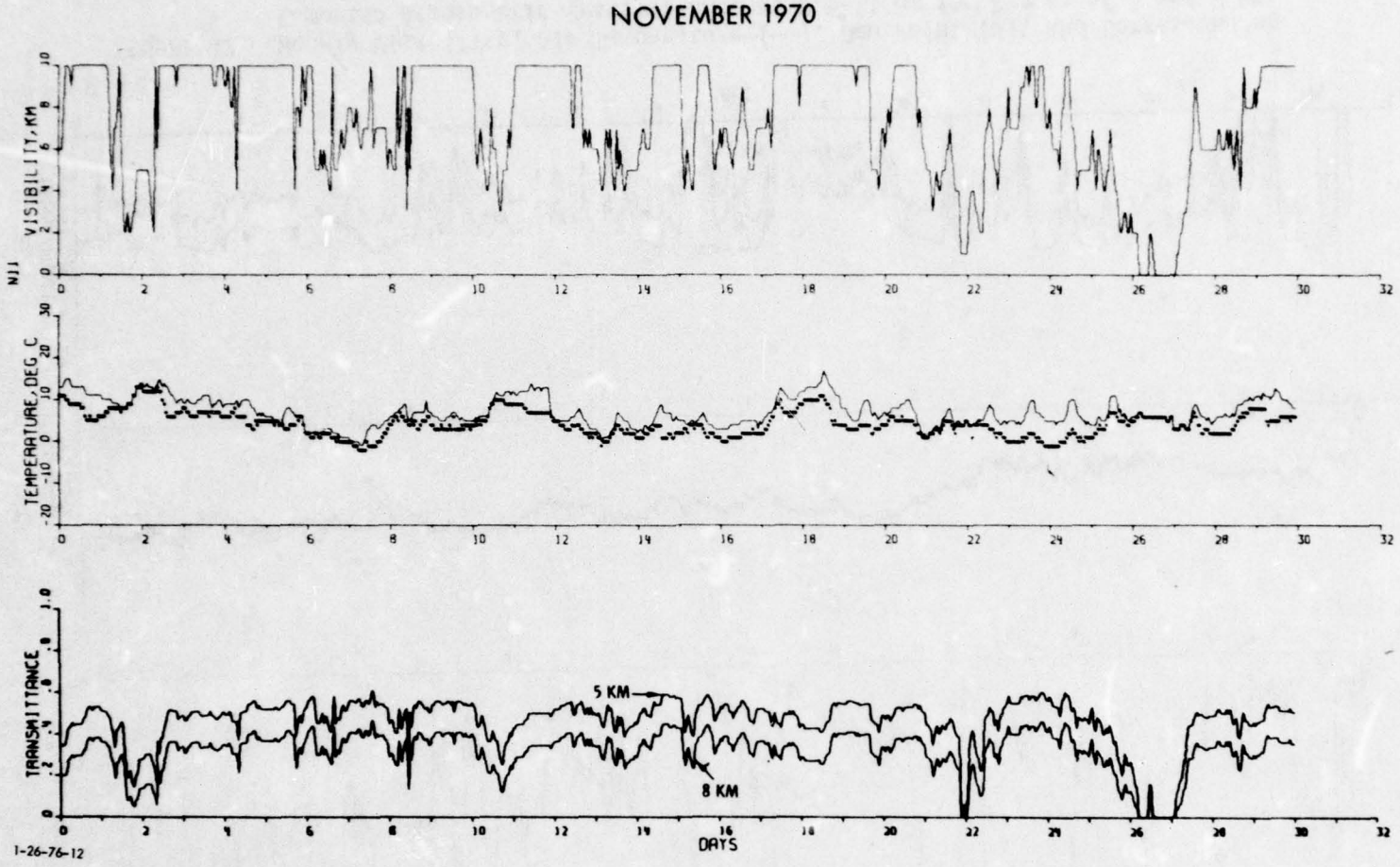


FIGURE 11. Hourly Visibility, Air Temperature (—), Dew Point (o), and Corresponding Computed Atmospheric Transmittance at 8.5-11 μm for Ranges of 5 and 8 km; Hannover, Germany; November 1970. (Visibility curve is truncated at 10 km. Each tick on abscissa marks end of a day.)

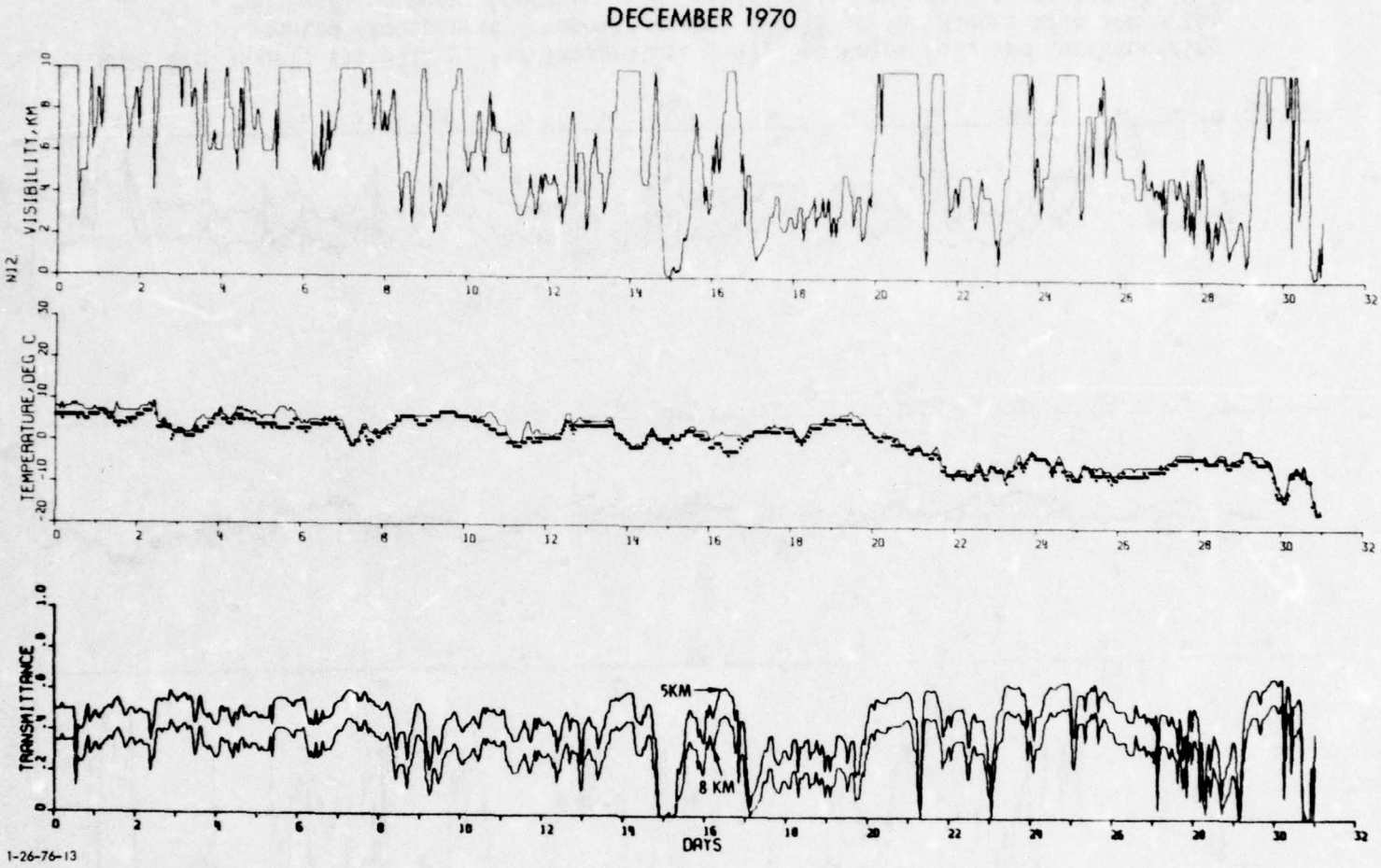


FIGURE 12. Hourly Visibility, Air Temperature (—), Dew Point (o), and Corresponding Computed Atmospheric Transmittance at 8.5-11 μm for Ranges of 5 and 8 km; Hannover, Germany; December 1970. (Visibility curve is truncated at 10 km. Each tick on abscissa marks end of a day.)

The May record (Fig. 5) is a good example for easy examination. The diurnal temperature oscillates, dipping toward the dew point early in the morning. On 3 May the temperature stayed close to the dew point for the entire day, resuming the diurnal cycle on 4 May. Note that the visibility on 3 May was very low, rising to normal levels on 4 May but showing the usual sharp dip the morning of 5 May. This effect recurs on the 13th and 30th.

E. VISIBILITY AS A MEASURE OF AEROSOL ATTENUATION

In the past, sensor performance was almost always predicted on the basis of computations of molecular absorption, while the effects of aerosol attenuation were ignored. Our data show, however, that extreme aerosols (e.g., heavy fog) can reduce atmospheric transmission of infrared and visible radiation far more severely than molecular absorbers.

Aerosols are difficult to measure. The instruments for their direct measurement are notorious for the poor data they provide in the hands of most operators. Visibility, which is relatively easy to measure, is therefore often taken as a useful indicator of aerosol concentrations and distributions. The modified LOWTRAN 3 mathematical model (Appendix A) that we use to calculate atmospheric transmittance in this study employs visibility as a measure of the aerosol attenuation that is of more direct concern.

F. SOME STATISTICS ON HOURLY VISIBILITY IN 1970

Figure 13 shows the fractions of hourly readings in which visibility at Hannover was equal to or less than indicated distances from 0 to 10 km in the year 1970, and Figs. 14-17 show comparable data for the four seasons of 1970. Figures 18-22 are histograms showing the numbers of hourly readings at Hannover in which the visibility was equal to indicated distances from 0 to 10 km for the year and for each of its seasons.

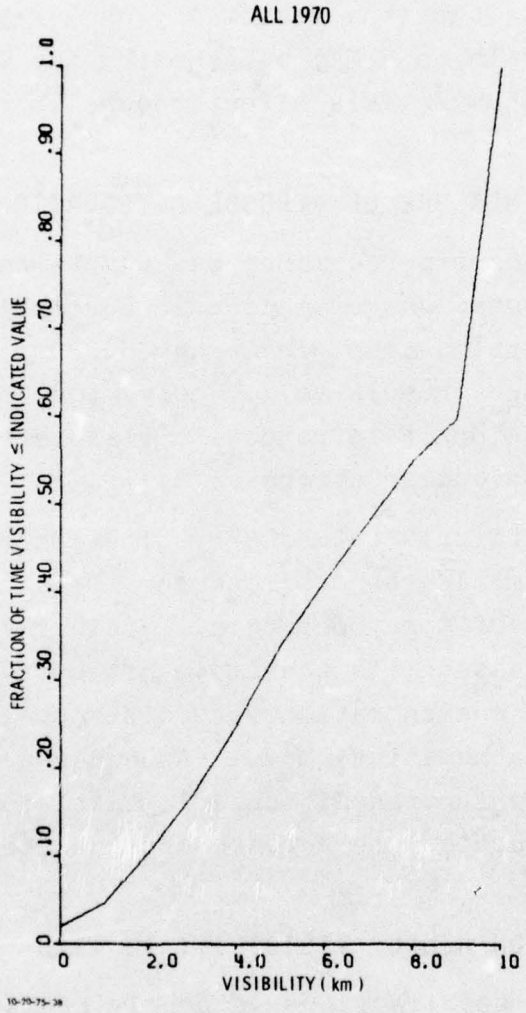


FIGURE 13. Fractions of Hourly Readings in Which Visibility at Hannover, Germany, was Equal to or Less than Indicated Distances from 0 to 10 km, All 1970. (Note effect of truncating "infinite" readings at 10 km.)

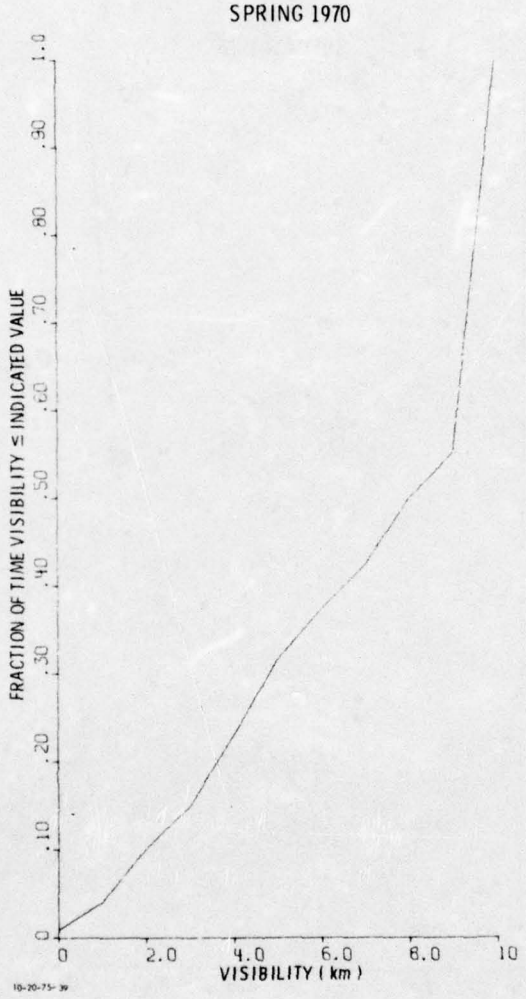


FIGURE 14. Fractions of Hourly Readings in Which Visibility at Hannover, Germany, was Equal to or Less than Indicated Distances from 0 to 10 km, Spring 1970. (Note effect of truncating "infinite" readings at 10 km.)

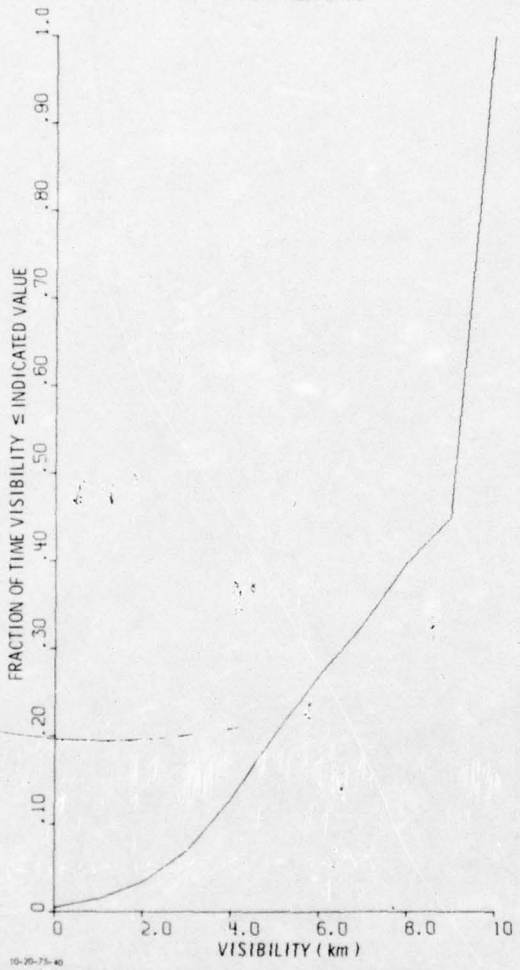


FIGURE 15. Fractions of Hourly Readings in Which Visibility at Hannover, Germany, was Equal to or Less than Indicated Distances from 0 to 10 km, Summer 1970. (Note effect of truncating "infinite" readings at 10 km.)

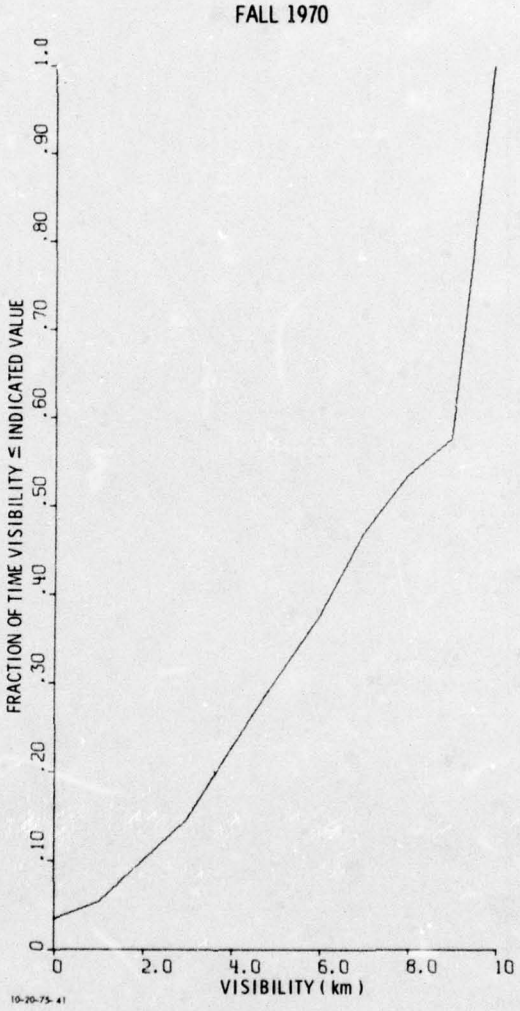


FIGURE 16. Fractions of Hourly Readings in Which Visibility at Hannover, Germany, was Equal to or Less than Indicated Distances from 0 to 10 km, Fall 1970. (Note effect of truncating "infinite" readings at 10 km.)

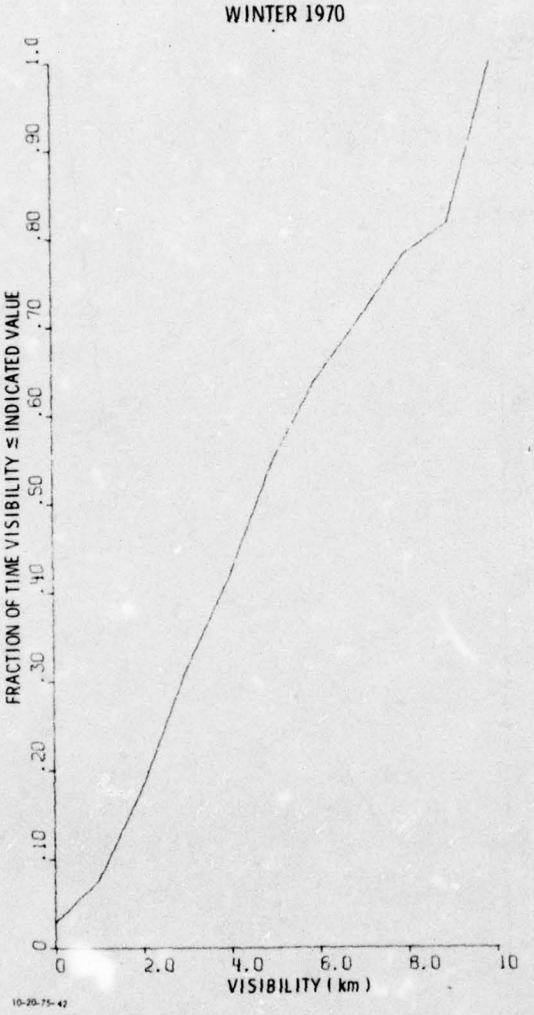


FIGURE 17. Fractions of Hourly Readings in Which Visibility at Hannover, Germany, was Equal to or Less than Indicated Distances from 0 to 10 km, Winter 1970. (Note effect of truncating "infinite" readings at 10 km.)

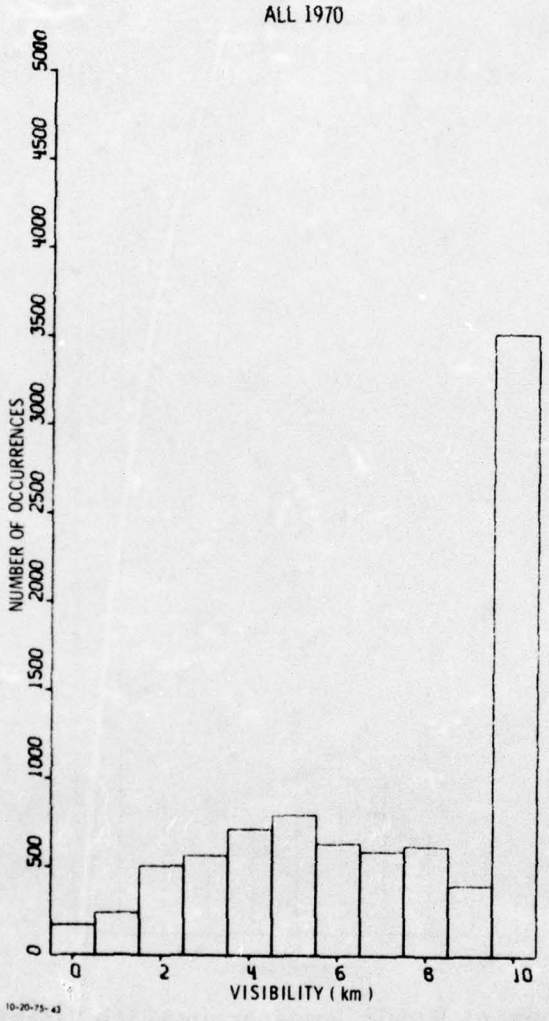


FIGURE 18. Numbers of Hourly Readings in Which Visibility at Hannover, Germany, was Equal to Indicated Distances from 0 to 10 km, All 1970. (Note effect of truncating "infinite" readings at 10 km.)

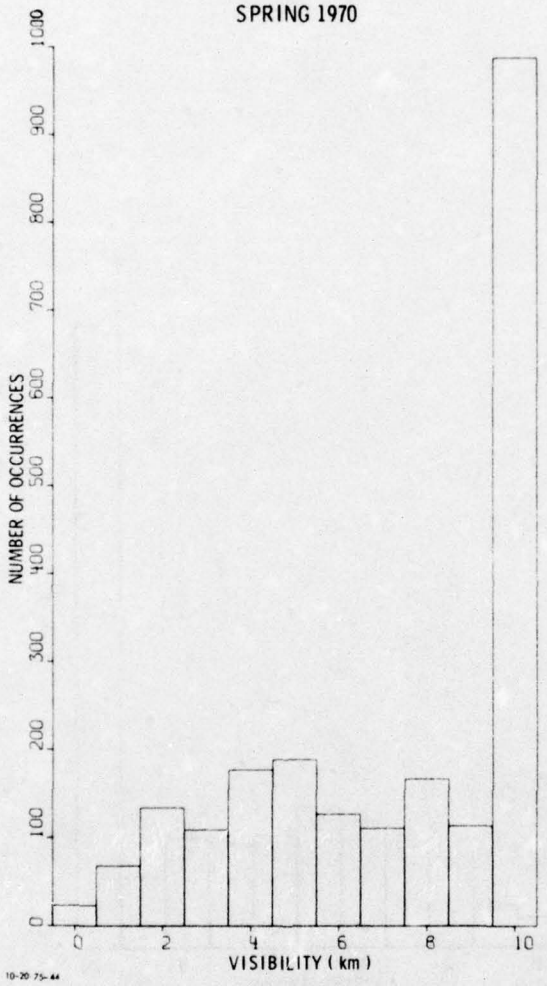


FIGURE 19. Numbers of Hourly Readings in Which Visibility at Hannover, Germany, was Equal to Indicated Distances from 0 to 10 km, Spring 1970. (Note effect of truncating "infinite" readings at 10 km.)

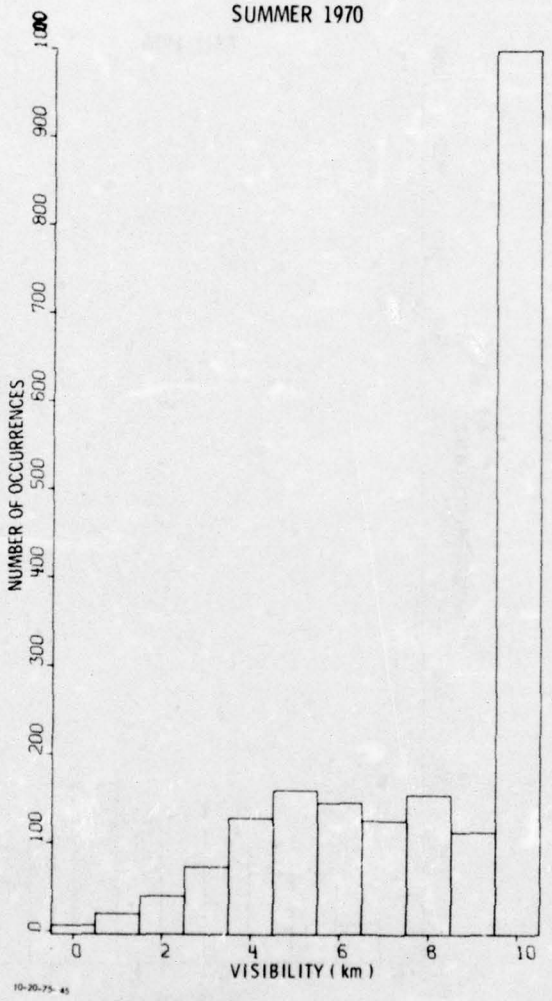


FIGURE 20. Numbers of Hourly Readings in Which Visibility at Hannover, Germany, was Equal to Indicated Distances from 0 to 10 km, Summer 1970. (Note effect of truncating "infinite" readings at 10 km.)

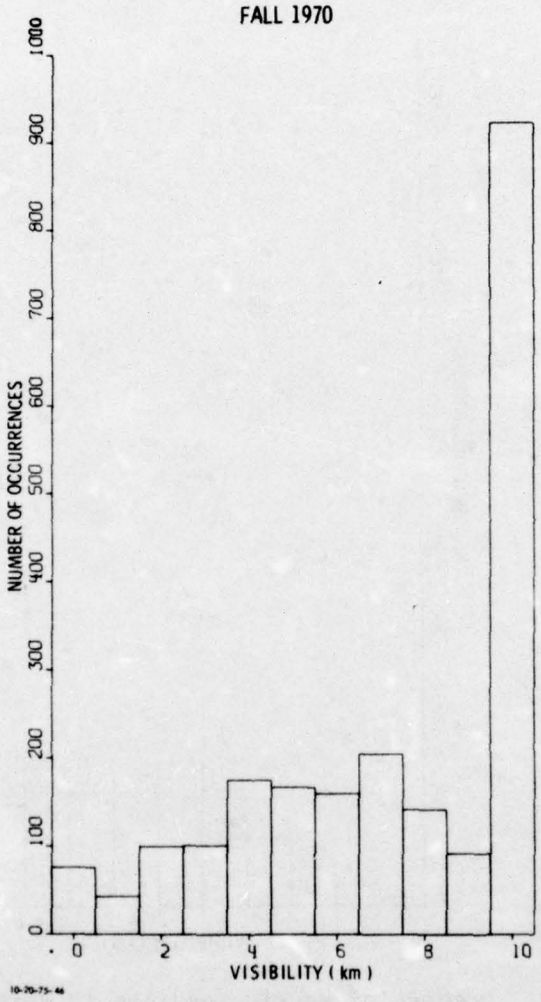


FIGURE 21. Numbers of Hourly Readings in Which Visibility at Hannover, Germany, was Equal to Indicated Distances from 0 to 10 km, Fall 1970. (Note effect of truncating "infinite" readings at 10 km.)

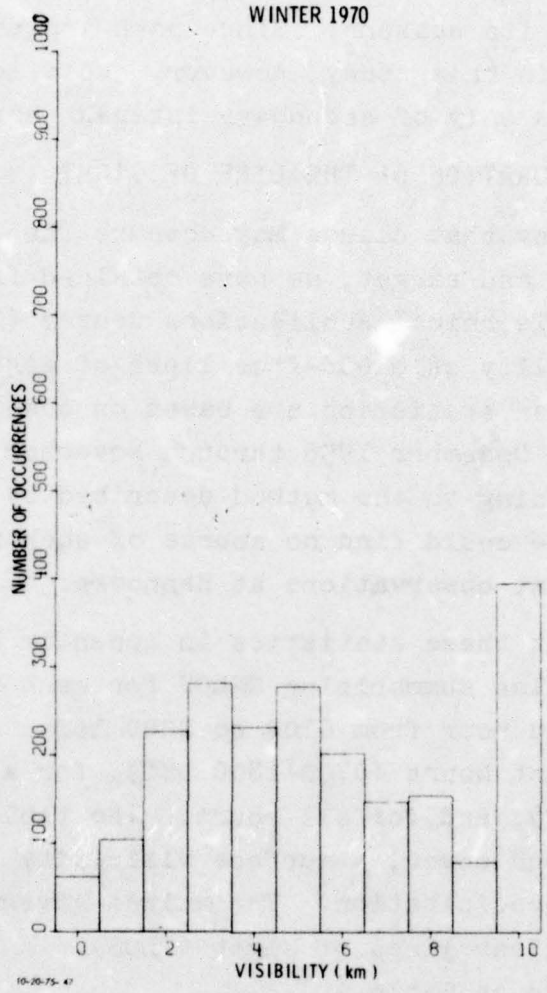


FIGURE 22. Numbers of Hourly Readings in Which Visibility at Hannover, Germany, was Equal to Indicated Distances from 0 to 10 km, Winter 1970. (Note effect of truncating "infinite" readings at 10 km.)

G. SOME STATISTICS ON HOURLY DEW POINT IN 1970

Because the dew point is important in calculations of atmospheric transmittance over very long path lengths, we show in Figs. 23-27 the fractions of hourly readings in which the dew point was at or below indicated temperatures in all of 1970 and in each of its seasons. Since path lengths exceeding 10 km do not figure in this study, however, the effect of dew point on transmission is only of secondary interest here.

H. CLOUD OBSCURATION OF THE LINE OF SIGHT

Recognizing that clouds may obscure the line of sight between aircraft and target, we have obtained from the USAF Environmental Technical Applications Center (ETAC) statistics on the probability of cloud-free lines of sight (CFLOS) at Hannover. These statistics are based on observations at 3-hour intervals from December 1956 through November 1971 and were computed according to the method described by Lund and Shanklin in Ref. 13. We could find no source of such statistics based on more frequent observations at Hannover.

We present these statistics in Appendix B, which is a collection of tables summarizing CFLOS for each month, averaged for every third hour from 0100 to 2200 local standard time (LST), for all daylight hours (0700-1800 LST), for all nighttime hours (1900-0600 LST), and for all hours. The tables are for various heights of cloud cover, a surface visibility of 2.5 miles or more, and no precipitation. The values given are considered estimates of clear lines of sight (CLOS). A sample of these tables is shown as Table 1.

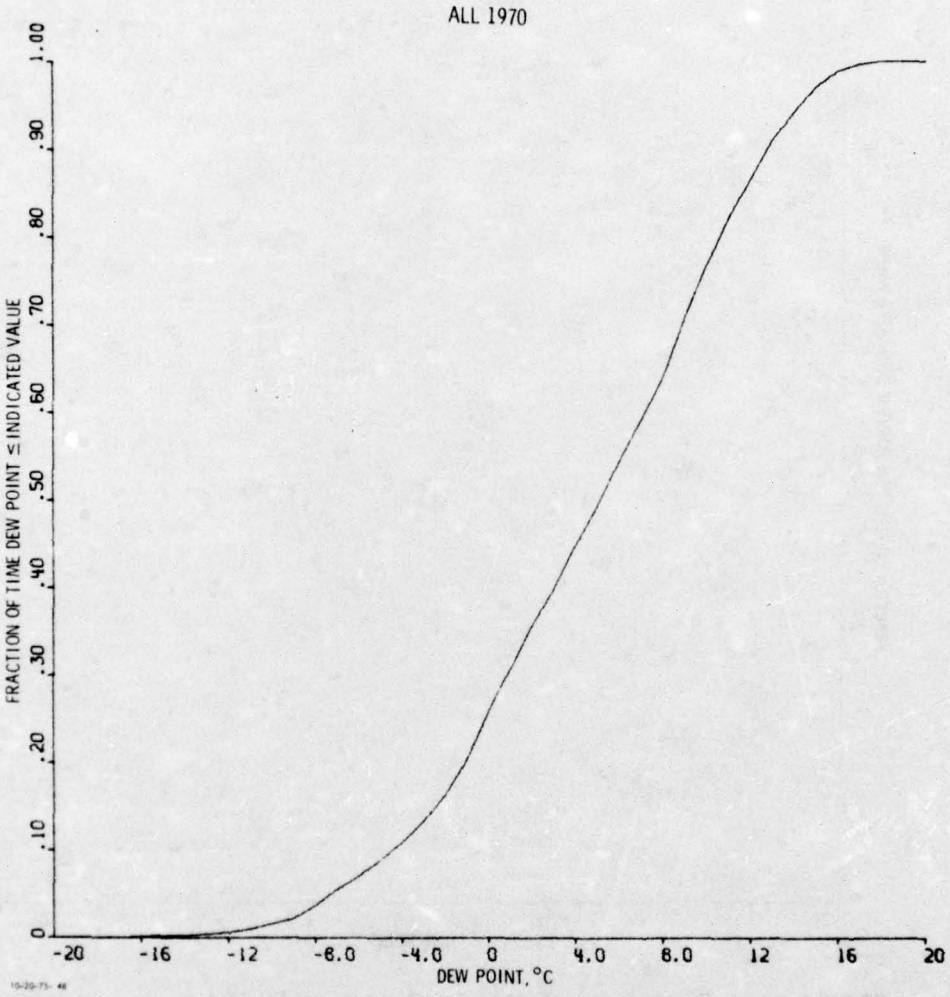


FIGURE 23. Fractions of Hourly Readings in Which Dew Point at Hannover, Germany, was at or below Indicated Temperatures, All 1970.

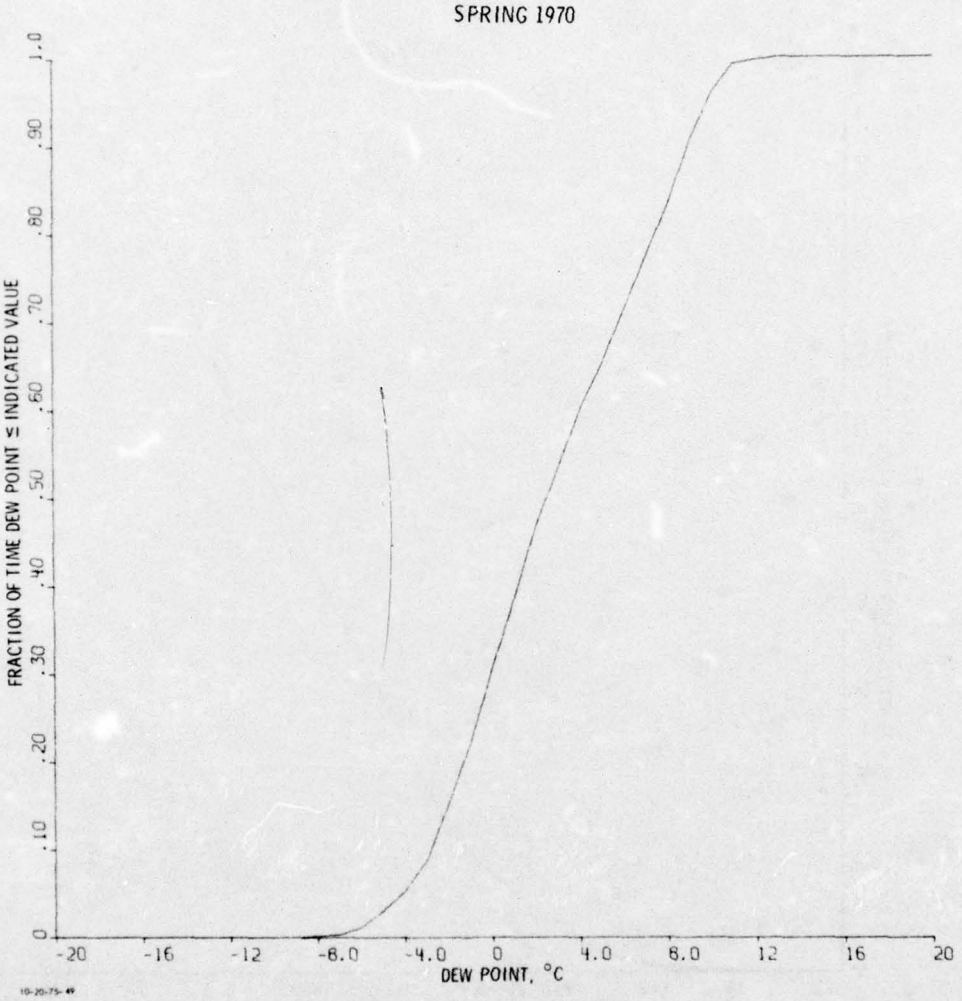


FIGURE 24. Fractions of Hourly Readings in Which Dew Point at Hannover, Germany, was at or below Indicated Temperatures, Spring 1970.

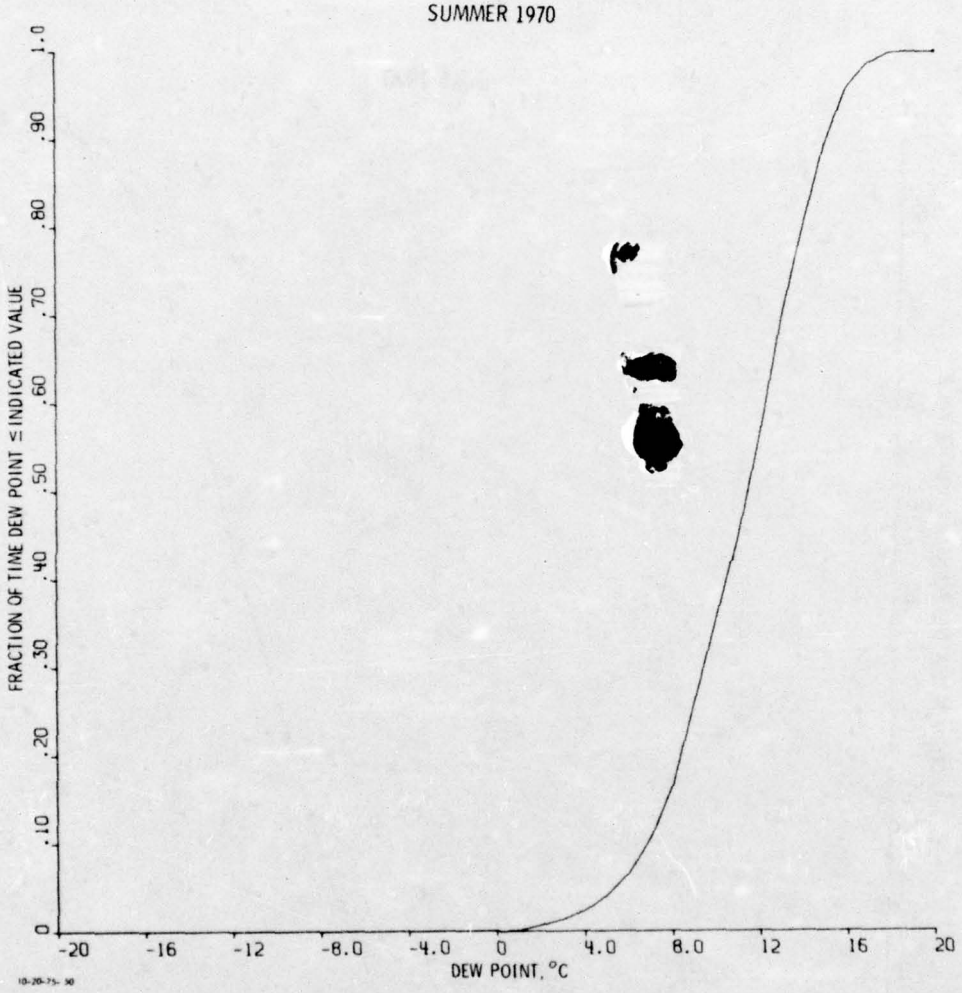


FIGURE 25. Fractions of Hourly Readings in Which Dew Point at Hannover, Germany, was at or below Indicated Temperatures, Summer 1970.

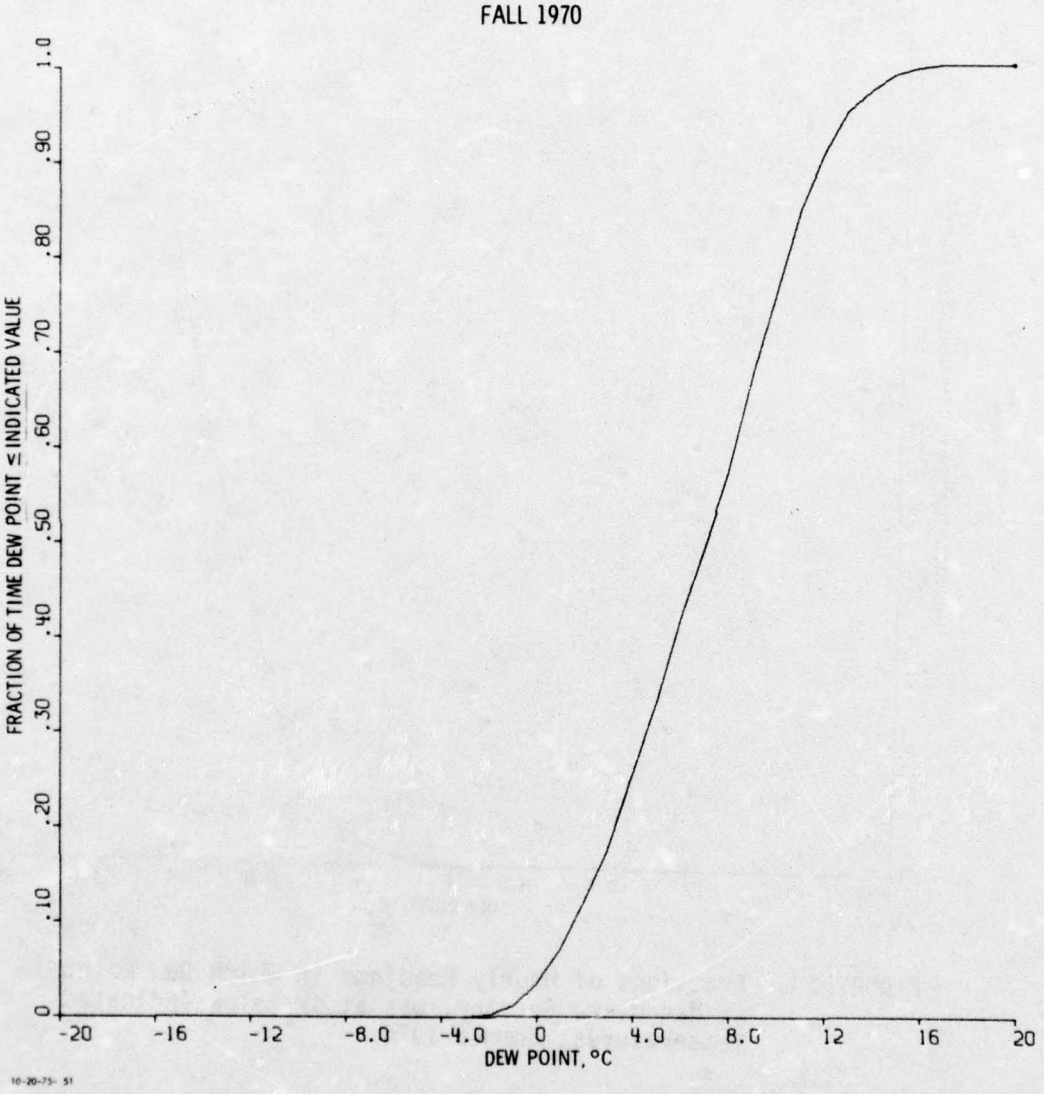


FIGURE 26. Fractions of Hourly Readings in Which Dew Point at Hannover, Germany, was at or below Indicated Temperatures, Fall 1970.

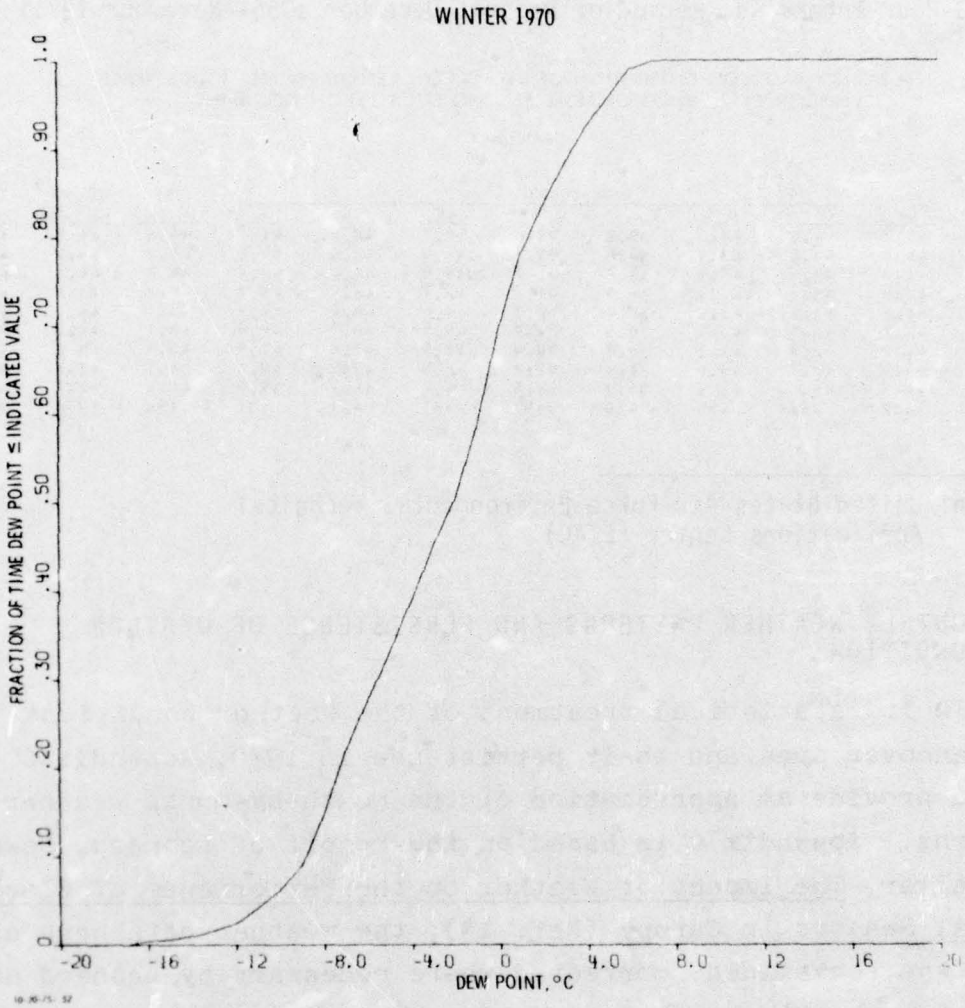


FIGURE 27. Fractions of Hourly Readings in Which Dew Point at Hannover, Germany, was at or below Indicated Temperatures, Winter 1970.

TABLE 1. AVERAGE PERCENTAGE PROBABILITIES IN JANUARY OF CLOUD-FREE LINES OF SIGHT BETWEEN GROUND AND INDICATED ALTITUDES ABOVE GROUND ALONG INDICATED VIEWING ANGLES AT HANNOVER, GERMANY[a]

(3-Hour Intervals; Period of Record: December 1956--November 1971)

PROBABILITY BASED ON DISTRIBUTION OF CLOUD COVER BELOW 984 FEET WITH SURFACE VISIBILITY OF 2.5 MILES OR MORE AND NO PRECIPITATION OCCURRING

JANUARY

Viewing (Elevation) Angle, deg	Hour (LST) 01	04	07	10	13	16	19	22	Day (07-18)	Night (19-06)	All
90	45.2	44.0	44.3	39.2	52.2	50.3	48.5	41.3	46.6	44.8	45.7
80	44.8	43.6	43.9	38.8	51.7	49.8	48.0	40.9	46.2	44.4	45.3
70	44.8	43.6	43.9	38.8	51.7	49.8	48.0	40.9	46.2	44.4	45.3
60	44.8	43.6	43.9	38.8	51.7	49.7	48.0	40.9	46.2	44.4	45.3
50	44.8	43.5	43.9	38.7	51.6	49.6	48.0	40.9	46.1	44.4	45.3
40	44.7	43.3	43.7	38.5	51.5	49.5	48.0	40.8	46.1	44.3	45.3
30	44.2	42.8	43.2	38.1	50.8	48.9	47.4	40.4	45.5	43.8	44.7
20	43.9	42.7	43.0	37.9	50.5	48.8	47.2	40.2	45.1	43.5	44.4
10	43.3	41.8	42.3	37.2	49.6	48.2	46.7	39.6	44.4	42.7	43.6
NO OBS	452	456	455	435	455	451	451	437	1796	1796	3592

[a]Source: United States Air Force Environmental Technical Applications Center (ETAC).

I. MONTHLY WEATHER PATTERNS AND PERSISTENCE OF WEATHER CONDITIONS

In its statistical treatment of the weather conditions in the Hannover area and their persistence in 1970, Appendix C should provide an appreciation of the month-by-month weather patterns. Appendix C is based on the report of Leonard, Sowell, and Waller, The Impact of Weather on the Performance of Electro-optical Sensors in Europe (Ref. 14), the weather data base of which was reexamined, corrected where necessary by Leonard et al., and put onto punched cards for our computations.

III. MODELING OF SENSOR PERFORMANCE IN THE ATMOSPHERE

In this study we model the performance of three kinds of electrooptical imaging sensors: FLIR, active television, and passive television. These sensors are rather well understood, as their performance against test patterns has been thoroughly studied in the laboratory. Field tests in the United States, England, and Germany have yielded results that closely match predicted values. M. H. A. Deller, of the Royal Aircraft Establishment, Farnborough, has told us informally that the results of recent careful field trials of FLIRs in England consistently matched predictions based upon our models.

The performance of electrooptical sensors depends heavily upon atmospheric transmission, which varies widely because of varying amounts of gaseous absorption and aerosol extinction. The effects of gaseous absorption are well researched and documented, but the effects of aerosol extinction are not.

Aerosol extinction has two components, absorption and scatter. To a rough first approximation, aerosol absorption and aerosol scatter can be about equal, depending upon the relative humidity, the constitution of the particles in the aerosol, and the wavelength of interest. For a fuller discussion, see Appendix A.

Aerosol effects are more important than gaseous absorption for infrared systems in the 8.5-11 μm radiation band, and

aerosols dominate in the near-visible region of low-light-level television.*

A. FORWARD-LOOKING INFRARED

Modeling of tank detection by 8.5-11 μm forward-looking infrared (FLIR) sensors comprises the following sequential steps suitable for computer programming:

1. The tank characteristics, including size, shape, and thermal signature distributions as well as a "temperature map," are extracted from appropriate thermal data prepared by J. R. Moulton of the U. S. Army Night Vision Laboratory and are inserted into our program so that dimensions and thermal properties will be properly scaled to range.

2. For 0.5-km intervals from 0.5 to 10 km, the LOWTRAN 3 model (Appendix A) is used to compute the hourly atmospheric transmittance from the weather data.

3. Rosell's equivalent-bar-pattern method (Section IV-A) is used to specify the appropriate spatial frequencies for computations of probability of detection (or recognition).

4. The signal-to-noise ratios are calculated for the specified spatial frequencies.

5. The signal-to-noise ratio at the appropriate spatial frequency is entered into the cumulative normal distribution curve (Fig. 29) to determine the probability of detection or recognition (Chapter IV).

---

*For television sensors, two effects of aerosol scatter are important. One is due to image radiant power scattered out of the viewing path. The other is due to nonimage radiant power scattered into the beam, thus diluting the contrast that <u>is</u> the image.

6. The data are put in disk storage for random computer access, and the data file is then interrogated with such questions as:

   - What was the hour-by-hour range for a 50% probability of detection in April for a given FLIR?
   - What was the hour-by-hour probability of detection in April for a specified range for that FLIR?
   - What was the frequency of probabilities of detection less than 20% for a given range, a given time of year, and a given FLIR?
   - How long did such low-probability periods persist?

7. The answers to these and other questions are tabulated or plotted.

B. ACTIVE TELEVISION

The basic procedure for modeling the performance of 0.86 μm active television is as follows:

1. The Equivalent Scene--Real objects are of infinite variety. While rather exact methods of describing any particular object under known conditions are available, the exact methods are too time-consuming and costly to use. Therefore, the real object is replaced by an equivalent bar pattern of similar contrast and reflectivity, of length equal to the real object, and of spatial frequency appropriate to the desired level of discrimination desired. The equivalent bar pattern is assumed to be normal to the line of sight.

2. System Light Source--The source of scene irradiation is located adjacent to the TV camera. The source wavelength is essentially monochromatic at 0.86 μm, and light is emitted in short pulses of 2-6 μsec duration at the line rate (15.75 kHz for a conventional system) or at some submultiple of the line rate

such as 1/2 or 1/4. In good design, the field of view of the source is matched to that of the sensor.

3. Sky Condition--The sky condition, whether overcast or clear, is irrelevant to active TV as long as a clear line of sight exists between scene and sensor and the sky is not so bright as to provide a competing passive image during the period of the gated sensor.

4. Aerosol Extinction--The LOWTRAN 3 model (Appendix A) is used to calculate atmospheric transmittance for each leg of the transmission path.

5. Atmospheric Degradation of Image Contrast--The equivalent bar pattern is assumed to be at the near edge of the range-gate interval, in which case the image contrast is not degraded by the atmosphere. Very little apparent contrast loss has been noted in practice, but active TV equipment has not been flown in conditions of very low visibility.

6. System Parameters--The primary system parameters included in the analysis are the field of view, the lens diameter, the image sightline instability, and the modulation transfer functions of the lens, the image intensifier, and the TV camera tube. The overall camera tube gain before readout by the electron beam is high enough to eliminate preamplifier noise as a consideration.

7. Observer Parameters--The two levels of visual discrimination considered are detection and recognition. The equivalent bar pattern for the frontal aspect of a tank is square, and either two or eight lines (one or four cycles) are assumed to encompass the scene object. The display signal-to-noise ratio is used to determine the threshold range(s) for any given level of probability.

C. PASSIVE TELEVISION

The basic procedure for modeling the performance of passive television is as follows:

1. The Equivalent Scene--As in the modeling of active TV, the real object is replaced by an equivalent bar pattern of similar contrast and reflectivity, of length equal to the real object, and of spatial frequency appropriate to the desired level of visual discrimination. The equivalent bar pattern is assumed to be diffusely reflecting and normal to the line of sight.

2. Scene Irradiance--The scene object and background are assumed to be neutral gray with respect to spectral reflectivity. One can then calculate the sensor signal currents knowing the spectral irradiance of the scene and the spectral responsivity of the TV camera. Alternatively, an equivalence between scene illuminance and scene effective irradiance can be generated. In this case, the scene light level and the sensor's luminous response can be used together with the equivalence factor.

3. Sky Conditions--The sky condition, whether clear or overcast, determines the sky-to-ground brightness ratio, which can have a rather drastic effect on image contrast.

4. Atmospherics--The atmospheric extinction coefficient is first calculated for the average sensor wavelength. Usually, TV sensors are spectrally filtered to pass only the 0.6 to 0.8 μm band, and the average wavelength is then 0.7 μm. By using the atmospheric extinction coefficient and the sky-to-ground brightness ratio, the apparent image contrast is calculated as a function of range.

5. System Parameters--The primary system parameters included in the analysis are the field of view, the lens diameter, the image sightline instability, and the modulation transfer functions of the lens, the image intensifier, and the TV camera tube. Except under unusual conditions (very low light levels and low contrast, or very high light levels), the sensor gain is sufficiently high to eliminate preamplifier noise as a problem.

6. Observer Parameters--The two levels of visual discrimination considered are detection and recognition. The equivalent bar pattern for the frontal aspect of a tank is square, and either two or eight lines (one or four cycles) are assumed to encompass the scene object. The display signal-to-noise ratio is used to determine the threshold range(s) for any given level of probability.

IV. PROBABILITY OF DETECTION OR RECOGNITION

A. GENERAL FOUNDATIONS

In past work, Rosell has discovered (Ref. 15), and, with Willson, has shown (Refs. 6, 7, 16) that the ability of an observer to detect, recognize, or identify an object in a displayed image is best predicted by the signal-to-noise ratio of the object's image. Further, Rosell has developed the concept of the equivalent bar pattern.

This concept goes back to the work of John Johnson (Ref. 17), who showed that an observer who could just detect, recognize, or identify an object such as a man or a vehicle could also just resolve one, four, or six and one-half pairs of black and white bars (or a typical photographic resolution chart) when one, four, or six and one-half pairs of such bar widths fit inside the critical (usually the minor) dimension (Tables 2 and 3).

TABLE 2. JOHNSON'S LEVELS OF OBJECT DISCRIMINATION

Classification of Discrimination Level	Meaning
Detection	An object is present.
Orientation	The object is approximately symmetric or asymmetric and its orientation may be discerned.
Recognition	The class to which the object belongs may be discerned (e.g., house, truck, man).
Identification	The target can be described to the limit of the observer's knowledge (e.g., motel, pickup truck, policeman).

TABLE 3. JOHNSON'S CRITERIA FOR THE RESOLUTION REQUIRED PER MINOR DIMENSION OF AN OBJECT VERSUS DISCRIMINATION LEVEL

Discrimination Level	Resolution per Minor Dimension of an Object, TV lines
Detection	$2.0^{+1.0}_{-0.5}$
Orientation	$2.8^{+0.8}_{-0.4}$
Recognition	$8.0^{+1.6}_{-0.4}$
Identification	$12.8^{+3.2}_{-2.8}$

Little more was said about the concept in a quantitative sense until Rosell's work, referenced above. Here it became clear that the work done by Johnson related the number of line pairs of a bar chart corresponding to the minor dimension of an object with the ability of an observer to detect, recognize, or identify the object liminally, i.e., at the level of 50% probability.

Rosell went further to establish the concept of the equivalent bar pattern illustrated in Fig. 28. In this concept, a bar pattern is created equivalent in dimensions to the object to be viewed. For various increasingly difficult visual tasks, the bar pattern is composed of increasingly narrow bars, according to the demands of Johnson's criteria. If the sensor in question produces an image of the bar chart that permits an observer to "break out" the individual bars in the pattern 75% of the time, that observer should, for example, be able to recognize the real object 75% of the time if the equivalent bar pattern were composed for four pairs of black and white bars.

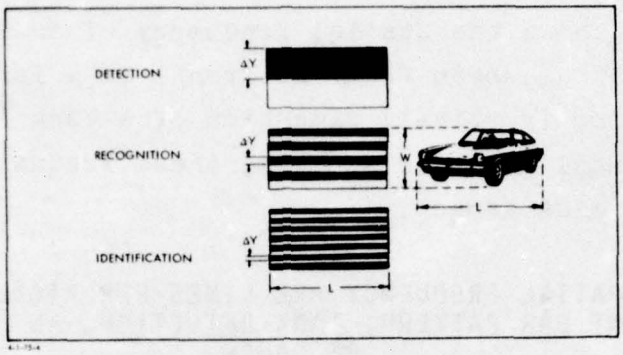


FIGURE 28. Resolution Required per Minor Dimension of Object to Achieve a Given Level of Object Discrimination, Expressed in Terms of an Equivalent Bar Pattern.

The concept of the equivalent bar pattern is a little more complex than this, however, in that it specifies that if the signal-to-noise ratio in the image of a single bar is some value as specified in Table 4, and if the size (and therefore the spatial frequency) of that bar is as required by the equivalent bar pattern, the observer has a 50% probability of achieving the desired discrimination level.

TABLE 4. BEST ESTIMATE OF THRESHOLD SNR_D FOR DETECTION, RECOGNITION, AND IDENTIFICATION OF IMAGES

Discrimination Level	Background	k_d, TV lines per minor dimension of target	Threshold SNR_D[a] for a Single Bar of Spatial Frequency (in lines/picture height) equal to			
			100	300	500	700
Detection	Uniform[b]	1	2.8	2.8	2.8	2.8
Detection	Clutter	2	4.8	2.9	2.5	2.5
Recognition	Uniform	8	4.8	2.9	2.5	2.5
Recognition	Clutter	8	6.4	3.9	3.4	3.4
Identification	Uniform	13	5.8	3.6	3.0	3.0

[a] For a viewing-distance-to-picture-height ratio of 3.5.

[b] Treated as an aperiodic object.

Table 5 shows the spatial frequency of an equivalent bar pattern for a tank seen from the front, as a function of range. Since the minor (vertical) dimension of a tank is the same in both the frontal and side aspects, these frequencies would also apply to the side aspect.

TABLE 5. SPATIAL FREQUENCY AND LINES PER PICTURE HEIGHT FOR EQUIVALENT BAR PATTERN, TANK DETECTION, AS A FUNCTION OF RANGE

Distance, km	Target Angle, mrad	Bar Angle, mrad	Lines Per Picture Height for Field of View Indicated[a]			
			2.5°	5.0°	7.5°	10.0°
0.5	7.8	3.9	9	18	27	36
1.0	3.9	1.95	18	36	53	71
1.5	2.6	1.3	27	53	80	107
2.0	1.95	0.975	36	71	107	142
2.5	1.56	0.78	45	89	134	178
3.0	1.30	0.65	53	107	160	214
3.5	1.11	0.55	63	126	189	252
4.0	0.975	0.48	72	145	215	289
4.5	0.867	0.44	79	158	236	316
5.0	0.780	0.39	88	178	266	356
5.5	0.709	0.36	96	193	289	386
6.0	0.650	0.33	105	210	315	420
6.5	0.600	0.30	116	231	347	463
7.0	0.557	0.28	124	248	371	435
7.5	0.520	0.26	134	267	400	533
8.0	0.487	0.24	145	289	433	578
8.5	0.459	0.23	151	302	453	603
9.0	0.433	0.22	158	316	473	630
9.5	0.411	0.21	163	334	496	661
10.0	0.390	0.20	174	347	521	694

[a]The fields of view shown are in the horizontal dimension. Usually, the vertical dimension is three-fourths of the horizontal. The lines per picture height are therefore taken across three-fourths of the horizontal dimension.

For a distance indicated in Column 1 of Table 5, the frontal aspect of the tank target subtends an angle in milliradians shown in Column 2. The equivalent bar width for the detection model is shown in Column 3. The bar widths in lines per picture height for four fields of view are shown in Columns 4-7.

For any probability other than 50%, the value of the signal-to-noise ratio needs to be adjusted according to the Gaussian form shown in Fig. 29. Here the value of 50% probability is related to a normalized SNR_D of 1.0, and other probabilities require greater or lesser values, i.e., 90% probability corresponds to 1.5, and 10% probability corresponds to 0.5. To compute the signal-to-noise value for, say, 90% or 10% probability, these normalization constants would be applied to the signal-to-noise value for 50% probability. That is, if a signal-to-noise ratio of 2.8 is required for 50% probability of detection, 1.5 x 2.8 is required for 90% probability of detection, and 0.5 x 2.8 is required for 10% probability of detection.

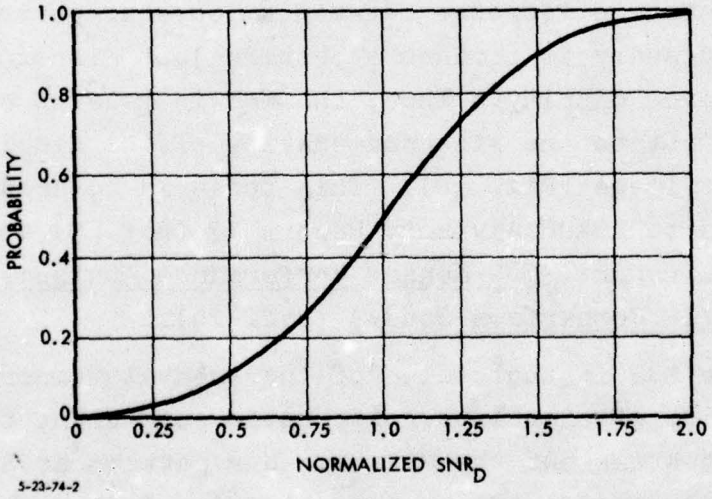


FIGURE 29. Normalized Display Signal-to-Noise Ratio.

For a range of object sizes (and thus for a range of spatial frequencies), a range of signal-to-noise ratios is indicated, rather than a single value. This effect is due to the decreasing efficiency of the eye as an integrator for images larger than a given angular size.

The details of this topic will not be given here but can be found primarily in Chapter 5 and the related Chapter 4 of Perception of Displayed Information (Refs. 6, 18), and in Low-Light-Level Devices: A Designers' Manual (Ref. 19). These two texts give detailed equations and other data for analyzing the performance of image-forming devices.

B. FORWARD-LOOKING INFRARED

1. Minimum Resolvable Temperature

For image-forming infrared devices such as forward-looking infrared (FLIR) sensors, a new concept has grown up that is closely related to the material above. The concept is that of minimum resolvable temperature (MRT). The MRT is the incremental temperature difference between a four-bar pattern and its background necessary to produce a pattern just discernible to a viewer on a given display. Thus, the MRT is related not only to the device but to the size and quality of the display producing the output image (Fig. 30). This topic is covered in detail in an Appendix to AGARD Advisory Report 73 (Ref. 5) and in the Sendall-Rosell report, E/O Sensor Performance Analysis and Synthesis (TV/IR Comparison Study) (Ref. 20).

Since the MRT is that value of incremental temperature that produces a value of signal-to-noise ratio sufficient to allow an observer to break out the MRT test bar pattern at 50% probability, $\frac{\Delta T}{MRT}$ corresponds to the normalization factor relating signal-to-noise to probability, where ΔT is the incremental difference in temperature between the target and its background.

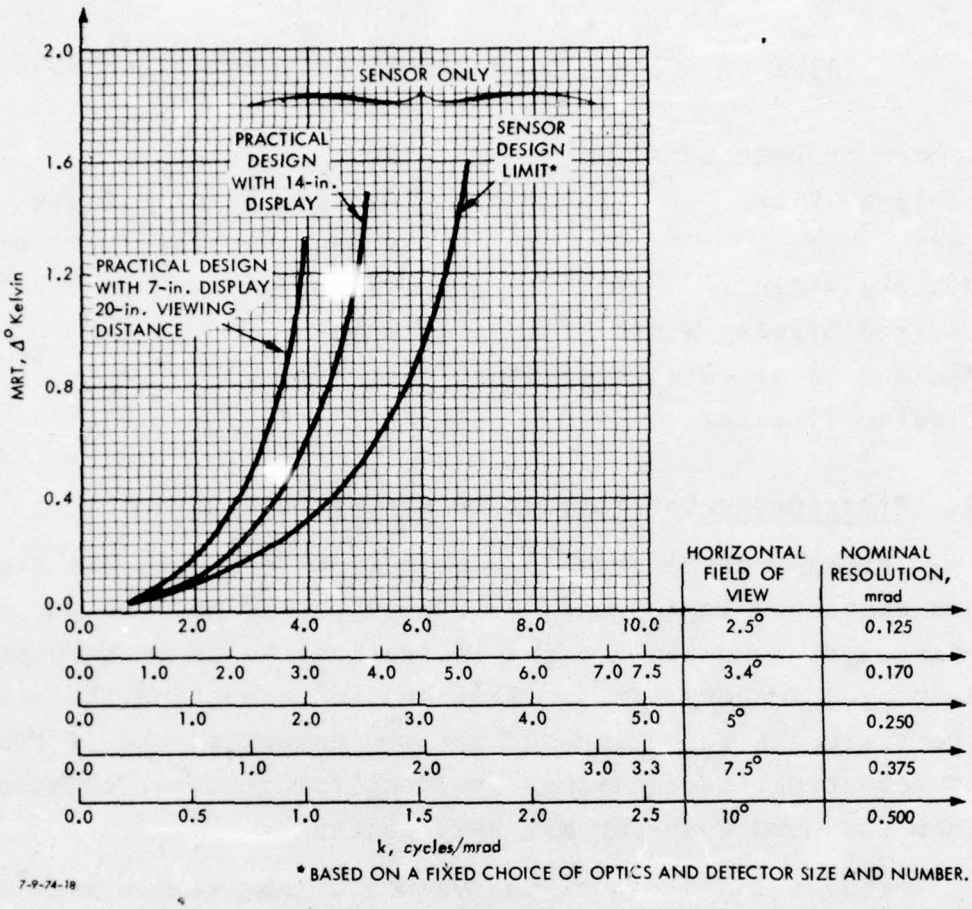


FIGURE 30. Typical MRT Curves

MRT curves such as those in Fig. 30 represent the ability of an observer to resolve vertical bar patterns with a horizontally scanning FLIR. Unless specific care is taken to compensate for the usual scanning modes, the vertical performance will fall appreciably short of these values. It is unfortunately true that the MRT is rarely measured against horizontal bars with a horizontally scanning FLIR.

2. FLIR Characteristics

Table 6 lists the characteristics of the family of FLIRs considered in this paper. The members of the family have basic FLIR bodies with interchangeable fore optics to produce the various fields of view discussed.

TABLE 6. FLIR SYSTEM PARAMETERS, 1974 TECHNOLOGY

Number of Detectors	180
Field of View	10, 7.5, 5, or 2.5 deg
Lens	As required for field of view
Display Width	7.2 in.
Desired Display Width	14 in.
Minimum Resolvable Temperature	See Fig. 30
Viewing Distance	20-28 in.

3. First-Order Corrections to Bar-Pattern Data

First-order corrections to bar-pattern data are explained and discussed in Appendix D. Though it is not the purpose of this paper to establish the theoretical basis of perception of displayed imagery, it is important to understand the means and the rationale for using MRT data to establish the probability of detecting, recognizing, or identifying actual objects rather than standard four-bar MRT test patterns.

Tables 7 and 8 show the values of MRT versus spatial frequency for the standard-aspect bar target and for an equivalent bar pattern representing the frontal aspect of a tank in which the individual bars exhibit a length-to-width (aspect) ratio ε of approximately 2:1. These two tables show the uncorrected MRT values (Table 7) as well as the bar-aspect corrected values (Table 8). The reason for applying the aspect correction and the means for calculating it are discussed in Appendix D.

As explained in Appendix D, $\Delta T/(MRT/\sqrt{\varepsilon/7})$ is used to establish the signal-to-noise ratio in an image and/or the probability that the equivalent bar pattern or its counterpart object will be detected or recognized.

One further important approximation concerning the computation of ΔT at the sensor is used in this work. It can be shown (Refs. 5, 20) that if a small incremental temperature difference

TABLE 7. MINIMUM RESOLVABLE TEMPERATURE, UNCOMPENSATED FOR ASPECT RATIO ε, TABULATED FOR FOUR FIELDS OF VIEW AND TWO DISPLAY SIZES AND FOR SPATIAL FREQUENCIES CORRESPONDING TO THE ANGLES SUBTENDED BY A SUBJECT AT VARIOUS RANGES

Range, km	Angle, mrad	Spatial Frequency, cycles/mrad	Minimum Resolvable Temperature, $\Delta^{\circ}K$							
			2.5-deg FOV		5-deg FOV		7.5-deg FOV		10-deg FOV	
			Large Display	7-in. Display	Large Display	7-in. Display	Large Display	7-in. Display	Large Display	7-in. Display
.5	7.900	.128	.010	.010	.010	.010	.010	.010	.010	.010
1.0	3.900	.256	.010	.010	.010	.010	.010	.010	.051	.063
1.5	2.600	.385	.010	.010	.010	.010	.068	.079	.097	.127
2.0	1.950	.513	.010	.010	.061	.063	.087	.127	.131	.213
2.5	1.560	.641	.010	.010	.074	.095	.114	.185	.242	.349
3.0	1.300	.769	.010	.010	.087	.127	.187	.277	.322	.569
3.5	1.114	.897	.010	.010	.105	.159	.264	.389	.476	.834
4.0	.975	1.026	.061	.063	.131	.213	.322	.570	.671	1.240
4.5	.867	1.154	.068	.079	.187	.277	.432	.757	.953	
5.0	.780	1.282	.074	.095	.242	.349	.566	1.154	1.390	
5.5	.709	1.410	.081	.111	.283	.428	.736	1.240		
6.0	.650	1.538	.087	.127	.322	.569	.963			
6.5	.600	1.667	.095	.143	.387	.707	1.391			
7.0	.557	1.795	.105	.159	.476	.834	1.390			
7.5	.520	1.923	.114	.185	.566	1.154				
8.0	.487	2.051	.131	.213	.671	1.240				
8.5	.459	2.179	.159	.245	.799					
9.0	.433	2.308	.187	.277	.963					
9.5	.411	2.436	.214	.311	1.206					
10.0	.390	2.564	.242	.349	1.380					

TABLE 8. MINIMUM RESOLVABLE TEMPERATURE, COMPENSATED FOR ASPECT RATIO ε, TABULATED FOR FOUR FIELDS OF VIEW AND TWO DISPLAY SIZES AND FOR SPATIAL FREQUENCIES CORRESPONDING TO THE ANGLES SUBTENDED BY A SUBJECT AT VARIOUS RANGES

Range, km	Angle, mrad	Spatial Frequency, cycles/mrad	Minimum Resolvable Temperature, $\Delta^{\circ}K$							
			2.5-deg FOV		5-deg FOV		7.5-deg FOV		10-deg FOV	
			Large Display	7-in. Display	Large Display	7-in. Display	Large Display	7-in. Display	Large Display	7-in. Display
.5	7.800	.128	.010	.010	.010	.010	.010	.010	.010	.010
1.0	3.900	.256	.010	.010	.010	.010	.010	.010	.115	.119
1.5	2.600	.385	.010	.010	.010	.010	.127	.148	.153	.239
2.0	1.950	.513	.010	.010	.115	.118	.163	.238	.245	.398
2.5	1.560	.641	.010	.010	.139	.178	.214	.345	.459	.653
3.0	1.300	.769	.010	.010	.163	.238	.349	.518	.602	1.065
3.5	1.114	.897	.010	.010	.196	.298	.494	.725	.891	1.560
4.0	.975	1.026	.115	.118	.245	.398	.602	1.065	1.256	2.320
4.5	.867	1.154	.127	.148	.349	.518	.808	1.417	1.802	
5.0	.780	1.282	.139	.178	.453	.653	1.059	2.160	2.592	
5.5	.709	1.410	.151	.208	.530	.801	1.376	2.320		
6.0	.650	1.538	.163	.238	.602	1.065	1.803			
6.5	.600	1.667	.178	.268	.723	1.322	2.593			
7.0	.557	1.795	.196	.298	.891	1.560	2.592			
7.5	.520	1.923	.214	.345	1.059	2.159				
8.0	.487	2.051	.245	.398	1.256	2.320				
8.5	.459	2.179	.297	.459	1.496					
9.0	.433	2.308	.349	.518	1.802					
9.5	.411	2.436	.401	.581	2.257					
10.0	.390	2.564	.453	.653	2.592					

ΔT between an object and its background is seen by a sensor through an attenuating atmosphere with a transmittance at a given range of τ_R, the value of ΔT sensed at the sensor location is an apparent ΔT, or ΔT_{AP}, equal to $\Delta T \tau_R$.

Appendix D describes the perceptual factors associated with the aspect ratio of a bar in a bar pattern, the variation of MRT with that aspect ratio, and the method of correctly applying standard MRT data to nonstandard bar patterns and thus to the "equivalent bar pattern" stressed in this report.

If we now refer to the various sources of data on the values of the signal-to-noise ratios required for the visual tasks of detection, recognition, and identification listed in Table 4, it becomes clear that the signal-to-noise ratios required are different for various tasks and are different for different-sized objects of interest.

Table 4 lists the perceived signal-to-noise ratio thresholds at 50% probability of accomplishing several visual tasks. The derivation of these values is explained in a number of publications such as Refs. 5-7, 16, 19, 20. For reasons explained in those references, the perceived signal-to-noise ratio, sometimes referred to as the signal-to-noise ratio at the display (SNR_D) or the signal-to-noise ratio in the displayed image, must be larger for large images than for moderately small ones.

In the case of a FLIR, the measured value of MRT is the measured response of a human observer, and thus, the effects of integration of the human eye are included in the measured response.

In the case of computed values of MRT, this factor must be introduced into the calculation.

In the case of predictions of observer performance computed from a description of the scene and FLIR parameters, such corrections are also necessary.

4. The Calculation Procedure

Based upon the factors discussed above, we have constructed an algorithm for the successive computation of atmospheric transmission, signal-to-noise ratios at a series of ranges and thus at a series of appropriate spatial frequencies, and, finally, the probability of detection of a tank for each range of interest. The successive operations are listed below:

1. Determine from tables or records the value of ΔT to be expected for a given target.
2. Determine the dimensions of the target.
3. Decide on the various ranges of interest.
4. Determine temperature, dew point, and visibility for time and place of interest.
5. Using the atmospheric transmission model, calculate what the atmospheric transmittance is for the chosen spectral band and range.
6. Calculate the angular subtense of the minimum dimension of the object at each range.
7. Calculate the "equivalent bar pattern" frequency for the target at each range.
8. Calculate the aspect ratio ε of the bar in the equivalent bar pattern.
9. Obtain or calculate the MRT as a function of spatial frequency for the sensor or sensors of interest.
10. For the ranges of interest and therefore for the "equivalent bar pattern" frequency, determine the values of $MRT/\sqrt{\varepsilon/7}$.

11. Calculate the value of ΔT_{AP} by multiplying the ΔT of the object at zero range by the atmospheric transmission at the range of interest.

12. Calculate $\Delta T_{AP}/(MRT/\sqrt{\varepsilon/7})$.

13. Enter the normalized probability curve (Fig. 31).

14. Note the probability of achieving the given function.

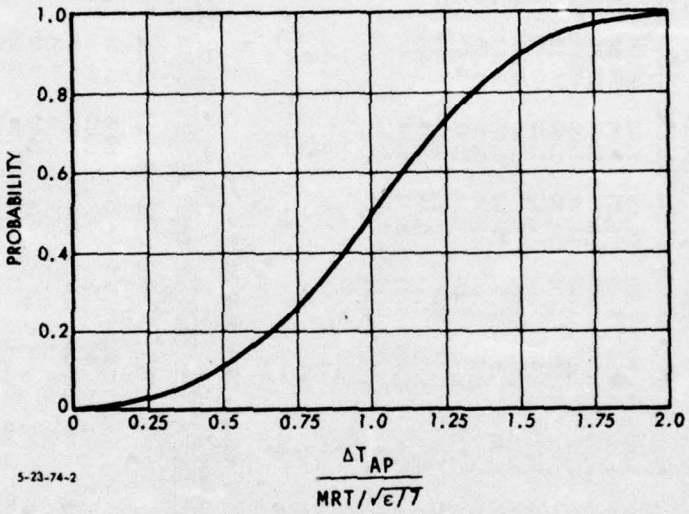


FIGURE 31. Probability of Detection Versus $\frac{\Delta T_{AP}}{MRT/\sqrt{\varepsilon/7}}$

5. Probability of Detection of Tank in Frontal* Aspect at Hannover, Germany, January and August 1970

The application of this algorithm to actual data gives the results tabulated in Tables 9 and 10. Tables 9 and 10 show the probabilities of detection of a tank in frontal aspect at one hour in January and at another hour in August, uncorrected (Table 9) as well as corrected (Table 10) for aspect.

When the normalized SNR_D or the value of $\Delta T/MRT$, corrected or uncorrected for bar aspect ratio, is significantly greater

*Detection and recognition of a tank in side aspect are treated in Part 2 of this series of reports.

TABLE 9. PERCEIVED SIGNAL-TO-NOISE RATIO AND PROBABILITY OF FLIR DETECTION OF TANK IN FRONTAL ASPECT, HANNOVER, GERMANY, UNCOMPENSATED FOR ASPECT RATIO ε, FOR FOUR FIELDS OF VIEW AND TWO DISPLAY SIZES

8 JANUARY 1970, 1800 HOURS

Range, km	Apparent Target Temperature, °C	2.5-deg Field of View				5.0-deg Field of View				7.5-deg Field of View				10.0-deg Field of View			
		Large Display		7-in. Display		Large Display		7-in. Display		Large Display		7-in. Display		Large Display		7-in. Display	
		SNR	Probability	SNR	Probability	SNR	Probability	SNR	Probability	SNR	Probability	SNR	Probability	SNR	Probability	SNR	Probability
0.5	1.77	99.00	1.00	99.00	1.00	99.00	1.00	99.00	1.00	99.00	1.00	99.00	1.00	99.00	1.00	99.00	1.00
1.0	1.58	99.00	1.00	99.00	1.00	99.00	1.00	99.00	1.00	99.00	1.00	99.00	1.00	25.79	1.00	25.00	1.00
1.5	1.42	99.00	1.00	99.00	1.00	99.00	1.00	99.00	1.00	20.91	1.00	17.86	1.00	16.28	1.00	11.12	1.00
2.0	1.27	99.00	1.00	99.00	1.00	20.73	1.00	20.10	1.00	14.62	1.00	9.98	1.00	9.69	1.00	5.97	1.00
2.5	1.14	99.00	1.00	99.00	1.00	15.42	1.00	12.00	1.00	10.00	1.00	6.19	1.00	4.72	1.00	3.27	1.00
3.0	1.03	99.00	1.00	99.00	1.00	11.84	1.00	8.08	1.00	5.51	1.00	3.71	1.00	3.20	1.00	1.81	0.99
3.5	0.93	92.75	1.00	92.75	1.00	8.87	1.00	5.82	1.00	3.51	1.00	2.39	1.00	1.95	1.00	1.11	0.63
4.0	0.84	13.66	1.00	13.24	1.00	6.38	1.00	3.93	1.00	2.60	1.00	1.47	0.91	1.25	0.76	0.68	0.18
4.5	0.76	11.17	1.00	9.54	1.00	4.05	1.00	2.73	1.00	1.75	0.98	1.00	0.50	0.78	0.27	--	--
5.0	0.68	9.22	1.00	7.17	1.00	2.82	1.00	1.96	1.00	1.21	0.72	0.59	0.12	0.49	0.07	--	--
5.5	0.62	7.67	1.00	5.55	1.00	2.18	1.00	1.44	0.90	0.84	0.32	0.50	0.08	--	--	--	--
6.0	0.56	6.43	1.00	4.39	1.00	1.74	0.98	0.98	0.48	0.58	0.12	--	--	--	--	--	--
6.5	0.51	5.33	1.00	3.53	1.00	1.31	0.81	0.72	0.21	0.37	0.04	--	--	--	--	--	--
7.0	0.46	4.39	1.00	2.88	1.00	0.96	0.46	0.55	0.10	0.33	0.03	--	--	--	--	--	--
7.5	0.42	3.64	1.00	2.25	1.00	0.74	0.22	0.36	0.03	--	--	--	--	--	--	--	--
8.0	0.38	2.88	1.00	1.77	0.99	0.56	0.11	0.30	0.02	--	--	--	--	--	--	--	--
8.5	0.34	2.16	1.00	1.40	0.87	0.43	0.05	--	--	--	--	--	--	--	--	--	--
9.0	0.31	1.67	0.97	1.12	0.64	0.32	0.03	--	--	--	--	--	--	--	--	--	--
9.5	0.28	1.32	0.82	0.91	0.40	0.23	0.01	--	--	--	--	--	--	--	--	--	--
10.0	0.26	1.06	0.57	0.74	0.23	0.19	0.01	--	--	--	--	--	--	--	--	--	--

8 AUGUST 1970, 0100 HOURS

Range, km	Apparent Target Temperature, °C	2.5-deg Field of View				5.0-deg Field of View				7.5-deg Field of View				10.0-deg Field of View			
		Large Display		7-in. Display		Large Display		7-in. Display		Large Display		7-in. Display		Large Display		7-in. Display	
		SNR	Probability	SNR	Probability	SNR	Probability	SNR	Probability	SNR	Probability	SNR	Probability	SNR	Probability	SNR	Probability
0.5	1.65	99.00	1.00	99.00	1.00	99.00	1.00	99.00	1.00	99.00	1.00	99.00	1.00	99.00	1.00	99.00	1.00
1.0	1.39	99.00	1.00	99.00	1.00	99.00	1.00	99.00	1.00	99.00	1.00	99.00	1.00	22.69	1.00	22.00	1.00
1.5	1.18	99.00	1.00	99.00	1.00	99.00	1.00	99.00	1.00	17.44	1.00	14.90	1.00	13.59	1.00	9.28	1.00
2.0	1.01	99.00	1.00	99.00	1.00	16.43	1.00	15.93	1.00	11.58	1.00	7.91	1.00	7.68	1.00	4.73	1.00
2.5	0.86	86.04	1.00	86.04	1.00	11.61	1.00	9.03	1.00	7.53	1.00	4.66	1.00	3.55	1.00	2.46	1.00
3.0	0.74	73.66	1.00	73.66	1.00	8.47	1.00	5.79	1.00	3.95	1.00	2.66	1.00	2.29	1.00	1.29	0.80
3.5	0.63	63.17	1.00	63.17	1.00	6.04	1.00	3.96	1.00	2.39	1.00	1.63	0.96	1.33	0.82	0.76	0.24
4.0	0.54	8.85	1.00	8.58	1.00	4.14	1.00	2.55	1.00	1.69	0.98	0.95	0.45	0.81	0.29	0.44	0.05
4.5	0.47	6.88	1.00	5.88	1.00	2.50	1.00	1.68	0.97	1.08	0.59	0.62	0.14	0.48	0.07	--	--
5.0	0.40	5.40	1.00	4.20	1.00	1.65	0.97	1.15	0.66	0.71	0.20	0.35	0.03	0.29	0.02	--	--
5.5	0.34	4.28	1.00	3.10	1.00	1.22	0.73	0.80	0.29	0.47	0.06	0.28	0.02	--	--	--	--
6.0	0.30	3.41	1.00	2.33	1.00	0.92	0.41	0.52	0.09	0.31	0.02	--	--	--	--	--	--
6.5	0.26	2.69	1.00	1.78	0.99	0.66	0.17	0.36	0.03	0.19	0.01	--	--	--	--	--	--
7.0	0.22	2.11	1.00	1.38	0.86	0.46	0.06	0.26	0.02	0.16	0.01	--	--	--	--	--	--
7.5	0.19	1.66	0.97	1.03	0.53	0.34	0.03	0.16	0.01	--	--	--	--	--	--	--	--
8.0	0.16	1.25	0.76	0.77	0.26	0.24	0.02	0.13	0.01	--	--	--	--	--	--	--	--
8.5	0.14	0.89	0.38	0.58	0.11	0.18	0.01	--	--	--	--	--	--	--	--	--	--
9.0	0.12	0.65	0.16	0.44	0.06	0.13	0.01	--	--	--	--	--	--	--	--	--	--
9.5	0.11	0.49	0.07	0.34	0.03	0.09	0.00	--	--	--	--	--	--	--	--	--	--
10.0	0.09	0.38	0.04	0.26	0.02	0.07	0.00	--	--	--	--	--	--	--	--	--	--

TABLE 10. PERCEIVED SIGNAL-TO-NOISE RATIO AND PROBABILITY OF FLIR DETECTION OF TANK IN FRONTAL ASPECT, HANNOVER, GERMANY, CONPENSATED FOR ASPECT RATIO ε, FOR FOUR FIELDS OF VIEW AND TWO DISPLAY SIZES

8 JANUARY 1970, 1800 HOURS

Range, km	Apparent Target Temperature, °C	2.5-deg Field of View				5.0-deg Field of View				7.5-deg Field of View				10.0-deg Field of View			
		Large Display		7-in. Display		Large Display		7-in. Display		Large Display		7-in. Display		Large Display		7-in. Display	
		SNR	Probability	SNR	Probability	SNR	Probability	SNR	Probability	SNR	Probability	SNR	Probability	SNR	Probability	SNR	Probability
0.5	1.77	99.00	1.00	99.00	1.00	99.00	1.00	99.00	1.00	99.00	1.00	99.00	1.00	99.00	1.00	99.00	1.00
1.0	1.58	99.00	1.00	99.00	1.00	99.00	1.00	99.00	1.00	99.00	1.00	13.78	1.00	13.78	1.00	13.35	1.00
1.5	1.42	99.00	1.00	99.00	1.00	99.00	1.00	99.00	1.00	9.55	1.00	8.70	1.00	8.70	1.00	5.94	1.00
2.0	1.27	99.00	1.00	99.00	1.00	11.08	1.00	10.74	1.00	5.33	1.00	5.18	1.00	5.18	1.00	3.19	1.00
2.5	1.14	99.00	1.00	99.00	1.00	8.24	1.00	6.41	1.00	3.31	1.00	2.52	1.00	2.52	1.00	1.75	0.98
3.0	1.03	99.00	1.00	99.00	1.00	6.33	1.00	4.32	1.00	1.99	1.00	1.71	0.98	1.71	0.98	0.97	0.46
3.5	0.93	92.75	1.00	92.75	1.00	4.74	1.00	3.11	1.00	1.28	0.79	1.04	0.55	1.04	0.55	0.59	0.12
4.0	0.84	7.30	1.00	7.08	1.00	3.41	1.00	2.10	1.00	0.79	0.27	0.67	0.17	0.67	0.17	0.36	0.03
4.5	0.76	5.97	1.00	5.10	1.00	2.16	1.00	1.46	0.91	0.53	0.09	0.42	0.05	0.42	0.05	--	--
5.0	0.68	4.93	1.00	3.83	1.00	1.51	0.93	1.05	0.55	0.32	0.03	0.26	0.02	0.26	0.02	--	--
5.5	0.62	4.10	1.00	2.97	1.00	1.17	0.68	0.77	0.26	0.27	0.02	--	--	--	--	--	--
6.0	0.56	3.44	1.00	2.35	1.00	0.93	0.42	0.53	0.09	--	--	--	--	--	--	--	--
6.5	0.51	2.85	1.00	1.89	0.99	0.70	0.20	0.38	0.04	--	--	--	--	--	--	--	--
7.0	0.46	2.35	1.00	1.54	0.94	0.51	0.08	0.29	0.02	--	--	--	--	--	--	--	--
7.5	0.42	1.95	1.00	1.20	0.72	0.39	0.04	0.19	0.01	--	--	--	--	--	--	--	--
8.0	0.38	1.54	0.94	0.95	0.44	0.30	0.02	0.16	0.01	--	--	--	--	--	--	--	--
8.5	0.34	1.15	0.67	0.75	0.24	0.23	0.01	--	--	--	--	--	--	--	--	--	--
9.0	0.31	0.89	0.38	0.60	0.13	0.17	0.01	--	--	--	--	--	--	--	--	--	--
9.5	0.28	0.70	0.20	0.49	0.07	0.13	0.01	--	--	--	--	--	--	--	--	--	--
10.0	0.26	0.57	0.11	0.39	0.04	0.10	0.01	--	--	--	--	--	--	--	--	--	--

8 AUGUST 1970, 0100 HOURS

Range, km	Apparent Target Temperature, °C	2.5-deg Field of View				5.0-deg Field of View				7.5-deg Field of View				10.0-deg Field of View			
		Large Display		7-in. Display		Large Display		7-in. Display		Large Display		7-in. Display		Large Display		7-in. Display	
		SNR	Probability	SNR	Probability	SNR	Probability	SNR	Probability	SNR	Probability	SNR	Probability	SNR	Probability	SNR	Probability
0.5	1.65	99.00	1.00	99.00	1.00	99.00	1.00	99.00	1.00	99.00	1.00	99.00	1.00	99.00	1.00	99.00	1.00
1.0	1.39	99.00	1.00	99.00	1.00	99.00	1.00	99.00	1.00	99.00	1.00	99.00	1.00	12.13	1.00	11.75	1.00
1.5	1.18	99.00	1.00	99.00	1.00	99.00	1.00	99.00	1.00	9.32	1.00	7.96	1.00	7.26	1.00	4.95	1.00
2.0	1.01	99.00	1.00	99.00	1.00	8.78	1.00	8.52	1.00	6.19	1.00	4.23	1.00	4.10	1.00	2.53	1.00
2.5	0.86	86.04	1.00	86.04	1.00	6.21	1.00	4.83	1.00	4.03	1.00	2.49	1.00	1.90	0.99	1.32	0.82
3.0	0.74	73.66	1.00	73.66	1.00	4.53	1.00	3.09	1.00	2.11	1.00	1.42	0.59	1.22	0.74	0.69	0.19
3.5	0.63	63.17	1.00	63.17	1.00	3.23	1.00	2.12	1.00	1.28	0.79	0.87	0.36	0.71	0.20	0.40	0.04
4.0	0.54	4.73	1.00	4.59	1.00	2.21	1.00	1.36	0.85	0.90	0.39	0.51	0.08	0.43	0.05	0.23	0.01
4.5	0.47	3.68	1.00	3.14	1.00	1.33	0.83	0.90	0.39	0.58	0.11	0.33	0.03	0.26	0.02	--	--
5.0	0.40	2.89	1.00	2.25	1.00	0.88	0.37	0.61	0.13	0.38	0.04	0.19	0.01	0.16	0.01	--	--
5.5	0.34	2.29	1.00	1.66	0.97	0.65	0.16	0.43	0.05	0.25	0.02	0.15	0.01	--	--	--	--
6.0	0.30	1.82	0.99	1.25	0.76	0.49	0.07	0.28	0.02	0.16	0.01	--	--	--	--	--	--
6.5	0.26	1.44	0.89	0.95	0.45	0.35	0.03	0.19	0.01	0.10	0.01	--	--	--	--	--	--
7.0	0.22	1.13	0.64	0.74	0.23	0.25	0.02	0.14	0.01	0.09	0.00	--	--	--	--	--	--
7.5	0.19	0.89	0.38	0.55	0.10	0.18	0.01	0.09	0.00	--	--	--	--	--	--	--	--
8.0	0.16	0.67	0.17	0.41	0.05	0.13	0.01	0.07	0.00	--	--	--	--	--	--	--	--
8.5	0.14	0.48	0.07	0.31	0.02	0.09	0.00	--	--	--	--	--	--	--	--	--	--
9.0	0.12	0.35	0.03	0.24	0.01	0.07	0.00	--	--	--	--	--	--	--	--	--	--
9.5	0.11	0.26	0.02	0.18	0.01	0.05	0.00	--	--	--	--	--	--	--	--	--	--
10.0	0.09	0.20	0.01	0.14	0.01	0.04	0.00	--	--	--	--	--	--	--	--	--	--

than about 2.0, the correction matters little, and the probability of detection appears to be near 100 percent for any case.

When $\Delta T/MRT$ falls off appreciably below that point, however, the slopes get increasingly steep (Fig. 31), and the difference in corrected and uncorrected data can be a factor of five and more. For example, the values that previously indicated a probability of detection of, say, 0.63 now become 0.12 when corrected.

Although Tables 9 and 10 were carefully calculated, they refer to specific instants and should be considered valid only for those instants. The tables do not take weather variations into account, and these can be wide and rapid. If a glance at the sample weather data in Tables 11 and 12 gives the impression of little change, examine the visibility column. The humidity and temperature do not vary widely, but the visibility does, and related effects in the infrared can significantly influence the performance of FLIRs. Although FLIRs respond to radiation in the 8.5-11 μm band and not in the visible, the same particulates and aerosols that cause poor visibility also cause poor transmission at 8.5-11 μm, though not with equal degradations.

From data on MRT, weather and equivalent bar patterns for given targets, we have computed and plotted a series of curves showing the effects of some of the important parameters of weather and sensor. As a simple example, we show some FLIR results. In the following figures, each tick on the abscissa marks the end of a day of the month.

Figures 32 and 33* show the hourly visibility, air temperature, and dew point for the months of January and August 1970. The figures also show the corresponding atmospheric transmittances at 8.5-11 μm as computed for ranges of 5 and 8 km. The choice of ranges was made to best illustrate the typical effect of

*These figures duplicate Figs. 1 and 8.

TABLE 11. WEATHER DATA FOR 8 JANUARY 1970, HANNOVER, GERMANY

Month	Day	Hour	Dew Point, °C	Air Temp., °C	Visibility, km	Cloud Cover, eighths	Lumb Factor	Wind Velocity, knots	Wind Direction, deg	Barometric Pressure, millibars (every 3rd hour)
1	8	0100	-5	-4	1.6	8	0.35	5	60	
1	8	0200	-5	-4	1.6	8	0.35	4	80	
1	8	0300	-5	-4	2.0	8	0.35	5	80	1027
1	8	0400	-5	-5	1.6	8	0.35	7	70	
1	8	0500	-6	-5	1.2	8	0.35	8	100	
1	8	0600	-8	-7	0.4	8	0.35	9	110	1027
1	8	0700	-8	-7	0.4	8	0.35	8	90	
1	8	0800	-8	-7	0.3	8	0.35	8	90	
1	8	0900	-8	-7	0.4	8	0.35	9	90	1028
1	8	1000	-9	-8	0.6	8	0.35	8	90	
1	8	1100	-9	-8	0.6	8	0.35	7	100	
1	8	1200	-9	-8	1.3	8	0.35	10	90	1028
1	8	1300	-9	-8	1.8	8	0.35	8	90	
1	8	1400	-9	-8	2.0	7	0.55	8	90	
1	8	1500	-8	-7	1.8	7	0.55	13	90	1026
1	8	1600	-8	-8	1.6	7	0.76	14	80	
1	8	1700	-8	-7	1.8	7	0.76	12	100	
1	8	1800	-8	-7	2.5	6	0.90	12	100	1026
1	8	1900	-8	-7	2.0	6	0.90	15	110	
1	8	2000	-8	-7	3.5	3	0.90	15	110	
1	8	2100	-8	-7	3.0	6	0.90	17	90	1025
1	8	2200	-8	-8	3.0	7	0.76	13	90	
1	8	2300	-8	-7	3.0	7	0.76	17	100	
1	8	2400	-8	-6	4.0	7	0.76	17	90	1024

TABLE 12. WEATHER DATA FOR 8 AUGUST 1970, HANNOVER, GERMANY

Month	Day	Hour	Dew Point, °C	Air Temp., °C	Visibility, km	Cloud Cover, eighths	Lumb Factor	Wind Velocity, knots	Wind Direction, deg	Barometric Pressure, millibars (every 3rd hour)
8	8	0100	16	17	6.0	8	0.55	0	0	
8	8	0200	15	16	6.0	8	0.55	2	90	
8	8	0300	15	16	5.0	8	0.55	2	90	1012
8	8	0400	15	16	5.0	8	0.55	2	40	
8	8	0500	15	16	5.0	7	0.55	2	90	
8	8	0600	17	17	4.0	7	0.55	5	50	1012
8	8	0700	17	19	4.0	7	0.55	4	70	
8	8	0800	19	20	4.0	6	0.76	6	60	
8	8	0900	19	22	5.0	7	0.55	7	90	1012
8	8	1000	19	23	7.0	6	0.55	9	100	
8	8	1100	16	24	9.0	6	0.76	10	90	
8	8	1200	16	23	7.0	8	0.55	10	100	1011
8	8	1300	17	19	3.0	8	0.20	8	220	
8	8	1400	17	17	7.0	8	0.20	4	90	
8	8	1500	17	17	8.0	8	0.35	1	90	1012
8	8	1600	17	18	8.0	6	0.55	2	90	
8	8	1700	17	18	8.0	8	0.35	4	10	
8	8	1800	17	18	7.0	7	0.55	2	360	1012
8	8	1900	16	16	3.8	5	0.76	4	350	
8	8	2000	16	16	3.0	8	0.35	5	270	
8	8	2100	15	16	3.0	8	0.35	6	310	1012
8	8	2200	16	16	4.0	8	0.35	5	310	
8	8	2300	16	16	2.0	8	0.35	5	250	

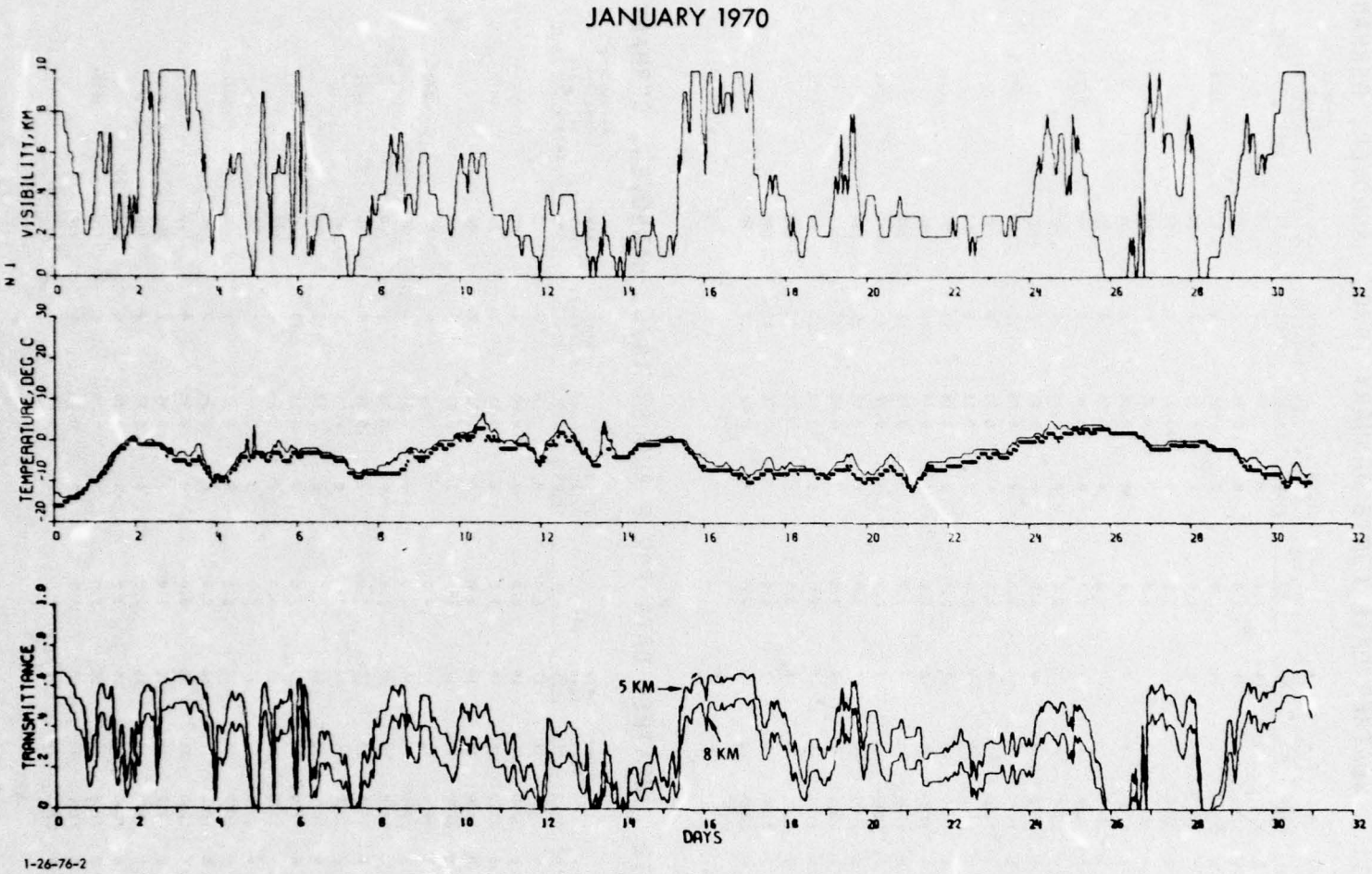
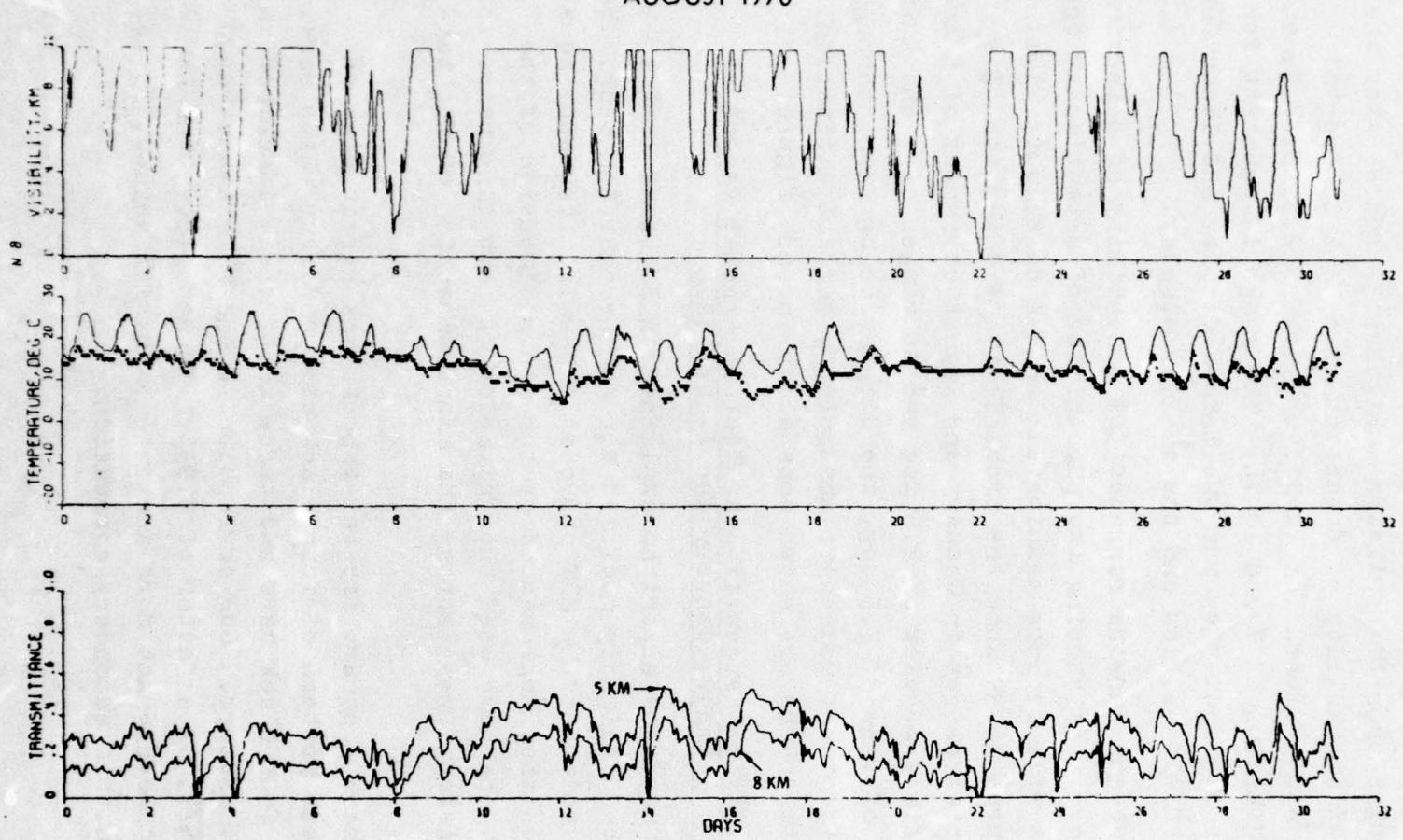


FIGURE 32. Hourly Visibility, Air Temperature (—), Dew Point (o), and Corresponding Computed Atmospheric Transmittances at 8.5-11 μm for Ranges of 5 and 8 km; Hannover, Germany; Jaunary 1970. (Visibility curve is truncated at 10 km. Each tick on abscissa marks end of a day.)



1-26-76-9

FIGURE 33. Hourly Visibility, Air Temperature (—), Dew Point (o), and Corresponding Computed Atmospheric Transmittances at 8.5-11 μm for Ranges of 5 and 8 km; Hannover, Germany; August 1970. (Visibility curve is truncated at 10 km. Each tick on abscissa marks end of a day.)

tactical ranges upon transmission. Figures 34 and 35 show the range for 50% probability of detection of a tank in frontal aspect in a winter month for fields of view of 2.5, 5, 7.5, and 10 deg and displays of 7 and 14 in. The range is greatest for the smallest field of view and the larger display and least for the largest field of view and the smaller display.

We have begun showing range at 50% probability of detection, but we believe that showing the probability of detection at specified ranges will be more meaningful, and we do this in Figs. 36-39. Figures 36-39 show the probability of detection of a tank in frontal aspect in January and August at ranges of 5 and 8 km for a field of view of 2.5 deg and at ranges of 3 and 4 km for a field of view of 7.5 deg, the display being 7 in. throughout. The effects of molecular absorption, aerosol extinction, and total atmosphere are shown separately in each figure.

6. Probability of Recognition of Tank in Frontal Aspect at Hannover, Germany, January and August 1970

We have used the algorithm explained in Sections IV-B-1 through IV-B-3, slightly modified for the recognition task. We have chosen to enter the MRT curve at a spatial frequency equal to four times that represented by the minor dimension of the target, i.e., we have used the criterion of four line pairs (or eight television lines) across the minor dimension of the target.

Now we have a square frontal-aspect tank target with an equivalent bar pattern of four black bars and four white bars, rather than four black bars and three white bars, inscribed in the MRT test pattern. Our correction to the MRT values would thus be $1/\sqrt{8/7}$, or a factor of 0.935. In actuality, the MRT values are probably not more accurate than ±10% anyhow, so we have ignored this secondary correction.

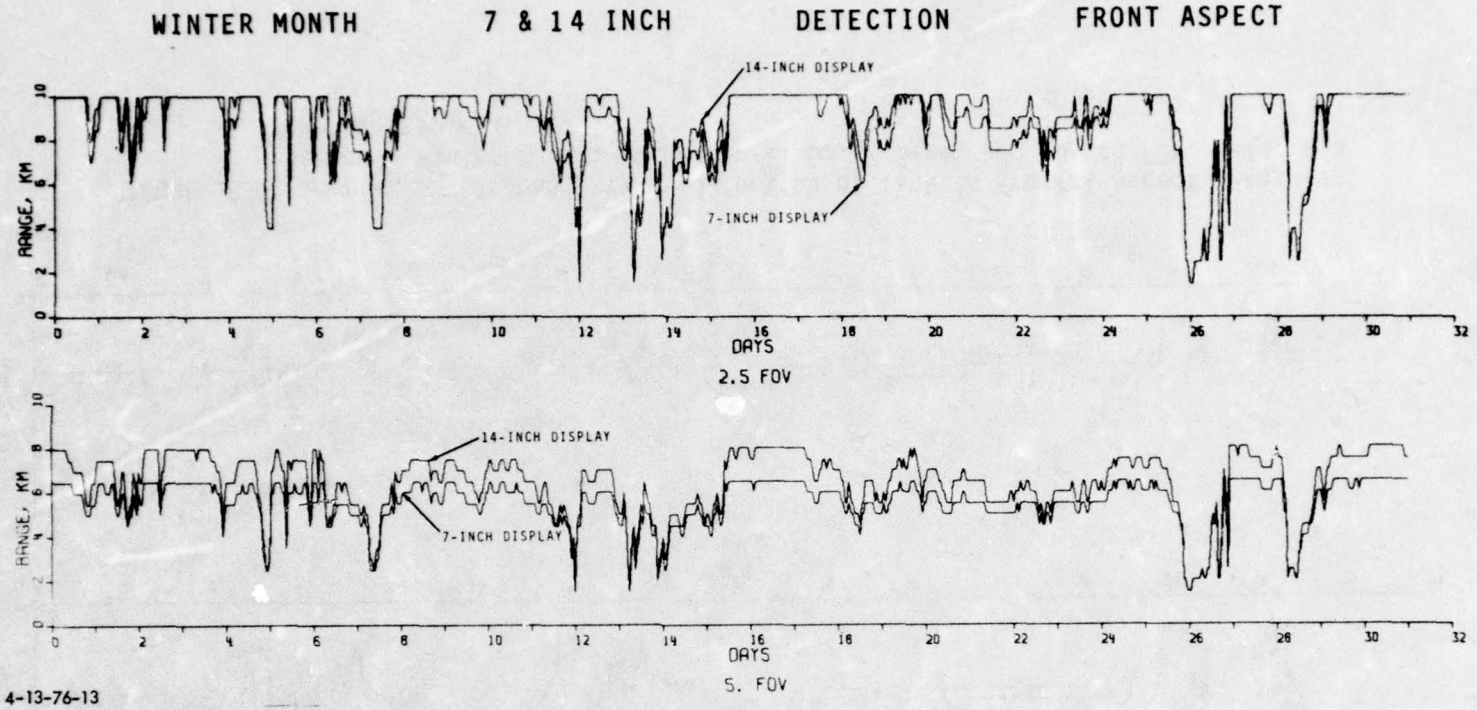


FIGURE 34. Range at 50% Probability of Detection of Tank in Frontal Aspect, Hannover, Germany, Winter Month; FLIR, 8.5-11 μm, 2.5-deg and 5-deg FOV, 7-in. and 14-in. Displays.

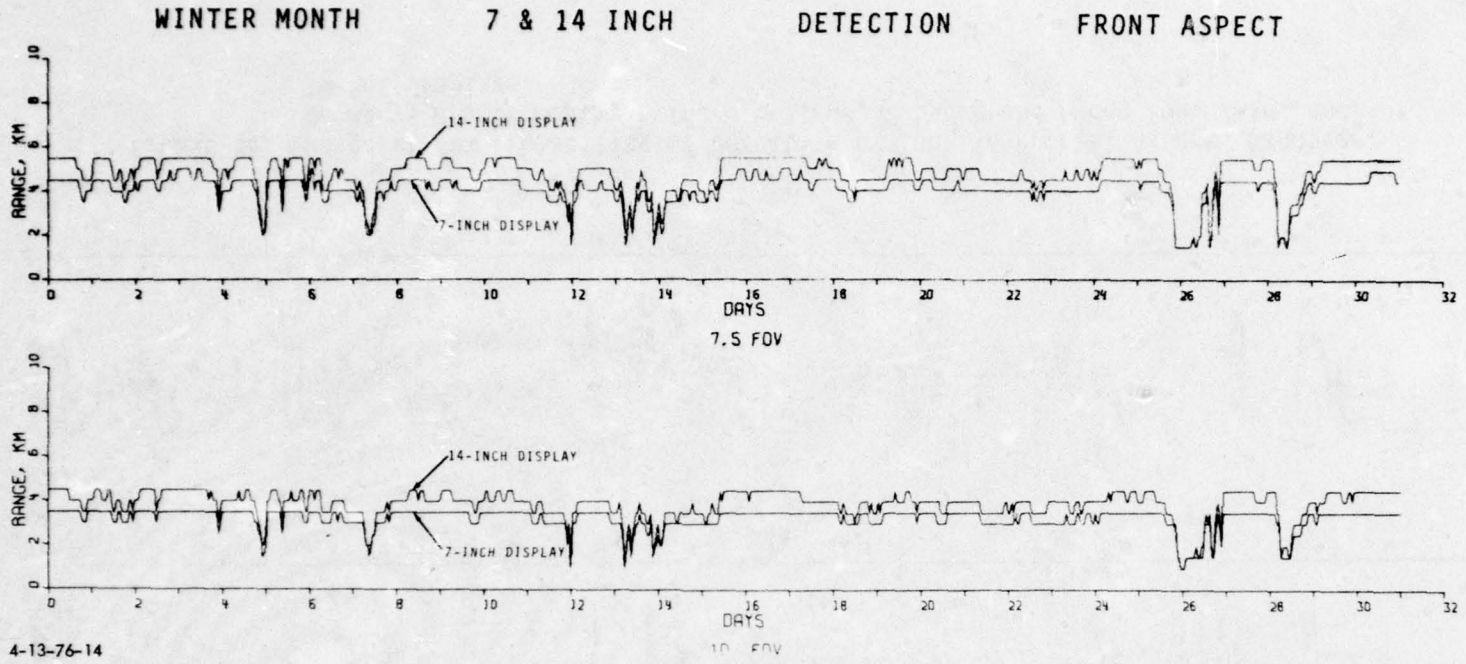


FIGURE 35. Range at 50% Probability of Detection of Tank in Frontal Aspect, Hannover, Germany, Winter Month; FLIR, 8.5-11 μm, 7.5-deg and 10-deg FOV, 7-in. and 14-in. Displays.

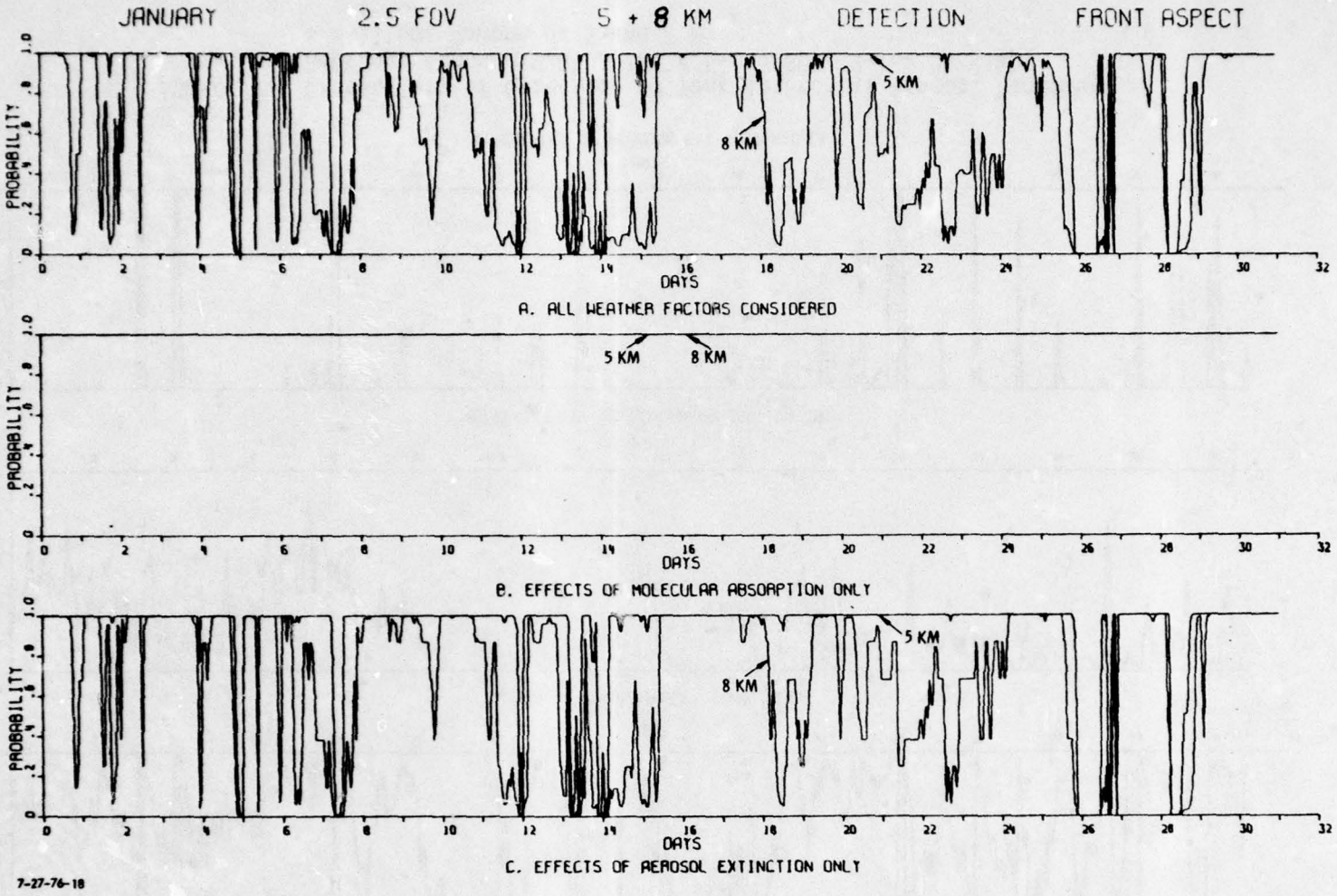


FIGURE 36. Probability of Detection of Tank in Frontal Aspect, Hannover, Germany, January 1970; FLIR, 2.5-deg FOV, 7-in. Display, 8.5-11 μm, Ranges of 5 and 8 km.

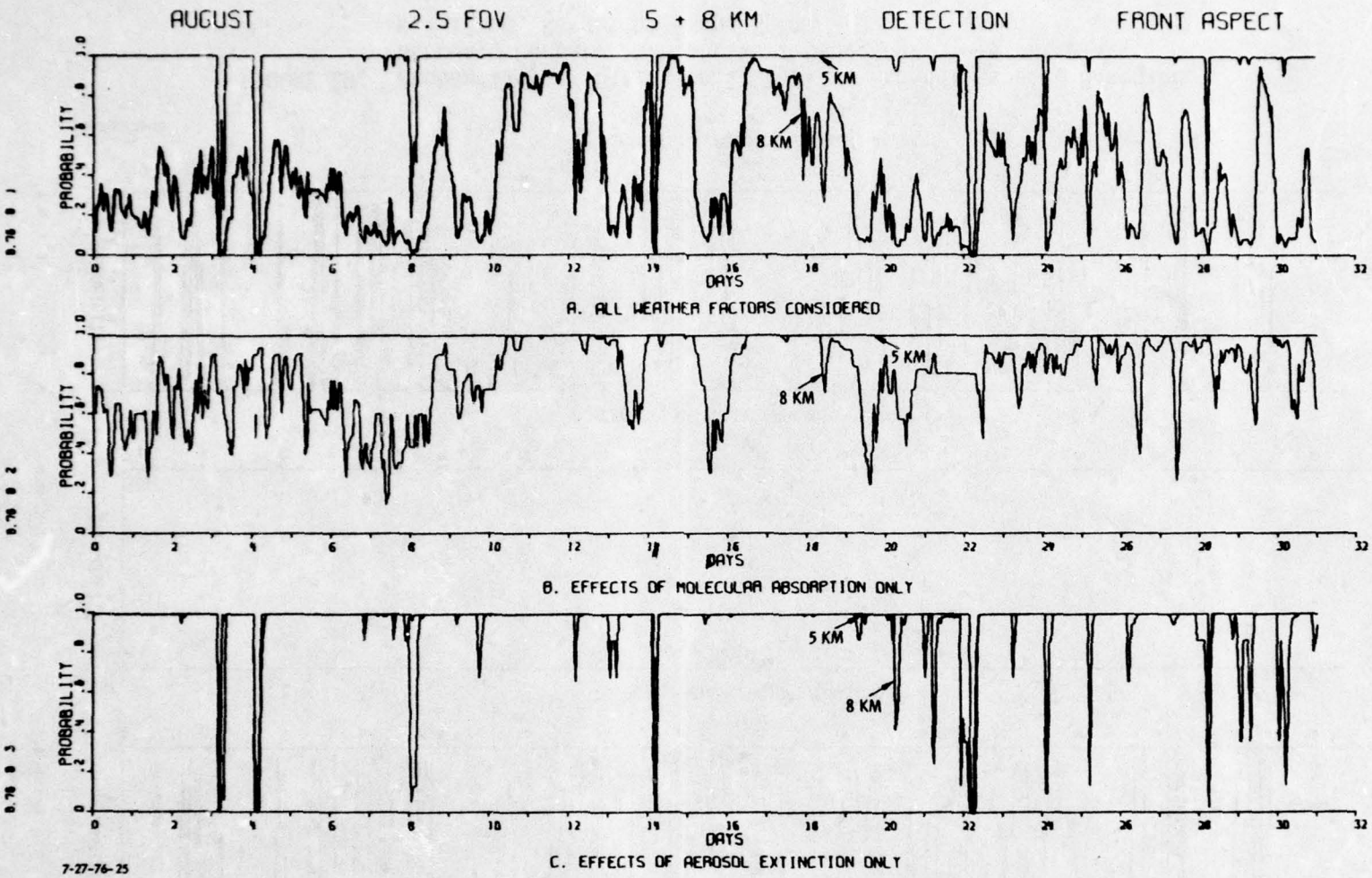


FIGURE 37. Probability of Detection of Tank in Frontal Aspect, Hannover, Germany, August 1970; FLIR, 2.5-deg FOV, 7-in. Display, 8.5-11 μm, Ranges of 5 and 8 km.

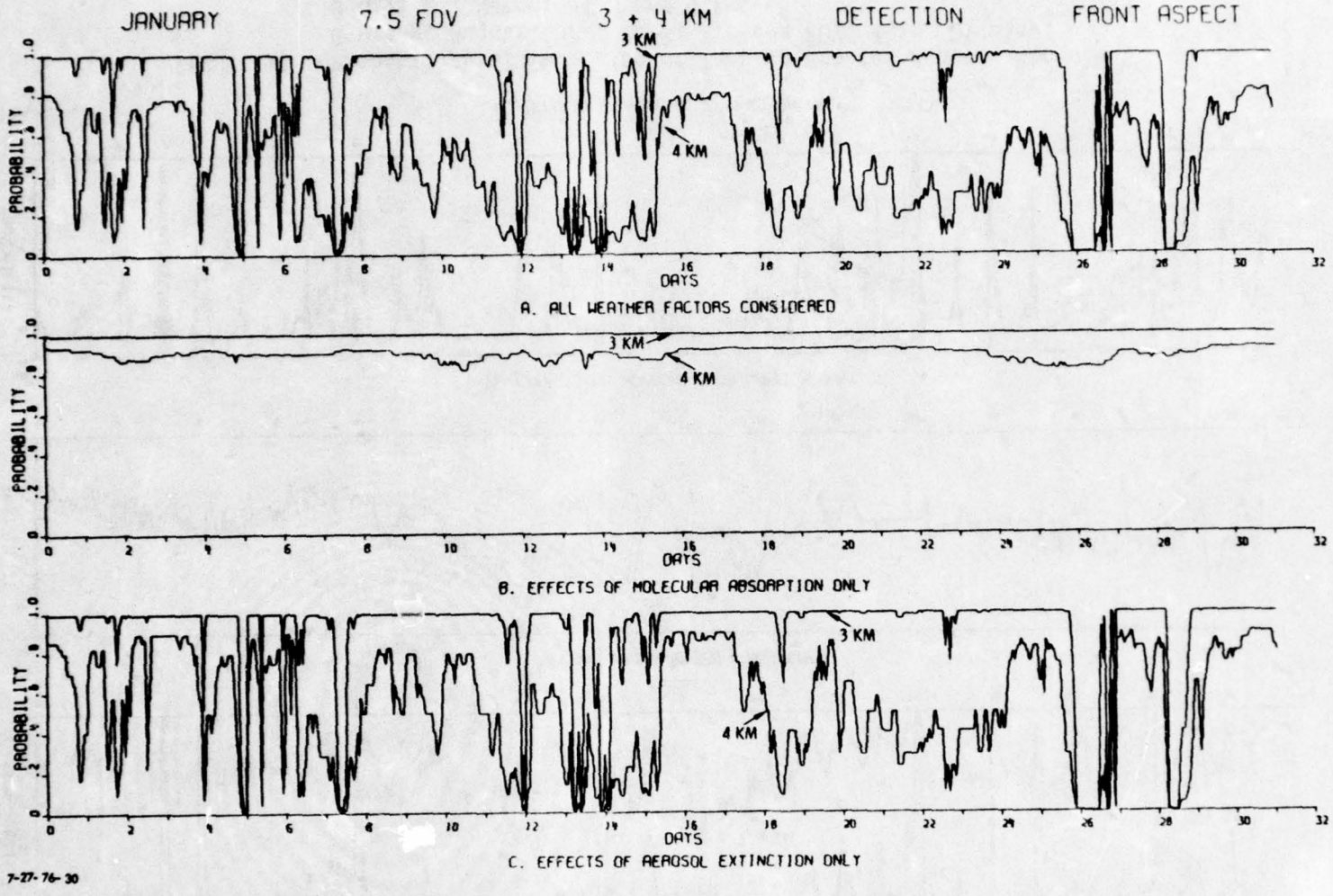


FIGURE 38. Probability of Detection of Tank in Frontal Aspect, Hannover, Germany, January 1970; FLIR, 7.5-deg FOV, 7-in. Display, 8.5-11 μm, Ranges of 3 and 4 km.

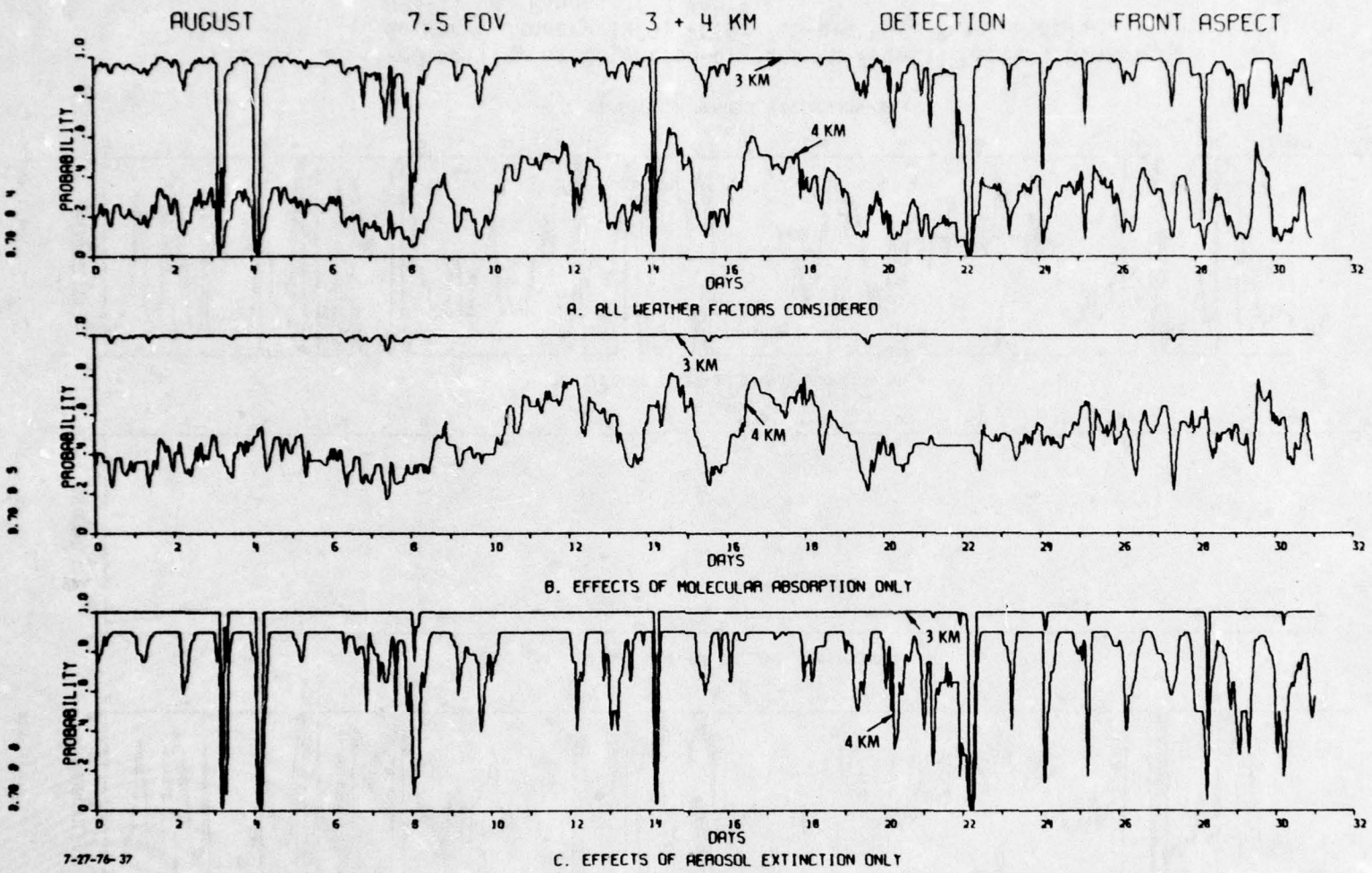


FIGURE 39. Probability of Detection of Tank in Frontal Aspect, Hannover, Germany, August 1970; FLIR, 7.5-deg FOV, 7-in. Display, 8.5-11 μm, Ranges of 3 and 4 km.

Figures 40 and 41 show the probability of recognition in January and August 1970 at ranges of 3 and 4 km for a FLIR having a 2.5-deg FOV, and at ranges of 1 and 1.5 km for a FLIR having a 7.5-deg FOV. In all cases the display is 7 inches.

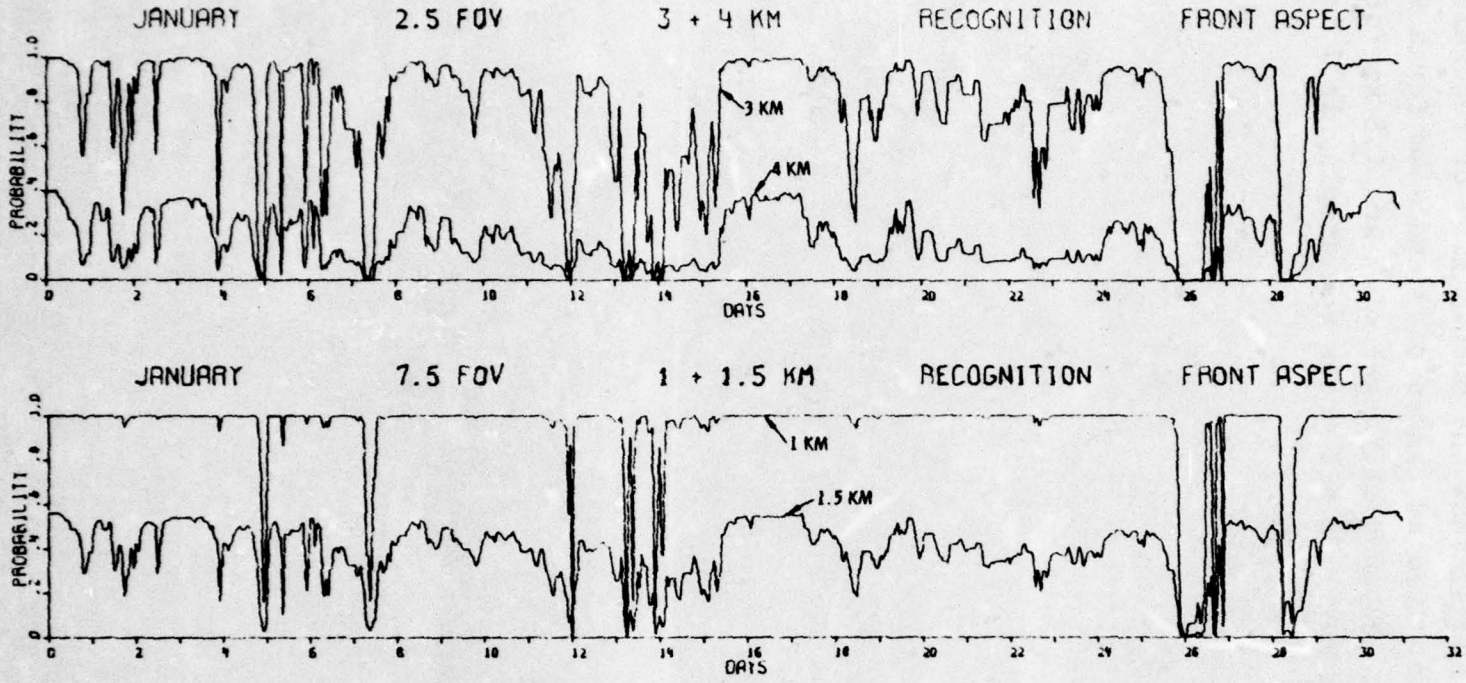


FIGURE 40. Probability of Recognition of Tank in Frontal Aspect, Hannover, Germany, January 1970; FLIR, 8.5-11 μm, 7-in. Display; 3-km and 4-km Ranges for 2.5-deg FOV; 1-km and 1.5-km Ranges for 7.5-deg FOV.

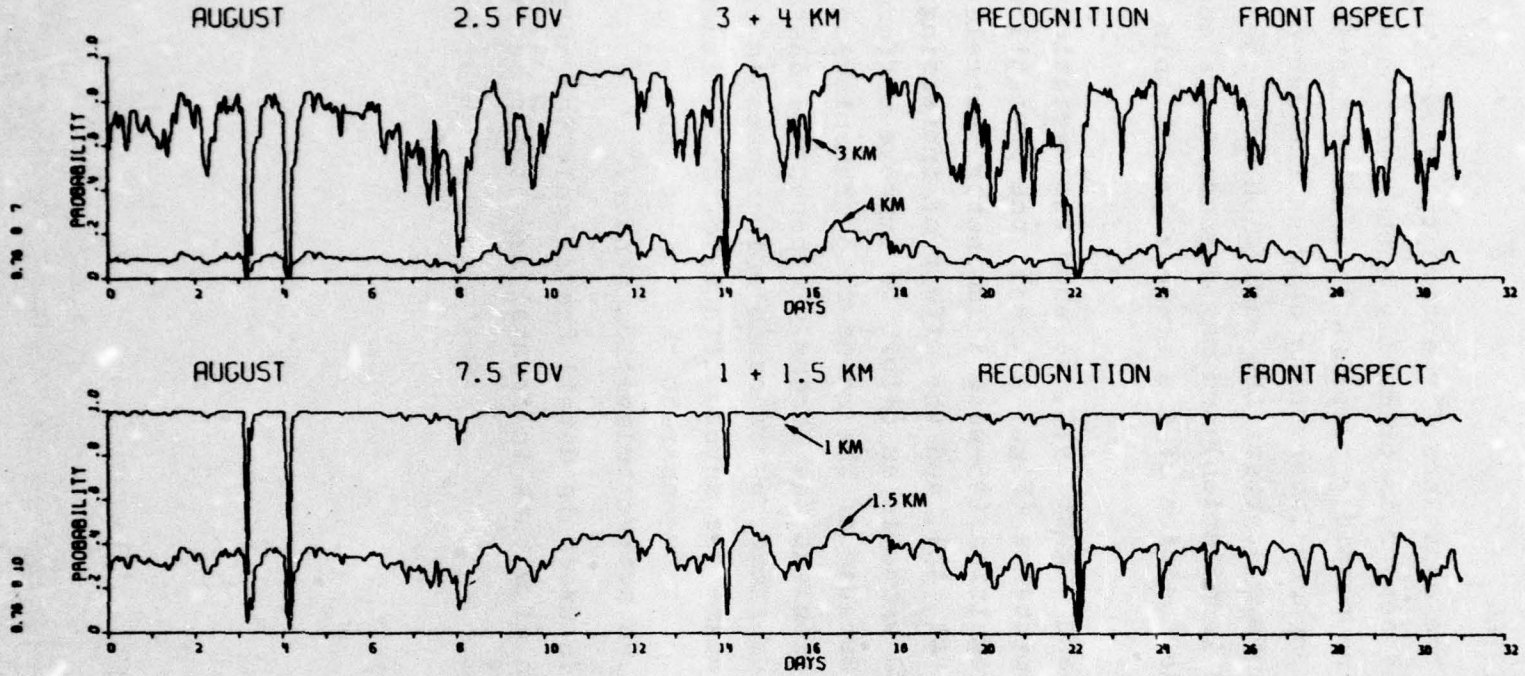


FIGURE 41. Probability of Recognition of Tank in Frontal Aspect, Hannover, Germany, August 1970; FLIR, 8.5-11 μm, 7-in. Display; 3-km and 4-km Ranges for 2.5-deg FOV; 1-km and 1.5-km Ranges for 7.5-deg FOV.

C. ACTIVE TELEVISION

In general, the equations for active television are quite simple because the sensor is primarily photoelectron noise limited. There are possible complications in estimating the effect of the atmosphere intervening between the sensor and the scene. The atmosphere scatters the radiation from the system source (the scene irradiation) and may degrade image contrast, depending upon the position of the scene object within the sensor range gate.

For January and August 1970, we show the variation in atmospheric transmittance (Figs. 42, 43), the probabilities of detection and recognition (45-watt illuminator) correlated with visibility (Figs. 44, 45), and the effect of increasing illuminator power to 180 watts in an effort to improve performance (Figs. 46, 47). Because of the round-trip transmission needed for active television and the strongly exponential character of transmission versus range, no reasonable increases in illuminator power can overcome the severe effects of bad weather on active television. It is apparent that heavy aerosol concentrations can stop an active television sensor.

Appendix E discusses in detail the calculation of probability of recognition of a tank in frontal aspect for active television sensors.

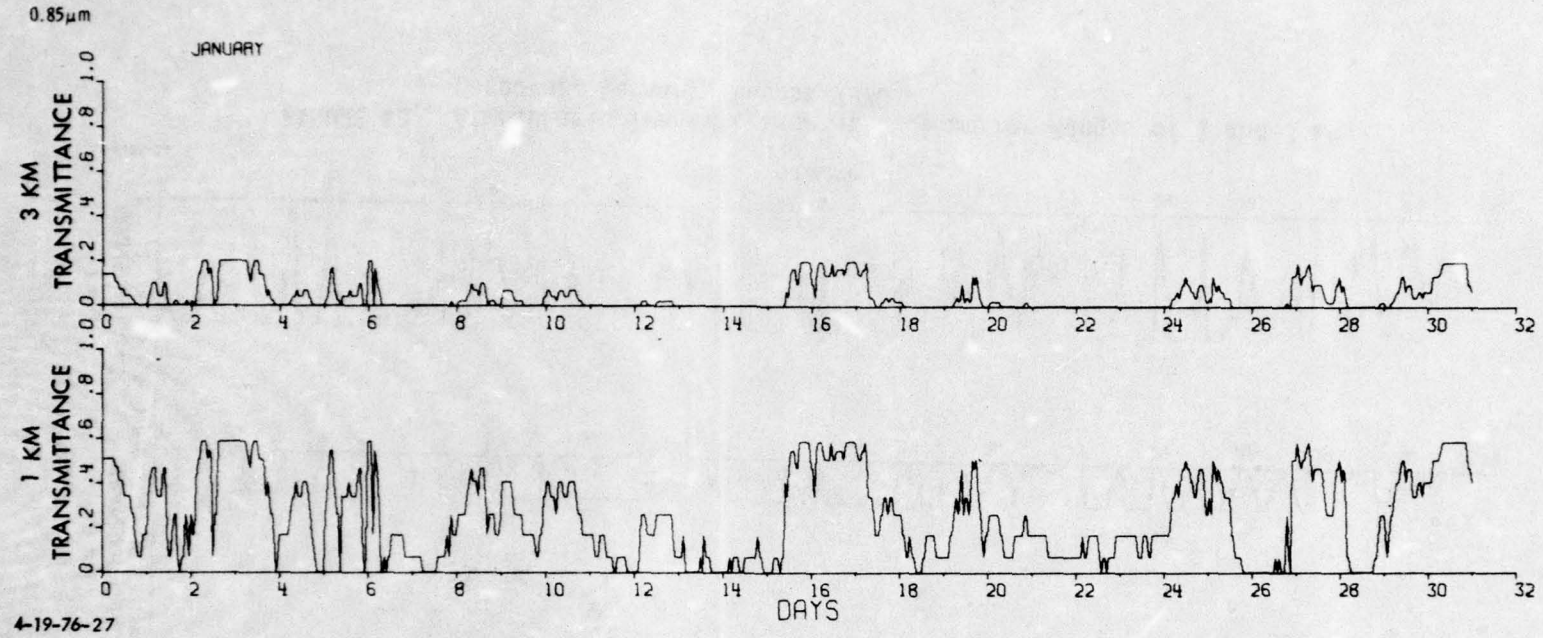


FIGURE 42. Atmospheric Transmittance at 0.85 μm for Ranges of 1 and 3 km, Hannover, Germany, January 1970.

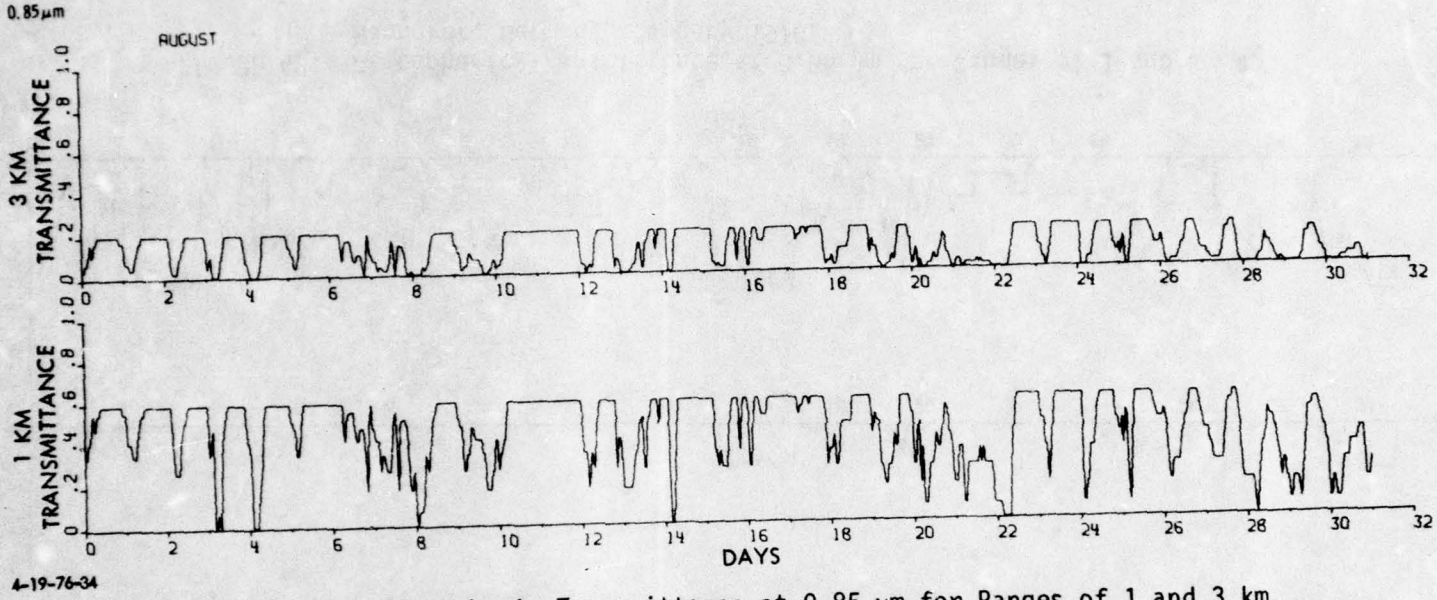


FIGURE 43. Atmospheric Transmittance at 0.85 μm for Ranges of 1 and 3 km, Hannover, Germany, August 1970.

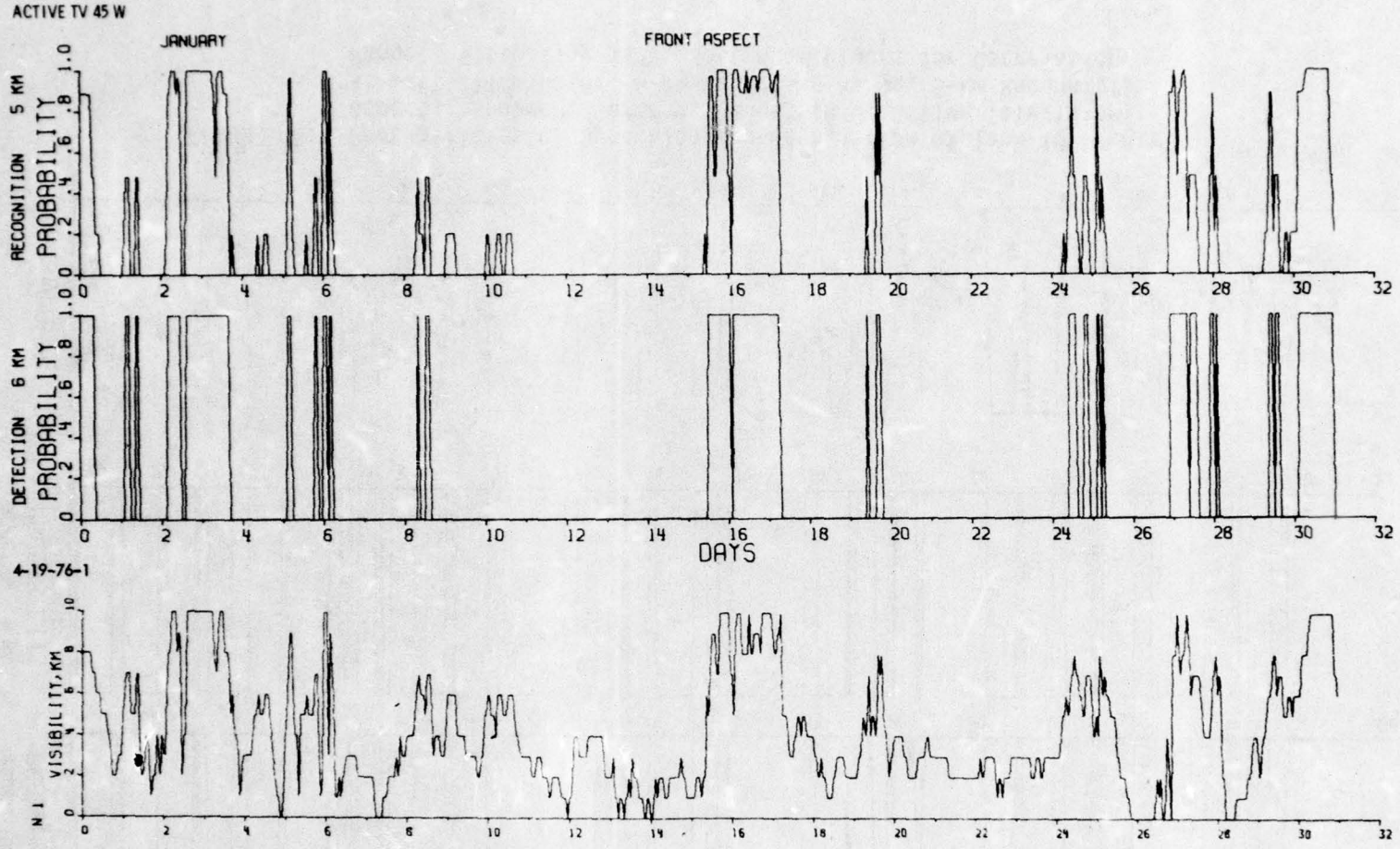


FIGURE 44. Probabilities of Detection and Recognition of Tank in Frontal Aspect, Hannover, Germany, January 1970; Active Television, 45-watt Illuminator, 6-km Detection Range, 5-km Recognition Range. Visibility is at Bottom of Figure for Correlation.

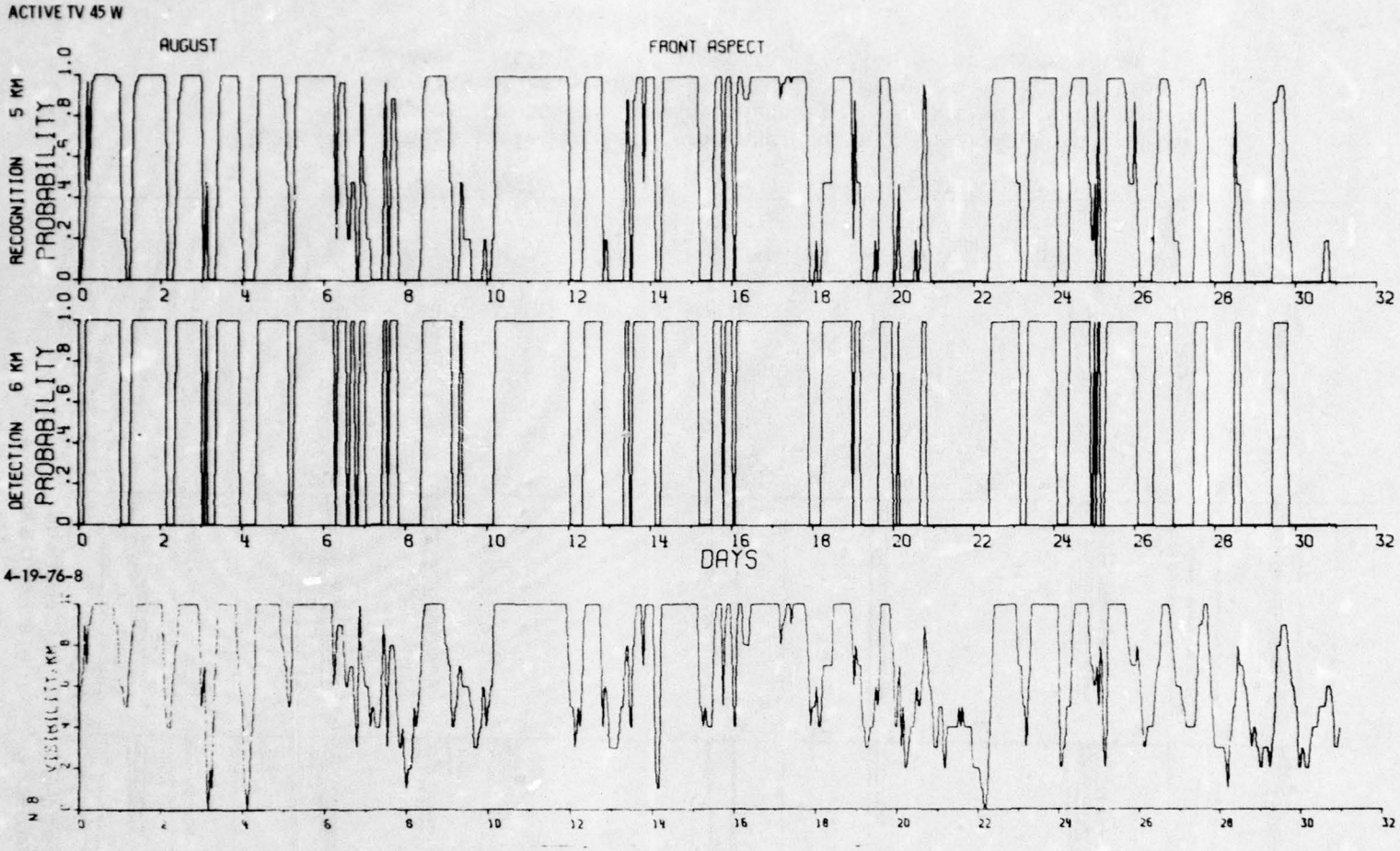


FIGURE 45. Probabilities of Detection and Recognition of Tank in Frontal Aspect, Hannover, Germany, August 1970; Active Television, 45-watt Illuminator, 6-km Detection Range, 5-km Recognition Range. Visibility is at Bottom of Figure for Correlation.

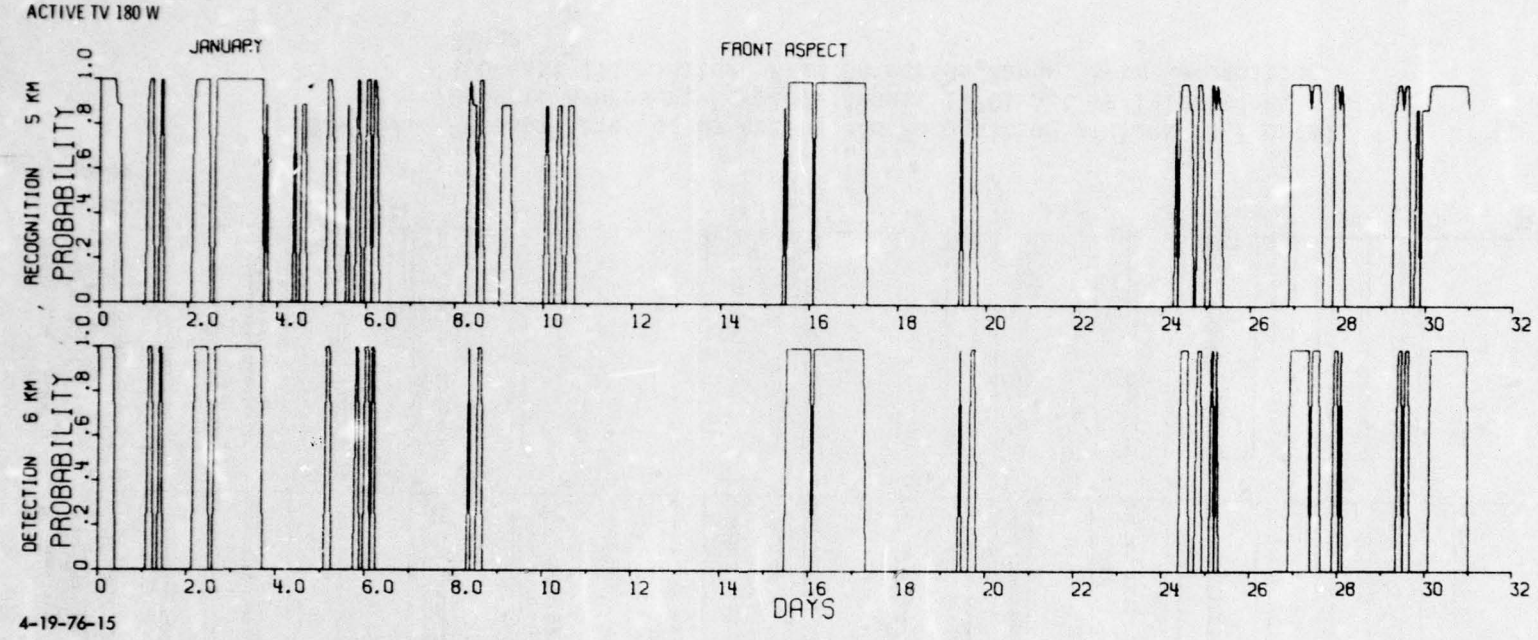


FIGURE 46. Probabilities of Detection and Recognition of Tank in Frontal Aspect, Hannover, Germany, January 1970; Active Television, 180-watt Illuminator, 6-km Detection Range, 5-km Recognition Range.

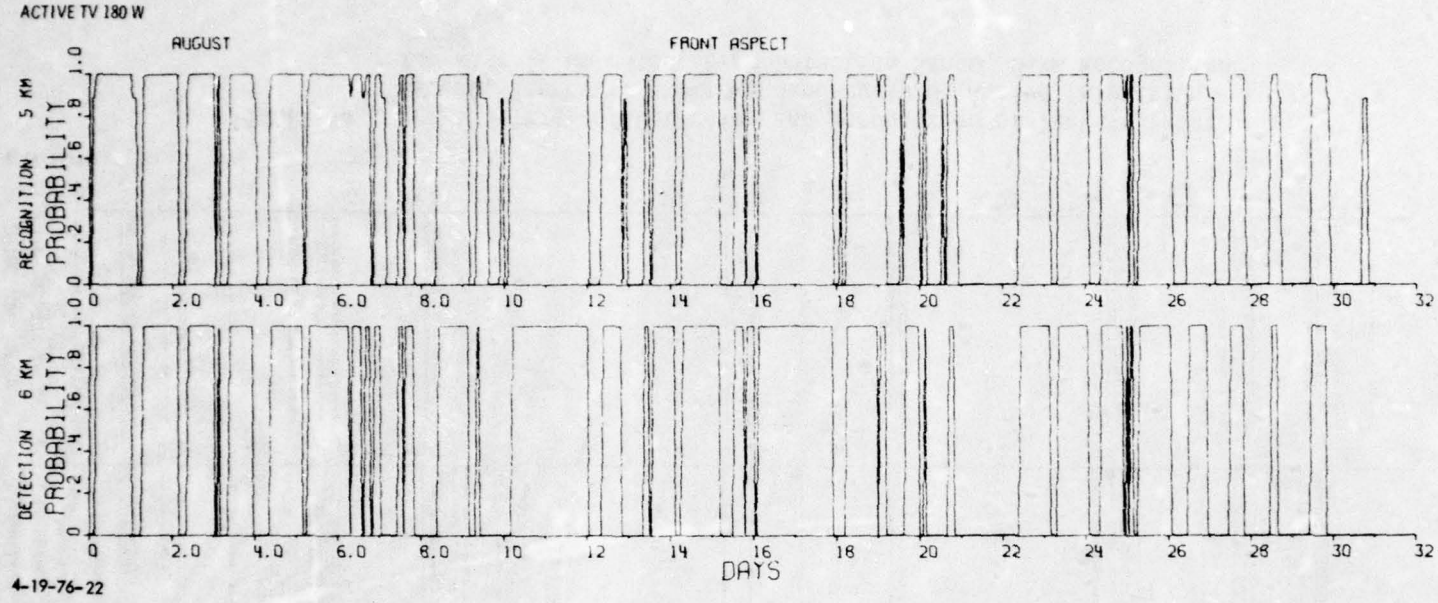


FIGURE 47. Probabilities of Detection and Recognition of Tank in Frontal Aspect, Hannover, Germany, August 1970; Active Television, 180-watt Illuminator, 6-km Detection Range, 5-km Recognition Range.

AD-A032 182 INSTITUTE FOR DEFENSE ANALYSES ARLINGTON VA SCIENCE A--ETC F/G 17/8
EFFECT OF WEATHER AT HANNOVER, FEDERAL REPUBLIC OF GERMANY, ON --ETC(U)
AUG 76 L M BIBERMAN

UNCLASSIFIED P-1123 IDA/HQ-76-18660 NL

2 OF 3
AD A032182



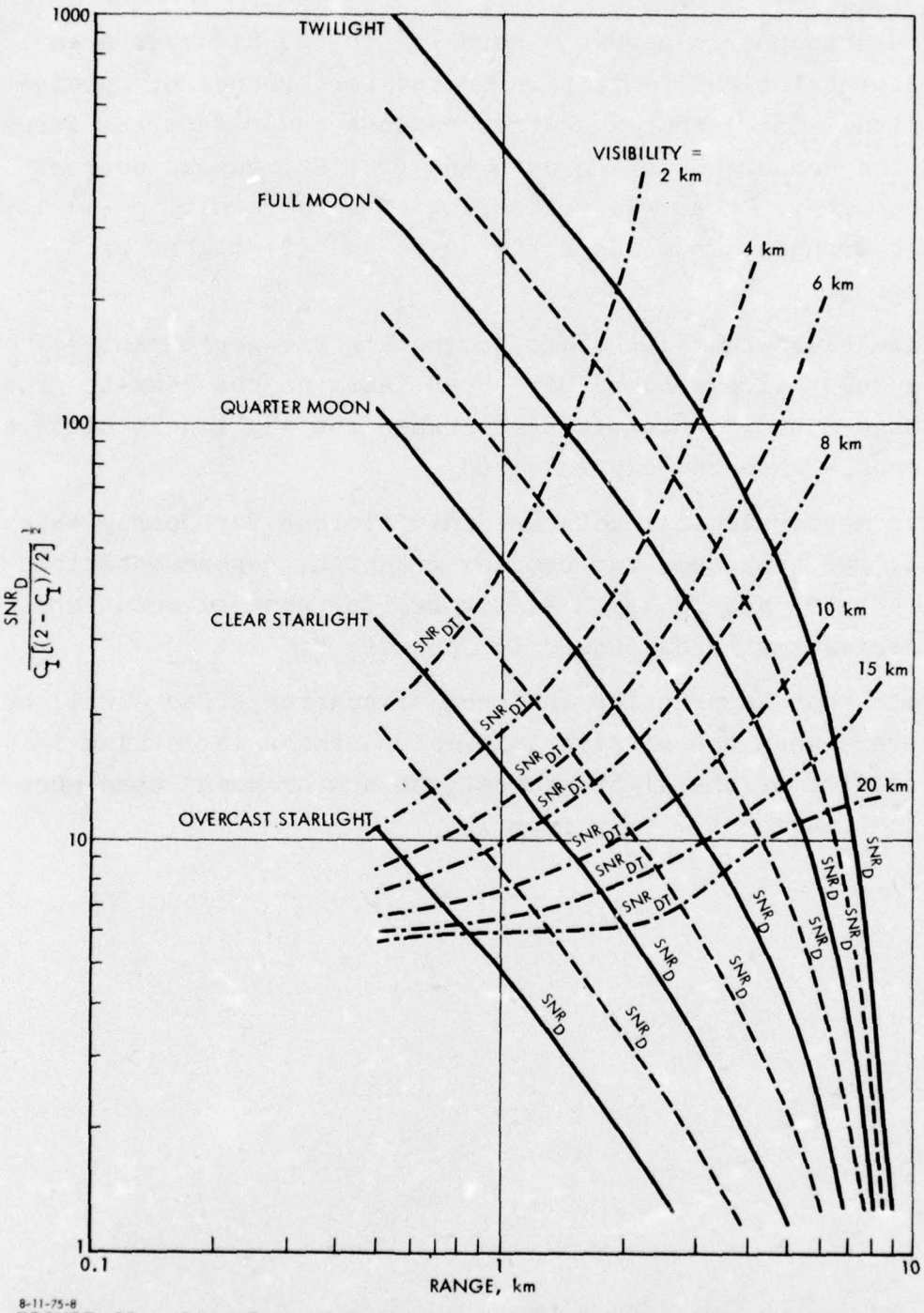
D. PASSIVE TELEVISION

The atmospheric aerosols normally in the Hannover area impose the principal limitation on the performance of passive television. The aerosols scatter radiant power from the scene out of the sensor's viewing path and from extraneous sources into the path. These two scattering effects result in (1) lower contrast transfer from scene to sensor and (2) higher path radiance.

The "classical" methods of computing the performance of passive television sensors have been based on the "sky-to-ground brightness ratio," which is useful when the sky is cloudless but questionable when the sky is cloudy.

Our meteorological data are insufficient for hourly calculations. We thus show two complex graphical respresentations (Figs. 48, 49) and Table 13 as first-order general solutions. Their derivation is discussed in Appendix F.

Note that in practice the aerosol scatter effects will be more severe when the passive television sensor is looking in the direction of the light source (the sun or moon) than when the sensor is looking away from it.



8-11-75-8

FIGURE 48. Signal-to-Noise Ratio at the Display (SNR_D) versus Range for Various Light Levels, and Threshold Signal-to-Noise Ratio at the Display (SNR_{DT}) versus Range for Various Light Levels and Visibilities.

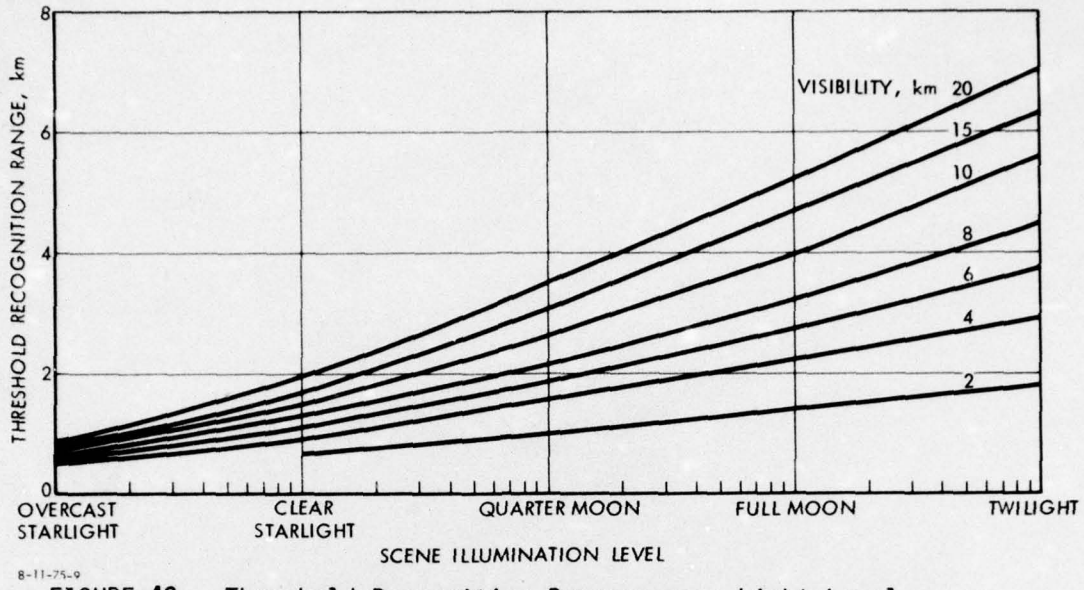


FIGURE 49. Threshold Recognition Range versus Light Level for Various Visibilities, C_o = 0.5, ρ_{max} = 0.5, λ_{av} = 0.7 μm.

TABLE 13. THRESHOLD RECOGNITION RANGE AS A FUNCTION OF LIGHT LEVEL AND VISIBILITY

	Threshold Recognition Range, km, for Tank in Frontal Aspect for Visibility of						
Light Level, fc	2 km	4 km	6 km	8 km	10 km	15 km	20 km
10^{-1}	1.85	2.95	3.80	4.60	5.60	6.28	6.90
3.16×10^{-2}	1.62	2.55	3.25	3.82	4.80	5.60	6.10
10^{-2}	1.40	2.20	2.75	3.20	4.00	4.75	5.30
3.16×10^{-3}	1.20	1.82	2.28	2.60	3.30	3.90	4.30
10^{-3}	1.00	1.48	1.85	2.13	2.62	3.08	3.40
3.16×10^{-4}	0.81	1.18	1.45	1.68	2.03	2.35	2.75
10^{-4}	0.63	0.90	1.10	1.25	1.50	1.72	2.00
3.16×10^{-5}	--	0.67	0.80	0.91	1.06	1.20	1.30
10^{-5}	--	0.50	0.57	0.62	0.71	0.79	0.83

V. COMPUTER PROGRAMMING

A. FORWARD-LOOKING INFRARED

The following is a brief description of the computer program FLIR, which is intended to simulate the performance of FLIRs using the methodology described in Section III-A. FLIR is a FORTRAN program designed to be run on a CDC 6400 computer. We shall attempt to indicate what features of the program are peculiar to the machine on which the program was developed and to give some general rules for using the model.

1. LOWTRAN 3

A general description of LOWTRAN 3 may be found in Appendix A. To be used in the FLIR model, the LOWTRAN 3 program was converted to a subroutine. The input parameters were put into labeled COMMON statements. All print statements (except those in error exits) were removed from LOWTRAN 3. Finally, the operation of LOWTRAN 3 was amended slightly. The first call to the subroutine LOWTRAN by the main program serves only to read in the data; no calculations are performed. Subsequent calls to LOWTRAN return the average transmittance calculated for the spectral band specified by the parameters V1 and V2. All such calculations in our work were made at a resolution of five wave numbers.

2. Inputs

Input data required for the FLIR model include the critical dimension of the target (in meters) and the temperature difference between the target and its background, as well as the weather data described below. The curves relating spatial

PRECEDING PAGE BLANK-NOT FILMED

frequency to MRT were entered in digital form along with scaling factors for each FOV (Fig. 30). A linear interpolation was performed between the input points of the curves. No curve fitting was used.

There is also a parameter to determine which of the three curves shown in Fig. 30 are to be used. Any one, any two, or all three may be chosen.

3. Output Tables

The data shown in Tables 7-10 have their shape and size determined by program constants. That is to say, the arrays and calculation loops of the program were set up specifically to handle a set of 20 ranges and eight combinations of FOV and display size. However, the user has the option of specifying whether he wants to have the probability of detection or the probability of recognition calculated.

If it is desired to change the number of ranges and FOVs the program works with, the various arrays and loops of the program must have their sizes adjusted accordingly.

The angular subtense of the target at each range (and the equivalent number of cycles per milliradian) is calculated in a subroutine that returns the values for both recognition and detection, although only one will be used.

Note that the apparent target temperature (see Fig. 31 and Section III) is simply the transmittance times the ΔT of the target. Since the latter is an input value, the transmittance is effectively available as an output (since the apparent target temperature is an output).

4. Hour-by-Hour Calculations

The weather data for one hour is read in and used to set the appropriate variables in LOWTRAN via the COMMON statements mentioned earlier. These values are the air temperature, pressure, dew point, and visibility.

For each range of interest, we find the transmittance from LOWTRAN (averaged over the band) and hence find the apparent target temperature as perceived by the sensor.

Using the ratio $\Delta T/MRT$ corrected for aspect ($\sqrt{\varepsilon/7}$), which is the normalization constant for the signal-to-noise ratio, we find the probability of detection for each device (i.e., for each FOV and display size) by use of the cumulative normal distribution.

After the above steps are complete, we have for the one hour's data a table such as Tables 9 and 10. This table is then written onto mass storage so that the results may be kept in machine-usable form for statistical analyses.

5. Machine Dependence

The only parts of the program that are machine dependent are the input and output of data and the subroutine which calculates the cumulative normal distribution. In particular, the END OF FILE checks on input are unique to computers of the CDC 6000 series. The remainder of the program is standard FORTRAN code and should be easily transferable to other computers.

B. ACTIVE AND PASSIVE TELEVISION

Programming for active and passive television is similar to the foregoing but is based upon the methodology discussed in Appendixes E and F.

VI. CONCLUSIONS

We show in this report that water-vapor attenuation of infrared radiation at wavelengths in the region of 8-12 μm is usually not a limiting factor in predicting the utility of FLIR sensors in tactical applications, although it is still a factor to be considered.

A far more serious factor for both FLIR and television sensors is the extinction due to aerosols in the path. Aerosols can, and do for 10% of the time in winter, 5% of the time in spring and fall, and 3% of the time in summer, impede the sensors considered in these reports to such a degree that they are useless beyond about a kilometer at ground level.

This report shows that changes in the weather affect the performance of electrooptical imaging sensors widely, frequently, and often rapidly, and that averaged weather data are consequently of little use in computing sensor performance at a given time.

In this context, terms such as midlatitude continental winter (or summer) air mass are meaningless, since the variations in transmission due to fluctuations in visibility or atmospheric water content within a single day can exceed a factor of ten. The diurnal cyclical variations that lead to early morning ground fogs can produce cyclical variations in atmospheric transmission that are far greater than the differences in transmission between a tropical maritime summer air mass and an arctic winter air mass.

Probably the only data useful for insight into the operational impact of weather upon sensor utility involve statistical

PRECEDING PAGE BLANK-NOT FILMED

processing of detailed sensor performance calculations, based upon frequent weather samples.

Early in our study we began using the LOWTRAN 3 atmospheric transmission model. Our results led us to conclude that FLIRs, which were seen to be adversely affected by high humidity in summer, were inferior in performance to active television in summer. Both FLIRs and active and passive television sensors were found to be seriously limited by the frequent fogs and ice fogs of winter in North Central Germany.

Some discrepancies between computed and measured transmittance values prompted us to reexamine the water vapor continuum as modeled in LOWTRAN 3 and to recommend a significant change in constants used to represent the effect of the continuum on atmospheric transmission. The revision generally increases calculated values of transmittance due to the water vapor continuum by a factor of about two for the ranges and conditions of interest, and our computed values now agree quite well with measured values.

Use of the revised LOWTRAN 3 model in calculating probabilities of target detection and recognition consistently predicts that FLIR will have greater detection and recognition capabilities than active television in foggier weather (winter). In clearer weather (summer), indications are that active television will outperform FLIR in recognition but that FLIR will continue to excel in detection.*

We have computed our data for a path near ground level, but we question whether this will give realistic results for an airborne sensor, even aboard a low-flying aircraft, because of the lapse rate of fog. Fog may lapse with altitude in such a way that a sensor at, say, 200-ft altitude will see more than twice

*As will be discussed in reports on the Grafenwöhr results, FLIR contrast tends to be very high, and observer time of response is considerably faster than with active television.

as far along a slant path to the ground as the same sensor at ground level will see along a horizontal path. This effect, and the reverse, has been measured in December 1975 tests at Grafenwöhr, Germany, but statistically useful data from those tests are not yet available. Such data for a limited range of altitudes have been obtained and are currently being processed.

The modeling methods followed in this series of reports have been used in field trials to predict ranges for detection and recognition of operating tanks. Predicted and measured values in those trials have been informally reported to agree quite well. A detailed examination of the data is now in progress.

Finally, we note once again that our results do not take account of three important operational factors: terrain masking of targets, cloud masking of targets, and effects on the performance of airborne observers caused by buffeting in air turbulence. These factors must be considered in final calculations. Statistics on terrain masking are not yet available in a form convenient for our use. Some statistics on the effect of clouds on clear lines of sight at Hannover are presented in Appendix B. Some quantitative data showing degradations in the performance of airborne sensor operators as a result of adverse operating conditions in flight are presented in Appendix H.

REFERENCES

1. USAF Environmental Technical Applications Center, Estimating Mean Cloud and Climatological Probability of Cloud-Free Lines of Sight, Technical Report 186, 1965.

2. I. A. Lund, "Estimating the Probability of Clear Lines of Sight from Sunshine and Cloud Cover Observations," J. Appl. Meteor., Vol. 4, 1965, pp. 714-722.

3. I. A. Lund, "Methods for Estimating the Probability of Clear Lines of Sight, or Sunshine, through the Atmosphere," J. Appl. Meteor., Vol. 5, 1966, pp. 769-777.

4. I. A. Lund and M. D. Shanklin, "Photogrammetrically Determined Cloud-Free Lines of Sight through the Atmosphere," J. Appl. Meteor., Vol. 11, 1972, pp. 773-782.

5. Aerospace Applications Studies Committee, Advisory Group for Aerospace Research and Development, North Atlantic Treaty Organization, Study No. 5 on Night Vision Devices for Fast Combat Aircraft (U), AGARD Advisory Report 73, Vol. I, January 1976, and Vols. II and III, December 1975 (NATO SECRET).

6. F. A. Rosell and R. H. Willson, "Recent Psychophysical Experiments and the Display Signal-to-Noise Ratio Concept," Chapter 5 in L. M. Biberman, ed., Perception of Displayed Information, Plenum Press, New York, 1973, pp. 167-232.

7. Systems Development Division, Defense and Electronic Systems Center, Westinghouse Electric Corporation, Performance Synthesis of Electro-Optical Sensors, Report AFAL-TR-74-104, F. A. Rosell and R. H. Willson, April 1974.

8. S. Q. Duntley, "The Reduction of Apparent Contrast by the Atmosphere," J. Opt. Soc. Am., Vol. 38, 1948, pp. 179-191.

9. S. Q. Duntley, "The Visibility of Distant Objects," J. Opt. Soc. Am., Vol. 38, 1948, pp. 237-249.

10. W. E. K. Middleton, Vision through the Atmosphere, University of Toronto Press, Toronto, 1952.

PRECEDING PAGE BLANK-NOT FILMED

11. Air Force Institute of Technology, Atmospheric Contrast Transmission: Application to the Visual Detection and Electro-Optical Lock-On Problem, M. S. Thesis, Graduate Physics Engineering, Report GEP/PH/72-4, E. A. Duff, June 1972.

12. Institute for Defense Analyses, Infrared Continuum Absorption by Atmospheric Water Vapor in the 8-12 μm Window, IDA Paper P-1184, R. E. Roberts, J. E. A. Selby, and L. M. Biberman, April 1976; also R. E. Roberts, J. E. A. Selby, and L. M. Biberman, "Infrared Continuum Absorption by Atmospheric Water Vapor in the 8-12-μm Region," Applied Optics, September 1976.

13. I. A. Lund and M. D. Shanklin, "Universal Methods for Estimating Probabilities of Cloud-Free Lines of Sight through the Atmosphere," J. Appl. Meteorol., Vol. 12, pp. 28-35.

14. Defense and Electronic Systems Center, Westinghouse Electric Corporation, The Impact of Weather on the Performance of Electrooptical Sensors in Europe, AFAL Contract F-33615-70C-1461, K. C. Leonard, Jr., L. G. Sowell, and D. A. Waller, 22 November 1972.

15. F. A. Rosell, "The Limiting Resolution of Low-Light-Level Imaging Sensors," Chapter 14 in L. M. Biberman and S. Nudelman, eds., Photoelectronic Imaging Devices, Vol. 1, Physical Processes and Methods of Analysis, Plenum Press New York, 1971, pp. 307-329.

16. Defense and Electronic Systems Center, Westinghouse Electric Corporation, Recent Psychophysical Experiments and the Display Signal-to-Noise Ratio Concept, Report ADTM 110, F. A. Rosell and R. H. Willson, 7 September 1972.

17. John Johnson, paper presented at Image Intensifier Symposium, Ft. Belvoir, Virginia, 6-7 October 1958. (AD 220160)

18. A. D. Schnitzler, "Analysis of Noise-Required Contrast and Modulation in Image-Detecting and Display Systems," Chapter 4 in L. M. Biberman, ed., Perception of Displayed Information, Plenum Press, New York, 1973, pp. 119-166.

19. Institute for Defense Analyses, Low-Light-Level Devices: A Designers' Manual, IDA Report R-169, L. M. Biberman et al., August 1971. (NTIS AD735006)

20. Electro-Optical Systems, Xerox Corporation, E/O Sensor Performance Analysis and Synthesis (TV/IR Comparison Study), Report AFAL-TR-72-374, R. L. Sendall and F. A. Rosell, April 1973.

APPENDIX A

PRINCIPLES OF THE LOWTRAN 3 & 3a MODELS

John E.A. Selby
Eric P. Shettle
Robert W. Fenn
Robert A. McClatchey
Frederic E. Volz

Air Force Geophysics Laboratory
Air Force Systems Command

CONTENTS

A.	Introduction	A-5
B.	Basic Assumptions	A-6
C.	Molecular Absorption	A-8
D.	Water Vapor Continuum	A-10
E.	Aerosol Attenuation	A-16
F.	Additional Aerosol Models	A-20
	1. Rural Model	A-22
	2. Urban Model	A-25
	3. Maritime Model	A-25
	4. Tropospheric Model	A-27
	5. LOWTRAN 3 Aerosol Model	A-27
	6. Optical Properties of the Aerosol Model	A-27
G.	Summary and Conclusions	A-32
	References	A-42

PRECEDING PAGE BLANK-NOT FILMED

A. INTRODUCTION

The need for predicting the transmittance of the atmosphere over a broad spectral interval at low resolution is not a new one, and many methods have been proposed to do this. The major problems with most of the various techniques are that they are often difficult to apply and that they predict widely different results for the same input conditions. To alleviate this situation and to provide a fairly accurate, simple, and rapid way of estimating atmospheric transmittance in the 0.25 to 28.5 μm region, an empirical graphical prediction scheme was devised using some techniques originally suggested by Altshuler in 1961 (Ref. 1). The prediction scheme is based mainly on recent laboratory transmittance measurements complemented by using available theoretical molecular line constants in line-by-line transmittance calculations, and was presented by McClatchey et al. in 1972 (Ref. 2).

Because of the large amount of interest shown in this work, the latter prediction scheme and atmospheric models were developed into a computer code called LOWTRAN 2 (Ref. 3).

Essentially, LOWTRAN 3 (Ref. 4) is a modification of the LOWTRAN 2 computer code. LOWTRAN 3 updates the original data and gives more flexibility to the user.

The FORTRAN computer code LOWTRAN 3 is designed to calculate the transmittance (averaged over a 20 cm^{-1} interval) for

PRECEDING PAGE BLANK-NOT FILMED

any given atmospheric path at steps of 5 cm^{-1}* from 350 to 40,000 cm^{-1} (0.25 to 28.5 μm). Refraction and earth curvature effects are included in the calculation scheme for slant atmospheric paths.

The transmittance due to molecular absorption (including continuum absorption by water vapor and nitrogen in the 10 μm and 4 μm regions), molecular (Rayleigh) scattering, and aerosol extinction are accounted for in the computer code. It should be noted that angular scattering effects are not considered in LOWTRAN 3; only the direct attenuation loss or beam transmittance is calculated.

A choice of six atmospheric models is given with an option to insert a seventh model, which can be in the form of radiosonde data. The six standard model atmospheres include: tropical (15°N); midlatitude summer (45°N); midlatitude winter (45°N); subarctic summer (60°N); subarctic winter (60°N); and the 1962 U.S. Standard Model (mean 45°N).

The above model atmospheres contain the variation of water vapor and ozone with altitude. It is also assumed that the mixing ratios of the gases CO_2, N_2O, CH_4, CO, O_2, and N_2 remain constant at all altitudes with values of 330, 0.28, 1.6, 0.075, 2.095×10^5 and 7.905×10^5 parts per million, respectively.

B. BASIC ASSUMPTIONS

The basic assumptions made in LOWTRAN 3 (as in the previous LOWTRAN codes and the earlier graphical scheme) are that:

1. The atmosphere can be represented by a 33-layer model between sea level and 100 km.

---

*The data used in LOWTRAN were generated on a linear wavenumber (cm^{-1}) scale for convenience, since most of the laboratory transmittance measurements on which they were based were plotted versus wavenumber ν rather than wavelength λ. Note that λ (μm) = $10^4/\nu$ (cm^{-1}).

2. The average transmittance $\bar{\tau}$ over a 20 cm^{-1} interval (due to molecular absorption) can be represented by a function of the form

$$\bar{\tau} = f\ (C(\lambda)\omega^*), \qquad \text{(A-1)}$$

where $C(\lambda)$ is a wavelength-dependent absorption coefficient, and ω^* is an "equivalent absorber amount" for the atmospheric path, which is defined in terms of the pressure $P(z)$, the temperature $T(z)$, the concentration of absorber ΔL, and an empirical constant n, as follows:

$$\omega^* = \Delta L \left\{ \frac{P(z)}{P_o} \sqrt{\frac{T_o}{T(z)}} \right\}^n . \qquad \text{(A-2)}$$

3. The total transmittance at a given wavelength λ, averaged over a 20 cm^{-1} interval, is given by the product of the average transmittances due to (a) molecular absorption, (b) molecular scattering, (c) aerosol extinction, and (d) continuum absorption. It is further assumed (in Eq. A-3) that the molecular absorption is broken into three components, namely the separate transmittance of (a) water vapor, (b) ozone, and (c) the combined contributions of the uniformly mixed gases CO_2, N_2O, CO, CH_4 and O_2, i.e.:

$$\bar{\tau}(\text{total}) = \bar{\tau}(H_2O) \times \bar{\tau}(O_3) \times \bar{\tau}(CO_2), \text{ etc.} \qquad \text{(A-3)}$$

$$\times\ \bar{\tau}(\text{Rayleigh}) \times \bar{\tau}(\text{aerosol}) \times \bar{\tau}(\text{continua}).$$

4. Aerosol attenuation at all wavelengths can be described in terms of visual range for an "average continental aerosol model," based on the following assumptions.

5. Particle size distribution is similar to Deirmendjian's Haze Model C (Ref. 5), but the large particle radius cutoff has been extended to 100 μm (compared to 5 μm in Ref. 5 and 10 μm in LOWTRAN 2 and Ref. 2).

6. The shape of the particle size distribution is assumed to remain constant with altitude, i.e.,

$$n(r,z) = N(z) \cdot f(r),$$

where N(z) is the aerosol number density as a function of height (z), and f(r) is the normalized size distribution.

7. Aerosol number density variation with altitude is assumed to be the same as previously given in LOWTRAN 2 for the 23-km and 5-km visual range models. Those aerosol number densities were adjusted to give extinction coefficients at a wavelength of 0.55 μm, which corresponded to those obtained by Elterman (Refs. 6, 7) at each altitude.

8. Aerosol refractive index variation with wavelength has been obtained from measurements by Volz (Refs. 8, 9) (see also Ref. 10) and is assumed to be independent of altitude. Aerosol extinction and aerosol absorption values were calculated based on single scattering Mie theory using the above-mentioned aerosol size distribution and refractive index values, assuming the aerosols to be composed of 70% water-soluble substance and 30% dustlike substance, which appears to be representative of continental aerosols (Sections E and F).

C. MOLECULAR ABSORPTION

Initially, the LOWTRAN concept was introduced to provide a simple, graphical scheme for estimating atmospheric absorption, the emphasis being on molecular absorption. The absorption of radiation in the atmosphere at a given wavelength depends in general on three parameters: the number of absorbing molecules

along the path, and the pressure and temperature distributions along the path. The temperature dependence of molecular absorption is by far the least important of these three parameters.* Therefore, it was assumed constant at a value of 273°K. A detailed study of molecular absorption leads us to the understanding that the number of absorbing molecules m and the pressure p tend to enter as a product, and thus some function of the single parameter (mp) should give a reasonable fit to the actual transmittance. This was one reason for choosing the formulation given in Eqs. A-1 and A-2 above, where m and ΔL are synonymous.

Laboratory transmittance measurements, supplemented where necessary with synthetic transmittance data** (both degraded to a common resolution of 20 cm^{-1}), were used to empirically determine: (a) the functional form of transmittance, f, as given by Eq. A-1; (b) the exponent n; and (c) the coefficient $C(\lambda)$ for a wide range of pressures and absorber amounts. It was found that the functions f for the H_2O and the combined contributions of the uniformly mixed gases were essentially identical, although the parameter n differed in the two cases. Mean values for n were determined to be 0.9 for water vapor, 0.75 for the uniformly mixed gases, and 0.4 for ozone.

The parameters f, n, and $C(\lambda)$ having been determined over the entire spectrum, Eq. A-1 is applied directly (in digital form in LOWTRAN 3) to determine the transmittance due to molecular absorption for the three separate components described above.

The appropriate value of the parameter mp^n is calculated by the program for a given target-receiver geometrical configuration and set of meteorological conditions.

The procedure will be described below for the water vapor continuum.

---

*Except for the water vapor continuum (Section D).

**"Synthetic transmittance data" here refers to monochromatic (line-by-line) transmittance calculations degraded to a fixed spectral resolution.

D. WATER VAPOR CONTINUUM

The major spectral region under consideration here is the "window" region from 8 to 13 μm. In addition to aerosol effects, the major sea-level attenuator of radiation is water vapor, by virtue of the so-called water vapor continuum. This continuum occurs as a result of the accumulation of distant H_2O line wings and possibly as a result of H_2O dimer absorption. Due to the nature of the water vapor continuum, the equivalent sea-level absorption parameter per unit path length is given by

$$b_h(z) = P_{H_2O}(z)\, W(z) \exp\left[1800\left(\frac{1}{T(z)} - \frac{1}{296}\right)\right] \qquad \text{(A-4a)}$$

for horizontal paths, where $P_{H_2O}(z)$, $W(z)$ and $T(z)$ refer to the partial pressure (atm) and density (gm-m^{-3}) of water vapor and ambient temperature (°K), respectively, at altitude z (km).

The equivalent sea-level parameter for vertical paths is given by

$$b_v(z) = \int_z^\infty P_{H_2O}(z)\, W(z) \exp\left[1800\left(\frac{1}{T(z)} - \frac{1}{296}\right)\right] dz. \qquad \text{(A-4b)}$$

These quantities are plotted as a function of altitude in Figs. A-1a and A-1b for five atmospheric models.

The water vapor continuum attenuation coefficients, which are used in conjunction with Figs. A-1a and A-1b to determine the transmittance for a given atmospheric path, are presented in Fig. A-2. The curve shown in Fig. A-2 was obtained from experimental measurements which included those of Burch (Ref. 12) together with more recent measurements (see R. Roberts et al., Ref. 11). An empirical expression for the fit is given below for 296°K:

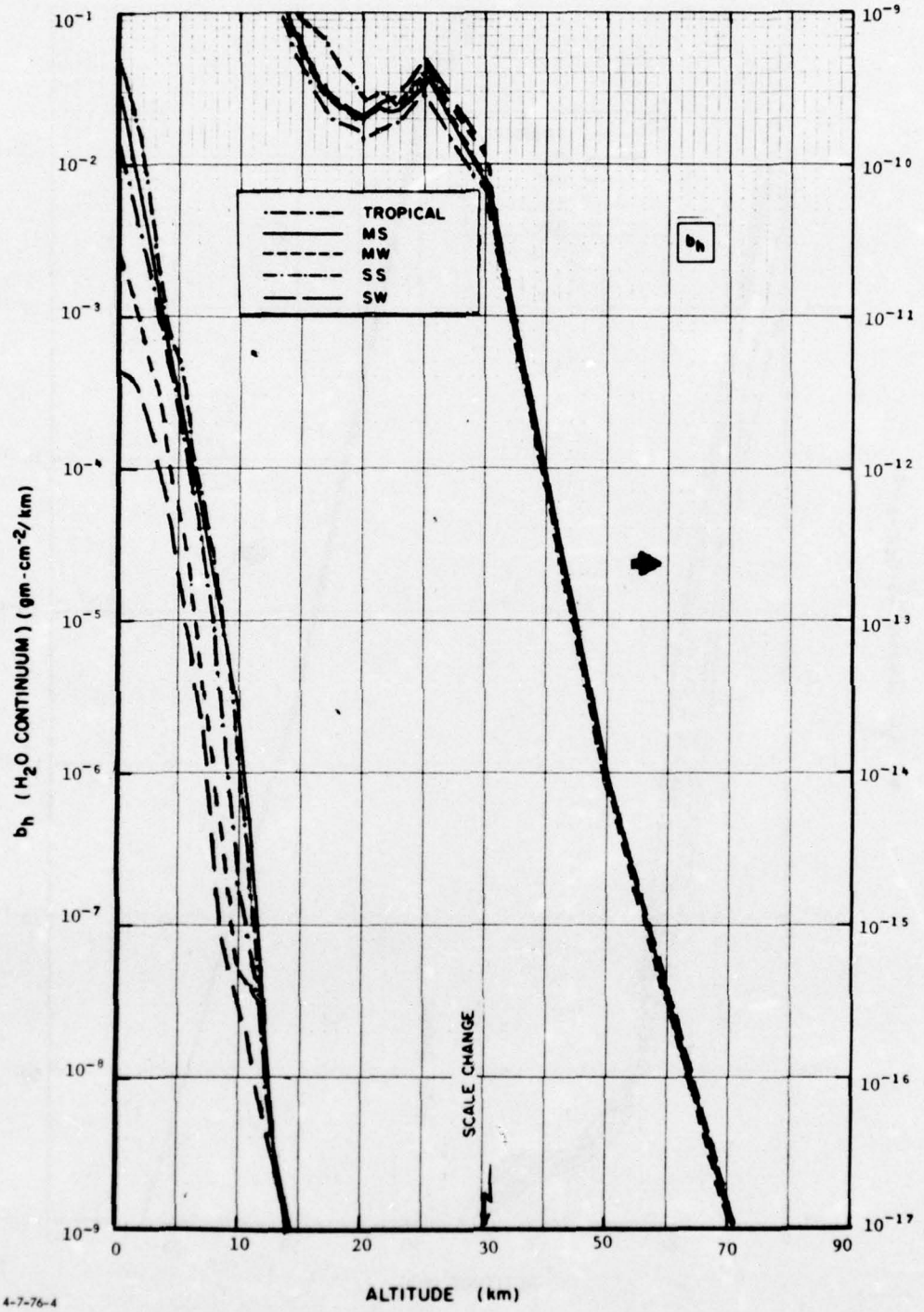


FIGURE A-1a. Equivalent Sea-Level Path Length for Water Vapor Continuum as a Function of Altitude for Horizontal Atmospheric Paths

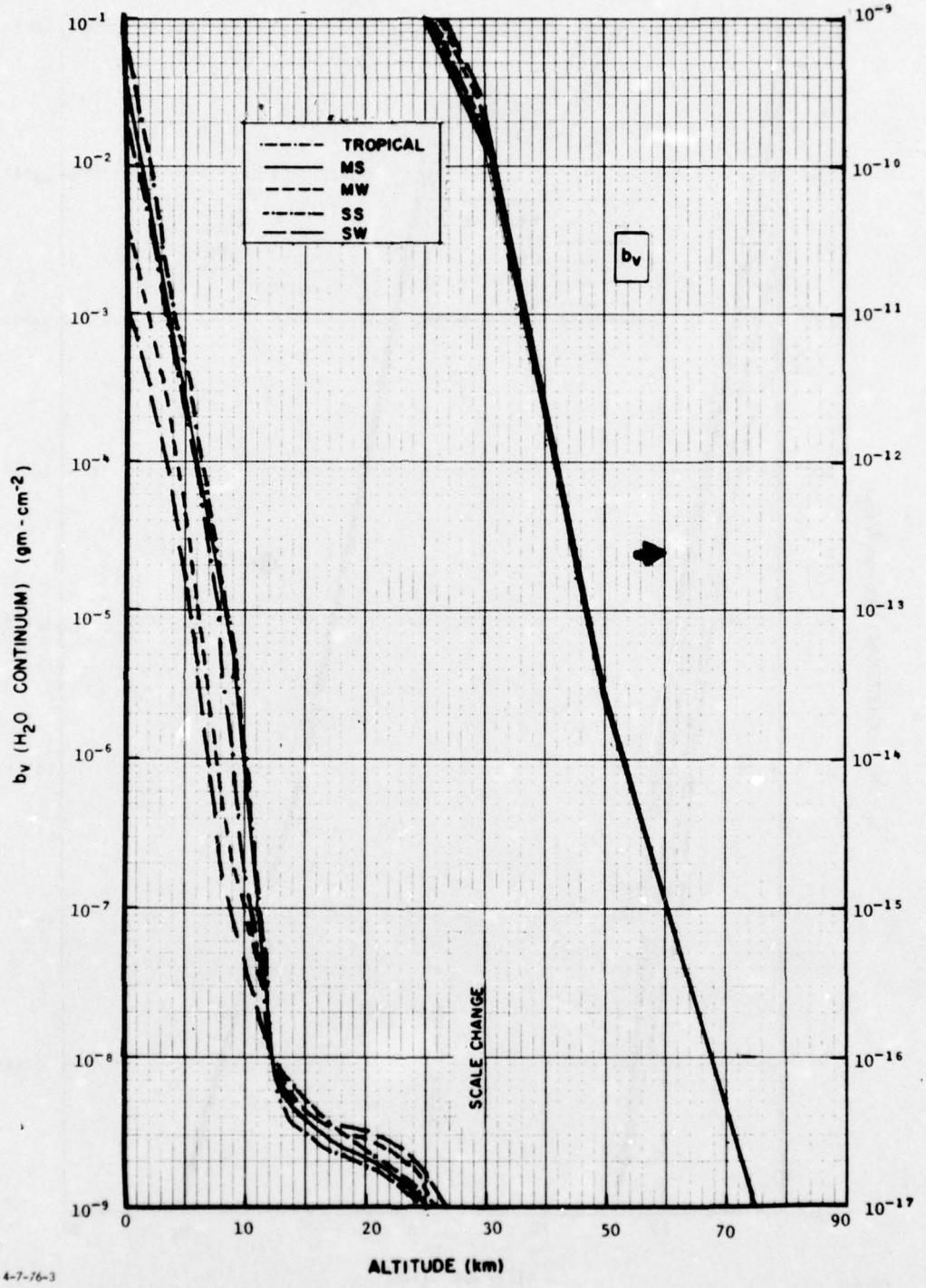


FIGURE A-1b. Equivalent Sea-Level Path Length for Water Vapor Continuum as a Function of Altitude for Vertical Atmospheric Paths

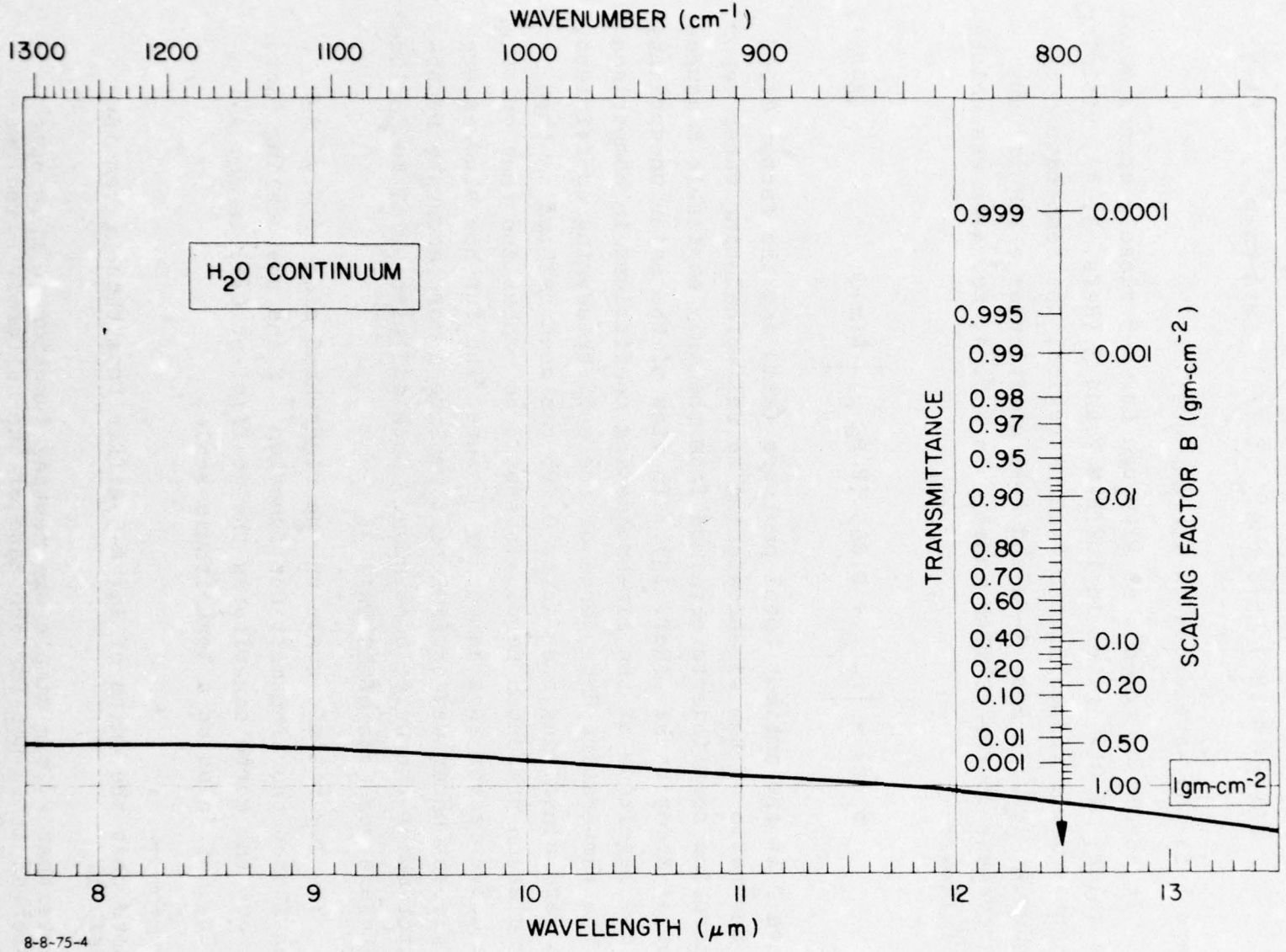


FIGURE A-2. Prediction Chart for Transmittance Due to Water Vapor Continuum

$$C(\lambda) = 4.18 + 5578 \exp(-78.7/\lambda) \quad (\text{atm-gm-m}^{-3}) \qquad (A\text{-}5)$$

where λ is the wavelength in micrometers.[†]

It should be noted that although Eq. A-5 closely approximates the values of $C(\lambda)$ given in LOWTRAN 2 and 3 (Refs. 3, 4), yielding slightly lower values in the 8-10 μm region, the temperature dependence given in Eqs. A-4a and A-4b constitutes a significant improvement to the LOWTRAN model. In Ref. 4, Eq. A-4a was written as follows:

$$b_h(z) = \left[P_{H_2O} + 0.005\ (P - P_{H_2O})\right] W(z), \qquad (A\text{-}4a')$$

where P is the ambient total pressure (atm) and the factor 0.005 is the ratio of the air-broadening to self-broadening water vapor absorption coefficients obtained from the only available measurement of McCoy et al. (Ref. 13). In view of the major uncertainty in the magnitude of the air-broadening coefficient in comparison to the temperature dependence of the self-broadening coefficient, the term containing the factor 0.005 has been omitted in the formulation presented here. It should be emphasized that omitting the above factor is a temporary measure, and further studies are at present under way at AFGL to formulate a more accurate representation of the water continuum. Such additions will be included in future versions of LOWTRAN 3.

The logarithmic scale on the right-hand side of Fig. A-2 constitutes the transmittance function[††] f and the scaling factor ω^*, and the curve constitutes the coefficient $C(\lambda)$ in Eq. A-1 or Eq. A-5 (also on a logarithmic scale).

[†]Note that the units of Eq. A-5 differ from those given in Ref. 11.

[††]Note that f is a simple exponential function in this case, whereas it is <u>not</u> for the case of the uniformly mixed gases O_3 and H_2O discussed previously.

To calculate the transmittance (due to the water vapor continuum) for a horizontal path of range R at altitude z, Figs. A-1 and A-2 are used as follows:

1. First, determine the appropriate absorber amount ω^*, which is given by $\omega^* = b_h(z) \times R$, where $b_h(z)$ is obtained from Fig. A-1a for the required atmospheric model and altitude z.
2. The transmittance/scaling-factor scale is then displaced vertically in Fig. A-2 until ω^* (on the B scale) is aligned with the base line (labeled 1 gm-cm^{-2}).
3. Shift the transmittance scale horizontally and read off the transmittance at each wavelength where the curve intersects the center of the transmittance scale.

This procedure is best understood by first tracing the transmittance/scaling-factor scale onto tracing paper, and it is described in detail in Ref. 2.

In the above example the operation is simply

$$\bar{\tau} \text{ (continuum)} = \exp\left(-C(\lambda)\omega^*\right). \qquad \text{(A-6)}$$

For a slant path of range R between altitudes z_1 and z_2,

$$\omega^* = \left[b_v(z_1) - b_v(z_2)\right]\left(R/(z_2 - z_1)\right), \qquad \text{(A-7)}$$

where b_v is determined from Fig. A-1b for the required atmospheric model at altitudes z_1 and z_2. Equation A-6 is then applied to determine the transmittance at each wavelength, as in the previous case.

E. AEROSOL ATTENUATION

The assumptions made in the aerosol models contained in LOWTRAN 3 have been outlined in Section B.

The application of LOWTRAN 3 to calculating aerosol transmittance is similar to that given in Section D.

Aerosol transmittance is a function of the variation of aerosol number density N(z) with altitude z, for a given size distribution. Therefore, the appropriate scaling parameters in LOWTRAN 3 can be defined as

$$a_h(z) = N(z)/N_o \qquad \text{(A-8)}$$

and

$$a_v(z) = \int_z^\infty [N(z)/N_o]\, dz \qquad \text{(A-9)}$$

for horizontal and vertical paths, respectively, where N_o is the sea-level aerosol number density for a given visual range.

Figures A-3a and A-3b show the variation with altitude of a_h and a_v for the 23-km and 5-km sea-level visual range aerosol models contained in LOWTRAN 3.

A procedure for calculating N(z) for an arbitrary sea-level visual range was determined and is described below.

The total extinction coefficient σ_T at 0.55 μm is inversely proportional to visual range VIS and can be written as follows (Ref. 14):

$$\sigma_T = \sigma_a + \sigma_m = \frac{3.91}{VIS}\ , \qquad \text{(A-10)}$$

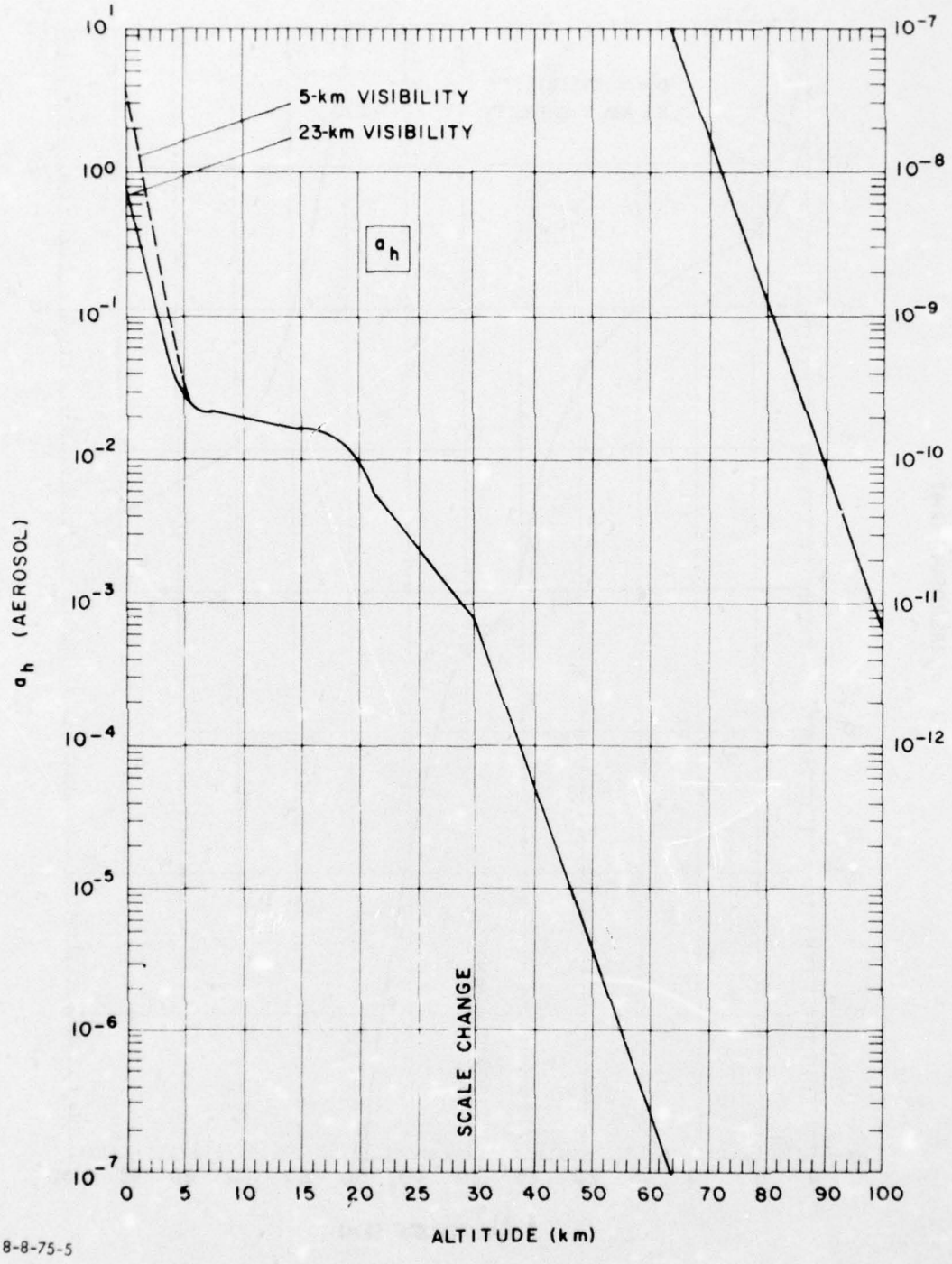


FIGURE A-3a. Equivalent Sea-Level Path Length for Aerosol Extinction as a Function of Altitude for Horizontal Atmospheric Paths

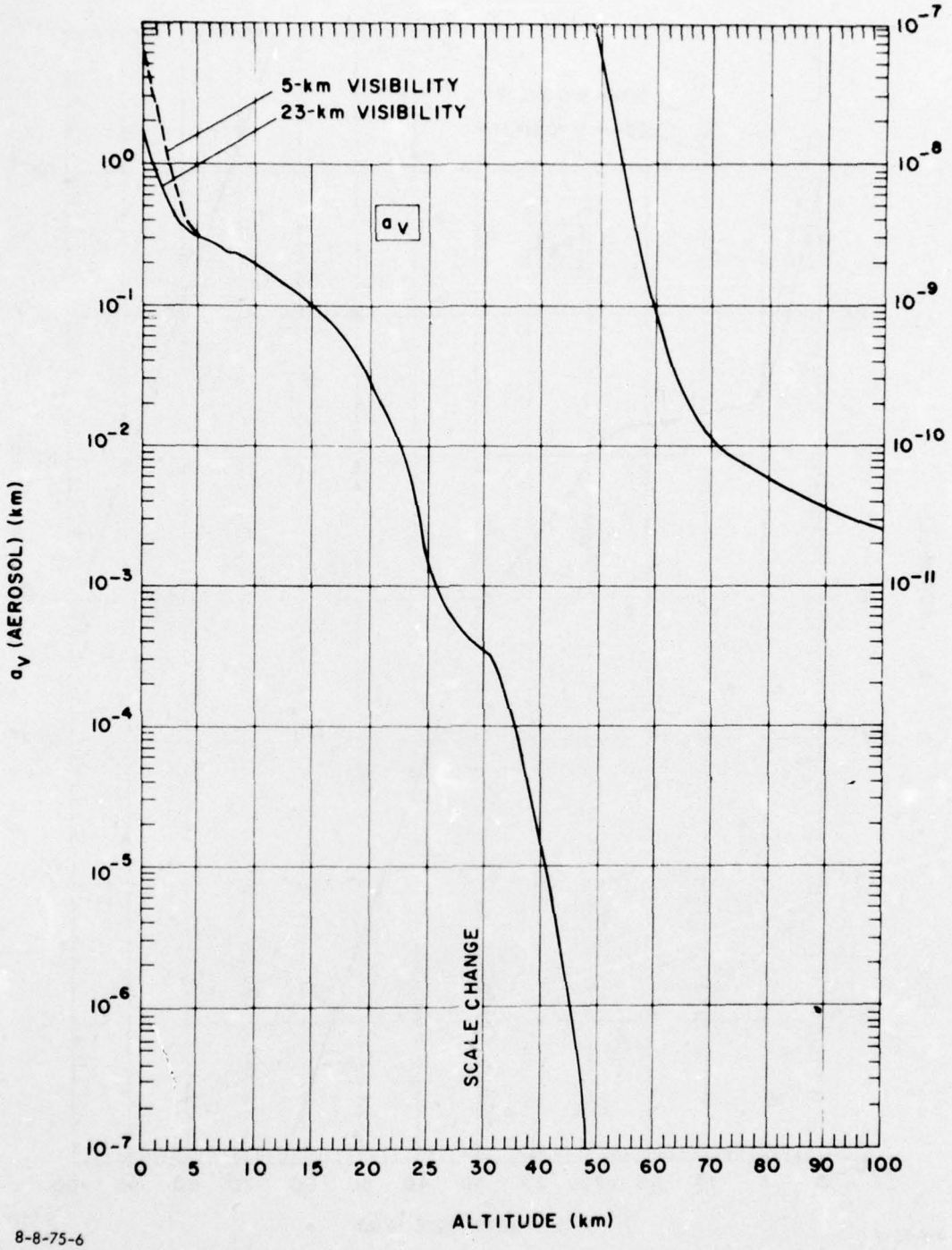


FIGURE A-3b. Equivalent Sea-Level Path Length for Aerosol Extinction as a Function of Altitude for Vertical Atmospheric Paths

assuming a 2% contrast threshold for the eye, and where the suffixes a and m refer to the aerosol and molecular components, respectively. The aerosol extinction coefficient can thus be written as

$$\sigma_a = \frac{3.91}{VIS} - \sigma_m. \qquad \text{(A-10')}$$

Since in our model the aerosol extinction coefficient σ_a is directly proportional to the aerosol number density N(z), we can write

$$N(z) = \frac{A(z)}{VIS} + B(z), \qquad \text{(A-11)}$$

where A(z) and B(z) are constants for a given altitude z. It will be noted that B(z) is proportional to the molecular scattering coefficient σ_m at 0.55 μm at altitude z.

Equation A-11 forms the basis for the interpolation/extrapolation procedure used in LOWTRAN 3 to determine aerosol attenuation at any given sea-level visual range. The coefficents A and B are determined from Eq. A-11 at each altitude z using the 5-km and 23-km aerosol model number densities $N_5(z)$ and $N_{23}(z)$, respectively, i.e.,

$$A(z) = [N_5(z) - N_{23}(z)]/[1/5 - 1/23]$$

$$B(z) = [N_{23}(z)/5 - N_5(z)/23]/[1/5 - 1/23]. \qquad \text{(A-12)}$$

Note that the above procedure is used only in the lower 5 km of the atmosphere, since the two aerosol models are identical above 5-km altitude.

Figure A-4 provides the aerosol extinction (and absorption) coefficients for a 1-km path at sea level for the 23-km visual

range model. The same procedure as described in Section D is used to determine the transmittance for horizontal or slant paths, using Fig. A-4 in conjunction with Figs. A-3a and A-3b, respectively, and Eq. A-12, e.g.,

$$\bar{\tau}\ (\text{aerosol}) = \exp\left(-C(\lambda)\ N(z)\ R/N_o\right) \qquad \text{(A-13)}$$

for a horizontal path of range R at altitude z, where $C(\lambda)$ is obtained from the left-hand scale in Fig. A-4 for a given wavelength λ.

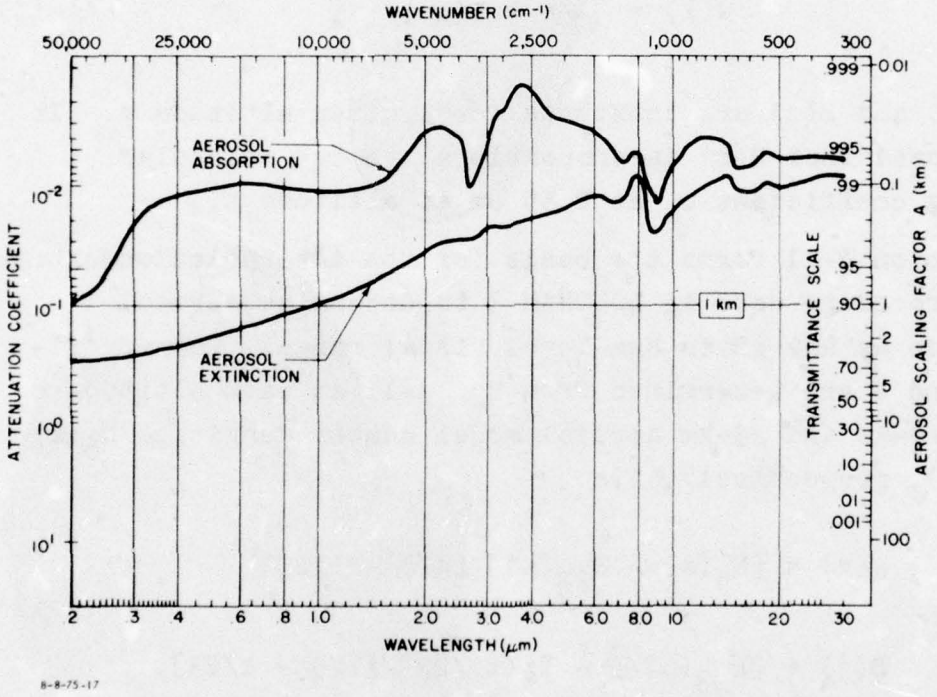


FIGURE A-4. Attenuation Coefficients for Aerosol Transmittance (Absorption and Total Extinction)

F. ADDITIONAL AEROSOL MODELS

To study the effect of different aerosol types on transmission, several other aerosol models were used with LOWTRAN 3, and these

additional models will be discussed here. These models were not, however, used in the analysis of Hannover weather data presented in Chapter II, since both the rural and urban aerosol models gave transmittances similar to the LOWTRAN 3 model when averaged over the 8.5-11 μm region. It should be noted that these three models have important differences in other spectral regions or when the distinction between scattering and extinction is significant.

These aerosol models have been developed recently at AFGL, and a detailed description and discussion of them is presently in preparation as an AFGL technical report. They are also described by E.P. Shettle and R.W. Fenn in the Proceedings of a recent AGARD conference (Ref. 15).

These aerosol models apply to the atmosphere from the surface up to 100-km altitude in different environments. Since this study deals only with surface-layer phenomena, the discussion here will be limited to the boundary layer below 2-km altitude. For this layer, models for rural and urban environments as well as the maritime sea aerosol and the troposphere with various surface visibilities between 2 and 50 km have been developed.

The models describe the number density, the size distribution, and the refractive index as functions of wavelength of the aerosol substance. By applying the Mie theory (Ref. 16) for scattering and absorption of electromagnetic radiation by small particles, the total extinction coefficient, the scattering and absorption coefficients for a unit volume of air, and the angular scattering intensity and polarization were determined.

A sufficient amount of experimental data on aerosol composition and distribution in the surface layer has been collected within the past 10-20 years to allow the development of general models for rural, urban, or maritime environments. It must be emphasized, however, that these models represent only the typical conditions. Present experimental data are not sufficient to derive the variance or frequency of occurrence of these various model conditions.

1. Rural Model

The rural model is assumed to be composed of a mixture of 70% water-soluble and 30% dustlike aerosols. The relative proportions of aerosol types are assumed to be independent of size. This is partly for simplicity and partly because available data are inadequate to form the basis for a realistic differentiated aerosol model.

The refractive indices for these aerosols are based primarily on the measurements of Volz (Refs. 8, 9).

The size distribution for both aerosol types is the sum of two log-normal distributions which can be expressed as:

$$\frac{dN}{dr} = \sum_{i=1}^{2} \left(\frac{N_i}{\ell n(10)\ r\ \sigma_i \sqrt{2\pi}} \right) \exp \left[- \frac{(\log r - \log r_i)^2}{2\ \sigma_i^2} \right],$$

where N is the number density, σ is the scattering coefficient, and r is the particle radius. The parameters defining the size distribution are given in Table A-1, and the size distribution is illustrated in Fig. A-5.

This size distribution was chosen to approximate the Junge distribution. Junge (Ref. 17) suggested that a large body of aerosol size measurements could be characterized by a simple power law for the differential number density distribution:

$$n(r) = \frac{dN}{dr} = Cr^{\nu},$$

where $\nu = -4$. This is supported by other data, which show that the power law is approximately valid over the size range of radius between 0.1 and more than 10 μm.

TABLE A-1. AEROSOL SIZE DISTRIBUTION PARAMETERS NORMALIZED TO 1 PARTICLE/cm^3

Type of Aerosol	N_1[a]	r_1, μm	σ_1	N_2[a]	r_2, μm	σ_2
Rural	0.9999975	0.005	0.475	2.5×10^{-6}	0.5	0.475
Urban	0.9999975	0.005	0.475	2.5×10^{-6}	0.5	0.475
Maritime, Continental Origin	1.	0.005	0.475	--	--	--
Maritime, Sea Origin	1.	0.3	0.4	--	--	--
Tropospheric	1.	0.005	0.475	--	--	--

[a] $N_1 + N_2 = 1$

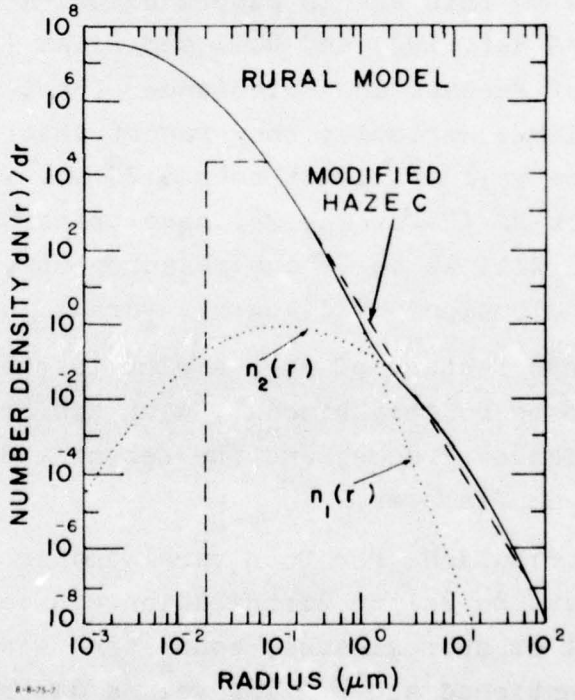


FIGURE A-5. Size Distribution for the Present Rural Aerosol Model (solid line) Compared with the Modified Haze C Model (dashed line). Also shown are the individual log-normal distributions (dotted lines) that make up the rural model.

Over this size range the present model is similar to the modified "haze C" used by McClatchey et al. (Ref. 2), which was based on Diermendjian's "haze C" (Ref. 5).

The "haze C" model has several disadvantages. It has unrealistic discontinuities, and it underestimates both the number of Aitken nuclei and the number of very large particles ($r > r_{max}$). While the first two do not have a major effect on the aerosol optical properties, for wavelengths considered in this report, the neglect of the large-particle aerosols will lead to greatly underestimating the aerosol attenuation and scattering in the infrared.

There are relatively few measurements of the aerosol size distributions for the very large ($r > 10$ μm) particles which have a major effect on the optical properties in the infrared. Notable exceptions to this are in papers by Okita (Ref. 18), Jaenicke and Junge (Ref. 19), and Noll and Pilat (Ref. 20). Some of the data of Pasceri and Friedlander (Ref. 21) also include these very large aerosols; they report that a power-law model appears to be valid at least to $r \approx 70$ μm. Whitby (Ref. 22) and his co-workers (Refs. 23, 24) have transformed the data of Refs. 18-20, as well as their own measurements, into a graph of the volume distribution, $dV/d(\log r)$, versus $\log r$.

The significant feature of such a plot is that nearly all the data appear to be roughly bimodal, with one broad peak in the 0.1 to 1 μm diameter range, and the second and larger peak between 5 and 100 μm diameter.

The size distributions for both rural and urban conditions were chosen so that the volume distribution was consistent with these data as well as approximately consistent with the Junge distribution as mentioned above. The volume distribution for the model has peaks at diameters of 0.36 and 36 μm, with the large-particle peak being 2.5 times the small-particle peak at their centers.

2. Urban Model

The urban aerosol model is taken to be a mixture of the rural aerosol with sootlike particulates. The rural component is identical with the rural aerosol model described above. The refractive index of the sootlike aerosols was based on the soot data in Twitty and Weinman's survey of the refractive index of carbonaceous materials (Ref. 25). The sootlike aerosols were assumed to have the same size distribution as both aerosol types making up the rural model.

The basic urban model takes the proportions to be 35% sootlike and 65% rural aerosol (or 45.5% water soluble and 19.5% dustlike).

3. Maritime Model

The maritime aerosol model is taken to be a mixture of sea-spray-produced particles and a background of aerosols of continental origin. The larger particles are taken to be predominantly the former, as in the model proposed by Junge (Refs. 17, 26), based largely on his data (Refs. 27, 28).

This model is also supported by the measurements of Meszaros and Vissy (Ref. 29), taken in the South Atlantic and Indian Oceans. They found the larger particles predominantly had a cubic crystalline structure characteristic of sodium chloride. The smaller particles were a mixture of other aerosol types, the largest identification component being ammonium sulphate.

For the size distribution of the sea-spray-produced component, a log-normal distribution is used, with r_2=0.3 and σ_2=0.4. This is consistent with the measurements of Woodcock (Ref. 30), as well as the more recent measurements of Winkler and Junge (Ref. 31) and the sea-salt type component of the data of Meszaros and Vissy (Ref. 29).

It should be noted that this size distribution is sensitive to the recent wind conditions (Ref. 30). As the wind speed

increases, there is an increase in the numbers of particles of the sea-spray-produced aerosol in all size ranges, but particularly for the larger particles. The present model is typical of moderate wind speeds. The size distribution will also depend on the prevailing humidity, because of the growth of aerosols (particularly the hygroscopic ones such as salts) with increasing relative humidity.

The refractive index is based on that for a solution of sea salt in water, using a weighted average of the refractive indices of water and sea salt. The weights were taken from the mass fractions of water condensed on sea salt at approximately 80% relative humidity. While such an average is, strictly speaking, incorrect [e.g., see Bullrich (Ref. 31) or Hänel (Ref. 32)], it does have the advantage of simplicity. Also, the error introduced by this simplification is within the range of the other uncertainties which will affect the optical properties of the model (i.e., the choice of size distribution, the relative proportions of water and sea salt, and the refractive index of the sea salt). A value of 2.5 for the mass ratio of water to sea salt is used on the basis of data of Winkler (Ref. 33), Winkler and Junge (Refs. 34, 35), Hänel (Ref. 36) and Kasten (Ref. 37).

The refractive index of the sea salt is primarily taken from the measurements of Volz (Ref. 9). His data for the imaginary part was limited to wavelengths longer than 2.5 μm, but this was extended to 0.2 μm by using the absorption measurements for sea water and pure water compiled by Dorsey (Ref. 38).

For the refractive index of water, the survey of Hale and Querry (Ref. 39) was used.

The continental component of the maritime model was taken to have the same composition as the rural model (70% water soluble and 30% dustlike). The size distribution was modified

by eliminating the large-particle component, since these bigger aerosols have a shorter residence time in the atmosphere (Ref. 17) and are preferentially lost as the aerosols become distant from their source. This leaves only the smaller-particle log-normal size distribution, with r_1=0.005 μm and σ_1=0.475.

4. Tropospheric Model

The tropospheric aerosol model represents the aerosols within the troposphere above the boundary layer. There aerosols are assumed to have the same composition as the rural model (70% water soluble and 30% dustlike). The size distribution is modified from the rural model by eliminating the large-particle (r_2=0.5 μm) component of the size distribution, because of the longer residence of aerosols above the boundary and the expected differential loss of the larger particles. This leaves the log-normal distribution with r_1=0.005 μm and σ_1=0.475.

The troposperhic model also represents an extremely clear surface condition with little or no wind and a minimum number of large aerosol particles.

5. LOWTRAN 3 Aerosol Model

The aerosol model which is incorporated presently in LOWTRAN 3 and which is labeled as LOWTRAN 3 Continental in Fig. A-6 has been described by McClatchey and Selby (Ref. 10). It was derived from the aerosol model in LOWTRAN 2 by extending the large-particle cutoff from 5 to 100 μm and by substituting more realistic values for the aerosol refractive index according to Volz (Refs. 8, 9). This size distribution is the Modified Haze C discussed above and shown in Fig. A-5. This model is essentially a preliminary version of the rural model.

6. Optical Properties of the Aerosol Model

Figure A-6 gives the extinction coefficients for the five models as a function of wavelength. The curves are normalized at 0.55 μm. Figures A-7 through A-10 show separately the

coefficients for scattering and absorption and also the sum of both (extinction) for the rural, urban, maritime, and tropospheric models. It is significant to note that for wavelengths greater than 5 μm the aerosol absorption is comparable to the scattering.

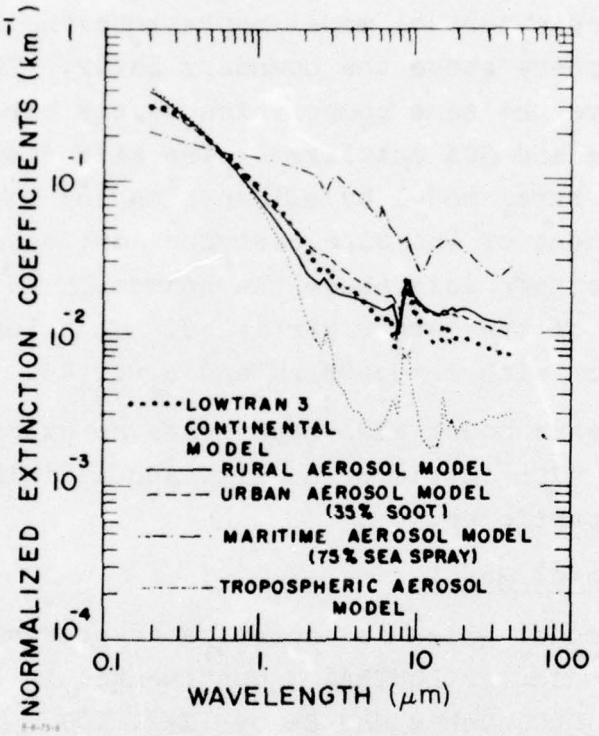


FIGURE A-6. Extinction Coefficients for the Lower Atmospheric Aerosol Models. To facilitate a comparison of the wavelength dependence of the extinction for the different models, the particle concentrations have been normalized so that the extinction at 0.55 μm corresponds to 23-km visual range.

A comparison of these curves in Fig. A-6 shows that the extinction coefficients for the LOWTRAN 3 continental model and the urban and rural models over the spectral band from 8.5 to 11 μm are very much the same. This is not so in other spectral regions. These will be examined (especially the 3.4-4.2 μm band).

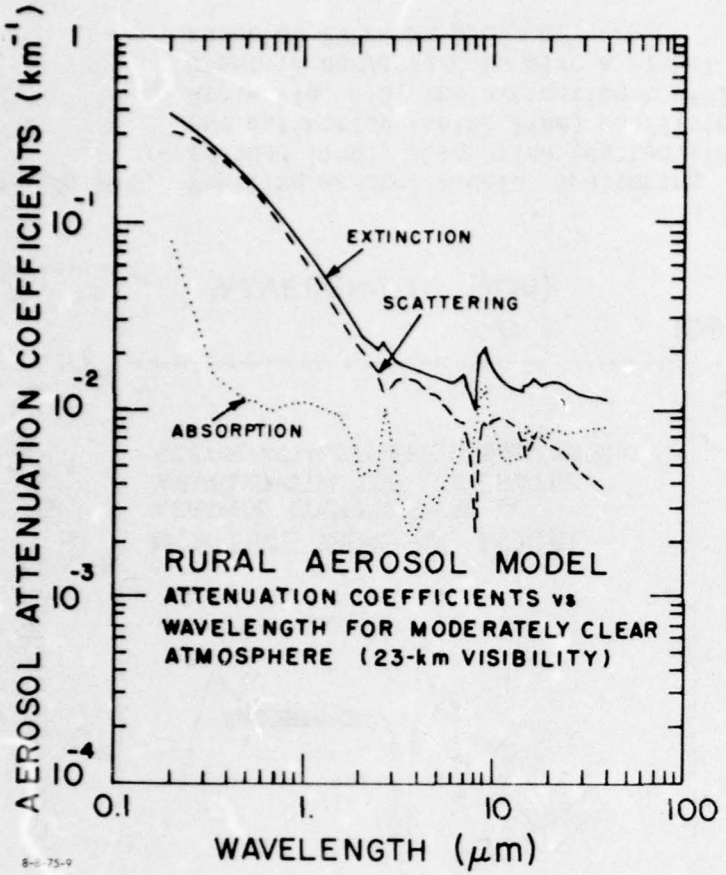


FIGURE A-7. Rural Aerosol Model. Scattering (dashed line), absorption (dotted line), and extinction (solid line) coefficients. As in Fig. A-6, the extinction coefficient is normalized to give a visual range of 23 km at 0.55 μm

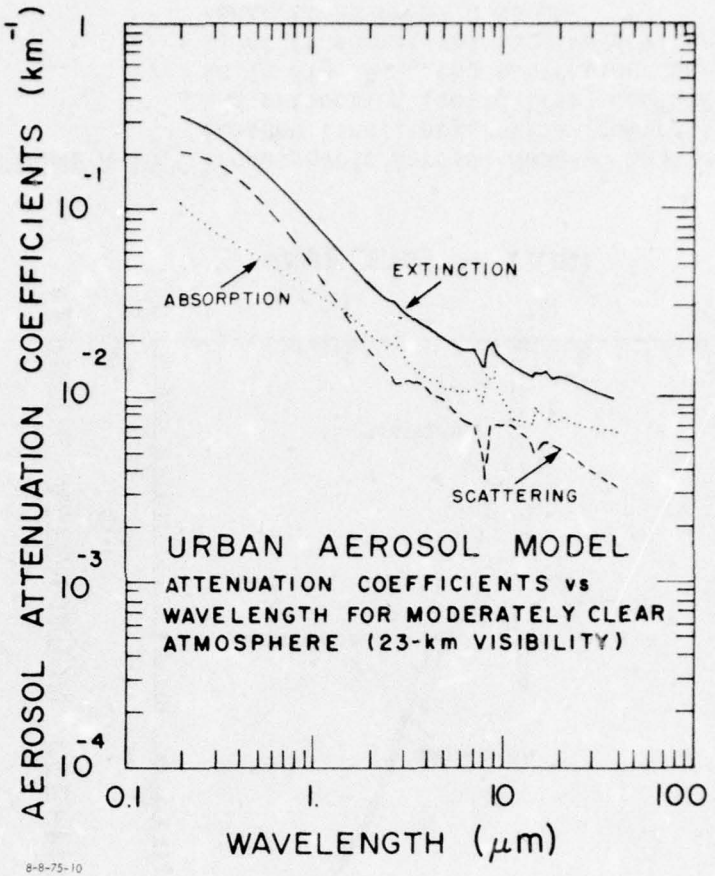


FIGURE A-8. Urban Aerosol Model. Scattering (dashed line), absorption (dotted line), and extinction (solid line) coefficients. As in Fig. A-6, the extinction coefficient is normalized to give a visual range of 23 km at 0.55 μm

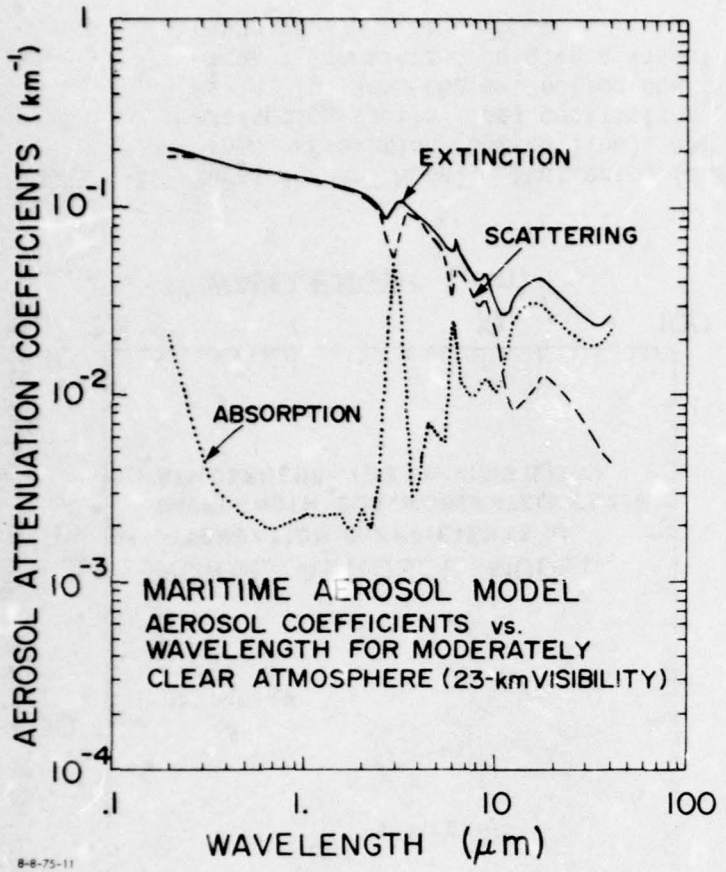


FIGURE A-9. Maritime Aerosol Model. Scattering (dashed line), absorption (dotted line), and extinction (solid line) coefficients. As in Fig. A-6, the extinction coefficient is normalized to give a visual range of 23 km at 0.55 μm

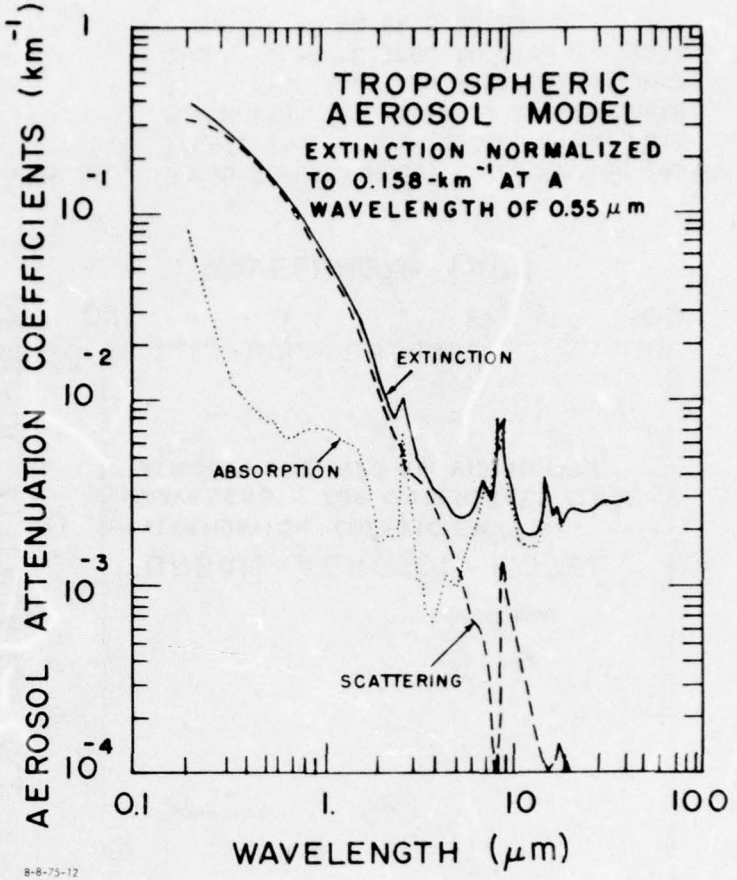


FIGURE A-10. Tropospheric Aerosol Model. Scattering (dashed line), absorption (dotted line), and extinction (solid line) coefficients. As in Fig. A-6, the extinction coefficient is normalized to give a visual range of 23 km at 0.55 μm

The similarity holds only for the extinction coefficient, and not for the scattering or absorption coefficients separately, especially in comparisons of the urban versus rural or LOWTRAN 3 models. Compare Figs. A-7 and A-8, where the relative amounts of scattering and absorption are similar for the rural and LOWTRAN 3 models. This is important to keep in mind for applications dealing with scattered radiation only.

The scaling of transmission data from visibility statistics in the visible spectrum to the IR region by applying the continental, rural, and urban aerosol models, we feel, can be done with confidence for visibilities larger than 1-2 km and for relative humidities lower than 90%. Visibility changes in this region can be assumed to be primarily due to changes in particle number and therefore are not associated with changes in wavelength dependence of the transmission properties. Furthermore, at least in the 8.5-11 μm region, the extinction coefficients are insensitive to the different size distributions and refractive indices of these three aerosol models, so that any variations of these parameters within the boundaries of the urban-rural models would have insignificant effects on transmission.

For visibilities lower than 2 km and for higher relative humidities, these assumptions may not be valid. For relative humidities above 90%, particle growth due to water absorption will occur. For conditions with relative humidities between 90 and 95%, the maritime aerosol model might be more representative because of its larger particle content, even for the continental environment, but it should be used with caution.

Except for isolated cases near industrial plants, visibilities below 1 to 2 km are usually due to fog formation and not high concentrations of aerosol particles. The scaling of optical properties for the visibility conditions of 1 km should therefore be based on fog models (Ref. 40). As a first approximation, the extinction of radiation of concern here may be assumed wavelength independent.

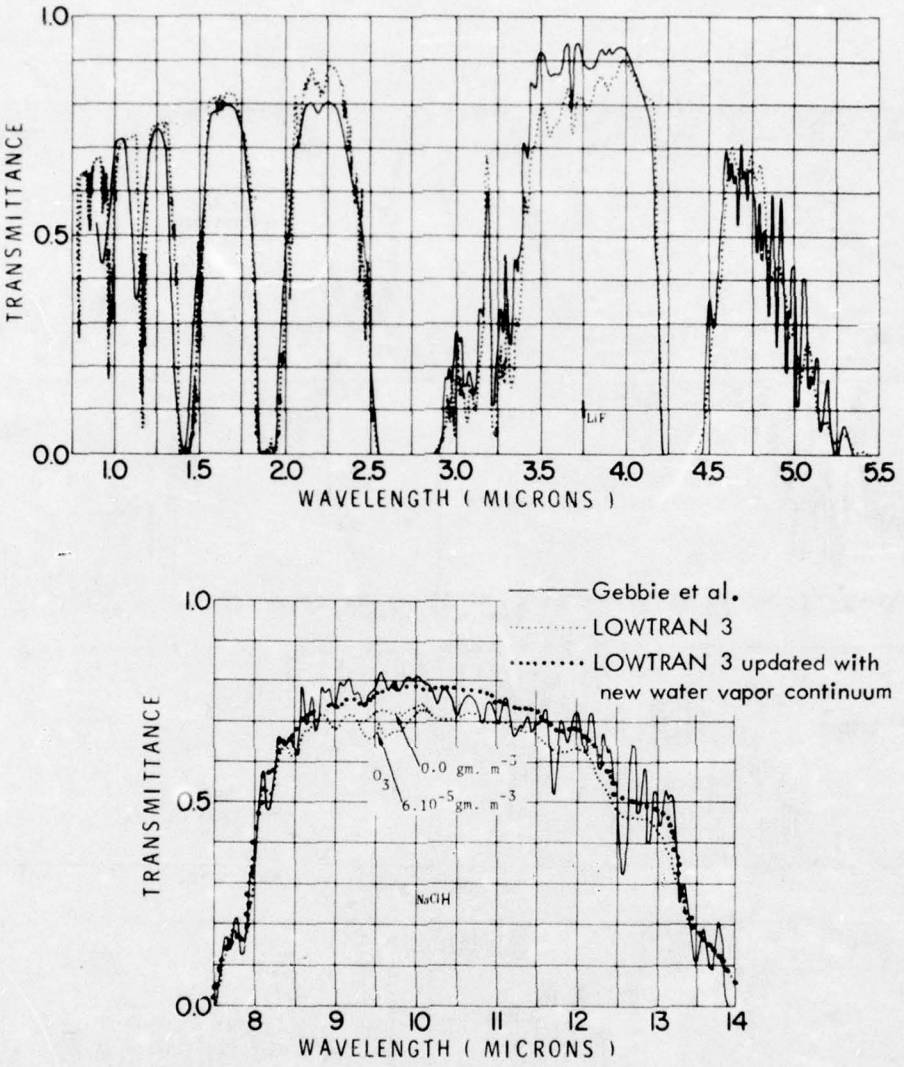
Only for the extremely clear conditions with light wind or no wind, which could be represented by the tropospheric aerosol model with very few large particles, the IR extinction could be less than that predicted by the LOWTRAN 3 continental, urban, or rural models. This condition, however, is very unlikely to occur in the central European environment at or near ground level.

Therefore, even if one would consider the possible effects of humidity and fog on the transmission of 8.5-11 μm radiation, the importance of aerosol attenuation over molecular absorption would be increased, and thus we believe quite strongly that our results, though possibly not as complete as might be hoped for, do show the effects we wished to demonstrate.

G. SUMMARY AND CONCLUSIONS

A great deal of effort has gone into validating LOWTRAN 3 for a wide range of applications by comparing LOWTRAN 3 transmittance predictions directly with available field and laboratory transmittance measurements. In each case the same meteorological inputs were used in the predictions, and these are discussed in detail by Selby and McClatchey (Ref. 4).

1. In general, fairly good agreement has been found between experimental field measurements and LOWTRAN 3 predictions, although a lack of accurate meteorological data (including visual range and actual aerosol characteristics) gives rise to some uncertainty. In Figs. A-11 and A-12 comparisons are given between LOWTRAN 3 predictions and two transmittance measurements of Gebbie et al. (Ref. 41) and Yates and Taylor (Ref. 42), both of which cover a wide spectral range. In simulating the spectrum of Gebbie et al. for a 1-nmi path (over water), the visual range was assumed to be 13 km (which gives a transmittance of 60% at 0.61 μm). Two calculations were made, one corresponding to the ozone amount of the midlatitude winter model atmosphere, and the other to no ozone. The latter case appears to agree better with Gebbie's measurement.



ATMOSPHERIC TRANSMITTANCE FOR A 1-nmi PATH
(WATER CONTENT 1.7 PRECIPITABLE CENTIMETERS)

8-8-75-13

FIGURE A-11. Comparison of LOWTRAN 3 and Updated LOWTRAN 3 (LOWTRAN 3a) Predictions with Measurements of Gebbie et al. (Ref. 41) for a 1-nmi Path at Sea Level.

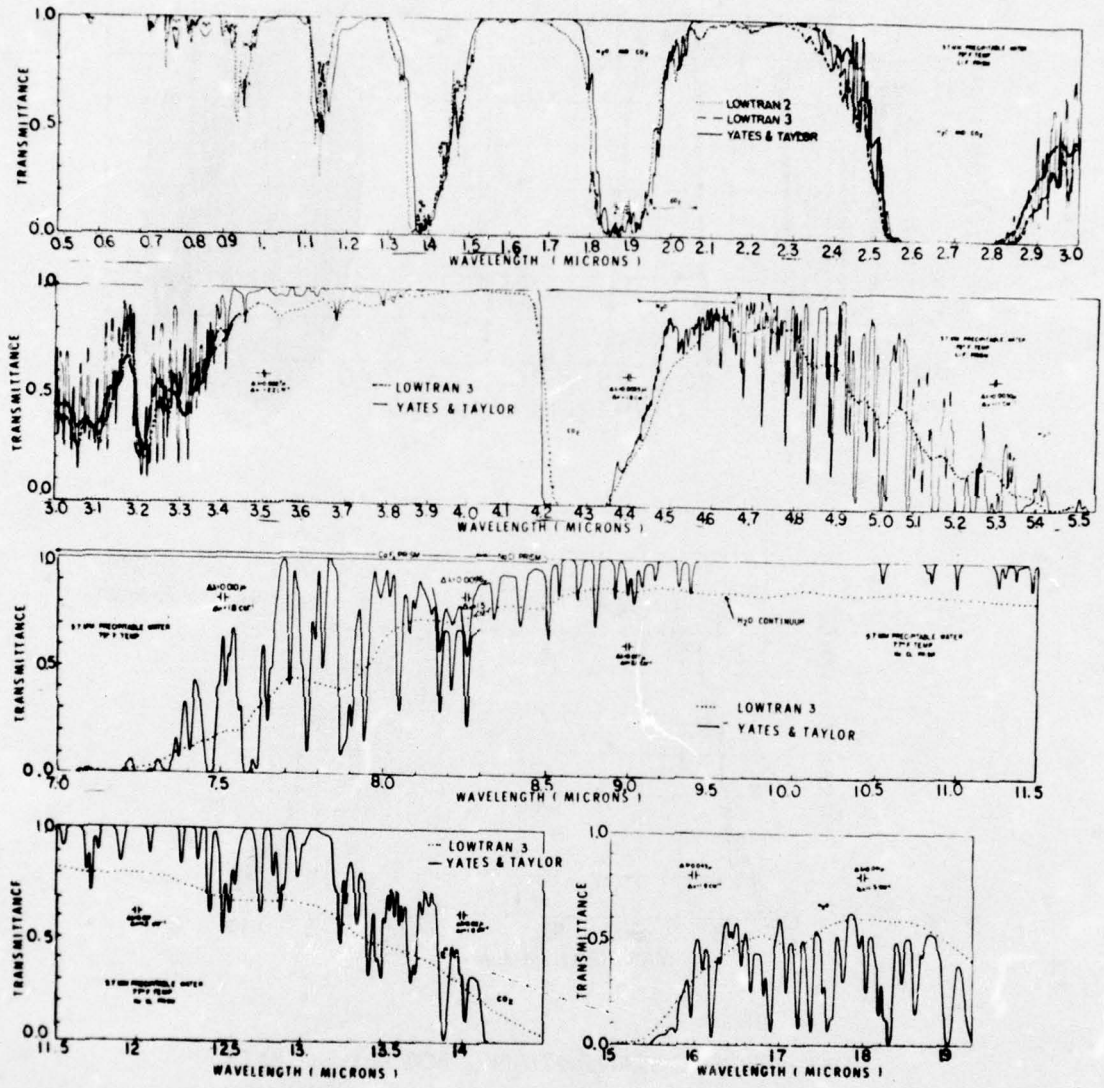
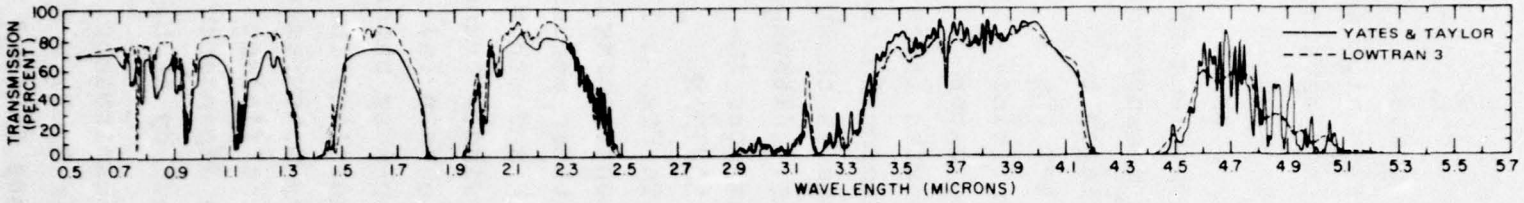


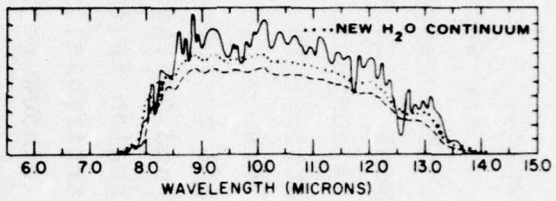
FIGURE A-12. Comparison of LOWTRAN 3 Predictions with Measurements of Yates and Taylor (Ref. 42) for a 0.3-km Path at Sea Level.

Also shown in Fig. A-11 (dashed curve) is the effect of including the more recent modification to the water vapor continuum contribution. It will be seen that somewhat better agreement is achieved with the measurement of Gebbie et al. No significant deviation from the LOWTRAN 3 comparison was obtained in the case of Fig. A-12. No aerosol attenuation was used in simulating Yates and Taylor's spectrum over a 0.3-km path at sea level. The apparent wavelength shift at short wavelengths is due to a calibration error in Yates and Taylor's measurements. The apparent discrepancy in the 10 μm region is believed to be due to the fact that Yates and Taylor artificially set the transmittance level to be 100% in this window region (since they were unable to estimate the contribution of the water vapor continuum). Other comparisons have been made with Yates and Taylor's longer path measurements, and the agreement in the 10-μm region is both good and bad. A typical example is shown in Fig. A-13 for 5.5-km and 16.25-km sea-level paths. Although the recent modification to the water vapor continuum does improve the agreement between these measurements and LOWTRAN predictions (as can be seen from the dashed curves in Fig. A-13), discrepancies are found when comparing the measurements among themselves, and therefore the reliability of using these measurements as a standard against which to compare LOWTRAN and other models is highly questionable. However, the 10 μm window transmittance dilemma cannot be fully resolved until we obtain (a) reliable atmospheric transmittance measurements over long paths at sea level for well-documented meteorological conditions in the 8-14 μm region, and (b) more accurate laboratory measurements of the self and foreign gas broadening absorption coefficients for the water vapor continuum and their temperature dependence. Work on these problems is presently being carried out by AFGL.

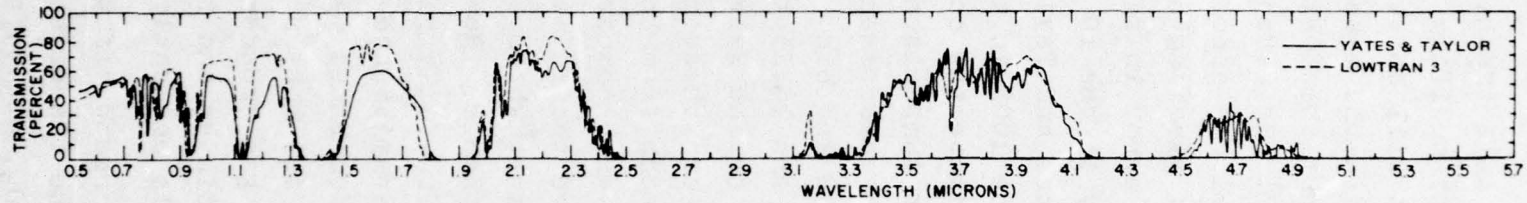
2. LOWTRAN 3 will round off the molecular transmittance components to zero <u>if</u> the transmittance is less than 0.001. This is for $\overline{\tau}(H_2O)$, $\overline{\tau}(CO_2$, etc.), and $\overline{\tau}(O_3)$ only (see Eq. A-3 in Section B) and does not include the H_2O continuum. Therefore, for very long atmospheric paths at sea level (i.e., greater than



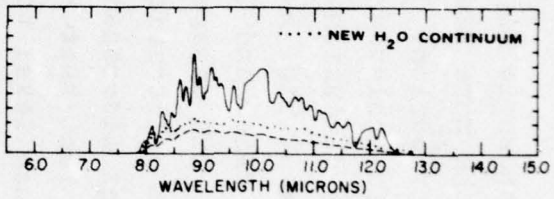
Path Length	5.5 km	Relative Humidity	51%
Time	2100 hr	H_2O in Path	4.18 cm
Temperature	64°F	Transmittance at 0.55 μm	70%
		LOWTRAN 3 visual range	60 km



(a)



Path Length	16.25 km	Relative Humidity	53%
Time	1600 hr	H_2O in Path	15.1 cm
Temperature	68.7°F	Transmittance at 0.55 μm	43%
		LOWTRAN 3 visual range	75 km



(b)

8-8-75-15

FIGURE A-13. Comparison of LOWTRAN 3 Predictions with Measurements of Yates and Taylor (Ref. 42) for (a) 5.5-km and (b) 16.25-km Paths at Sea Level.

15 km), the prediction from LOWTRAN 3 may be unreliable in certain spectral regions if a sensitivity of less than 0.001 in transmittance is required.

3. Using LOWTRAN 3, a simple empirical equation was determined for estimating the transmittance over the 8.5-11 μm region due to aerosols only, as a function of range R and visual range VIS, namely:

$$\bar{\tau}_a\ (8.5\text{-}11) = \exp\ (-0.44R/VIS). \qquad \text{(A-15a)}$$

For fogs, a more appropriate expression would be

$$\bar{\tau}_a\ (8.5\text{-}11) = \exp\ (-3.9R/VIS);\ VIS \leq 2\ km. \qquad \text{(A-15b)}$$

The coefficient 0.44 was found to be the same for rural and urban models discussed in Section F. The variation of aerosol transmittance with visual range and range is shown in Table A-2 (based on LOWTRAN 3, cf. Eq. A-15).

4. The average transmittance in the 8.5-11 μm region due to molecular absorption can be appreciable mainly due to the water vapor continuum. For a 10-km sea-level path, the average transmittance can vary from about 0.78 to 0.13 for dew point temperatures of -10° and 15°C, respectively. The absorption due to the continuum alone is a factor of six greater than the remaining molecular absorption in the latter case. The following empirical equation was derived for predicting the average transmittance in the 8.5-11 μm region due to the water vapor continuum in terms of temperature T (°C), fractional humidity H, and range R (km), namely:

$$\tau_c\ (8.5\text{-}11) = \exp\left[-\ 5.7\ H^2 G(T) R\right], \qquad \text{(A-16)}$$

where G(T) is the effective quantity of water vapor per unit path length weighted according to temperature using the formulation given in Section D. The variation of G(T) with temperature is given in Fig. A-14. The variation of the average transmittance τ_c as a function of range for specific temperatures (assuming 100% relative humidity) is given in Table A-3.

TABLE A-2. AVERAGE TRANSMITTANCE FROM 8.5 TO 11 μm FOR LOWTRAN 3 FOG MODEL[a] (1- AND 2-km VISIBILITY) AND CONTINENTAL AEROSOL MODEL[b] (3- TO 35-km VISIBILITY)

	Range, km					
Visibility, km	0.1	0.5	1.0	5.0	10.0	15.0
(Fog) 1	.677	.142	.020	0	0	0
(Fog) 2	.822	.377	.142	0	0	0
3	.985	.927	.864	.492	.247	.126
4	.989	.944	.895	.587	.349	.210
5	.991	.954	.915	.653	.431	.286
6	.992	.961	.928	.701	.496	.352
7	.993	.966	.938	.737	.548	.409
8	.993	.970	.945	.766	.591	.457
9	.994	.973	.950	.789	.627	.499
10	.994	.975	.955	.808	.657	.535
11	.994	.977	.959	.824	.683	.567
12	.994	.979	.962	.838	.706	.595
13	.994	.980	.965	.849	.725	.620
14	.995	.981	.967	.859	.742	.642
15	.995	.982	.969	.868	.758	.662
20	.995	.986	.976	.900	.814	.736
25	.995	.988	.980	.919	.849	.785
30	.995	.989	.983	.933	.874	.819
35	.996	.990	.985	.942	.892	.844

[a] From Eq. A-15b.
[b] From Eq. A-15a.

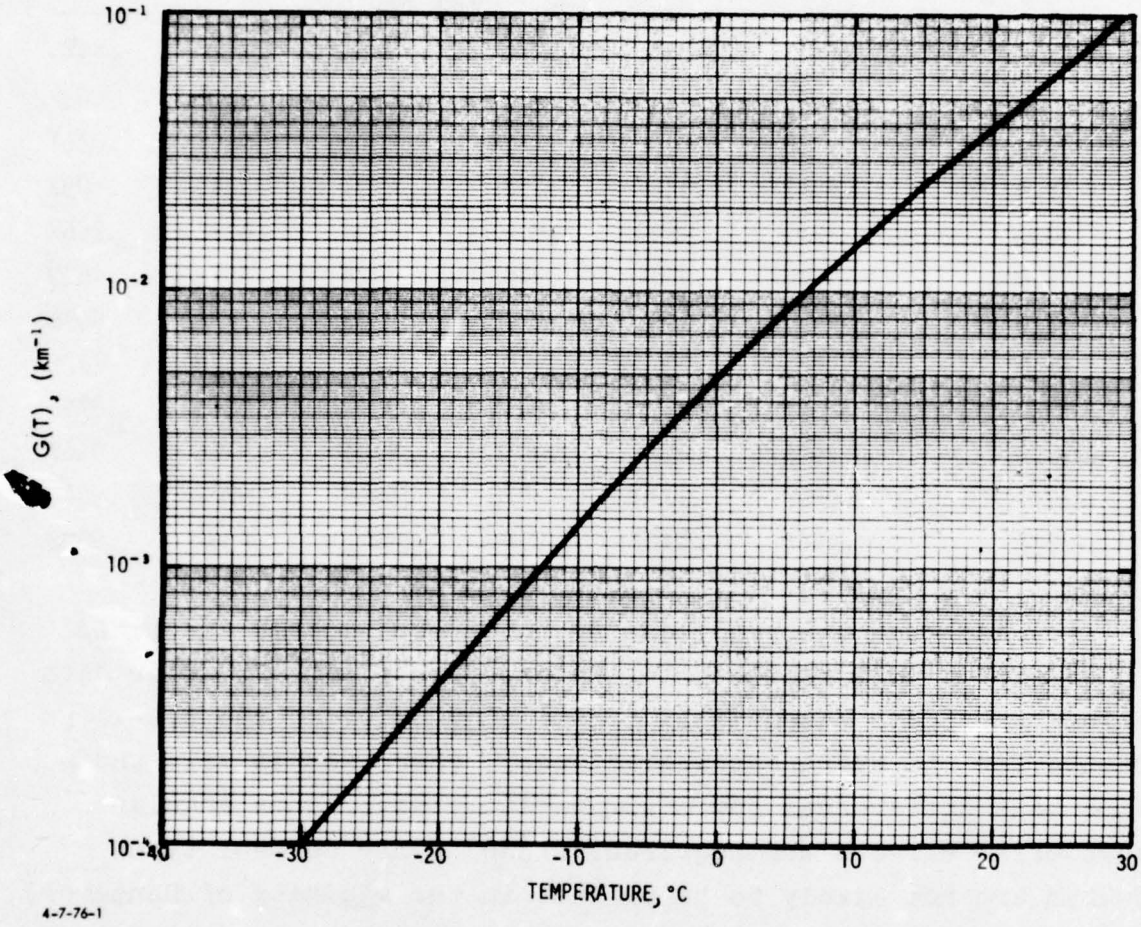


FIGURE A-14. Temperature Scaling Factor G(T) for Use with Equation A-16.

TABLE A-3. TRANSMITTANCE AT 8.5 TO 11 μm FOR THE WATER VAPOR CONTINUUM

	Range, km					
Temperature, °C	0.1	0.5	1.0	5.0	10.0	15.0
25.0	.9595	.8135	.6627	.1345	.0201	.0032
20.0	.9750	.8809	.7764	.2879	.0867	.0271
15.0	.9849	.9266	.8586	.4701	.2249	.1093
10.0	.9911	.9560	.9141	.6396	.4118	.2667
5.0	.9948	.9744	.9495	.7724	.5979	.4639
0.0	.9971	.9855	.9713	.8645	.7480	.6476
-5.0	.9984	.9920	.9841	.9232	.8524	.7878
-10.0	.9991	.9957	.9915	.9582	.9182	.8798
-15.0	.9996	.9978	.9956	.9781	.9566	.9357
-20.0	.9998	.9989	.9978	.9889	.9779	.9670
-25.0	.9999	.9995	.9989	.9946	.9892	.9838

5. Although the rural and urban aerosol models described in Section F were not used in the analysis of the Hannover data (since they give essentially identical results in the 8.5-11 μm region for the average transmittance), these models will show important differences for other wavelengths or when angular scattering effects are required. Also, other aerosol types (which are not likely to be present in the vicinity of Hannover), such as maritime aerosols, may have very different optical properties.

6. For visual ranges less than 1 or 2 km, fog conditions may exist, and LOWTRAN 3 will tend to underestimate the attenuation considerably. However, LOWTRAN 3 will print out a message if the input visual range is less than 2 km, warning the user of this fact. An estimated maximum fog attenuation value will also be printed (assuming the attenuation to be independent of wavelength and to be given by the value of 0.55 μm for the LOWTRAN 3 continental model). However, the attenuation at 10 μm

can be a factor of two less than in the visible, based on laser attenuation measurements in fog.

7. It is planned to add further aerosol and fog models to future versions of LOWTRAN.

8. More accurate expressions which account for the water vapor continuum in both the 8-14 μm and 3-5 μm regions will be included in future versions of LOWTRAN. A reevaluation of both spectral regions is currently under way at AFGL and at IDA.

REFERENCES, APPENDIX A

1. General Electric Company, Infrared Transmission and Background Radiation by Clear Atmospheres, GE Report 61 SD 199, T.L. Altshuler, 1961. (AD 401923)

2. Air Force Cambridge Research Laboratories, Optical Properties of the Atmosphere, Third Edition, Report AFCRL-72-0497, R.A. McClatchey, R.W. Fenn, J.E.A. Selby, F.E. Volz, and J.S. Garing, 1972.

3. Air Force Cambridge Research Laboratories, Atmospheric Transmittance from 0.25 to 28.5 μm: Computer Code LOWTRAN 2, Report AFCRL-72-0745, Environmental Research Paper 427, J.E.A. Selby and R.A. McClatchey, 1972.

4. Air Force Cambridge Research Laboratories, Atmospheric Transmittance from 0.25 to 28.5 μm: Computer Code LOWTRAN 3, Report AFCRL-75-0255, Environmental Research Paper 513, J.E.A. Selby and R.A. McClatchey, 1975.

5. D. Deirmendjian, "Scattering and Polarization Properties of Water Clouds and Hazes in the Visible and Infrared," Appl. Opt., Vol. 3, 1964, pp. 187-196.

6. Air Force Cambridge Research Laboratories, UV, Visible, and IR Attenuation for Altitudes up to 50 km, Report AFCRL-68-0153, Environmental Research Paper 285, L. Elterman, 1968.

7. Air Force Cambridge Research Laboratories, Vertical-Attenuation Model with Eight Surface Meteorological Ranges 2 to 13 Kilometers, Report AFCRL-70-0200, Environmental Research Paper 310, L. Elterman, 1970.

8. F.E. Volz, "Infrared Absorption by Atmospheric Aerosol Substances," J. Geophys. Res., Vol. 77, 1972, pp. 1017-1031.

9. F.E. Volz, "Infrared Refractive Index of Atmospheric Aerosol Substance," Appl. Opt., Vol. 11, pp. 755-759.

10. Air Force Cambridge Research Laboratories, Atmospheric Attenuation of Laser Radiation from 0.76 to 31.25 μm, Report AFCRL-TR-74-0003, R.A. McClatchey and J.E.A. Selby, 1974.

11. Institute for Defense Analyses, Infrared Continuum Absorption by Atmospheric Water Vapor in the 8-12 μm Window, IDA Paper P-1184, R.E. Roberts, J.E.A. Selby, and L.M. Biberman, April 1976.

12. Aeronutronic Division, Philco Ford Corporation, Investigation of the Absorption of Infrared Radiation by Atmospheric Gases, Semiannual Technical Report, Aeronutronic Report U-4784, D.E. Burch, 31 January 1971.

13. J.H. McCoy, D.B. Rensch, and R.K. Long, Appl. Opt., Vol. 8, 1969, p. 1471

14. W.E.K. Middleton, Vision through the Atmosphere, University of Toronto Press, Toronto, 1952.

15. E.P. Shettle and R.W. Fenn, "Models of the Atmospheric Aerosols and their Optical Properties," Proc. AGARD Conference on Optical Propagation in the Atmosphere, Lyngby, Denmark, 27-31 October 1975.

16. G. Mie, Ann. de Phys., Vol. 25, 1908, p. 377.

17. C.E. Junge, Air Chemistry and Radioactivity, Academic Press, New York, 1963, p. 382.

18. T. Okita, "Size Distribution of Large Haze Particles," J. Meteor. Soc. Japan, Vol. 33, 1955, pp. 291-295.

19. R. Jaenicke and C. Junge, "Studien zur oberer Grenzgrösse des natürlichen Aerosoles," Beitr. Phys. Atmos., Vol. 40, 1967, pp. 129-143.

20. K.E. Noll and M.J. Pilat, "Size Distribution of Atmospheric Giant Particles," Atmos. Environ., Vol. 5, 1971, pp. 527-540.

21. R.E. Pasceri and S.K. Friedlander, "Measurements of the Particle Size Distribution of the Atmospheric Aerosol: II. Experimental Results and Discussion," J. Atmos. Sci., Vol. 22, 1965, pp. 577-584.

22. K.T. Whitby, "On the Multimodal Nature of Atmospheric Aerosol Size Distribution," paper presented at VIII International Conference on Nucleation, Leningrad, USSR, September 28, 1973.

23. K.T. Whitby, R.B. Husar, and B.Y.H. Lin, "The Aerosol Size Distribution of Los Angeles Smog," J. Colloid Interfac. Sci., Vol. 39, 1972, pp. 177-204.

24. K. Willeke, K.T. Whitby, W.E. Clark, and V.A. Marpie, "Size Distributions of Denver Aerosols--A Comparison of Two Sites," Atmos. Environ., Vol. 8, 1974, pp. 609-633.

25. J.T. Twitty and J.A. Weinman, "Radiative Properties of Carbonaceous Aerosols," J. Appl. Meteor., Vol. 10, 1971, pp. 725-731.

26. C.E. Junge, "Our Knowledge of the Physics-Chemistry of Aerosols in the Undisturbed Marine Environment," J. Geophys. Res., Vol. 77, 1972, pp. 5183-5200.

27. C.E. Junge and R. Jaenicke, "New Results in Background Aerosols, Studies from the Atlantic Expedition of the R.V. Meteor, Spring 1969," Aerosol Sci., Vol. 2, 1971, pp. 305-314.

28. C.E. Junge, E. Robinson, and F.L. Ludwig, "A Study of Aerosols in the Pacific Land Masses," J. Appl. Meteor., Vol. 8, 1969, pp. 340-347.

29. A. Meszaros and K. Vissy, "Concentration, Size Distribution and Chemical Nature of Atmospheric Aerosol Particles in Remote Oceanic Areas," Aerosol Sci., Vol. 5, 1974, pp. 101-109.

30. A.H. Woodcock, "Salt Nuclei in Marine Air as a Function of Altitude and Wind Force," J. Meteor., Vol. 10, 1953, pp. 362-371.

31. K. Bullrich, "Scattered Radiation in the Atmosphere and the Natural Aerosol," in Advances in Geophysics, Vol. 10, pp. 99-260.

32. G. Hänel, "The Real Part of the Mean Complex Refractive Index and the Mean Density of Samples of Atmospheric Aerosol Particles," Tellus, Vol. 20, 1968, pp. 371-379.

33. P. Winkler, "The Growth of Atmospheric Aerosol Particles as a Function of the Relative Humidity: II. An Improved Concept of Mixed Nuclei," Aerosol Sci., Vol. 4, 1973, pp. 373-387.

34. P. Winkler and C.E. Junge, "Comments on Anomalous Deliquescence of Sea Spray Aerosols," J. Appl. Meteor., Vol. 10, 1971, pp. 159-163.

35. P. Winkler and C.E. Junge, "The Growth of Atmospheric Aerosol Particles as a Function of the Relative Humidity: Part I. Method and Measurements at Different Locations," J. Dech. Atmos. (Memorial Henri Dessens), Vol. 6, 1972, pp. 619-638.

36. G. Hänel, "Computation of the Extinction of Visible Radiation by Atmospheric Aerosol Particles as a Function of the Relative Humidity, Based Upon Measured Properties," Aerosol Sci., Vol. 3, 1972, pp. 377-386.

37. F. Kasten, "Visibility Forecast in the Phase of Pre-Condensation," Tellus, Vol. 21, 1969, pp. 631-635.

38. N.E. Dorsey, Properties of Ordinary Water-Substance in all its Phases: Water Vapor, Water and All the Uses, Am. Chem. Soc. Monograph Series, Reinhold Publishing Corporation, New York, 1940.

39. G.M. Hale and M.R. Querry, "Optical Constants of Water in the 200-nm to 200-μm Wavelength Region," Appl. Opt., Vol. 12, 1973, pp. 555-563.

40. G.H. Ruppersberg, R. Scheilhase, and H. Schuster, "Calculations about the Transmittance Window of Clouds and Fog at about 10.5 μm Wavelength," Atmospheric Environment, Vol. 9, 1975, pp. 723-730.

41. H.A. Gebbie, W.R. Harding, C. Hilsum, A.W. Pryce, and V. Roberts, Proc. Roy. Soc., Vol. 206A, No. 87, 1951.

42. Naval Research Laboratory, Infrared Transmission of the Atmosphere, NRL Report 5453, H.W. Yates and J.H. Taylor, 1960.

APPENDIX B

MONTHLY AVERAGE PERCENTAGE PROBABILITIES OF CLOUD-FREE LINES OF SIGHT BETWEEN THE GROUND AND ALTITUDES OF 984, 3280, AND 4920 FEET ABOVE GROUND LEVEL ALONG INDICATED VIEWING ANGLES, STATION 10338, HANNOVER, FEDERAL REPUBLIC OF GERMANY

3-Hour Intervals, January-December

Period of Record: December 1956--November 1971

Produced by the
United States Air Force Environmental Technical Applications Center (ETAC)

The ETAC data on clear lines of sight through clouds, sometimes called cloud-free lines of sight (CFLOS), are of two forms. We show examples of both forms in this appendix.

The first form gives the probability of CFLOS between the ground and various altitudes at various viewing angles, based on the distribution of cloud cover. The examples shown here are for altitudes of 984, 3280, and 4920 feet above ground level.

The second form gives the probability of CFLOS between the ground and various altitudes at various viewing angles, based on the distribution of cloud cover and conditional on a surface visibility of 2.5 miles or more and the absence of precipitation. The examples shown here are for altitudes of 984 and 3280 feet above ground level.

PRECEDING PAGE BLANK-NOT FILMED

PROBABILITY BASED ON DISTRIBUTION OF CLOUD COVER BELOW 984 FEET

JANUARY

Viewing (Elevation) Angle, deg	Hour (LST) 01	04	07	10	13	16	19	22	Day (07-18)	Night (19-06)	All
90	76.4	74.3	72.5	73.9	77.1	78.4	80.4	78.3	75.6	77.4	76.5
80	75.7	73.6	71.8	73.1	76.4	77.7	79.6	77.6	74.9	76.7	75.8
70	75.7	73.6	71.8	73.1	76.4	77.7	79.6	77.6	74.9	76.7	75.8
60	75.7	73.5	71.8	73.0	76.4	77.7	79.6	77.5	74.8	76.6	75.8
50	75.5	73.5	71.8	72.9	76.3	77.5	79.5	77.5	74.6	76.4	75.5
40	75.0	73.0	71.4	72.4	75.7	77.3	79.2	77.1	74.3	75.9	75.1
30	74.0	71.9	70.3	71.3	74.6	76.1	78.1	75.9	73.0	74.9	74.1
20	73.3	71.0	69.7	70.4	73.8	75.1	77.7	75.3	72.3	74.5	73.4
10	71.7	69.3	67.8	68.7	71.9	73.6	76.2	73.6	70.7	72.7	71.8
NO OBS	452	456	455	435	455	451	451	438	1796	1797	3593

FEBRUARY

Viewing (Elevation) Angle, deg	Hour (LST) 01	04	07	10	13	16	19	22	Day (07-18)	Night (19-06)	All
90	76.3	74.4	73.2	73.2	79.0	86.6	86.2	84.6	78.0	80.3	79.1
80	75.6	73.7	72.5	72.5	78.2	85.8	85.4	83.8	77.3	79.5	78.3
70	75.6	73.7	72.5	72.5	78.2	85.8	85.4	83.8	77.2	79.5	78.3
60	75.6	73.6	72.4	72.5	78.2	85.8	85.4	83.7	77.2	79.5	78.3
50	75.6	73.6	72.3	72.4	78.2	85.8	85.4	83.6	77.1	79.5	78.3
40	75.4	73.4	71.9	72.0	77.9	85.6	85.3	83.4	76.9	79.2	78.1
30	74.0	71.9	70.8	70.9	76.8	84.4	84.2	82.3	75.7	78.3	77.0
20	73.5	71.6	70.2	70.3	76.4	84.0	83.9	81.9	75.2	77.7	76.5
10	71.9	70.0	68.7	68.8	74.8	82.7	82.5	80.5	73.6	76.1	74.8
NO OBS	382	388	371	371	379	367	369	368	1488	1487	2975

MARCH

Viewing (Elevation) Angle, deg	Hour (LST) 01	04	07	10	13	16	19	22	Day (07-18)	Night (19-06)	All
90	86.0	83.0	81.8	80.3	89.7	90.7	88.2	87.7	85.6	86.4	85.9
80	85.2	82.2	81.0	79.6	88.8	89.8	87.3	86.8	84.8	85.6	85.1
70	85.1	82.2	81.0	79.6	88.8	89.8	87.3	86.8	84.8	85.6	85.1
60	85.1	82.2	81.0	79.5	88.8	89.8	87.3	86.8	84.8	85.6	85.1
50	85.0	82.1	80.7	79.4	88.8	89.8	87.3	86.8	84.6	85.4	85.1
40	84.9	81.7	80.3	79.0	88.5	89.7	87.0	86.5	84.4	85.0	84.8
30	83.6	80.7	79.2	77.7	87.5	88.5	86.1	85.6	83.4	83.9	83.7
20	83.5	80.2	78.8	77.0	87.2	88.3	85.6	85.3	82.9	83.8	83.3
10	82.2	78.6	77.0	75.2	85.8	87.0	84.2	84.1	81.3	82.5	81.7
NO OBS	410	407	401	409	404	393	402	401	1607	1626	3233

APRIL

Viewing (Elevation) Angle, deg	Hour (LST) 01	04	07	10	13	16	19	22	Day (07-18)	Night (19-06)	All
90	87.4	82.1	76.4	80.7	92.1	95.2	94.4	92.5	86.3	89.0	87.6
80	86.5	81.3	75.7	79.9	91.2	94.3	93.5	91.6	85.5	88.1	86.8
70	86.5	81.3	75.7	79.9	91.2	94.3	93.5	91.6	85.5	88.1	86.8
60	86.5	81.3	75.6	79.9	91.2	94.3	93.4	91.6	85.4	88.1	86.7
50	86.4	81.2	75.3	79.9	91.1	94.3	93.4	91.6	85.3	88.1	86.7
40	86.2	80.9	75.0	79.5	90.9	94.2	93.3	91.5	84.9	88.0	86.5
30	85.1	79.8	73.8	78.4	89.9	93.0	92.1	90.3	83.8	87.0	85.3
20	84.9	79.4	73.1	77.8	89.6	92.8	92.0	90.2	83.4	86.5	85.0
10	83.5	78.2	71.1	75.9	88.4	91.5	90.7	88.9	81.7	85.2	83.4
NO OBS	402	404	400	403	402	400	403	398	1605	1607	3212

PROBABILITY BASED ON DISTRIBUTION OF CLOUD COVER BELOW 984 FEET

MAY

Viewing (Elevation) Angle, deg	Hour (LST) 01	04	07	10	13	16	19	22	Day (07-18)	Night (19-06)	All
90	92.7	87.6	83.7	88.6	95.6	96.3	96.5	96.6	91.0	93.5	92.1
80	91.8	86.8	82.9	87.8	94.7	95.4	95.5	95.6	90.1	92.6	91.2
70	91.8	86.8	82.9	87.8	94.7	95.4	95.5	95.6	90.1	92.6	91.2
60	91.8	86.8	82.9	87.8	94.9	95.4	95.5	95.6	90.0	92.5	91.2
50	91.8	86.7	82.7	87.8	94.5	95.4	95.4	95.6	89.9	92.4	91.2
40	91.6	86.5	82.5	87.6	94.3	95.3	95.4	95.5	89.7	92.2	90.9
30	90.6	85.4	81.2	86.3	93.4	94.1	94.4	94.5	88.7	91.2	89.7
20	90.6	85.0	80.6	85.8	93.2	94.0	94.2	94.4	88.4	90.9	89.6
10	89.2	83.7	78.9	84.4	92.1	92.8	93.0	93.1	87.1	89.8	88.3
NO OBS	411	418	415	407	406	402	405	400	1630	1624	3254

JUNE

Viewing (Elevation) Angle, deg	Hour (LST) 01	04	07	10	13	16	19	22	Day (07-18)	Night (19-06)	All
90	95.1	93.0	87.2	94.0	97.6	98.0	97.9	96.5	94.1	95.7	94.9
80	94.2	92.1	86.4	93.1	96.6	97.0	96.9	95.6	93.2	94.8	94.0
70	94.2	92.1	86.4	93.1	96.6	97.0	96.9	95.6	93.2	94.8	94.0
60	94.2	92.1	86.4	93.1	96.6	97.0	96.8	95.5	93.2	94.8	94.0
50	94.2	92.0	86.4	93.1	96.6	97.0	96.8	95.5	93.2	94.8	94.0
40	94.1	91.9	86.0	92.9	96.5	97.0	96.7	95.4	92.9	94.6	94.0
30	93.0	90.7	84.5	91.7	95.3	96.0	95.8	94.3	92.0	93.4	92.8
20	92.5	90.4	83.8	91.4	95.2	95.9	95.6	93.9	91.5	93.2	92.5
10	91.2	89.2	82.1	90.1	93.8	94.6	94.3	92.8	90.2	91.9	91.0
NO OBS	385	390	388	392	392	386	388	390	1558	1549	3107

JULY

Viewing (Elevation) Angle, deg	Hour (LST) 01	04	07	10	13	16	19	22	Day (07-18)	Night (19-06)	All
90	95.3	91.3	85.7	92.5	97.6	98.0	98.0	96.4	93.5	95.5	94.4
80	94.4	90.4	84.9	91.6	96.6	97.0	97.0	95.4	92.6	94.6	93.5
70	94.4	90.3	84.9	91.6	96.6	97.0	97.0	95.4	92.6	94.6	93.5
60	94.4	90.3	84.9	91.6	96.6	97.0	97.0	95.4	92.6	94.6	93.4
50	94.3	90.2	84.7	91.5	96.5	97.0	97.0	95.4	92.5	94.6	93.3
40	94.3	90.0	84.4	91.1	96.4	97.0	97.0	95.4	92.4	94.5	93.2
30	93.2	88.9	83.0	90.2	95.4	96.1	96.1	94.4	91.3	93.3	92.3
20	93.0	88.6	82.4	89.9	95.1	96.0	96.1	94.2	91.0	93.1	91.8
10	91.8	87.3	80.6	88.4	94.0	95.0	94.9	93.1	89.7	91.8	90.6
NO OBS	411	409	401	406	406	406	401	409	1619	1630	3249

AUGUST

Viewing (Elevation) Angle, deg	Hour (LST) 01	04	07	10	13	16	19	22	Day (07-18)	Night (19-06)	All
90	94.6	89.9	87.0	92.3	97.2	98.1	98.1	96.2	93.6	94.7	94.1
80	93.7	89.0	86.2	91.3	96.2	97.1	97.1	95.2	92.7	93.8	93.2
70	93.7	89.0	86.1	91.3	96.2	97.1	97.1	95.2	92.7	93.8	93.2
60	93.7	89.0	86.1	91.3	96.2	97.1	97.1	95.2	92.7	93.8	93.2
50	93.5	89.0	86.1	91.2	96.1	97.1	97.0	95.2	92.7	93.7	93.2
40	93.4	88.7	85.7	90.9	95.9	97.1	96.9	95.0	92.4	93.6	93.1
30	92.4	87.7	84.5	89.8	94.9	96.1	95.9	94.1	91.4	92.5	92.1
20	92.1	87.4	83.8	89.4	94.7	96.0	95.8	93.9	91.1	92.2	91.8
10	90.8	86.0	82.0	87.8	93.5	95.1	94.6	92.7	89.7	91.0	90.5
NO OBS	441	439	430	435	439	433	432	440	1734	1752	3486

PROBABILITY BASED ON DISTRIBUTION OF CLOUD COVER BELOW 984 FEET

SEPTEMBER

Viewing (Elevation) Angle, deg	Hour (LST) 01	04	07	10	13	16	19	22	Day (07-18)	Night (19-06)	All
90	95.2	92.0	89.0	87.7	95.6	96.9	97.9	96.0	92.4	95.2	93.6
80	94.3	91.1	88.2	86.9	94.7	95.9	96.9	95.1	91.5	94.3	92.7
70	94.3	91.0	88.2	86.9	94.6	95.9	96.9	95.1	91.5	94.3	92.7
60	94.3	91.0	88.2	86.8	94.5	95.9	96.9	95.1	91.4	94.3	92.6
50	94.3	90.9	87.9	86.7	94.4	95.9	96.9	95.1	91.3	94.3	92.6
40	94.2	90.8	87.7	86.5	94.3	95.8	96.8	95.1	91.0	94.2	92.6
30	93.1	89.5	86.5	85.2	93.2	94.8	95.8	93.9	90.0	93.1	91.5
20	92.8	89.2	86.1	84.6	92.8	94.6	95.8	93.9	89.6	92.9	91.2
10	91.7	87.9	84.6	83.1	91.6	93.5	94.7	92.8	88.3	91.8	90.1
NO OBS	399	393	395	384	405	399	400	389	1583	1571	3154

OCTOBER

Viewing (Elevation) Angle, deg	Hour (LST) 01	04	07	10	13	16	19	22	Day (07-18)	Night (19-06)	All
90	85.7	82.4	80.6	78.5	87.8	92.1	92.2	90.0	84.8	87.7	86.2
80	84.9	81.6	79.8	77.8	87.0	91.2	91.3	89.1	84.0	86.9	85.4
70	84.9	81.5	79.8	77.8	87.0	91.2	91.3	89.1	84.0	86.9	85.4
60	84.9	81.4	79.8	77.8	87.0	91.2	91.3	89.0	84.0	86.9	85.4
50	84.9	81.2	79.8	77.7	87.0	91.1	91.3	88.9	84.0	86.9	85.3
40	84.6	80.9	79.2	77.3	86.6	91.0	91.3	88.8	83.7	86.6	84.8
30	83.6	79.9	78.2	76.0	85.3	89.9	90.2	87.8	82.6	85.4	83.8
20	83.3	79.4	77.9	75.3	84.9	89.6	90.1	87.4	82.1	85.2	83.6
10	81.7	78.1	76.2	73.8	83.3	88.3	89.0	86.3	80.6	83.8	82.1
NO OBS	420	417	426	409	436	414	427	402	1685	1666	3351

NOVEMBER

Viewing (Elevation) Angle, deg	Hour (LST) 01	04	07	10	13	16	19	22	Day (07-18)	Night (19-06)	All
90	76.6	76.2	71.3	73.6	78.5	78.7	79.2	77.5	75.5	77.5	76.5
80	75.9	75.5	70.5	72.9	77.8	78.0	78.5	76.8	74.8	76.8	75.8
70	75.8	75.5	70.5	72.9	77.8	78.0	78.5	76.8	74.8	76.8	75.7
60	75.8	75.5	70.4	72.9	77.8	78.0	78.5	76.8	74.8	76.8	75.7
50	75.7	75.5	70.3	72.6	77.6	77.9	78.3	76.8	74.7	76.7	75.6
40	75.3	75.1	70.0	72.1	77.3	77.6	78.0	76.4	74.2	76.3	75.3
30	74.2	74.0	69.1	70.9	75.9	76.4	76.8	75.3	72.9	75.2	74.1
20	73.9	73.7	68.4	70.2	75.2	75.6	76.2	75.0	72.4	74.6	73.5
10	72.2	72.0	66.7	68.2	73.4	74.1	74.6	73.5	70.5	73.2	71.8
NO OBS	404	401	416	399	405	410	407	403	1630	1615	3245

DECEMBER

Viewing (Elevation) Angle, deg	Hour (LST) 01	04	07	10	13	16	19	22	Day (07-18)	Night (19-06)	All
90	73.8	73.5	71.4	73.1	76.3	76.5	77.5	75.9	74.3	75.2	74.7
80	73.1	72.7	70.8	72.3	75.5	75.8	76.8	75.2	73.6	74.5	74.0
70	73.1	72.7	70.8	72.3	75.5	75.8	76.8	75.2	73.6	74.5	74.0
60	73.1	72.6	70.6	72.3	75.3	75.8	76.8	75.2	73.6	74.5	74.0
50	73.0	72.5	70.6	72.2	75.3	75.8	76.7	75.1	73.5	74.3	74.0
40	72.6	72.1	70.2	71.7	74.7	74.9	76.1	74.7	73.0	73.9	73.6
30	71.5	70.9	69.0	70.4	73.5	73.8	75.0	73.5	71.8	72.7	72.2
20	70.8	70.3	68.3	69.5	72.6	72.7	74.6	73.0	71.0	72.1	71.7
10	69.1	68.4	66.5	67.6	70.6	70.9	73.0	71.1	69.0	70.4	69.8
NO OBS	416	429	429	406	428	430	425	413	1693	1683	3376

PROBABILITY BASED ON DISTRIBUTION OF CLOUD COVER BELOW 3280 FEET

JANUARY

Viewing (Elevation) Angle, deg	Hour (LST) 01	04	07	10	13	16	19	22	Day (07-18)	Night (19-06)	All
90	53.7	51.0	49.1	52.0	55.5	58.5	57.9	54.3	53.7	54.2	54.0
80	53.3	50.6	48.8	51.6	55.0	58.1	57.5	53.9	53.4	53.8	53.6
70	53.2	50.5	48.7	51.5	55.0	57.8	57.5	53.8	53.4	53.8	53.4
60	53.0	50.4	48.4	51.2	54.8	57.6	57.4	53.6	53.0	53.8	53.3
50	52.6	49.9	48.2	50.9	54.4	57.2	57.1	53.5	52.8	53.3	53.0
40	52.1	49.1	47.4	49.9	53.3	56.3	56.4	52.5	51.6	52.4	52.2
30	50.4	47.5	45.7	48.0	51.4	54.1	55.0	51.1	49.9	51.0	50.4
20	49.1	46.2	44.0	45.9	49.1	51.9	53.5	49.5	47.7	49.5	48.6
10	46.1	43.2	41.2	42.2	45.2	48.1	50.7	46.7	44.2	46.7	45.5
NO OBS	452	456	455	435	455	451	451	438	1796	1797	3593

FEBRUARY

Viewing (Elevation) Angle, deg	Hour (LST) 01	04	07	10	13	16	19	22	Day (07-18)	Night (19-06)	All
90	58.0	56.0	53.8	53.5	55.9	59.1	58.0	61.2	55.6	58.0	56.7
80	57.6	54.6	53.4	53.1	55.5	58.6	57.5	60.7	55.1	57.6	56.3
70	57.6	54.5	53.4	53.1	55.2	58.4	57.5	60.7	55.0	57.4	56.2
60	57.4	54.4	53.2	52.8	54.8	58.1	57.2	60.4	54.9	57.3	56.1
50	57.1	54.3	52.9	52.5	54.4	57.7	56.7	60.2	54.5	57.1	55.7
40	56.2	53.2	52.1	51.6	53.1	56.6	56.1	59.5	53.3	56.2	54.8
30	54.5	52.0	50.6	49.7	51.2	54.2	54.1	57.9	51.4	54.5	53.1
20	53.5	50.4	48.8	47.6	48.4	51.5	52.5	56.4	49.3	52.9	51.1
10	50.7	47.7	46.0	44.0	44.1	47.3	49.2	53.5	45.2	50.3	47.7
NO OBS	382	368	371	371	379	367	369	368	1488	1487	2975

MARCH

Viewing (Elevation) Angle, deg	Hour (LST) 01	04	07	10	13	16	19	22	Day (07-18)	Night (19-06)	All
90	65.4	65.2	60.6	59.6	61.9	64.5	66.4	70.3	61.6	66.7	64.4
80	64.9	64.7	60.0	59.3	61.4	63.9	65.9	69.7	61.1	66.2	64.0
70	64.9	64.7	59.9	59.1	61.1	63.8	65.7	69.7	61.0	66.1	63.8
60	64.7	64.6	59.5	58.9	60.7	63.4	65.5	69.5	60.6	66.0	63.4
50	64.5	64.2	59.3	58.3	60.1	62.9	65.0	69.2	60.0	65.8	63.1
40	63.8	63.8	58.5	57.5	58.8	61.8	64.1	68.7	59.0	65.3	62.2
30	62.4	62.4	56.5	55.5	56.2	59.4	62.1	67.4	56.8	63.5	60.2
20	61.2	61.3	54.9	53.1	53.4	56.9	60.0	66.3	54.5	62.2	58.3
10	58.7	59.0	51.5	49.3	48.5	52.4	56.2	63.9	50.2	59.5	55.1
NO OBS	410	407	401	409	404	393	402	407	1607	1626	3233

APRIL

Viewing (Elevation) Angle, deg	Hour (LST) 01	04	07	10	13	16	19	22	Day (07-18)	Night (19-06)	All
90	76.0	69.2	65.4	63.5	70.3	74.9	80.4	82.2	68.5	76.9	72.5
80	75.3	68.6	64.9	63.1	69.7	74.3	79.7	81.5	68.1	76.3	71.9
70	75.3	68.6	64.8	62.9	69.4	74.2	79.5	81.4	67.8	76.3	71.8
60	75.2	68.5	64.5	62.6	69.0	73.8	79.2	81.3	67.6	76.0	71.6
50	75.1	68.3	64.1	61.9	68.5	73.1	78.7	80.9	67.1	75.7	71.3
40	74.7	67.8	63.4	60.9	67.3	72.2	78.0	80.6	65.9	75.2	70.4
30	73.4	66.6	61.4	58.6	65.1	69.9	76.0	79.2	63.7	73.6	68.5
20	72.5	65.5	59.5	56.0	62.2	67.4	74.2	78.3	61.2	72.6	66.7
10	70.5	63.7	56.0	51.5	57.7	63.3	70.5	76.0	57.2	70.0	63.6
NO OBS	402	404	400	403	402	400	403	398	1605	1607	3212

PROBABILITY BASED ON DISTRIBUTION OF CLOUD COVER BELOW 3280 FEET

MAY

Viewing (Elevation) Angle, deg	Hour (LST) 01	04	07	10	13	16	19	22	Day (07-18)	Night (19-06)	All
90	85.2	77.5	71.9	69.7	73.8	79.4	84.0	86.3	73.7	83.0	78.3
80	84.4	76.8	71.4	69.1	73.3	78.8	83.3	85.5	73.2	82.3	77.6
70	84.3	76.7	71.3	69.0	73.0	78.6	83.1	85.4	73.0	82.2	77.4
60	84.3	76.5	71.0	68.7	72.7	78.5	82.9	85.3	72.7	82.2	77.3
50	84.2	76.2	70.7	68.0	72.1	77.9	82.6	85.2	72.3	82.0	77.0
40	84.0	75.7	70.1	66.9	71.1	77.2	81.9	84.1	71.1	81.4	76.3
30	82.5	74.6	68.2	64.5	68.6	75.2	80.0	83.1	69.0	80.1	74.5
20	81.9	73.5	66.6	61.7	66.2	73.3	78.5	82.2	66.9	79.0	72.8
10	80.2	71.3	63.4	57.0	61.8	69.6	75.4	80.0	63.0	76.6	69.8
NO OBS	411	408	415	407	406	402	405	400	1630	1624	3254

JUNE

Viewing (Elevation) Angle, deg	Hour (LST) 01	04	07	10	13	16	19	22	Day (07-18)	Night (19-06)	All
90	87.5	79.5	77.4	73.8	79.1	82.5	85.8	85.0	78.3	84.4	81.4
80	86.6	78.8	76.8	73.3	78.4	81.8	85.1	84.3	77.7	83.7	80.6
70	86.5	78.7	76.6	73.1	78.3	81.6	85.0	84.1	77.4	83.5	80.6
60	86.4	78.6	76.5	72.7	78.0	81.4	84.8	83.9	77.2	83.4	80.5
50	86.1	78.4	76.0	72.1	77.5	80.9	84.3	83.9	76.7	83.3	80.0
40	85.8	77.9	75.2	71.1	76.6	80.3	83.7	82.8	75.8	82.5	79.2
30	84.6	76.3	73.5	68.8	74.5	78.2	81.8	80.9	73.7	81.0	77.6
20	83.7	75.2	71.8	66.0	72.3	76.4	80.2	79.7	71.6	79.7	75.9
10	82.0	72.8	68.6	61.6	68.4	73.3	77.4	76.7	68.0	77.2	72.5
NO OBS	385	380	388	392	392	386	388	396	1558	1549	3107

JULY

Viewing (Elevation) Angle, deg	Hour (LST) 01	04	07	10	13	16	19	22	Day (07-18)	Night (19-06)	All
90	83.2	74.2	73.0	67.4	75.6	78.6	82.7	83.1	73.6	81.8	77.6
80	82.5	77.5	72.4	66.9	75.1	77.9	82.0	82.3	73.0	81.1	77.0
70	82.5	77.4	72.2	66.7	74.9	77.7	81.8	82.3	72.9	80.9	76.9
60	82.5	77.3	72.0	66.0	74.5	77.4	81.4	82.0	72.4	80.9	76.7
50	82.1	76.9	71.6	65.4	73.8	76.9	81.0	81.7	71.8	80.4	76.2
40	81.8	76.4	70.7	63.8	72.8	75.9	80.0	81.2	70.9	79.8	75.4
30	80.3	74.8	68.8	61.0	70.5	73.6	78.0	79.4	68.6	78.1	73.3
20	79.3	73.3	66.9	57.7	68.0	71.5	75.9	77.9	65.9	76.7	71.2
10	77.2	70.5	63.3	52.1	63.5	67.5	71.9	75.0	61.7	73.6	67.7
NO OBS	411	409	401	406	409	406	401	409	1610	1630	3249

AUGUST

Viewing (Elevation) Angle, deg	Hour (LST) 01	04	07	10	13	16	19	22	Day (07-18)	Night (19-06)	All
90	84.4	78.4	74.5	70.2	76.9	78.7	83.7	83.8	75.3	82.4	78.9
80	83.5	77.6	73.9	69.7	76.3	78.1	83.1	83.1	74.6	81.7	78.3
70	83.5	77.6	73.7	69.5	76.1	78.0	82.9	83.0	74.4	81.7	78.0
60	83.4	77.4	73.5	69.0	75.7	77.6	82.6	82.8	74.1	81.5	77.6
50	83.3	77.3	73.1	68.3	75.1	77.0	82.1	82.7	73.6	81.3	77.3
40	82.9	76.7	72.2	67.0	74.0	76.2	81.1	82.0	72.3	80.6	76.5
30	81.6	75.3	70.1	64.2	71.7	74.0	79.1	80.4	70.1	79.0	74.4
20	80.7	74.0	68.4	61.1	69.2	71.3	76.7	79.1	67.6	77.5	72.6
10	78.4	71.6	65.0	55.7	65.0	67.5	73.0	76.5	63.5	74.8	69.1
NO OBS	441	439	430	435	436	433	432	440	1734	1752	3486

PROBABILITY BASED ON DISTRIBUTION OF CLOUD COVER BELOW 3280 FEET

SEPTEMBER

Viewing (Elevation) Angle, deg	Hour (LST) 01	04	07	10	13	16	19	22	Day (07-18)	Night (19-06)	All
90	87.8	82.5	76.6	69.2	72.5	78.6	84.0	85.9	74.3	85.0	79.9
80	87.0	81.8	76.0	68.7	71.9	78.1	83.4	85.0	73.6	84.3	79.2
70	87.0	81.7	75.8	68.6	71.8	78.0	83.1	85.0	73.4	84.2	79.0
60	87.0	81.6	75.6	68.2	71.3	77.7	83.0	84.9	73.1	84.2	78.7
50	86.8	81.4	75.3	67.8	70.5	77.0	82.5	84.7	72.6	83.9	78.2
40	86.5	81.1	74.3	66.5	69.3	76.1	81.8	84.4	71.6	83.5	77.6
30	85.2	79.4	72.7	64.4	67.0	74.0	80.1	83.1	69.6	81.8	75.6
20	84.6	78.7	70.9	61.7	63.9	71.4	78.3	82.2	67.0	81.0	74.0
10	82.9	76.4	67.6	57.4	58.8	67.4	75.0	80.2	62.9	78.6	70.7
NO OBS	399	393	395	384	405	399	400	389	1583	1571	3154

OCTOBER

Viewing (Elevation) Angle, deg	Hour (LST) 01	04	07	10	13	16	19	22	Day (07-18)	Night (19-06)	All
90	72.5	67.8	63.1	62.7	68.8	72.2	75.1	74.9	66.6	72.6	69.7
80	71.7	67.2	62.5	62.2	68.3	71.8	74.4	74.2	66.1	72.0	69.1
70	71.7	67.2	62.4	62.2	68.0	71.5	74.4	74.2	65.8	72.0	68.9
60	71.6	67.1	62.3	61.9	67.6	71.1	74.2	73.9	65.6	71.7	68.8
50	71.5	67.0	62.1	61.4	67.0	70.6	73.8	73.9	65.1	71.6	68.2
40	71.1	66.5	61.3	60.5	65.7	69.6	73.3	73.4	64.3	70.9	67.6
30	69.5	65.1	59.8	58.5	63.3	67.1	71.6	71.9	62.1	69.6	65.8
20	68.7	64.1	57.9	56.2	60.2	64.5	70.3	70.9	59.8	68.6	64.2
10	66.4	61.8	55.0	52.6	55.5	60.0	68.0	68.7	55.6	66.2	61.0
NO OBS	420	417	426	409	436	414	427	405	1685	1666	3351

NOVEMBER

Viewing (Elevation) Angle, deg	Hour (LST) 01	04	07	10	13	16	19	22	Day (07-18)	Night (19-06)	All
90	55.2	54.6	51.2	53.8	54.8	55.9	56.5	55.7	53.7	55.5	54.5
80	54.7	54.2	50.8	53.5	54.5	55.5	56.1	55.6	53.2	55.1	54.1
70	54.6	54.2	50.6	53.4	54.1	55.3	56.1	55.2	53.0	55.1	54.1
60	54.5	54.0	50.3	53.1	53.9	54.8	55.9	55.1	52.8	55.1	53.9
50	54.4	53.9	50.1	52.7	53.5	54.4	55.6	55.0	52.4	54.7	53.6
40	53.5	53.3	49.1	51.5	52.1	53.4	54.9	54.2	51.4	54.0	52.5
30	51.9	51.9	48.0	49.5	50.0	51.2	53.5	52.7	49.4	52.5	51.0
20	50.7	50.4	46.5	47.1	47.1	48.5	52.0	51.5	47.1	51.3	49.1
10	48.1	48.3	43.8	43.2	42.5	44.4	49.3	49.1	43.3	48.8	46.0
NO OBS	404	401	416	399	405	410	407	403	1630	1615	3245

DECEMBER

Viewing (Elevation) Angle, deg	Hour (LST) 01	04	07	10	13	16	19	22	Day (07-18)	Night (19-06)	All
90	52.8	50.4	48.2	50.8	54.7	55.8	54.4	53.5	52.5	52.8	52.6
80	52.3	49.9	47.9	50.4	54.3	55.4	53.8	53.0	52.2	52.4	52.1
70	52.2	49.8	47.9	50.4	54.2	55.2	53.8	52.9	52.0	52.1	52.1
60	52.1	49.6	47.7	49.9	53.9	54.9	53.6	52.8	51.8	51.8	51.8
50	51.6	49.4	47.5	49.4	53.3	54.4	53.4	52.5	51.2	51.7	51.6
40	51.1	48.5	46.6	48.4	52.3	53.1	52.6	51.5	50.3	50.9	50.6
30	49.2	46.8	45.0	46.2	50.1	51.0	51.0	49.9	48.1	49.2	48.6
20	47.7	45.2	43.2	44.0	47.6	48.3	49.4	48.4	46.0	47.6	46.9
10	44.6	42.1	40.3	40.1	43.3	44.0	46.3	45.4	41.8	44.5	43.4
NO OBS	416	429	429	406	428	430	425	413	1693	1683	3376

PROBABILITY BASED ON DISTRIBUTION OF CLOUD COVER BELOW 4920 FEET

JANUARY

Viewing (Elevation) Angle, deg	Hour (LST) 01	04	07	10	13	16	19	22	Day (07-18)	Night (19-06)	All
90	49.0	48.8	48.5	49.8	53.3	55.4	53.0	50.3	51.1	49.2	50.4
80	48.7	48.4	48.2	49.6	53.0	55.0	52.7	49.9	50.7	48.9	50.0
70	48.6	48.4	48.1	49.2	52.9	54.8	52.6	49.7	50.6	48.9	49.9
60	48.2	48.2	44.8	49.0	52.6	54.7	52.5	49.6	50.2	48.8	49.6
50	48.0	48.1	44.3	48.4	52.1	53.9	52.2	49.2	49.6	48.5	49.1
40	47.0	43.8	43.5	47.4	50.8	52.9	51.1	48.2	48.6	47.7	47.9
30	45.2	42.1	41.9	45.1	48.8	50.7	49.3	46.5	46.4	45.9	46.0
20	43.6	40.5	40.2	42.7	46.0	48.1	47.4	44.8	44.2	43.9	44.1
10	40.2	37.4	36.6	38.7	41.9	43.6	44.1	41.5	40.2	40.9	40.5
NO OBS	452	456	455	435	455	451	451	438	1796	1797	3593

FEBRUARY

Viewing (Elevation) Angle, deg	Hour (LST) 01	04	07	10	13	16	19	22	Day (07-18)	Night (19-06)	All
90	52.8	49.6	48.2	50.8	53.1	57.1	53.1	55.3	52.4	52.7	52.5
80	52.3	49.2	47.7	50.6	52.8	56.7	52.7	54.9	52.2	52.3	52.1
70	52.3	49.0	47.6	50.5	52.6	56.7	52.6	54.7	51.9	52.3	52.1
60	52.1	48.9	47.4	50.1	52.1	56.4	52.4	54.5	51.6	52.1	51.7
50	51.8	48.5	46.9	49.7	51.7	55.8	51.8	54.1	51.0	51.6	51.4
40	50.9	47.6	46.1	48.5	50.2	54.4	50.9	53.3	49.8	50.6	50.5
30	49.3	45.9	44.3	46.5	47.9	52.1	48.8	51.5	47.7	48.9	48.3
20	47.6	43.9	42.2	44.1	44.9	49.0	46.6	49.7	45.0	46.9	46.0
10	44.4	40.6	38.6	40.0	40.4	44.3	42.6	46.3	40.8	43.4	42.3
NO OBS	382	388	371	371	379	367	369	368	1488	1487	2975

MARCH

Viewing (Elevation) Angle, deg	Hour (LST) 01	04	07	10	13	16	19	22	Day (07-18)	Night (19-06)	All
90	59.5	59.6	56.4	57.5	59.6	61.1	62.2	63.7	58.6	61.2	60.0
80	59.0	59.2	55.9	57.0	59.4	60.7	61.8	63.5	58.1	60.8	59.7
70	58.9	59.2	55.8	56.9	59.1	60.4	61.4	63.3	57.9	60.7	59.3
60	58.8	59.0	55.7	56.6	58.7	59.8	61.2	63.0	57.5	60.3	59.2
50	58.7	58.5	55.2	56.1	57.8	59.1	60.4	62.7	57.0	59.9	58.6
40	57.8	57.8	54.2	54.9	56.4	57.8	59.2	61.9	55.6	59.1	57.5
30	56.1	56.3	52.2	52.8	53.6	55.0	56.8	60.0	53.3	57.2	55.4
20	54.8	54.7	50.1	50.4	50.5	51.7	54.1	58.3	50.7	55.6	53.2
10	51.8	51.7	46.0	46.3	45.0	46.2	49.5	55.3	45.9	52.1	49.0
NO OBS	410	407	401	409	404	393	402	407	1607	1626	3233

APRIL

Viewing (Elevation) Angle, deg	Hour (LST) 01	04	07	10	13	16	19	22	Day (07-18)	Night (19-06)	All
90	70.5	63.6	62.1	61.8	64.9	67.7	74.5	75.1	64.0	71.0	67.5
80	69.9	63.0	61.7	61.4	64.5	67.3	73.9	74.5	63.7	70.4	67.1
70	69.9	62.9	61.5	61.2	64.2	67.0	73.5	74.3	63.5	70.3	66.8
60	69.7	62.8	61.2	60.9	63.7	66.3	73.2	74.2	63.0	70.0	66.7
50	69.5	62.5	60.7	60.2	62.7	65.4	72.6	73.9	62.4	69.4	66.1
40	69.0	61.8	59.7	58.9	60.9	63.9	71.2	73.2	60.6	68.8	65.0
30	67.3	60.2	57.6	56.6	58.2	61.0	68.9	71.5	58.4	66.9	62.6
20	66.1	59.0	55.4	53.8	54.3	57.1	65.6	70.0	55.3	65.2	60.2
10	63.6	56.3	51.5	49.0	48.3	50.9	60.6	66.9	49.9	61.8	55.8
NO OBS	402	404	400	403	402	400	403	398	1605	1607	3212

PROBABILITY BASED ON DISTRIBUTION OF CLOUD COVER BELOW 4920 FEET

MAY

Viewing (Elevation) Angle, deg	Hour (LST) 01	04	07	10	13	16	19	22	Day (07-18)	Night (19-06)	All
90	80.0	71.8	68.6	67.9	67.1	69.9	77.6	78.3	68.4	76.9	72.6
80	79.1	71.2	68.1	67.4	66.7	69.4	77.0	77.7	67.9	76.2	72.1
70	79.1	71.1	67.9	67.2	66.2	69.0	76.7	77.6	67.6	76.1	71.9
60	79.1	70.9	67.7	66.9	65.6	68.4	76.3	77.5	67.1	75.9	71.6
50	78.8	70.4	67.3	66.1	64.6	67.7	75.5	76.8	66.4	75.4	70.9
40	78.3	69.7	66.3	64.7	63.0	65.9	74.3	75.9	65.1	74.4	69.9
30	76.8	68.0	64.5	62.1	59.9	63.0	72.0	74.1	62.3	72.7	67.5
20	75.5	66.4	62.1	59.0	55.8	58.7	68.7	72.0	59.0	70.6	64.9
10	73.0	63.2	58.6	53.9	49.2	52.1	63.7	68.3	53.5	67.1	60.5
NO OBS	411	418	415	407	406	402	405	400	1630	1624	3254

JUNE

Viewing (Elevation) Angle, deg	Hour (LST) 01	04	07	10	13	16	19	22	Day (07-18)	Night (19-06)	All
90	82.9	75.2	74.2	71.1	70.1	72.9	78.9	78.8	71.8	79.0	75.6
80	82.2	74.6	73.6	70.7	69.5	72.6	78.3	78.1	71.3	78.3	75.0
70	81.9	74.5	73.5	70.4	69.1	72.2	78.0	77.9	71.0	78.1	74.8
60	81.6	74.2	73.1	70.0	68.5	71.7	77.7	77.4	70.7	78.0	74.4
50	81.6	73.7	72.7	69.0	67.4	70.8	76.9	77.0	69.9	77.5	73.6
40	81.2	73.0	71.7	67.8	65.9	69.4	75.7	76.2	68.5	76.6	72.6
30	79.5	71.2	69.6	65.2	62.5	66.5	73.3	73.7	65.8	74.7	70.2
20	78.3	69.2	67.3	61.9	58.1	62.4	70.1	71.3	62.2	72.6	67.4
10	76.0	66.1	63.6	56.4	51.3	56.3	65.6	67.2	56.5	68.6	62.8
NO OBS	385	390	388	392	392	386	388	396	1558	1549	3107

JULY

Viewing (Elevation) Angle, deg	Hour (LST) 01	04	07	10	13	16	19	22	Day (07-18)	Night (19-06)	All
90	78.8	71.1	68.1	65.4	65.8	68.7	77.0	76.3	66.7	76.0	71.4
80	78.1	70.5	67.6	65.0	65.5	68.3	76.5	75.8	66.3	75.4	71.0
70	78.1	70.4	67.4	64.6	65.1	67.9	76.1	75.5	66.0	75.0	70.6
60	77.9	70.2	67.0	64.0	64.4	67.3	75.4	75.1	65.7	74.6	70.2
50	77.6	69.6	66.5	63.2	63.2	66.2	74.7	74.4	64.6	74.2	69.5
40	77.0	68.8	65.4	61.7	61.3	64.6	73.3	73.7	63.2	73.1	68.5
30	75.3	66.9	63.1	58.8	58.2	61.1	70.7	71.5	60.1	71.1	65.6
20	73.9	64.6	60.4	54.8	53.3	57.0	67.1	68.9	56.3	68.8	62.5
10	71.0	60.8	56.1	48.9	46.2	50.1	61.6	64.7	50.2	64.6	57.5
NO OBS	411	419	401	406	408	406	401	409	1619	1630	3249

AUGUST

Viewing (Elevation) Angle, deg	Hour (LST) 01	04	07	10	13	16	19	22	Day (07-18)	Night (19-06)	All
90	79.9	71.2	69.7	68.1	67.8	69.9	78.4	76.7	68.7	7 .6	72.8
80	79.3	70.7	69.2	67.7	67.4	69.4	77.9	76.1	68.2	76.0	72.2
70	79.3	70.5	69.0	67.3	66.7	69.0	77.5	75.8	67.9	75.8	71.9
60	79.0	70.3	68.7	66.8	66.1	68.5	77.0	75.4	67.5	75.4	71.5
50	78.7	70.0	68.1	66.0	65.1	67.5	76.1	75.0	66.5	74.9	70.9
40	78.2	69.1	67.0	64.5	63.2	65.6	74.7	74.2	65.1	74.0	69.7
30	76.5	67.3	64.8	62.0	60.2	62.6	72.0	71.9	62.2	72.0	67.2
20	75.1	65.5	62.3	58.3	55.6	58.1	68.2	69.7	58.4	69.9	64.1
10	72.5	62.2	58.0	52.8	48.6	51.5	62.5	65.8	52.6	65.7	59.2
NO OBS	441	439	430	435	439	433	432	440	1734	1752	3486

PROBABILITY BASED ON DISTRIBUTION OF CLOUD COVER BELOW 4920 FEET

SEPTEMBER

Viewing (Elevation) Angle, deg	Hour (LST) 01	04	07	10	13	16	19	22	Day (07-18)	Night (19-06)	All
90	82.3	76.9	72.5	67.4	69.0	72.5	79.1	81.0	70.5	79.7	74.8
80	81.4	76.2	71.8	66.9	68.6	72.1	78.5	80.3	70.0	78.9	74.3
70	81.3	76.0	71.8	66.6	68.2	71.8	78.2	80.1	69.6	78.8	74.1
60	81.3	75.9	71.3	66.1	67.8	71.2	78.0	79.9	69.1	78.7	73.9
50	81.0	75.8	71.0	65.6	67.0	70.5	77.4	79.7	68.6	78.3	73.3
40	80.8	75.0	69.9	64.3	65.3	69.1	76.4	79.1	67.2	77.5	72.3
30	79.1	73.5	68.0	61.9	62.4	66.3	74.0	77.4	64.6	76.0	70.2
20	78.1	72.1	65.6	59.1	58.6	62.5	71.0	75.9	61.6	74.2	67.6
10	75.5	69.5	61.6	54.3	52.6	56.9	66.9	73.2	56.4	71.0	63.7
NO OBS	399	393	395	384	405	399	400	388	1583	1571	3154

OCTOBER

Viewing (Elevation) Angle, deg	Hour (LST) 01	04	07	10	13	16	19	22	Day (07-18)	Night (19-06)	All
90	66.8	62.7	58.8	59.4	66.0	69.1	68.7	68.6	63.3	66.9	65.2
80	66.3	62.1	58.4	59.1	65.6	68.6	68.2	68.1	63.0	66.3	64.6
70	66.2	62.0	58.3	58.9	65.2	68.3	67.9	68.1	62.8	66.1	64.4
60	66.2	61.8	58.0	58.8	64.8	67.9	67.7	68.0	62.5	66.0	64.2
50	65.9	61.6	57.5	58.1	64.1	67.5	67.2	67.6	61.7	65.7	63.6
40	65.3	60.9	56.6	57.1	62.7	66.0	66.4	66.9	60.6	65.0	62.8
30	63.7	59.4	54.4	54.9	60.0	63.4	64.7	65.3	58.1	63.3	60.8
20	62.3	58.1	52.5	52.4	56.7	60.2	62.7	63.7	55.3	61.8	58.7
10	59.9	55.2	48.7	48.3	51.5	55.3	59.3	60.8	51.0	59.0	54.8
NO OBS	420	417	426	409	436	414	427	402	1685	1666	3351

NOVEMBER

Viewing (Elevation) Angle, deg	Hour (LST) 01	04	07	10	13	16	19	22	Day (07-18)	Night (19-06)	All
90	51.0	49.3	46.6	51.3	52.9	54.1	51.0	52.9	51.3	51.0	51.2
80	50.7	48.8	46.2	51.0	52.6	53.9	50.6	52.3	51.0	50.7	50.8
70	50.7	48.8	46.1	50.8	52.4	53.6	50.4	52.2	50.8	50.6	50.7
60	50.4	48.7	45.9	50.6	52.1	53.2	50.2	52.2	50.6	50.4	50.4
50	50.3	48.4	45.7	49.9	51.4	52.7	49.9	51.8	50.0	50.2	50.0
40	49.2	47.6	44.6	48.9	50.0	51.5	48.8	51.2	48.7	49.2	48.9
30	47.5	46.0	42.9	46.5	47.9	49.2	47.0	49.6	46.4	47.6	47.0
20	46.0	44.6	41.2	43.8	44.9	46.3	45.1	47.8	44.2	45.8	44.9
10	42.8	41.7	38.2	39.6	40.2	41.8	41.8	44.8	39.8	42.6	41.4
NO OBS	404	401	416	399	405	410	407	409	1630	1615	3245

DECEMBER

Viewing (Elevation) Angle, deg	Hour (LST) 01	04	07	10	13	16	19	22	Day (07-18)	Night (19-06)	All
90	48.5	45.8	44.5	48.3	52.3	53.4	50.7	50.8	49.7	48.8	49.3
80	48.2	45.3	44.3	48.0	52.1	53.2	50.2	50.2	49.3	48.5	49.0
70	48.0	45.2	44.3	47.7	51.9	52.9	50.0	50.0	49.1	48.3	48.8
60	47.8	45.1	44.0	47.4	51.5	52.5	49.9	49.8	48.8	48.1	48.6
50	47.5	44.8	43.6	46.7	50.8	51.9	49.5	49.5	48.3	47.8	48.1
40	46.6	43.9	42.6	45.6	49.7	50.6	48.3	48.6	47.1	46.9	46.9
30	44.6	42.1	40.7	43.4	47.2	48.2	46.5	46.8	45.0	45.0	44.9
20	42.6	40.2	38.9	40.6	44.3	45.3	44.5	44.8	42.4	42.9	42.8
10	39.3	36.8	35.7	36.3	39.7	40.4	40.8	41.4	38.1	39.6	38.8
NO OBS	416	429	429	406	428	430	425	413	1693	1683	3376

PROBABILITY BASED ON DISTRIBUTION OF CLOUD COVER BELOW 984 FEET WITH SURFACE VISIBILITY OF 2.5 MILES OR MORE AND NO PRECIPITATION OCCURRING

JANUARY

Viewing (Elevation) Angle, deg	Hour (LST) 01	04	07	10	13	16	19	22	Day (07-18)	Night (19-06)	All
90	45.2	44.0	44.3	39.2	52.2	50.3	48.5	41.3	46.6	44.8	45.7
80	44.8	43.6	43.9	38.8	51.7	49.8	48.0	40.9	46.2	44.4	45.3
70	44.8	43.6	43.9	38.8	51.7	49.8	48.0	40.9	46.2	44.4	45.3
60	44.8	43.6	43.9	38.8	51.7	49.7	48.0	40.9	46.2	44.4	45.3
50	44.8	43.5	43.9	38.7	51.6	49.6	48.0	40.9	46.1	44.4	45.3
40	44.7	43.3	43.7	38.5	51.5	49.5	48.0	40.8	46.1	44.3	45.3
30	44.2	42.8	43.2	38.1	50.8	48.9	47.4	40.4	45.5	43.8	44.7
20	43.9	42.7	43.0	37.9	50.5	48.8	47.2	40.2	45.1	43.5	44.4
10	43.3	41.8	42.3	37.2	49.6	48.2	46.7	39.6	44.4	42.7	43.6
NO OBS	452	456	455	435	455	451	451	437	1796	1796	3592

FEBRUARY

Viewing (Elevation) Angle, deg	Hour (LST) 01	04	07	10	13	16	19	22	Day (07-18)	Night (19-06)	All
90	52.4	51.4	48.4	45.8	57.4	63.8	58.7	59.1	54.0	55.6	54.5
80	51.9	50.9	47.9	45.4	56.8	63.2	58.1	58.5	53.5	55.1	54.0
70	51.9	50.9	47.9	45.4	56.8	63.2	58.1	58.5	53.5	55.1	54.0
60	51.9	50.9	47.9	45.3	56.7	63.2	58.1	58.4	53.5	55.0	54.0
50	51.9	50.9	47.9	45.3	56.7	63.2	58.1	58.4	53.5	55.0	54.0
40	51.9	50.8	47.7	45.3	56.6	63.0	58.1	58.3	53.2	54.8	53.9
30	51.1	50.0	47.1	44.4	56.0	62.3	57.4	57.6	52.7	54.2	53.2
20	50.9	49.9	46.9	44.4	55.8	62.1	57.4	57.6	52.4	53.9	53.1
10	50.3	49.1	46.1	43.7	55.0	61.4	56.7	56.9	51.6	53.2	52.4
NO OBS	382	388	371	371	379	367	368	368	1488	1486	2974

MARCH

Viewing (Elevation) Angle, deg	Hour (LST) 01	04	07	10	13	16	19	22	Day (07-18)	Night (19-06)	All
90	66.6	62.9	54.4	55.9	72.3	71.8	65.2	68.7	63.8	65.9	64.9
80	66.1	62.3	53.9	55.4	71.6	71.1	64.6	68.0	63.2	65.3	64.3
70	66.1	62.3	53.9	55.4	71.6	71.1	64.6	68.0	63.2	65.3	64.3
60	66.1	62.2	53.8	55.4	71.6	71.1	64.6	68.0	63.2	65.3	64.2
50	66.1	62.2	53.6	55.4	71.6	71.1	64.6	68.0	63.1	65.3	64.1
40	66.0	62.0	53.5	55.3	71.6	71.0	64.6	67.9	62.9	65.3	64.1
30	65.3	61.3	52.9	54.8	70.9	70.2	63.7	67.2	62.2	64.5	63.3
20	65.2	61.1	52.6	54.2	70.9	70.2	63.6	67.1	62.0	64.4	63.2
10	64.4	60.2	51.7	53.2	69.9	69.4	62.9	66.3	61.1	63.6	62.5
NO OBS	410	407	401	409	403	393	402	401	1606	1626	3232

APRIL

Viewing (Elevation) Angle, deg	Hour (LST) 01	04	07	10	13	16	19	22	Day (07-18)	Night (19-06)	All
90	72.5	63.9	51.3	67.7	81.0	80.8	81.9	79.3	70.1	74.5	72.4
80	71.8	63.3	50.8	67.1	80.2	80.0	81.1	78.5	69.4	73.8	71.7
70	71.8	63.3	50.7	67.1	80.2	80.0	81.1	78.5	69.4	73.8	71.7
60	71.7	63.3	50.7	67.0	80.1	80.0	81.1	78.5	69.4	73.8	71.6
50	71.6	63.3	50.6	67.0	80.0	80.0	81.1	78.5	69.3	73.8	71.6
40	71.6	63.2	50.5	66.8	80.0	80.0	81.1	78.4	69.1	73.7	71.4
30	70.8	62.5	49.8	65.7	79.2	79.1	80.3	77.6	68.4	72.9	70.7
20	70.6	62.3	49.6	65.6	78.9	79.0	80.2	77.5	68.2	72.8	70.4
10	69.7	61.6	48.8	64.5	78.1	78.2	79.3	76.7	67.3	71.8	69.4
NO OBS	401	404	400	403	402	400	403	398	1605	1606	3211

PROBABILITY BASED ON DISTRIBUTION OF CLOUD COVER BELOW 984 FEET WITH SURFACE VISIBILITY OF 2.5 MILES OR MORE AND NO PRECIPITATION OCCURRING

MAY

Viewing (Elevation) Angle, deg	Hour (LST) 01	04	07	10	13	16	19	22	Day (07-18)	Night (19-06)	All
90	80.9	69.0	68.6	77.3	84.3	84.7	85.9	83.0	78.6	79.8	79.3
80	80.1	68.3	67.9	76.5	83.5	83.9	85.0	82.2	77.8	79.0	78.5
70	80.1	68.3	67.9	76.5	83.5	83.9	85.0	82.2	77.8	79.0	78.5
60	80.1	68.3	67.9	76.5	83.5	83.9	85.0	82.2	77.8	79.0	78.5
50	80.1	68.2	67.8	76.5	83.5	83.8	85.0	82.2	77.8	79.0	78.4
40	80.1	68.1	67.8	76.4	83.5	83.7	84.9	82.2	77.8	79.0	78.4
30	79.2	67.4	66.9	75.5	82.6	82.8	84.1	81.3	77.1	78.1	77.5
20	79.1	67.3	66.5	75.3	82.6	82.7	83.9	81.3	76.9	78.0	77.4
10	79.2	66.4	65.4	74.2	81.7	81.8	82.9	80.4	75.9	77.0	76.5
NO OBS	411	408	415	406	406	402	405	400	1629	1624	3253

JUNE

Viewing (Elevation) Angle, deg	Hour (LST) 01	04	07	10	13	16	19	22	Day (07-18)	Night (19-06)	All
90	85.0	72.8	73.7	84.8	89.9	88.3	87.0	86.8	84.3	83.1	83.5
80	84.2	72.1	73.0	84.0	89.0	87.4	86.1	85.9	83.5	82.3	82.7
70	84.2	72.1	72.9	84.0	89.0	87.4	86.1	85.9	83.5	82.3	82.7
60	84.2	72.1	72.9	84.0	89.0	87.4	86.1	85.9	83.4	82.3	82.7
50	84.2	72.1	72.9	84.0	89.0	87.4	86.1	85.9	83.4	82.3	82.7
40	84.1	72.0	72.8	83.9	89.0	87.4	86.1	85.8	83.3	82.2	82.7
30	83.1	71.0	71.8	82.9	88.1	86.5	85.3	84.8	82.4	81.2	81.9
20	83.0	71.0	71.4	82.9	88.0	86.5	85.3	84.7	82.2	81.1	81.6
10	82.0	70.2	70.1	81.9	87.1	85.7	84.4	83.6	81.0	80.0	80.3
NO OBS	385	379	388	392	391	386	388	395	1557	1547	3104

JULY

Viewing (Elevation) Angle, deg	Hour (LST) 01	04	07	10	13	16	19	22	Day (07-18)	Night (19-06)	All
90	80.3	70.0	68.2	82.2	86.2	89.6	85.6	86.3	81.6	80.6	81.0
80	79.5	69.3	67.6	81.4	85.3	88.7	84.7	85.4	80.8	79.8	80.2
70	79.5	69.3	67.6	81.4	85.3	88.7	84.7	85.4	80.8	79.8	80.2
60	79.5	69.2	67.6	81.4	85.3	88.7	84.7	85.4	80.8	79.8	80.2
50	79.5	69.2	67.3	81.3	85.3	88.7	84.7	85.4	80.8	79.8	80.2
40	79.5	69.0	67.1	81.1	85.3	88.7	84.7	85.4	80.7	79.7	80.1
30	78.7	68.3	66.2	80.2	84.5	87.8	83.9	84.5	79.9	78.9	79.3
20	78.5	68.2	65.7	80.1	84.5	87.8	83.8	84.4	79.7	78.9	79.2
10	77.5	67.3	64.6	78.9	83.6	86.9	82.9	83.4	78.8	77.9	78.2
NO OBS	411	409	401	406	406	406	401	409	1619	1630	3249

AUGUST

Viewing (Elevation) Angle, deg	Hour (LST) 01	04	07	10	13	16	19	22	Day (07-18)	Night (19-06)	All
90	82.2	67.5	67.6	82.9	86.6	89.8	86.2	86.3	81.9	80.6	81.1
80	81.4	66.8	67.0	82.1	85.7	88.9	85.3	85.4	81.1	79.8	80.3
70	81.4	66.8	66.9	82.1	85.7	88.9	85.3	85.4	81.1	79.8	80.3
60	81.4	66.8	66.9	82.1	85.7	88.9	85.3	85.4	81.0	79.8	80.3
50	81.4	66.7	66.8	82.0	85.7	88.9	85.2	85.4	81.0	79.8	80.3
40	81.4	66.5	66.5	81.9	85.7	88.9	85.2	85.4	80.9	79.7	80.3
30	80.5	65.9	65.6	80.9	84.9	88.0	84.4	84.6	80.1	78.9	79.4
20	80.3	65.8	65.2	80.5	84.9	88.0	84.3	84.4	79.8	78.7	79.2
10	79.3	64.7	64.0	79.5	83.9	87.1	83.4	83.4	78.6	77.7	78.1
NO OBS	441	439	430	435	436	433	432	440	1734	1752	3486

PROBABILITY BASED ON DISTRIBUTION OF CLOUD COVER BELOW 984 FEET WITH SURFACE VISIBILITY OF 2.5 MILES OR MORE AND NO PRECIPITATION OCCURRING

SEPTEMBER

Viewing (Elevation) Angle, deg	Hour (LST) 01	04	07	10	13	16	19	22	Day (07-18)	Night (19-06)	All
90	76.0	67.0	55.6	71.9	84.9	88.3	82.3	79.6	75.3	76.4	75.8
80	75.3	66.3	55.1	71.2	84.1	87.4	81.5	78.8	74.6	75.6	75.1
70	75.3	66.3	55.1	71.2	84.1	87.4	81.5	78.8	74.6	75.6	75.1
60	75.3	66.3	55.0	71.1	84.1	87.4	81.5	78.8	74.6	75.6	75.1
50	75.3	66.3	55.0	71.0	84.1	87.4	81.5	78.8	74.5	75.6	75.1
40	75.3	66.2	54.8	70.8	84.1	87.3	81.5	78.8	74.4	75.5	75.1
30	74.3	65.4	54.0	70.1	83.1	86.4	80.7	77.8	73.5	74.8	74.2
20	74.2	65.3	53.8	69.7	83.0	86.3	80.7	77.8	73.4	74.8	74.1
10	73.4	64.5	53.1	68.7	82.1	85.4	79.8	77.0	72.5	73.8	73.1
NO OBS	396	392	395	384	405	399	400	389	1583	1567	3150

OCTOBER

Viewing (Elevation) Angle, deg	Hour (LST) 01	04	07	10	13	16	19	22	Day (07-18)	Night (19-06)	All
90	59.2	53.0	46.0	52.7	74.5	77.2	69.1	63.2	62.8	61.5	62.1
80	58.6	52.5	45.6	52.2	73.8	76.4	68.4	62.6	62.2	60.9	61.5
70	58.6	52.5	45.6	52.2	73.8	76.4	68.4	62.6	62.2	60.9	61.5
60	58.6	52.5	45.6	52.1	73.7	76.4	68.4	62.6	62.2	60.9	61.5
50	58.6	52.4	45.5	52.0	73.7	76.4	68.4	62.6	62.1	60.9	61.5
40	58.6	52.4	45.4	52.0	73.7	76.4	68.4	62.6	62.1	60.8	61.4
30	58.0	51.8	44.9	51.5	72.7	75.7	67.7	61.9	61.3	60.1	60.7
20	57.8	51.7	44.8	51.2	72.6	75.6	67.6	61.9	61.2	60.0	60.5
10	57.2	50.9	44.3	50.7	71.6	74.6	66.8	61.1	60.6	59.3	59.7
NO OBS	420	417	426	409	436	414	427	401	1685	1665	3350

NOVEMBER

Viewing (Elevation) Angle, deg	Hour (LST) 01	04	07	10	13	16	19	22	Day (07-18)	Night (19-06)	All
90	53.5	50.4	48.4	47.6	59.8	57.5	54.9	55.3	53.4	53.5	53.4
80	53.0	49.9	47.9	47.2	59.2	56.9	54.4	54.8	52.9	53.0	52.9
70	53.0	49.9	47.9	47.2	59.2	56.9	54.4	54.8	52.9	53.0	52.9
60	53.0	49.9	47.9	47.2	59.2	56.8	54.4	54.8	52.9	53.0	52.9
50	52.9	49.9	47.9	47.1	59.2	56.7	54.4	54.7	52.7	53.0	52.9
40	52.7	49.7	47.9	47.0	59.0	56.7	54.3	54.5	52.6	53.0	52.9
30	52.2	49.2	47.4	46.2	58.2	56.1	53.6	53.9	51.9	52.4	52.1
20	51.9	49.1	47.2	46.1	58.2	56.0	53.5	53.8	51.8	52.1	51.9
10	51.0	48.2	46.5	45.2	57.0	55.4	52.8	53.1	51.0	51.2	51.1
NO OBS	404	411	416	399	404	410	407	403	1629	1615	3244

DECEMBER

Viewing (Elevation) Angle, deg	Hour (LST) 01	04	07	10	13	16	19	22	Day (07-18)	Night (19-06)	All
90	51.7	47.0	46.4	38.4	51.3	51.5	48.2	45.7	47.1	48.2	47.7
80	51.2	46.6	46.0	38.0	50.8	51.0	47.7	45.3	46.7	47.7	47.2
70	51.2	46.6	46.0	38.0	50.8	51.0	47.7	45.3	46.7	47.7	47.2
60	51.2	46.6	46.0	37.9	50.7	51.0	47.7	45.3	46.7	47.7	47.1
50	51.2	46.5	46.0	37.9	50.6	51.0	47.6	45.3	46.6	47.7	47.1
40	50.9	46.3	45.7	37.8	50.5	50.7	47.6	45.1	46.4	47.7	46.9
30	50.4	45.7	45.0	37.3	49.9	50.2	47.1	44.5	45.7	47.0	46.4
20	50.2	45.4	45.0	37.0	49.5	49.8	47.0	44.4	45.4	46.8	46.0
10	49.4	44.7	44.1	36.2	48.3	49.0	46.2	43.6	44.6	46.0	45.0
NO OBS	416	429	429	406	428	430	425	412	1693	1682	3375

PROBABILITY BASED ON DISTRIBUTION OF CLOUD COVER BELOW 3280 FEET WITH SURFACE VISIBILITY OF 2.5 MILES OR MORE AND NO PRECIPITATION OCCURRING

JANUARY

Viewing (Elevation) Angle, deg	Hour (LST) 01	04	07	10	13	16	19	22	Day (07-18)	Night (19-06)	All
90	32.0	31.2	30.7	27.7	38.8	38.1	36.9	31.2	33.9	32.8	33.3
80	31.7	31.0	30.3	27.6	38.5	37.9	36.6	31.0	33.5	32.5	33.1
70	31.7	31.0	30.2	27.3	38.4	37.8	36.5	31.0	33.4	32.5	33.0
60	31.7	30.9	30.1	27.2	38.1	37.5	36.5	30.8	33.3	32.5	32.8
50	31.4	30.7	29.9	26.9	38.0	37.3	36.4	30.8	33.0	32.3	32.7
40	31.1	30.1	29.6	26.3	37.3	36.7	36.1	30.4	32.7	31.7	32.4
30	30.2	29.4	28.5	25.2	36.1	35.5	35.4	29.6	31.4	31.1	31.3
20	29.4	28.6	27.8	24.3	34.7	34.1	34.5	28.8	30.1	30.5	30.4
10	28.1	27.2	26.0	22.2	32.2	31.9	33.2	27.7	28.2	29.0	28.7
NO OBS	452	456	455	435	455	451	451	431	1796	1796	3592

FEBRUARY

Viewing (Elevation) Angle, deg	Hour (LST) 01	04	07	10	13	16	19	22	Day (07-18)	Night (19-06)	All
90	40.5	40.2	37.7	35.4	42.7	46.9	40.3	43.5	40.8	41.2	40.9
80	40.2	39.9	37.4	35.1	42.4	46.6	40.0	43.2	40.4	40.9	40.6
70	40.1	39.9	37.4	35.0	42.4	46.6	39.9	43.2	40.4	40.8	40.6
60	40.0	39.6	37.2	34.9	42.2	46.4	39.7	43.1	40.2	40.7	40.4
50	39.8	39.6	37.1	34.7	41.7	45.9	39.5	42.9	39.9	40.5	40.1
40	39.5	39.4	36.6	34.1	40.9	45.1	38.9	42.5	39.2	40.0	39.7
30	38.6	38.3	35.6	33.3	39.1	43.6	37.9	41.5	38.0	39.2	38.6
20	37.9	37.7	34.8	32.0	37.3	41.6	36.6	40.6	36.4	38.2	37.3
10	36.6	36.1	33.1	29.9	33.9	38.8	34.5	38.9	33.9	36.5	35.4
NO OBS	382	388	371	371	379	367	368	368	1488	1486	2974

MARCH

Viewing (Elevation) Angle, deg	Hour (LST) 01	04	07	10	13	16	19	22	Day (07-18)	Night (19-06)	All
90	51.9	49.5	38.9	43.2	52.1	54.5	51.9	56.2	47.1	52.2	49.8
80	51.5	49.1	38.7	43.0	51.8	54.1	51.3	55.7	46.7	51.8	49.4
70	51.4	49.1	38.6	42.8	51.5	53.9	51.2	55.7	46.6	51.8	49.4
60	51.3	49.0	38.5	42.7	51.2	53.4	51.1	55.6	46.5	51.7	49.1
50	51.1	48.9	38.2	42.3	50.9	53.1	50.7	55.4	46.1	51.7	48.9
40	50.7	48.5	37.8	41.7	49.7	52.4	50.1	55.0	45.4	51.2	48.5
30	49.6	47.5	36.5	40.2	48.1	50.5	49.0	54.1	43.8	50.0	47.0
20	48.8	47.0	35.1	38.7	45.6	48.4	47.7	53.4	42.0	49.1	45.6
10	47.1	45.4	33.2	36.1	41.9	45.2	45.1	51.8	39.0	47.4	43.3
NO OBS	410	407	401	409	403	393	402	407	1606	1626	3232

APRIL

Viewing (Elevation) Angle, deg	Hour (LST) 01	04	07	10	13	16	19	22	Day (07-18)	Night (19-06)	All
90	65.6	56.1	45.5	54.5	64.1	66.5	72.6	73.0	57.8	67.1	62.3
80	65.0	55.6	45.2	54.1	63.7	65.9	71.9	72.3	57.2	66.5	61.8
70	65.0	55.6	45.1	53.9	63.4	65.8	71.8	72.3	56.9	66.5	61.7
60	65.0	55.6	45.0	53.7	63.1	65.5	71.6	72.3	56.7	66.2	61.6
50	64.7	55.4	44.7	53.1	62.5	65.1	71.2	72.3	56.3	66.1	61.3
40	64.4	55.2	44.3	52.3	61.6	64.3	70.8	72.6	55.6	65.7	60.8
30	63.5	54.3	43.3	50.5	59.7	62.6	69.1	70.9	54.0	64.5	59.3
20	63.1	53.6	42.2	48.6	57.5	60.8	67.5	70.5	52.1	63.8	57.9
10	61.6	52.3	40.3	45.0	53.8	57.5	64.9	69.0	49.3	62.1	55.8
NO OBS	401	404	400	403	402	400	403	398	1605	1606	3211

PROBABILITY BASED ON DISTRIBUTION OF CLOUD COVER BELOW 3280 FEET WITH SURFACE VISIBILITY OF 2.5 MILES OR MORE AND NO PRECIPITATION OCCURRING

MAY

Viewing (Elevation) Angle, deg	Hour (LST) 01	04	07	10	13	16	19	22	Day (07-18)	Night (19-06)	All
90	75.5	62.5	59.7	62.2	67.8	72.2	77.9	77.2	65.4	73.3	69.2
80	74.8	61.9	59.1	61.7	67.2	71.6	77.3	76.5	64.8	72.7	68.6
70	74.8	61.9	58.9	61.5	67.1	71.5	77.1	76.5	64.7	72.7	68.6
60	74.8	61.8	58.8	61.2	66.7	71.3	76.9	76.4	64.5	72.4	68.4
50	74.7	61.6	58.6	60.8	66.3	70.8	76.6	76.3	64.1	72.3	68.1
40	74.5	61.4	58.1	59.7	65.4	70.4	76.3	75.9	63.6	71.9	67.6
30	73.6	60.4	56.8	57.9	63.6	68.9	74.7	74.8	61.7	70.9	66.2
20	73.1	59.7	55.5	55.6	61.6	67.4	73.4	74.2	60.0	70.1	64.9
10	71.8	58.1	53.2	51.9	58.2	64.5	71.0	72.2	57.1	68.3	62.5
NO OBS	411	408	415	406	406	402	405	400	1629	1624	3253

JUNE

Viewing (Elevation) Angle, deg	Hour (LST) 01	04	07	10	13	16	19	22	Day (07-18)	Night (19-06)	All
90	78.8	62.8	65.7	68.2	74.7	76.7	79.0	77.9	71.5	74.7	73.0
80	78.1	62.3	65.1	67.7	73.9	76.0	78.2	77.3	70.9	74.0	72.3
70	78.1	62.1	65.0	67.6	73.7	75.8	78.2	77.2	70.8	74.0	72.2
60	78.1	62.0	65.0	67.2	73.6	75.6	78.0	77.1	70.5	73.9	72.0
50	77.9	62.0	64.6	66.6	73.2	75.5	77.7	76.8	70.1	73.9	71.9
40	77.6	61.5	64.2	65.6	72.5	74.8	77.3	76.5	69.3	73.3	71.1
30	76.6	60.4	62.8	63.7	70.7	73.3	75.7	74.9	67.7	72.0	69.8
20	74.0	59.5	61.6	61.3	68.9	71.9	74.6	73.5	66.1	71.0	68.4
10	74.4	57.7	59.2	57.5	65.4	69.3	72.4	71.1	62.9	69.1	65.9
NO OBS	385	379	388	392	391	386	388	395	1557	1547	3104

JULY

Viewing (Elevation) Angle, deg	Hour (LST) 01	04	07	10	13	16	19	22	Day (07-18)	Night (19-06)	All
90	72.0	60.5	59.1	61.2	69.1	73.8	74.1	76.1	65.6	70.6	68.4
80	71.4	60.0	58.7	60.8	68.4	73.2	73.3	75.5	65.2	69.9	67.8
70	71.3	60.0	58.5	60.6	68.3	73.0	73.2	75.4	65.0	69.9	67.6
60	71.3	59.8	58.5	60.2	68.0	72.7	72.9	75.1	64.8	69.8	67.3
50	71.2	59.7	58.0	59.6	67.4	72.2	72.5	74.9	64.2	69.5	66.9
40	71.0	59.4	57.7	58.1	66.7	71.7	71.9	74.6	63.4	69.1	66.4
30	69.8	58.0	55.9	56.0	64.8	69.5	70.3	73.0	61.4	67.6	64.7
20	69.0	57.1	54.6	53.0	62.8	67.7	68.8	71.9	59.4	66.5	63.2
10	67.5	55.1	52.2	48.1	59.1	64.4	65.6	69.5	55.9	64.4	60.2
NO OBS	411	409	401	406	406	406	401	409	1619	1630	3249

AUGUST

Viewing (Elevation) Angle, deg	Hour (LST) 01	04	07	10	13	16	19	22	Day (07-18)	Night (19-06)	All
90	74.4	59.6	59.2	63.7	70.0	74.3	75.5	77.1	67.0	71.7	69.4
80	73.7	59.0	58.7	63.4	69.5	73.8	74.9	76.3	66.5	71.0	68.8
70	73.7	59.0	58.7	63.2	69.2	73.6	74.8	76.3	66.4	71.0	68.6
60	73.6	58.9	58.5	62.8	69.0	73.3	74.5	76.2	66.1	70.9	68.4
50	73.6	58.7	58.3	62.2	68.6	72.9	74.2	75.9	65.5	70.7	68.1
40	73.3	58.4	57.5	60.9	67.7	72.0	73.4	75.5	64.6	70.4	67.4
30	72.2	57.3	56.3	58.6	65.8	70.0	71.7	74.4	62.8	69.0	65.8
20	71.5	56.6	54.7	55.7	63.7	68.1	70.2	73.4	60.6	67.9	64.3
10	69.8	54.8	52.4	51.2	60.3	64.5	67.0	71.2	57.2	65.9	61.4
NO OBS	441	439	430	435	436	433	432	440	1734	1752	3486

PROBABILITY BASED ON DISTRIBUTION OF CLOUD COVER BELOW 3280 FEET WITH SURFACE VISIBILITY OF 2.5 MILES OR MORE AND NO PRECIPITATION OCCURRING

SEPTEMBER

Viewing (Elevation) Angle, deg	Hour (LST) 01	04	07	10	13	16	19	22	Day (07-18)	Night (19-06)	All
90	71.0	66.4	47.9	57.1	66.7	73.8	73.4	72.5	61.4	69.4	65.3
80	70.3	59.9	47.4	56.7	66.2	73.1	72.7	71.8	60.8	68.8	64.8
70	70.3	59.9	47.4	56.5	66.1	73.1	72.5	71.7	60.7	68.7	64.6
60	70.3	59.9	47.2	56.2	65.6	72.9	72.3	71.7	60.5	68.6	64.4
50	70.0	59.7	46.8	55.9	65.2	72.4	72.0	71.6	60.0	68.5	64.2
40	69.9	59.3	46.4	55.0	63.9	71.6	71.6	71.3	59.3	68.1	63.5
30	68.9	58.5	45.4	53.1	62.1	69.6	70.2	70.3	57.4	67.1	62.2
20	68.6	57.9	44.4	51.1	59.3	67.6	68.8	69.8	55.4	66.3	60.7
10	67.3	56.4	42.3	47.8	55.2	64.1	66.2	68.2	52.4	64.6	58.4
NO OBS	396	392	395	384	405	399	400	389	1583	1567	3150

OCTOBER

Viewing (Elevation) Angle, deg	Hour (LST) 01	04	07	10	13	16	19	22	Day (07-18)	Night (19-06)	All
90	50.0	44.7	35.9	42.3	58.0	61.6	57.6	53.9	49.4	51.6	50.7
80	49.5	44.3	35.6	42.1	57.6	61.1	57.0	53.4	49.0	51.0	50.2
70	49.4	44.3	35.5	42.0	57.4	60.9	57.0	53.4	48.9	51.0	49.9
60	49.4	44.3	35.1	41.8	57.0	60.6	56.9	53.4	48.8	50.9	49.8
50	49.3	44.2	34.9	41.6	56.4	60.3	56.7	53.1	48.4	50.8	49.6
40	49.1	43.8	34.6	40.9	55.5	59.4	56.2	52.9	47.7	50.5	49.0
30	48.3	43.0	33.8	39.6	53.6	57.6	55.1	51.9	46.3	49.6	48.1
20	47.9	42.6	32.9	38.4	51.1	55.7	54.2	51.5	44.5	49.2	46.8
10	46.7	41.4	31.1	35.8	47.3	52.1	52.4	50.1	41.5	47.6	44.7
NO OBS	420	417	426	409	439	414	427	401	1685	1665	3350

NOVEMBER

Viewing (Elevation) Angle, deg	Hour (LST) 01	04	07	10	13	16	19	22	Day (07-18)	Night (19-06)	All
90	38.9	38.5	35.7	35.6	42.0	42.1	40.6	40.5	38.7	39.6	39.1
80	38.6	38.2	35.3	35.3	41.8	41.7	40.3	40.2	38.5	39.3	38.8
70	38.6	38.2	35.3	35.3	41.6	41.6	40.2	40.1	38.3	39.3	38.6
60	38.5	38.2	35.2	35.2	41.4	41.4	40.2	40.1	38.1	39.3	38.6
50	38.0	37.9	35.1	34.9	41.0	41.0	40.0	39.9	37.8	39.3	38.3
40	37.9	37.7	34.8	34.2	40.1	40.3	39.9	39.7	37.3	38.8	37.9
30	36.8	36.9	34.0	32.9	38.7	38.9	39.0	38.9	36.0	37.8	36.9
20	36.0	36.4	33.2	31.5	36.6	37.4	38.3	37.9	34.4	37.1	35.9
10	34.4	35.1	31.5	29.0	33.4	34.7	36.8	36.7	32.2	35.5	33.8
NO OBS	404	401	416	399	404	410	407	403	1629	1615	3244

DECEMBER

Viewing (Elevation) Angle, deg	Hour (LST) 01	04	07	10	13	16	19	22	Day (07-18)	Night (19-06)	All
90	36.3	33.9	32.8	27.5	38.5	37.8	34.9	34.2	34.1	34.8	34.5
80	36.0	33.6	32.6	27.4	38.3	37.6	34.7	33.9	33.9	34.5	34.3
70	36.0	33.6	32.6	27.2	38.2	37.4	34.6	33.9	33.8	34.5	34.3
60	35.8	33.3	32.4	27.1	38.0	37.1	34.4	33.8	33.7	34.5	34.1
50	35.4	33.2	32.3	26.8	37.6	36.8	34.3	33.4	33.2	34.1	33.9
40	35.1	32.8	31.8	26.1	37.0	36.0	33.8	33.2	32.7	33.7	33.4
30	34.2	31.9	30.6	25.1	35.7	34.7	32.9	32.2	31.7	32.8	32.3
20	33.2	31.0	29.9	23.9	33.9	33.1	31.9	31.4	30.1	32.0	31.2
10	31.5	29.2	27.9	21.8	31.4	30.2	30.4	30.1	27.9	30.2	29.1
NO OBS	416	429	429	406	429	430	425	417	1693	1682	3375

APPENDIX C

WEATHER PATTERNS AT HANNOVER, FEDERAL REPUBLIC OF GERMANY, IN 1970

Based on a report* by

K.C. Leonard, Jr., L.G. Sowell, and D.A. Waller

Defense and Electronic Systems Center
Westinghouse Electric Corporation

CONTENTS

A.	Introduction	C-3
B.	Selection of Station	C-3
C.	Observations Extracted	C-5
D.	Incidence of Low Clouds	C-7
E.	Incidence of Low Visibility	C-12
F.	Incidence of High Dew Point	C-19
G.	Incidence of Total Cloud Cover	C-19
	Reference	C-22

*The Impact of Weather on the Performance of Electrooptical Sensors in Europe, AFAL Contract F-33615-70C-1461, 24 November 1972.

A. INTRODUCTION

Classically, the weather scenarios for operations research simulations are taken from climatic data. It is argued that climatic means present a picture of the weather which is close to the expected value for each parameter. In practice, of course, each parameter exceeds the expected value for half the time and falls below it for the other half. In evaluating the performance of electrooptical viewing systems, including both television and infrared, total viewing system performance is determined by a very complex combination of environmental parameters. Precisely those times when the critical parameters depart farthest from their means are of the most interest. It is usually said, for example, that poor visibility has more adverse effects on television than on infrared, while high dew point and nighttime cloudiness affect infrared far more than television. Actually, both factors affect both sensors. Combinations of these conditions affect the operation of installations which contain both sensors. Consequently, we have obtained and used in this analysis actual weather data taken at hourly intervals for a full year. The duration or persistence of each weather type, as well as its frequency of occurrence, has been determined for the year examined. In summary, we believe we have a fairly complete picture of the weather conditions throughout the year that would influence sensor performance.

B. SELECTION OF STATION

The primary interest of this weather analysis has been to approximate those conditions which would be encountered in

PRECEDING PAGE BLANK-NOT FILMED

Central Europe in a low-altitude defense against an attack from Eastern Europe. To represent daily weather conditions throughout the year, it was decided that hourly observations would be very desirable, permitting continuous assessment of the prevailing weather. The observation frequency of airport stations was found to meet or exceed this requirement. With the help of Central European aircraft navigation charts, which conveniently show local topography, several candidate weather stations were considered. Eastern (Communist bloc) stations were found to have unreliably complete observations, so West German stations were given the most attention. Berlin was considered very carefully but was finally rejected because the weather observed at the metropolitan location of the airport might not accurately represent the weather of the surrounding countryside. Another coastal plain station, Hannover, was ultimately selected. It is comparable to Berlin in its proximity to the ocean on the north and to the penetration corridors on the east, and the Hannover airport is outside the immediate metropolitan area.

The USAF Environmental Technical Applications Center (ETAC) weather analysis facility in Washington, D.C., was found to have on hand several years of complete aviation routine weather reports (METAR) and synoptic weather observations for Hannover. On the advice of the Air Force personnel, 1970 data were taken because they were known to be very complete. Hourly data were available with two exceptions where the report interval stretched to two hours. For the bulk of the year, there were 20- or 30-minute intervals between METAR reports. Three-hourly synoptic observations were very complete and timely throughout; three or four were missing, but the intervening METAR reports allowed complete continuity to be maintained.

C. OBSERVATIONS EXTRACTED

Data were taken at hourly intervals for each month of the year. The parameters extracted for analysis were:

- Dew point
- Temperature
- Visibility
- Cloud cover in 8ths
- Wind direction
- Wind speed.

In addition, ground-level illumination was estimated from the reported cloud and precipitation data. We have chosen to define a Lumb factor, which was recorded for each hour. This factor was assigned values on the basis of Table C-1, after F.E. Lumb (Ref. 1). The Lumb factor is the ratio of the illumination that reaches the earth's surface through the cloud conditions indicated to that which would reach the surface from a cloud-free sky.

TABLE C-1. LUMB FACTORS FOR VARIOUS KINDS OF CLOUDS

Cloud Type	Lumb Factor
Cumulus, Altocumulus, Cirrus	0.90
Cirrostratus	0.76
Stratocumulus	0.55
Altostratus and other midlevel, layered clouds	0.35
Nimbus, Nimbostratus	0.20

This made a total of seven hourly parameters of 168 daily observations. For 1970, then, 61,320 data points were taken as a data base for the calculations shown later. Atmospheric pressure in millibars was also taken from the 3-hour-interval synoptic observations, which made 64,240 points in all. The following trends can be noted at this time.

January:	• Visibility very poor much of the time. • Good visibility mostly in daylight.
February:	• Visibility much improved over January. • Good, clear weather most likely in afternoon. • Poor conditions in early morning hours.
March:	• Further improvement in visibility. • Poor visibility near sunrise. • Best visibility in mid-afternoon.
April:	• Little bad weather. • Best visibility in evening. • Poorest visibility before and near sunrise.
May:	• Visibility in daylight generally good. • Poor visibility mostly at sunrise.
June:	• Excellent visibility for long periods in daylight. • The only bad weather (fog) at sunrise. • Best visibility in morning. • High dew point most likely shortly after sunrise.
July:	• Best visibility likely in afternoon. • Poorest visibility during darkness. • Severest dew point in morning.
August:	• Best visibility in late afternoon, early evening. • Poorest visibility at night, particularly near sunrise. • Dew point bad in morning.
September:	• Visibility still good in late afternoon. • Visibility most likely to be poor in darkness. • Dew point worst in late morning.
October:	• Much bad weather. • Visibility best in afternoon.

November:
- Visibility slightly better at midday.
- Visibility somewhat poor at night.

December:
- Good visibility most likely in afternoon.
- Poor visibility at night.
- Worst visibility late in month.

D. INCIDENCE OF LOW CLOUDS

From the standpoint of electrooptical sensors, whether television or infrared, low clouds are likely to preclude operations if they impinge on the aircraft-to-target line of sight. While poor visibility restricts the use of television and high dew point restricts the use of infrared, clouds will restrict the use of both. We have therefore extracted all data on the incidence of 4/8 cloud cover or more from the raw observations for the 1000-ft, 500-ft, and 200-ft levels. Table C-2 presents these data for each month summarized by 3-hour periods. Shown at the bottom of each month is the summary by time of day for that month. (In addition, the incidence of high dew points in summer is noted and summarized on the same charts.)

A few tentative conclusions can be drawn from these cloud data which will affect air-to-ground operations significantly.

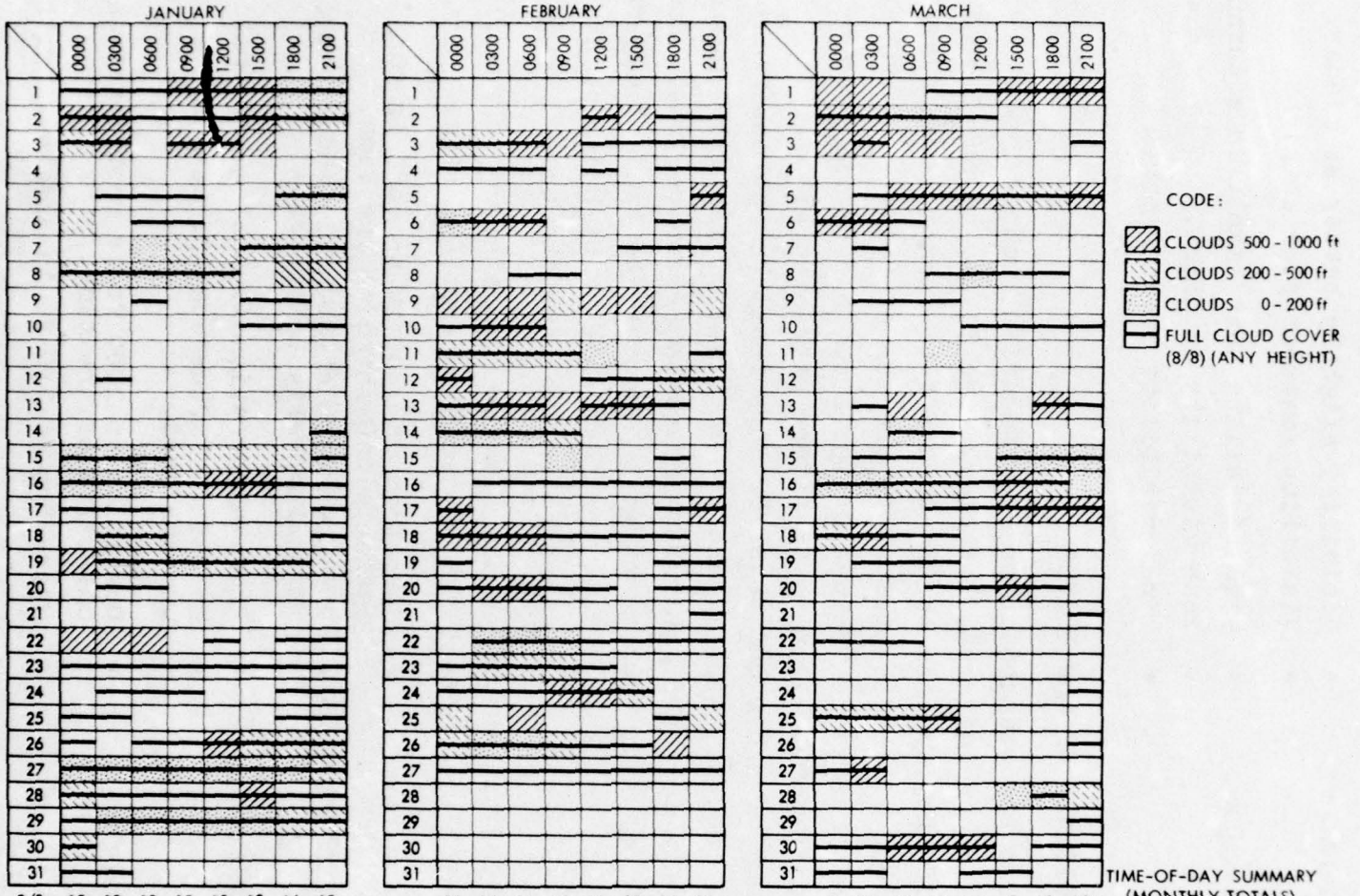
January:
- Operation at 1000 ft or more is not possible one-third of the time.
- For operation at 200 ft, conditions are least favorable before dawn.

February:
- Predawn operation is most questionable.
- At 200 ft, afternoon operations are unrestricted.

March:
- Operation at 1000 ft is restricted only one-fifth of the time.
- Operation at 200 ft is slightly restricted.

April:
- Midnight to dawn is the only bad time of day for operations.
- Afternoons and evenings are satisfactory for operations at lower altitudes.

TABLE C-2. OCCURRENCE OF LOW CLOUDS, FULL CLOUD COVER, AND HIGH DEW POINT AT HANNOVER, GERMANY, 1970



TIME-OF-DAY SUMMARY (MONTHLY TOTALS)

	JANUARY								
	0000	0300	0600	0900	1200	1500	1800	2100	
8/8	15	18	18	15	13	13	16	18	
<1000	11	10	9	9	10	11	10	11	CLOUDS
< 500	8	7	8	7	6	6	9	10	
< 200	3	5	6	4	2	2	2	4	

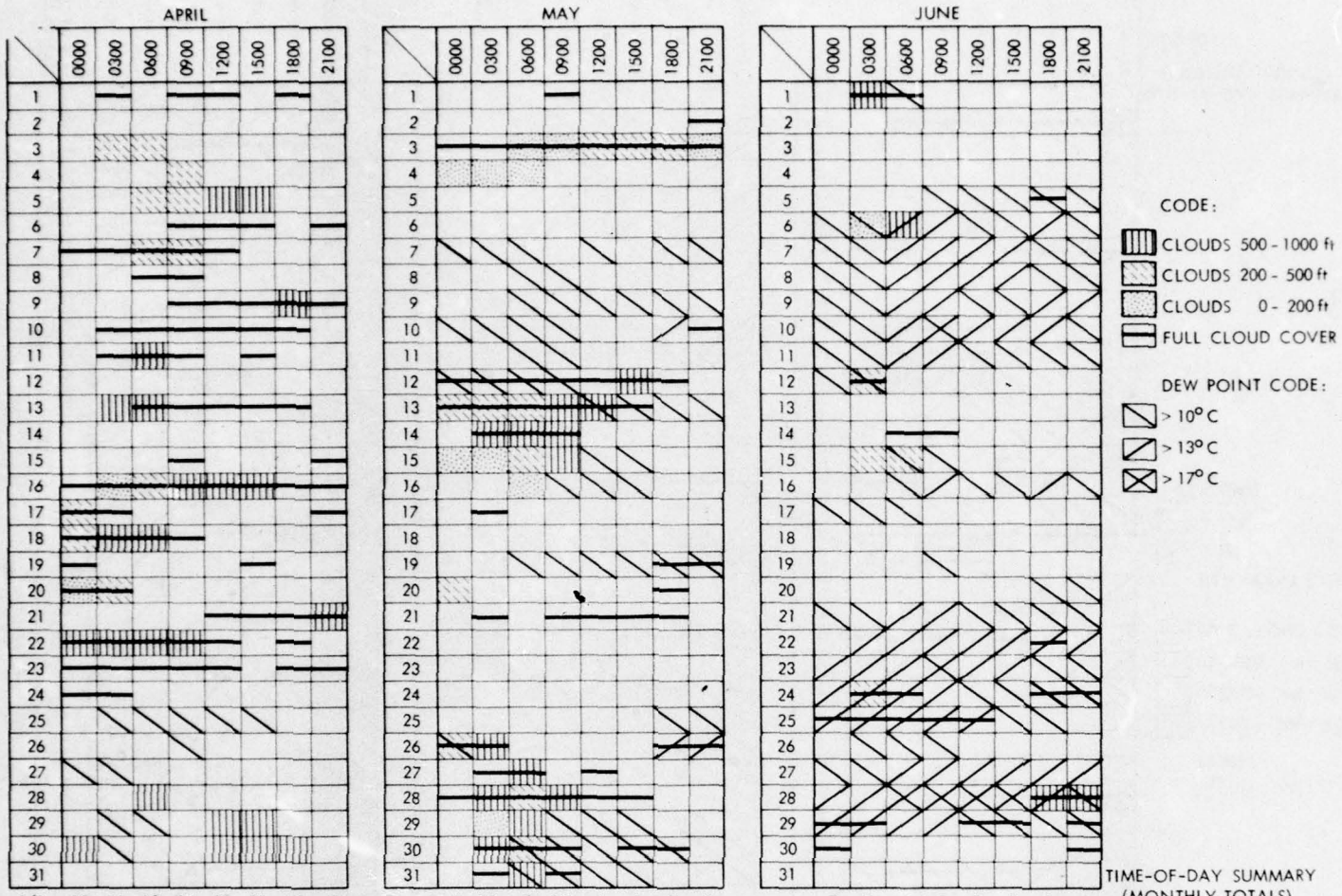
	FEBRUARY								
	0000	0300	0600	0900	1200	1500	1800	2100	
	15	14	16	12	13	10	16	15	
	11	12	13	10	5	4	2	5	CLOUDS
	7	6	5	7	1	1	1	3	
	2	3	3	2	1	0	0	0	

	MARCH								
	0000	0300	0600	0900	1200	1500	1800	2100	
	9	16	13	13	10	8	10	12	
	7	8	8	7	3	7	7	6	CLOUDS
	3	2	4	3	1	3	4	3	
	1	1	2	2	1	2	2	2	

(Continued)

6-19-74-13

TABLE C-2. OCCURRENCE OF LOW CLOUDS, FULL CLOUD COVER, AND HIGH DEW POINT AT HANNOVER, GERMANY, 1970 (cont'd.)



TIME-OF-DAY SUMMARY (MONTHLY TOTALS)

	APRIL							
8/8	10	16	13	16	12	10	8	7
< 1000	5	6	9	5	3	4	2	1
< 500	3	3	4	3	0	0	0	0
< 200	1	1	0	0	0	0	0	0
> 10° C	4	3	9	10	9	8	6	5
> 13° C	0	0	0	0	0	1	2	1

	MAY							
8/8	8	13	8	10	6	6	7	5
< 1000	5	8	11	5	2	2	1	1
< 500	5	4	7	1	1	1	1	1
< 200	2	3	3	1	0	0	0	1
> 10° C	4	3	9	10	9	8	6	5
> 13° C	0	0	0	0	0	1	2	1

	JUNE							
8/8	3	5	4	2	2	1	4	4
< 1000	0	5	2	0	0	0	1	1
< 500	0	4	1	0	0	0	0	0
< 200	0	1	0	0	0	0	0	0
> 10° C	10	11	4	4	8	9	10	13
> 13° C	5	5	12	12	7	6	7	3

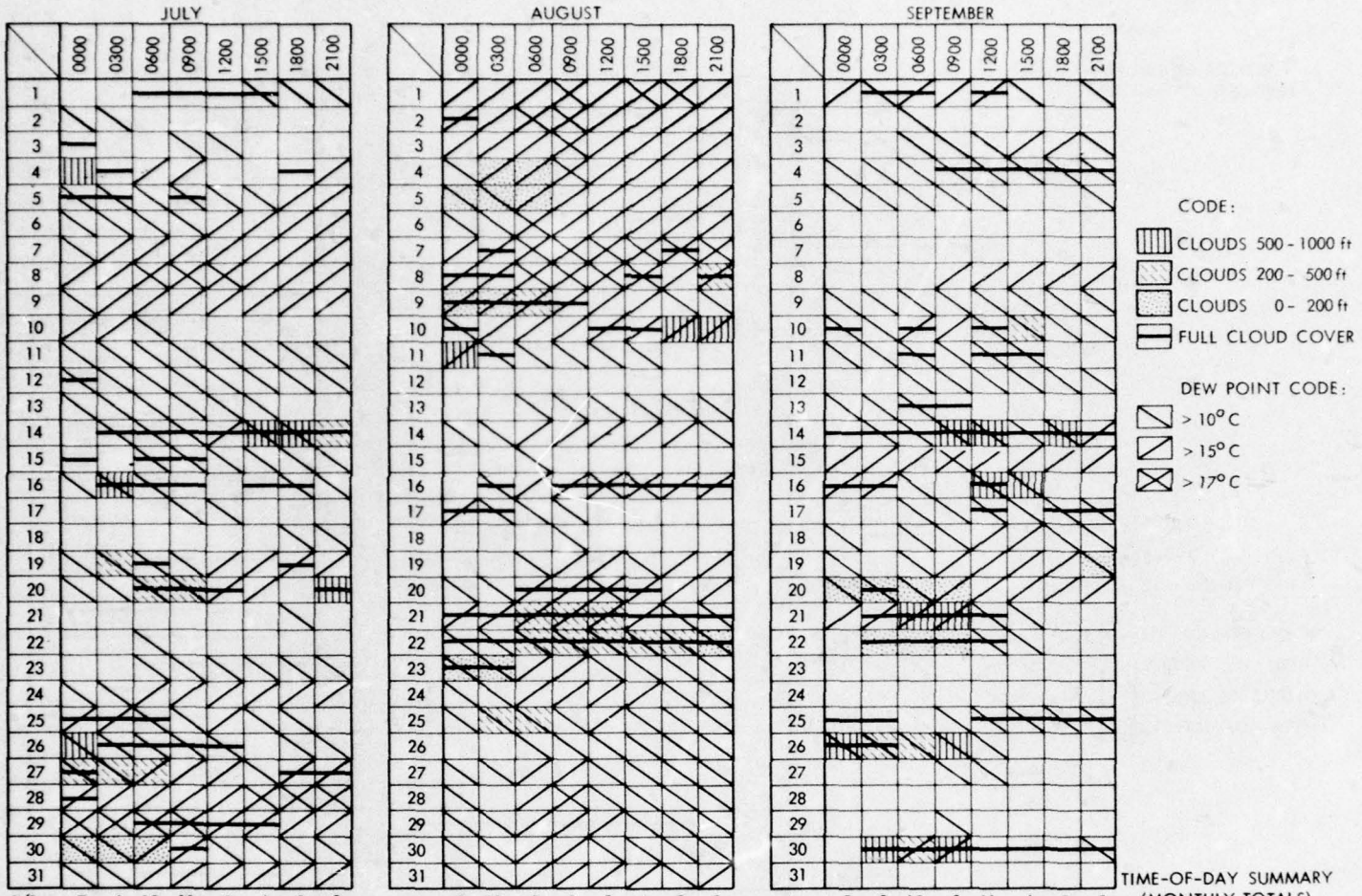
CLOUDS

DEWPOINT

6-19-74-14

(Continued)

TABLE C-2. OCCURRENCE OF LOW CLOUDS, FULL CLOUD COVER, AND HIGH DEW POINT AT HANNOVER, GERMANY, 1970 (cont'd.)



	JULY							
	0000	0300	0600	0900	1200	1500	1800	2100
8/8	7	6	10	11	5	4	5	3
<1000	4	4	3	1	0	1	1	2
< 500	2	3	3	1	0	0	0	1
<200	1	1	1	0	0	0	0	0
> 10°C	16	15	16	15	8	11	12	9
> 15°C	4	6	7	7	11	9	10	11
> 17°C	1	1	0	0	1	1	1	1

	AUGUST							
	0000	0300	0600	0900	1200	1500	1800	2100
	8	10	5	5	5	6	5	5
	4	5	6	2	2	1	2	2
	3	5	6	2	2	1	1	2
	3	4	2	0	0	0	0	1
	15	15	8	7	8	12	13	13
	9	9	17	15	14	11	11	12
	0	0	4	7	4	4	2	1

	SEPTEMBER							
	0000	0300	0600	0900	1200	1500	1800	2100
	5	8	10	8	11	6	5	5
	2	4	5	6	2	2	1	1
	1	3	4	2	0	1	0	1
	1	2	2	2	0	0	0	1
	10	10	13	13	15	12	8	11
	4	3	4	6	7	6	5	4
	0	0	0	0	0	0	0	0

TIME-OF-DAY SUMMARY (MONTHLY TOTALS)

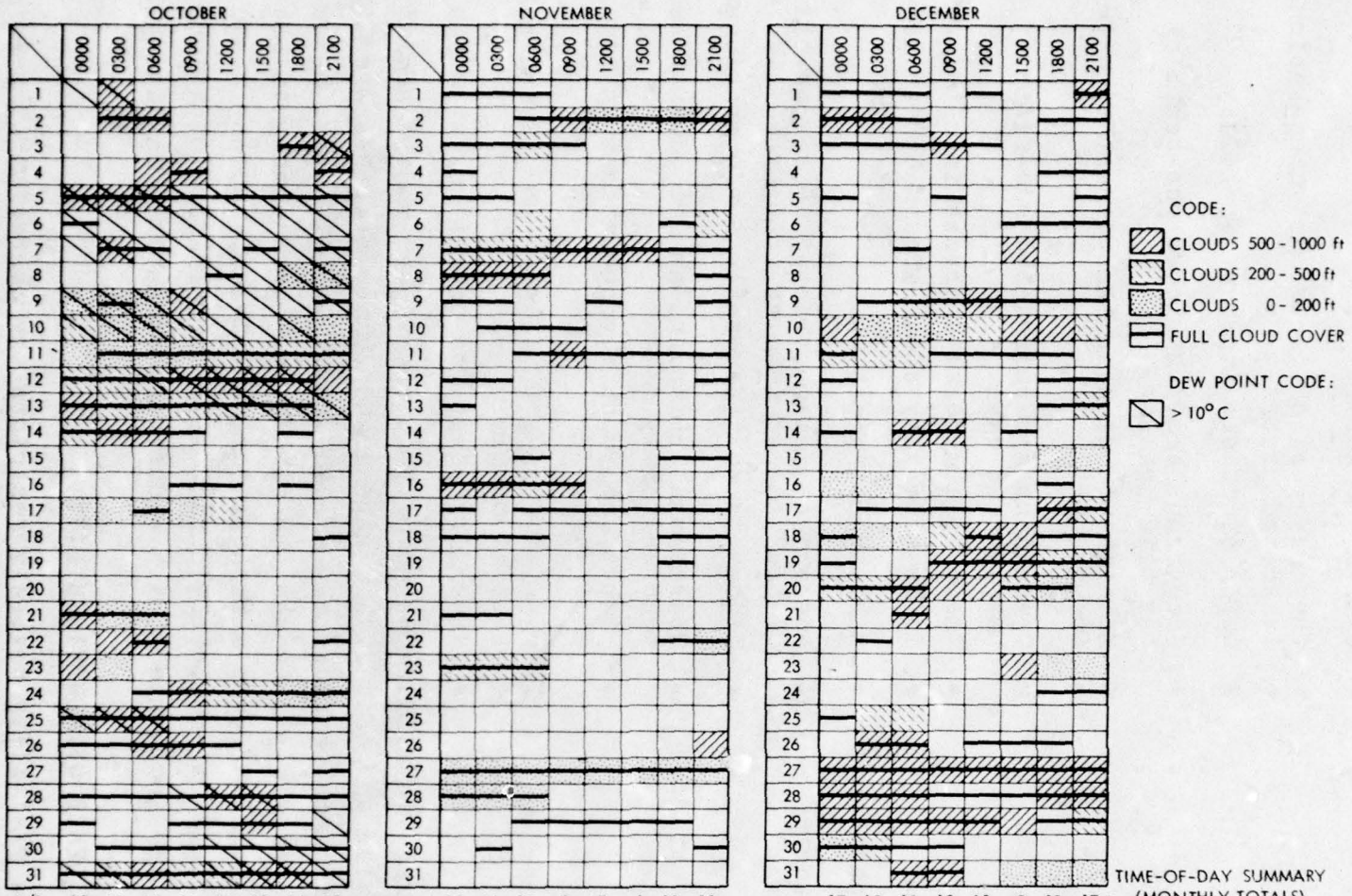
CLOUDS

DEWPOINT

(Continued)

6-19-74-15

TABLE C-2. OCCURRENCE OF LOW CLOUDS, FULL CLOUD COVER, AND HIGH DEW POINT AT HANNOVER, GERMANY, 1970 (cont'd.)



6-19-74-16

May:
- Similar to April.

June:
- The only period of restricted operations is around daybreak.
- Lower altitudes improve capability.

July:
- Operations are restricted one-tenth of the time or less.
- Midnight to dawn is the poorest time for operations.

August:
- Operations are restricted one-fifth of the time at dawn.
- There is a general increase in clouds.
- It is generally clear afternoons at 200 ft.

September:
- Similar to August.

October:
- Operations are restricted up to one-third of the time at dawn at 1000 ft.
- Midday is most favorable for operations.

November:
- Operational restrictions are distributed more uniformly.
- Nights are worst for operations at high altitudes.

December:
- Fairly uniformly bad for operations, but best at midday.
- Generally worst for operations at night.

In general, it will be observed that the winter months are most restrictive and that during spring and summer problems are likely to occur almost exclusively around dawn. In all cases, lower altitude markedly improves the situation, particularly in the afternoon. At 200-ft altitude, for example, operations would have been restricted completely during 1970 on only five occasions. Data on the incidence of low clouds are summarized in Fig. C-1.

E. INCIDENCE OF LOW VISIBILITY

Low visibility severely restricts the operation of passive television and strongly degrades active television. Its effects

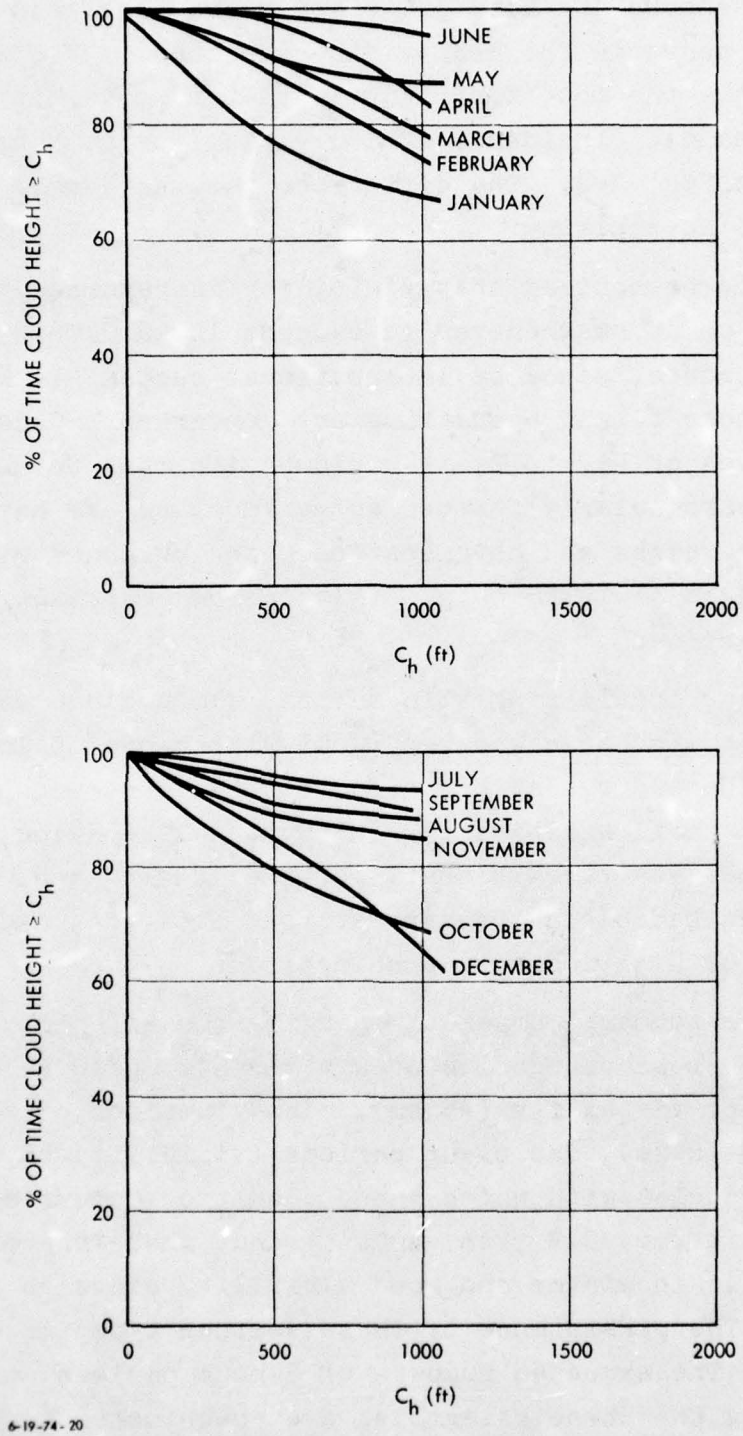


FIGURE C-1. Incidence of Low Clouds

on infrared sensors are also quite severe but are less than its effects on sensors in the near-visible spectrum. Visibility and light level are the most important parameters governing television performance. Incidence of low visibility at Hannover is summarized in Fig. C-2. The difference between summer and winter months is striking.

It should be noticed that visibility is reported in our calculations as 10 km whenever it exceeds 10 km. This is our standard procedure, since by international custom >10 km is shown as ∞ where flight operations are concerned. Clearly, from the curves of Fig. C-2, it would be improper to use 10 km as maximum, particularly for the summer months. We have, however, truncated our values and have assigned, for purposes of simulation, the values of 10 km only. *This introduces an unfavorable bias in summertime.*

It is also interesting to note that the periods of low visibility tend to correlate very well with those of low cloud incidence. These correlations are presented on a monthly basis in Fig. C-3. April exhibits the only unusual behavior, but examination of the data reveals that, for the 200-ft case, only two 3-hour periods had clouds present at that altitude, and both were associated with moderate precipitation.

Also, for summary purposes regarding the effects of visibility, three broad categories of weather have been selected: periods of poor visibility (<5 km), cloudy periods of moderate visibility (5-10 km), and clear periods (visibility >5 km). The monthly frequencies with which these conditions occurred in 1970 are depicted in Fig. C-4. An annual trend, wherein poor visibility prevails in winter and good visibility prevails in summer, is evident. The persistence of these weather types is examined in Fig. C-5. The expected numbers of 3-hour periods consecutively represented by the three categories are shown month by month. Full days of bad weather prevail in January, and full days of good weather prevail in June. Looking at the data, we find:

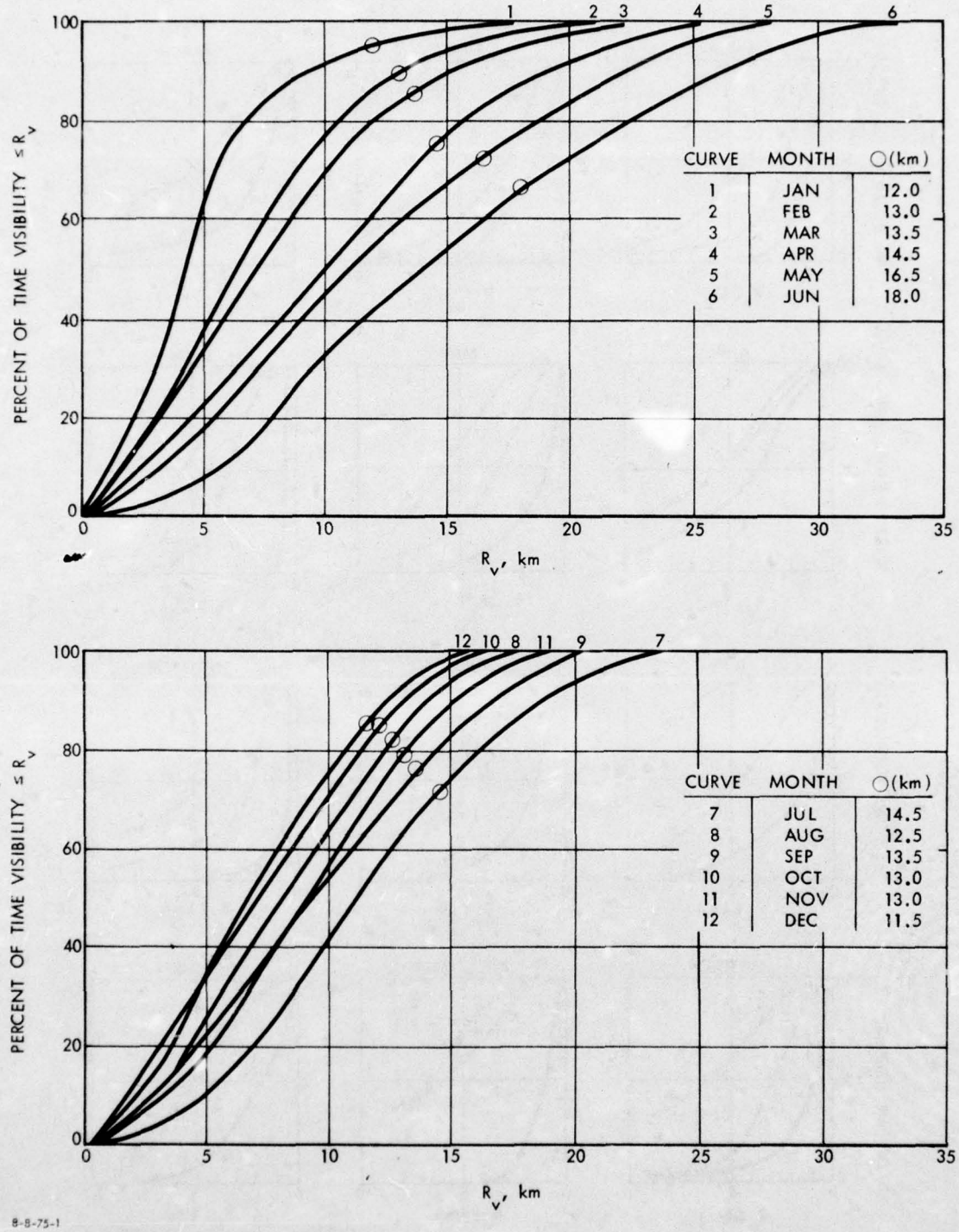


FIGURE C-2. Incidence of Restricted Visibility. Circles represent estimates of mean visibility when data indicate it is more than 10 km.

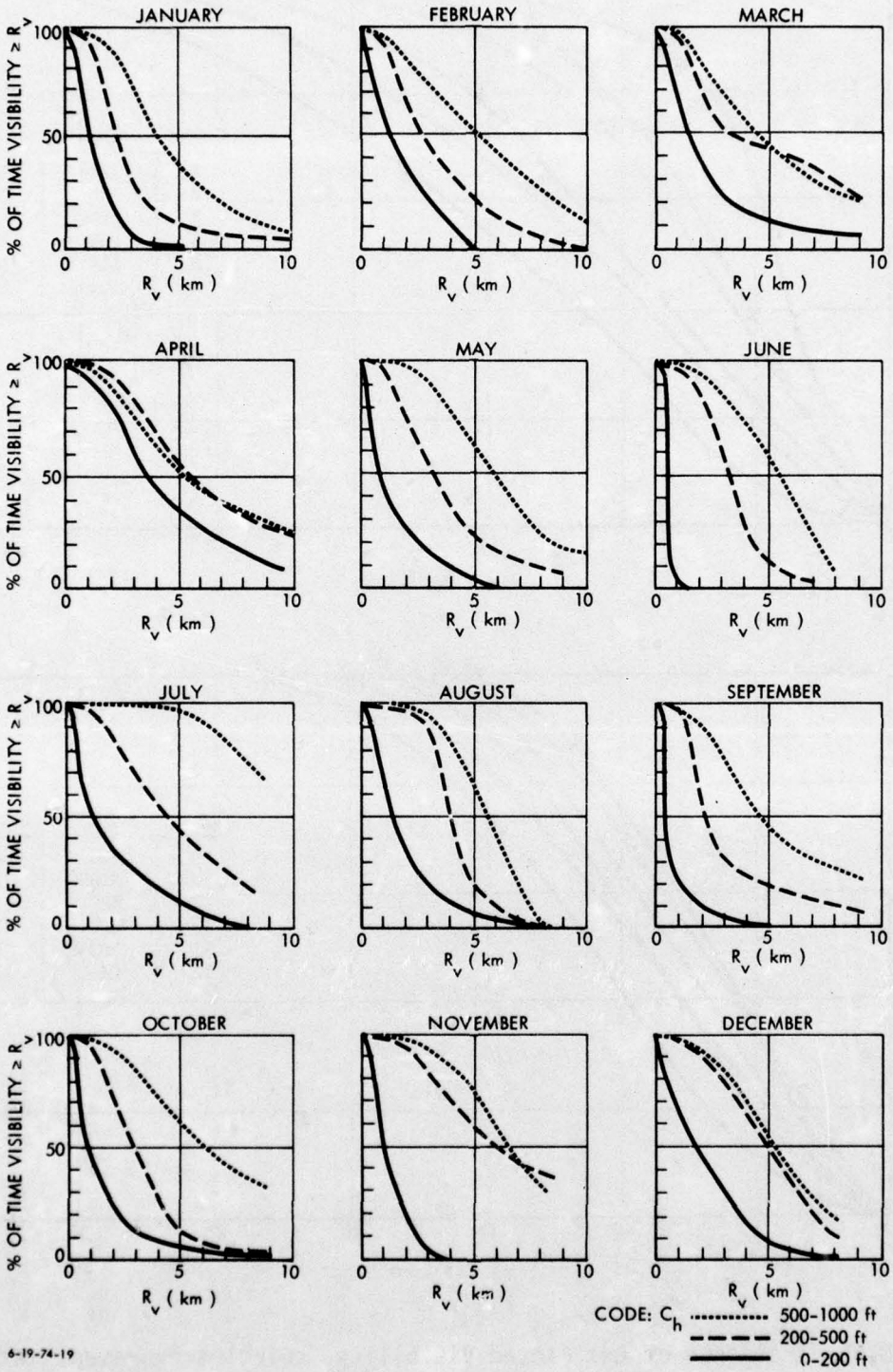


FIGURE C-3. Visibility as a Function of Cloud Height.

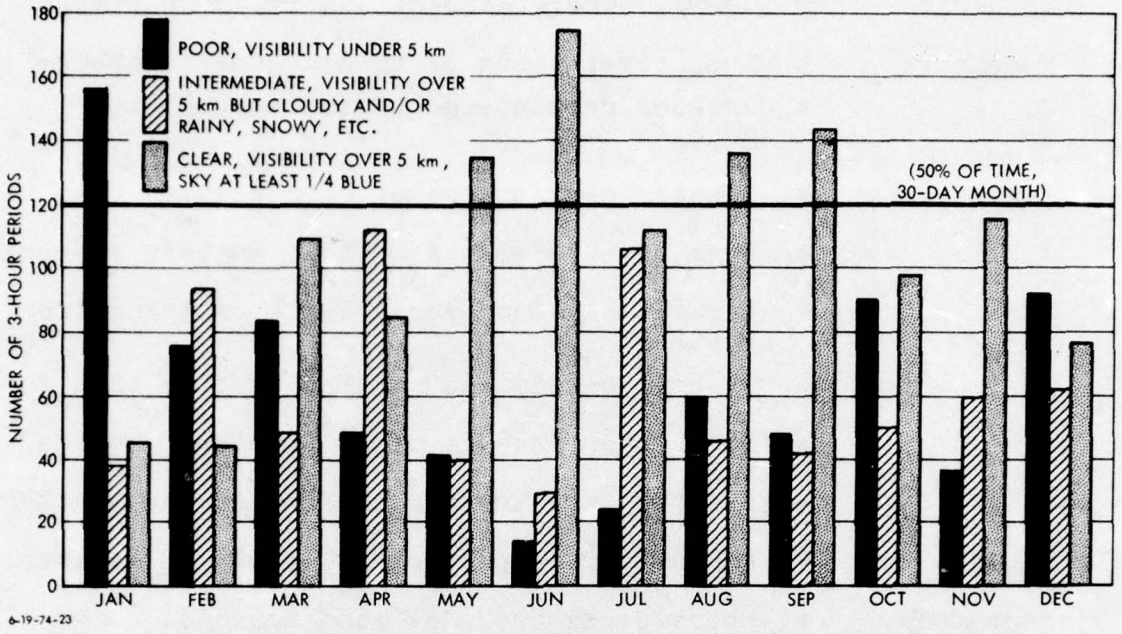


FIGURE C-4. Frequency of Weather Conditions.

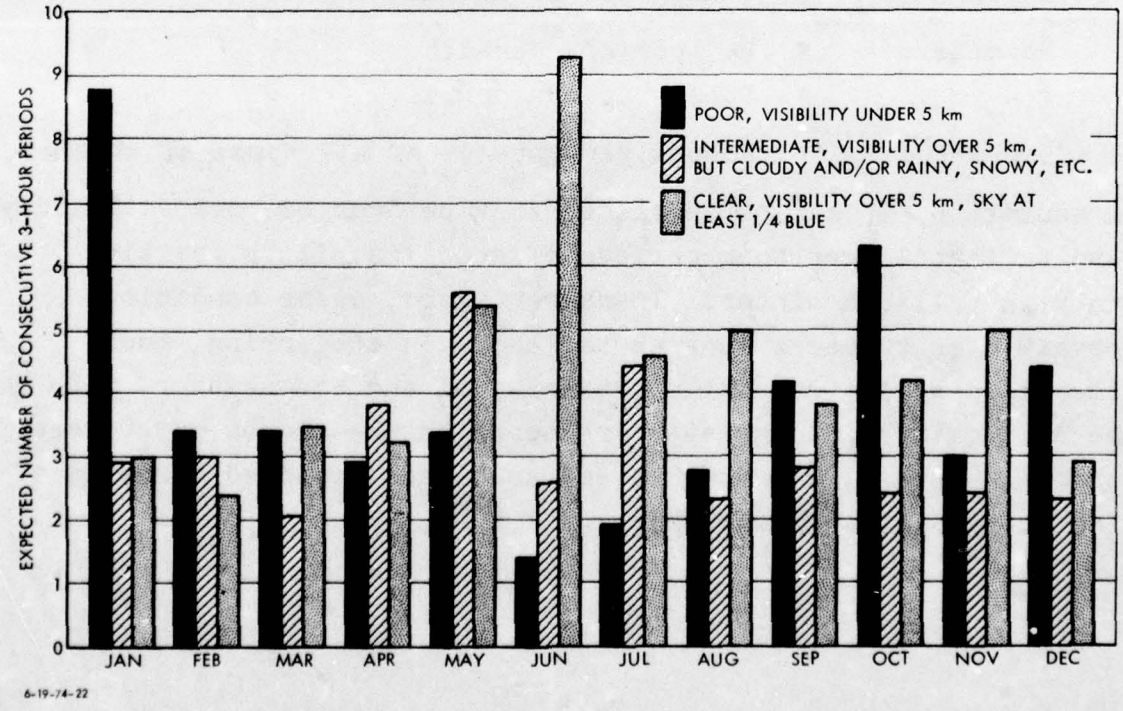


FIGURE C-5. Expected Duration of Prevailing Weather Conditions.

January:	• Normal persistence of all types of weather.
February:	• Less persistence of transitional weather. • Greater persistence of bad weather than good.
March:	• Greater persistence of good weather than bad.
April:	• Greater persistence of good weather than bad.
May:	• Anomalously long persistence of transitional weather. • Greater persistence of bad weather than good.
June:	• Normal persistence of all types of weather.
July:	• Slightly greater persistence of bad weather.
August:	• Normal persistence of all types of weather.
September:	• Short persistence of good periods. • Long persistence of bad periods.
October:	• Bad periods persist. • Other periods normal.
November:	• Bad periods persist. • Other periods normal.
December:	• Normal persistence of all types of weather.

In summation, it can be concluded that periods of poor visibility tend to last longer than periods of good visibility, particularly in fall and winter. In summer, good, clear conditions prevail over twice as long as the bad. In the spring, much time is spent in transition between good and bad weather, with the good gaining the greater frequency as the season progresses. Across the board, 8-9 hours seems to be the expected duration of a weather type as defined here.

F. INCIDENCE OF HIGH DEW POINT

In evaluating the operation of infrared (IR) sensors, the most frequent severe detriment to range performance is the occurrence of high dew points. While very high readings do not occur in the European area, we have nonetheless chosen to analyze the elevated water vapor levels that do occur during the summer months and significantly affect IR sensor performance.

Three categories of elevated dew point were logged: >10°C, >13°C, and >17°C. The frequency of these conditions is summarized for the warm months in Fig. C-6. August, where moderate degradation is present nearly half the time, is clearly the worst month, while in June and July moderate degradation occurs 25 percent of the time, and slight degradation occurs about 25 percent of the time also.

The persistence of these conditions is examined in Fig. C-7. It is apparent that, once present, elevated dew points tend to last. In midsummer some degradation can be expected for two or more days running, becoming moderate for 12-hour periods, usually peaking just after sunrise. In the data for Hannover, severe degradation occurred rarely; in July, however, when it was present, its expected persistence was 15 hours.

G. INCIDENCE OF TOTAL CLOUD COVER

Infrared sensor performance is adversely affected during cloudy nighttime hours. Essentially, cloud temperature is rather close to target temperature, particularly when clouds are low, and complete cloud cover causes thermal equilibrium to be reached between cloud and ground. Consequently, image contrast tends to vanish and the display shows only heat sources. We have, therefore, extracted data on the incidence of total cloud cover from the raw data for the year in Table C-2. Figure C-8 presents the monthly summaries of these data taken by time of day. Also included are approximate sunrise and sunset times for the 15th of each month.

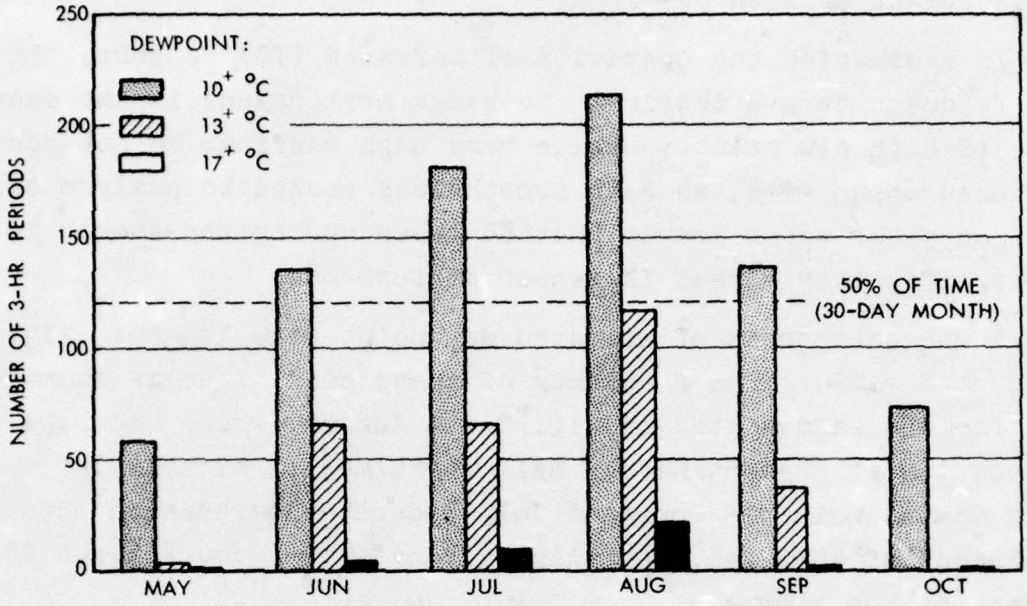


FIGURE C-6. Frequency of High Dew Points.

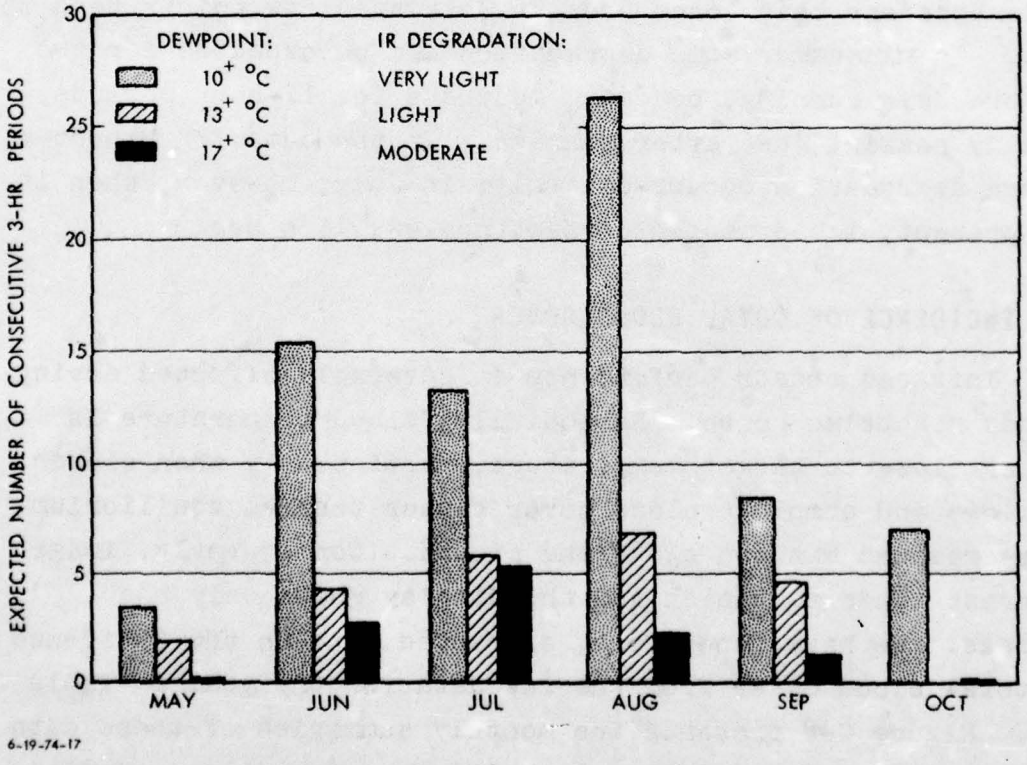


FIGURE C-7. Expected Persistence of High Dew Points.

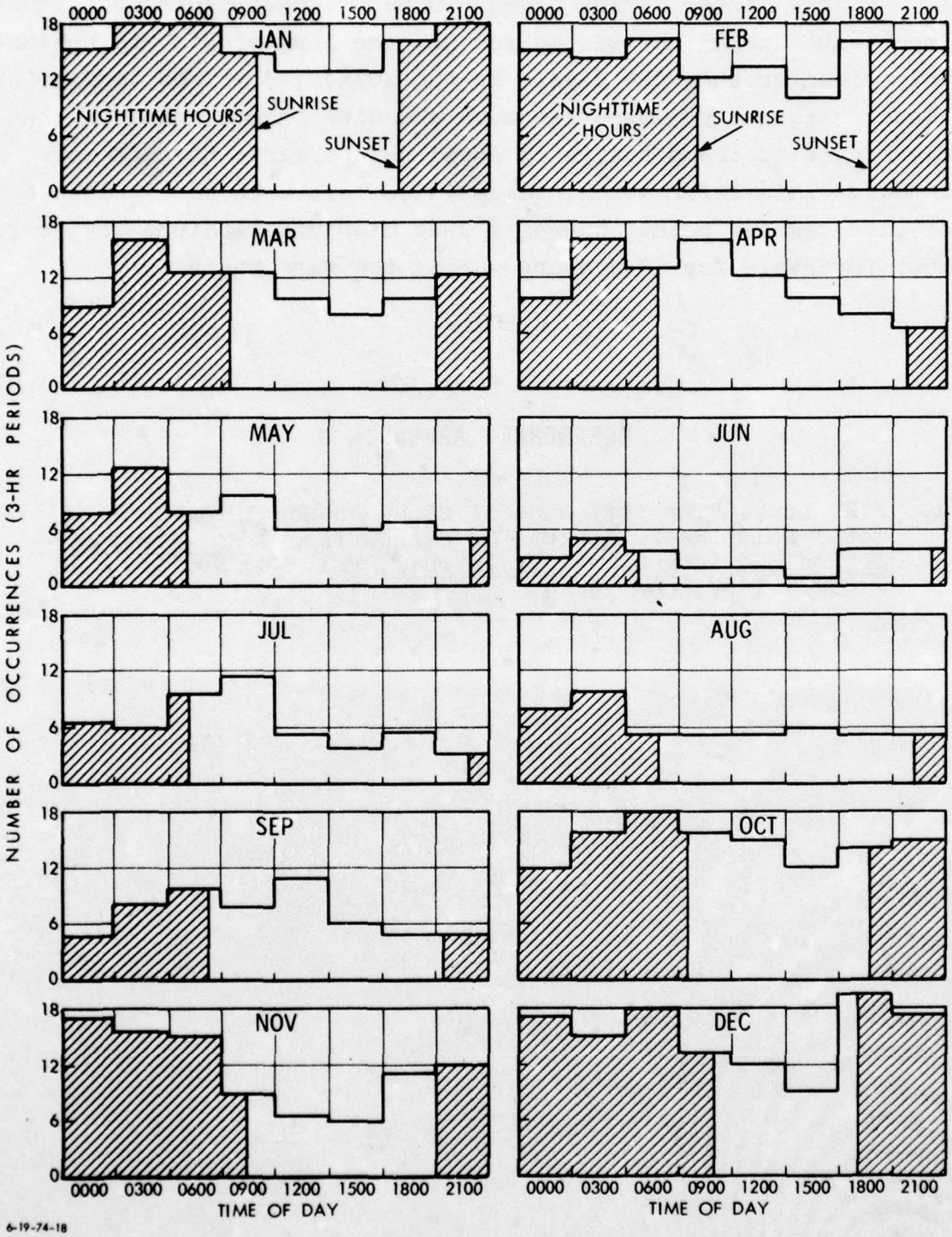


FIGURE C-8. Incidence of Total Cloud Cover.

Review of the figure reveals some interesting trends. Most important, during the winter months, the long nights are noticeably cloudier than the days. In the summer, daytimes tend toward cloudiness, but predawns are much cloudier than evenings. The clear evening trend starts in April and persists through September. This information, taken in concert with the incidence of elevated dew point, suggests that midnight missions may be most favorable for IR sensors during the warm months.

REFERENCE, APPENDIX C

1. F.E. Lumb, "The Influence of Cloud on Hourly Amounts of Total Solar Radiation at the Sea Surface," Royal Meteorological Society Quarterly Journal, Vol. 90, No. 383, January 1964, pp. 43-56.

APPENDIX D

FIRST-ORDER CORRECTIONS TO BAR-PATTERN DATA

Frederick A. Rosell and Robert H. Willson
Defense and Electronic Systems Center
Westinghouse Electric Corporation

APPENDIX D

FIRST-ORDER CORRECTIONS TO BAR-PATTERN DATA

It is important to understand the means and the rationale for using minimum resolvable temperature (MRT) data to establish the probability of detecting, recognizing, or identifying actual objects rather than standard four-bar MRT test patterns (Fig. D-1).



FIGURE D-1. Standard Four-Bar MRT Test Pattern

The relationship between the video signal-to-noise ratio and the detectability of bar patterns was investigated and reported by Coltman and Anderson in 1960 (Ref. 1). Reviewing their report has some historical merit and lends credence to the current approach espoused here. In addition, the Coltman and Anderson experiment is often cited to prove that the eye uses up to 14 lines in the process of detecting a bar pattern. This result is believed to be an error in interpretation, as will be discussed below. Coltman and Anderson derived the equation below through a thought experiment combined with a psychophysical experiment to obtain a necessary constant. The

PRECEDING PAGE BLANK-NOT FILMED

equation is

$$N_W = 615 \sqrt{\Delta f_v'}\, SNR_{vr}, \qquad \text{(D-1)}$$

where N_W is the bar-pattern spatial frequency in line pairs per picture width, $\Delta f_v'$ is the video bandwidth in megahertz, and SNR_{vr} is the threshold RMS video signal-to-noise ratio. On the basis of Eqs. 1-13 in Ref. 2, we can write

$$N = \left(\frac{t\varepsilon\Delta f_v}{\alpha}\right)^{\frac{1}{2}} \frac{SNR_{VO}}{SNR_{DT}}, \qquad \text{(D-2)}$$

where N is the number of bars, t is the integration time, ε is the aspect ratio of bars, α is the aspect ratio of picture format, SNR_{VO} is the video signal-to-noise ratio at zero spatial frequency, and SNR_{DT} is the threshold value of SNR_D. The purpose of the following analysis is to determine whether the above equation matches Eq. D-1 as experimentally derived by Coltman and Anderson. As a start, note that

$$\begin{aligned} \Delta f_v &= \Delta f_v' \cdot 10^6 \\ SNR_{VO} &= \sqrt{8}\, SNR_{vr} \qquad \text{(D-3)} \\ N_W &= \frac{\alpha N}{2}, \end{aligned}$$

since Coltman and Anderson's bandwidth is in megahertz rather than hertz, video SNR is in RMS signal rather than peak to peak, and spatial frequency is in line pairs per picture width rather than lines per picture height. With the above changes, Eq. D-2

becomes

$$N_W = \frac{1}{2}\left[8 \cdot 10^6 \alpha t \varepsilon \Delta f_v'\right]^{\frac{1}{2}} \frac{SNR_{vr}}{SNR_{DT}} . \qquad (D-4)$$

With $\alpha = 4/3$, $t = 0.1$ sec, $\varepsilon = 14$ and $SNR_{DT} = 3$, we have

$$N_W = 644 \sqrt{\Delta f_v'}\ SNR_{vr} , \qquad (D-5)$$

which is only 5% different from Coltman and Anderson's experimentally derived value. The length-to-width ratio of 14 used is an approximation, since the actual value used is unknown. It is not critical, however, as can be inferred from the discussion below.

Coltman and Anderson did not take the bar aspect ratio into account but stipulated only that bar length should be large relative to bar width.

To show the impact of reducing the number of bars available to the observer, Coltman and Anderson devised the experiment shown in Fig. D-2. The displayed pattern "was left fixed and a series of cardboard apertures were employed to vary the number of lines seen by the observer." The mask was presumably of square aspect ratio. The results, as shown in Fig. D-2, "show that the observer probably uses no more than seven line pairs in making an identification. As the number which he is permitted to see is decreased, the signal required rises rapidly, being greater by a factor of four when only one line pair is presented."

. 182 INSTITUTE FOR DEFENSE ANALYSES ARLINGTON VA SCIENCE A--ETC F/G 17/8
EFFECT OF WEATHER AT HANNOVER, FEDERAL REPUBLIC OF GERMANY, ON --ETC(U)
AUG 76 L M BIBERMAN

UNCLASSIFIED P-1123 IDA/HQ-76-18660 NL

3 OF 3
AD A032182



END
DATE FILMED
1-77

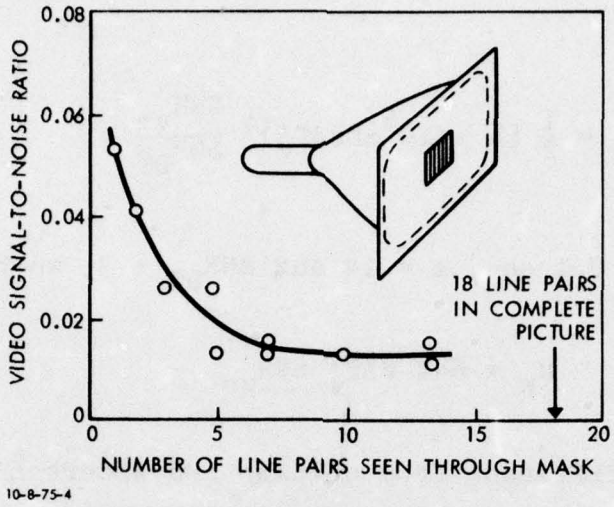


FIGURE D-2. Video SNR Required to Detect Pattern as Function of Number of Line Pairs Visible Through Mask. (Adapted from Ref. 1)

We have shown that the eye apparently does integrate over the entire bar length, at least for bar patterns whose angular extent in length is not too large. Thus, we believe that the interpretation made by Coltman and Anderson was incorrect. We feel that the main effect was not one of reducing the number of bars, but was really one of reducing the bar length or the aspect ratio. If this latter interpretation were correct, the SNR_{vr} should decrease with increase in bar length as

$$SNR_{vr} = \frac{N_W}{615\sqrt{\Delta f_v' \cdot \varepsilon/14}} . \qquad (D\text{-}6)$$

With a mask of square aspect ratio, ε = 2 times the number of line pairs seen through the mask. The $\varepsilon/14$ term under the radical in the above equation results from an assumption that the SNR_{vr} thresholds were measured with bars of 14:1 aspect ratio. Using Eq. D-6, we plot the threshold SNR_{vr} in Fig. D-3. Also shown in this figure are the experimentally measured data points from Fig. D-2. It appears clear that the hypothesis of

a change in aspect ratio is a valid interpretation of the measured results rather than the number of lines that are visible through the mask. It is further observed that the mask used by Coltman and Anderson was reduced in size until only a single cycle or one line pair was visible through it. If one assumes that the bar-aspect-ratio hypothesis is correct rather than the bar-number hypothesis, the theoretical fit to the data in Fig. D-3 lends credence to the notion that the eye uses only a single bar in discerning the presence of a bar pattern.

For the past 25 years or more, threshold resolution measurements have been made by various sensor manufacturers and users. The number of bars used in the experiment is not reported, showing a lack of concern for bar number. On the other hand, bar aspect ratio is not reported either. As is evident from Fig. D-3, the variation in bar aspect ratio is not particularly significant if the ratio is above about 10:1, since the dependence is proportional to the square root of bar aspect ratio.

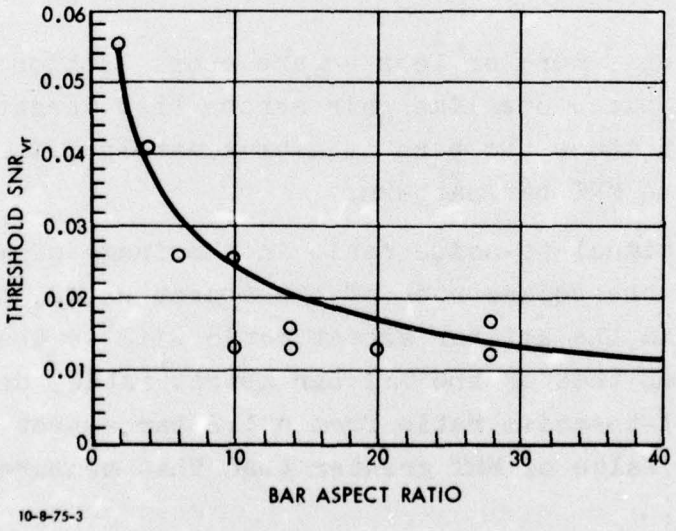


FIGURE D-3. Video SNR Required to Detect Bar Patterns Interpreted as Function of Bar Aspect Ratio.

The point of the above is that Coltman and Anderson reduced the number and length of the bars in their pattern and ascribed the variation in results to the number of bars, ignoring the effect of length. Our work predicts the same results based upon variation in bar length, ignoring the number of bars, and further shows similar results based upon as little as one bar of varying aspect ratio.

The aspect ratio of standard bar patterns is either 5:1 for the USAF standard three-bar test pattern (Fig. D-4) or 7:1 for the standard four-bar MRT test pattern (Fig. D-1).



FIGURE D-4. USAF Standard Three-Bar Test Pattern

If we choose a more or less square cross section of a tank as a target and place one line pair across that target, the aspect of one of those two bars is approximately 2:1, as opposed to the 7:1 of the MRT bar pattern.

Since the signal-to-noise ratio in the image of a bar is proportional to the square root of the aspect ratio, the signal-to-noise ratio in the 2:1 bar aspect ratio will be the square root of 2/7 times that of the 7:1 bar aspect ratio, or about 0.53. Thus, the signal-to-noise ratio from a 1:2 bar aspect ratio would require a value of MRT greater than that measured by the ratio of $1/\sqrt{2/7}$.

Using MRT data, one can correct for any value of aspect ratio ε by correcting the value of MRT at any spatial frequency by the factor $1/\sqrt{\varepsilon/7}$.

Thus, the important quantity in predicting the performance of devices such as FLIRs is the value of

$$\frac{\Delta T}{MRT/\sqrt{\varepsilon/\tau}} .$$

REFERENCES, APPENDIX D

1. J.W. Coltman and A.E. Anderson, "Noise Limitations to Resolving Power in Electronic Imaging," Proc. IRE, Vol. 48, No. 5, 1960, pp. 858-865.

2. F.A. Rosell and R.H. Willson, "Recent Psychophysical Experiments and the Display Signal-to-Noise Ratio Concept," Chapter 5 in L.M. Biberman, ed., Perception of Displayed Information, Plenum Press, New York, 1973, pp. 173-232.

APPENDIX E

CALCULATION OF PROBABILITY OF RECOGNITION OF TANK IN FRONTAL ASPECT, ACTIVE TELEVISION

Frederick A. Rosell

Defense and Electronic Systems Center
Westinghouse Electric Corporation

CONTENTS

A. Range Prediction for Active TV Systems E-5

B. General Equations for Computation of Basic Sensor Parameters E-5

1. General SNR_D Equation for Typical Linear TV Sensor (Periodic Images) E-5
2. Modulation Transfer Function $R_o(N)$, Given Square-Wave Response $R_{SQ}(N)$ E-6
3. Square-Wave Flux Response $R_{sf}(N)$, Given Modulation Transfer Function $R_o(N)$ E-7
4. Noise Filtering Factor $\beta(N)$ for Periodic Images, Given Modulation Transfer Function $R_o(N)$ E-7
5. Noise-Equivalent Aperture N_e, Given Modulation Transfer Function $R_o(N)$ E-7
6. Sensor Gain G E-7

C. System Source Parameters for Active Television E-8

D. Atmospheric Effects on Active TV Scene Irradiance E-9

E. Display Signal-to-Noise Ratio--Photoelectron Noise Limited E-10

F. Examples of Range Prediction for Tank Recognition Using a Simplified Atmospheric Transmission Model E-14

Reference E-32

PRECEDING PAGE BLANK-NOT FILMED

A. RANGE PREDICTION FOR ACTIVE TV SYSTEMS

In general, the equations for active TV systems are quite simple because the sensor is primarily photoelectron noise limited. There are possible complications in estimating the effect of atmosphere intervening between the sensor and the scene. The atmosphere scatters the radiation from the system source (scene irradiation) and may degrade image contrast, depending on the position of the scene object within the sensor range gate.

B. GENERAL EQUATIONS FOR COMPUTATION OF BASIC SENSOR PARAMETERS

The following general equations are used for modeling active and passive TV systems.

1. General SNR_D Equation for Typical Linear TV Sensor (Periodic Images)

$$SNR_D = \left[\frac{t\varepsilon}{\alpha}\right]^{\frac{1}{2}} \frac{R_{sf}(N)}{N} \frac{C_I G\, i_h}{\left[\left(\frac{2 - C_I}{2}\right) G^2 e\beta(N) i_h + I_p{}^2/2\Delta f_v\right]^{\frac{1}{2}}}, \quad \text{(E-1)}$$

where

t = observer's integration time (0.1 sec)

ε = length-to-width ratio of one bar in pattern

α = picture width-to-height ratio (typically 4/3)

$R_{sf}(N)$ = overall sensor square-wave flux response

N = bar-pattern line number (TV lines/picture height)

PRECEDING PAGE BLANK-NOT FILMED

C_I = apparent isolated image contrast ($\Delta L/L_{h\text{-}max}$) at sensor photosurface

G = sensor gain (variable with light level)

i_h = signal current due to scene object or background, whichever is higher (amperes)

e = charge of an electron (1.6×10^{-19} coulomb)

$\beta(N)$ = noise filtering factor for periodic image

I_p = RMS preamplifier noise (amperes)

Δf_v = video bandwidth (hertz)

2. <u>Modulation Transfer Function $R_o(N)$, Given Square-Wave Response $R_{SQ}(N)$</u>

$$R_o(N) = \frac{\pi}{4}\left[R_{SQ}(N) + \frac{R_{SQ}(3N)}{3} - \frac{R_{SQ}(N)}{5} + \frac{R_{SQ}(7N)}{7}\right.$$

$$+ 0 + \frac{R_{SQ}(11N)}{11} - \frac{R_{SQ}(13N)}{13} - \frac{R_{SQ}(15N)}{15} \qquad \text{(E-2)}$$

$$\left. - \frac{R_{SQ}(17N)}{17} + \frac{R_{SQ}(19N)}{19} + \frac{B_k R_{SQ}(kN)}{k}\right],$$

where k takes on odd values 1, 3, 5, etc., and

B_k = 1, 0, or -1, according to

$B_k = (-1)^m \, (-1)^{\frac{k-1}{2}}$ if $n = m$

$= 0$ if $n < m$,

where m is the total number of primes into which k can be factored, and n is the number of different prime factors in k.

3. Square-Wave Flux Response $R_{sf}(N)$, Given Modulation Transfer Function $R_o(N)$

$$R_{sf}(N) = \frac{8}{\pi^2} \sum_{k=1}^{\infty} \frac{R_o(kN)}{k^2} , \qquad \text{(E-3)}$$

where k takes on odd values 1, 3, 5, etc.

4. Noise Filtering Factor $\beta(N)$ for Periodic Images, Given Modulation Transfer Function $R_o(N)$

$$\beta(N) = \frac{\int_0^N R^2(N)dN}{N} \qquad \text{(E-4)}$$

NOTE: Suggested method of numerical integration is

$$\int_{x_1}^{x_p} y dx = \Delta x (y_1 + y_2 + y_3 + \ldots y_{n-1} + \frac{y_n}{2}$$

$$+ (x_p - x_n) \frac{(y_n + y_p)}{2} .$$

5. Noise-Equivalent Aperture N_e, Given Modulation Transfer Function $R_o(N)$

$$N_e = \int_0^{\infty} R_o^2(N)dN \qquad \text{(E-5)}$$

6. Sensor Gain G

Given

- Scene irradiance level E_s (watts/meter^2)

- Lens T/stop
- Maximum signal output current I_{max} (amperes)
- Effective photosurface sensitivity (amperes/watt)
- Effective photsurface area (meters^2)
- Maximum sensor dark current I_{dm} (amperes),

assume that scene reflectivity $\rho = 1.0$.
Find I_{op}:

$$I_{op} = I_{max} - I_{dm} .$$

Then,

$$G = G_{max} \text{ for } I \leq I_{op} \qquad \text{(E-6)}$$

$$= \frac{4T^2 I}{SAE_s} \text{ for } I = I_{op},\ G \leq G_{min} ,$$

when $G = G_{min}$, $E_s = E_{s_{max}}$, and lens T/stop is correspondingly adjusted to keep $E_s = E_{s_{max}}$ with light increase.

Simplifications are possible when the system is either (1) photoelectron noise limited or (2) preamplifier noise limited.

C. SYSTEM SOURCE PARAMETERS FOR ACTIVE TELEVISION

Assume that the scene is a diffuse reflector at the scene irradiator wavelength λ. Then, the scene radiance L_s is given by

$$L_s = \frac{\rho \tau_{al}(R)\phi}{\pi \Omega_s R^2} \frac{\text{watts}}{\text{m}^2\text{-sr}} , \qquad \text{(E-7)}$$

where

ρ is the scene reflectance

$\tau_{a1}(R)$ is the atmospheric transmittance from system source to the scene

ϕ is the source power (watts)

Ω_s is the solid angle (steradians) into which the source radiates

R is the slant range (meters) to the scene object.

Note that the system source is monochromatic, and the values of ρ, τ_{a1}, and ϕ are selected at the source wavelength.

The sensor input photocurrent i is given by

$$i = \frac{\pi SA\tau_{a2}(R)L_s}{4T^2} \qquad \text{(E-8)}$$

$$= \frac{\rho\tau_{a12}(R)SA\phi}{4T^2\Omega_s R^2}$$

where

S is the input photosurface sensitivity (amperes/watt)

A is the effective photosurface area (meters^2)

$\tau_{a2}(R)$ is the atmospheric transmittance from scene to sensor

$\tau_{a12}(R)$ is the two-way atmospheric transmittance from source to scene to sensor.

D. ATMOSPHERIC EFFECTS ON ACTIVE TV SCENE IRRADIANCE

Detailed calculations of hourly values of atmospheric transmittance and the probabilities of detection or recognition at Hannover, Germany, in 1970 are based on values of the atmospheric extinction coefficient σ as computed by means of

LOWTRAN 3 for a wavelength of 0.85 μm. This appendix was written without benefit of LOWTRAN 3, however, and in this discussion let us assume that $\tau_{a1} = 0.5$ and that

$$\tau_{a12} = 0.5 \exp(-\sigma R), \tag{E-9}$$

where R is the slant range. Let us further assume that σ is given by the following approximate equations from Ref. 1:

$$\sigma = \frac{3.912\, k_h (0.64)^{0.5} v^{1/3}}{v}, \quad v > 6 \text{ km}, \tag{E-10}$$

and

$$\sigma = \frac{3.912\, k_h (0.64)^{0.585} v^{1/3}}{v}, \quad v < 6 \text{ km}, \tag{E-11}$$

where v is the visibility measured in the visible spectrum in units consistent with the units of σ, and the value of k_h depends upon altitude above sea level.

E. DISPLAY SIGNAL-TO-NOISE RATIO--PHOTOELECTRON NOISE LIMITED

For the photoelectron noise-limited case, the sensor gain G is so high that the preamplifier noise becomes trivial, so that the display signal-to-noise ratio of Eq. E-1 reduces to the simplified equation

$$SNR_D = \left[\frac{t\varepsilon}{\alpha}\right]^{\frac{1}{2}} \frac{R_{sf}(N)}{N} \frac{C_I G\, i_h}{\left[\left(\frac{2 - C_I}{2}\right) G^2 e\beta(N) i_h\right]^{\frac{1}{2}}} \tag{E-12}$$

and, in normalized form with respect to contrast, to

$$\frac{SNR_D}{C_I/[(2 - C_I)/2]^{\frac{1}{2}}} = \left[\frac{t\varepsilon}{\alpha}\right]^{\frac{1}{2}} \frac{R_{sf}(N)}{N} \left[\frac{i_h}{e\beta(N)}\right]^{\frac{1}{2}} . \quad \text{(E-13)}$$

This simplified equation can be used in a variety of ways, depending on the type of information desired.

When only one specific scene object is being considered, some further simplifications can be made. Let the object dimensions be X_o and Y_o. Then, the equivalent bar pattern in object space will have bars of

$$\Delta x = X_o/k_D \quad \text{(E-14)}$$

and

$$\Delta y = Y_o, \quad \text{(E-15)}$$

where X_T is assumed to be the largest dimension of the object, and k_D is a number related to the desired level of visual discrimination. The aspect ratio ε of the bar pattern is given by

$$\varepsilon = \frac{\Delta y}{\Delta x} = \frac{k_D Y_o}{X_o} , \quad \text{(E-16)}$$

and the angular subtense $\Delta\theta$ of the bar pattern per bar width is given by

$$\Delta\theta = X_o/k_D R \text{ radians.} \quad \text{(E-17)}$$

The bar-pattern spatial frequency is given by

$$N = \frac{Y}{F_L \cdot \Delta\theta} \frac{\text{lines}}{\text{picture height}} , \qquad \text{(E-18)}$$

where Y is the focal plane or picture height and is equal to 0.6 of the diagonal or effective diameter D_p of the input photosurface, and F_L is the effective focal length of the objective lens. Now, by combining the above equations, one has

$$N = \frac{0.6 D_p k_D R}{F_L \cdot X_o} . \qquad \text{(E-19)}$$

Inserting this expression and Eq. E-16 into Eq. E-13, one has

$$\frac{SNR_D}{C_I/[(2 - C_I)/2]^{\frac{1}{2}}} = \left[\frac{t k_D Y_o}{\alpha X_o}\right]^{\frac{1}{2}} \frac{R_{sf}(R)}{R} \frac{X_o \cdot F_L}{0.6 D_p k_D} \left[\frac{i_h}{e\beta(R)}\right]^{\frac{1}{2}} \qquad \text{(E-20)}$$

$$= \left[\frac{t Y_o X_o}{\alpha k_D}\right]^{\frac{1}{2}} \frac{R_{sf}(R)}{R} \frac{F_L}{0.6 D_p} \left[\frac{i_h}{e\beta(R)}\right]^{\frac{1}{2}} .$$

Observe that the square-wave flux-response and noise-filtering factors are now functions of R rather than N. The procedure is to replot $R_{sf}(N)$ and $\beta(N)$ as functions of R by simple scale and to make new tables for these functions in equal ΔR increments. Next, we note that the solid angle covered by the viewfield Ω_c is, for small angles,

$$\Omega_c = A/F_L^2 , \qquad \text{(E-21)}$$

where A is the effective photosurface area. The lens T/stop is given by

$$T = F_L/\tau_o^{\frac{1}{2}} D_L \ , \tag{E-22}$$

where τ_o is the lens transmittance, and D_L is the objective lens diameter. With these two equations, Eq. E-8 may be written as

$$i = \frac{\rho \tau_{al2}(R) \tau_o D_L^2 F_L^2 S\phi}{4R^2 F_L^2} \cdot \frac{\Omega_c}{\Omega_s} \ . \tag{E-23}$$

Observe that, if the system source viewfield is matched to the camera viewfield, the signal current is independent of viewfield.

Using the above expression, the SNR_D may be written as

$$\frac{SNR_D}{C_I/[(2 - C_I)/2]^{\frac{1}{2}}} = \left[\frac{tX_o Y_o}{\alpha k_D}\right]^{\frac{1}{2}} \frac{R_{sf}(R)}{R} \frac{F_L}{0.6 D_p} \left[\frac{\rho \tau_{al2}(R) \tau_o D_L^2 S\phi}{4R^2 e\beta(R)} \frac{\Omega_c}{\Omega_s}\right]^{\frac{1}{2}} . \tag{E-24}$$

Note that $0.6\ D_p/F_L$ is the vertical field of view ϕ_y of the camera. Then, after simplification, Eq. E-24 becomes

$$\frac{SNR_D}{C_I/[(2 - C_I)/2]^{\frac{1}{2}}} = \left[\frac{tX_o Y_o}{\alpha k_D}\right]^{\frac{1}{2}} \frac{R_{sf}(R)}{R^2} \frac{D_L}{2\phi_y} \left[\frac{\rho \tau_{al2}(R) \tau_o S\phi}{e\beta(R)} \frac{\Omega_c}{\Omega_\sigma}\right]^{\frac{1}{2}} \tag{E-25}$$

This equation can be used in several ways. For example, we can solve for C_I. Then, by setting SNR_D equal to its threshold value (which may depend on spatial frequency or range), we can solve for minimum detectable contrast or for detectable contrast at any given level of probability by suitably selecting SNR_D. Alternatively, we can compute SNR_D, and, by graphical means or by trial and error, we can find the threshold range or the cumulative probability versus range for a given scene object contrast.

This procedure can be applied to detection, recognition, or identification of targets. We could illustrate the procedure with an example of any of the three based upon the choice of the value of k_D, the number of cycles across the minimum dimension of the target.

We set k_D equal to 8 lines (4 line pairs) and solve the sample problem for the *recognition* case.

F. EXAMPLES OF RANGE PREDICTION FOR TANK RECOGNITION USING A SIMPLIFIED ATMOSPHERIC TRANSMISSION MODEL

The following scene, source, sensor, and observer parameters are used for the examples below:

Scene

Highlight Reflectivity (ρ)	0.5
Scene Object Size (X_o, Y_o)	3 x 3 m
Visibility (V)	2,4,6,8,10,15,20 km
Altitude Factor (k_h)	1.0

System Source

Effective Power (ϕ)	45 W
Field of View (Ω_s)	1.5° x 2.0°
Wavelength (λ)	0.86 μm

Sensor

Type	25/25/27-mm I-Ebsicon*
Field of View (Ω_s)	1.5° x 2.0°
Lens Diameter (D_L)	0.150 m
Focal Length (F_L)	573 mm
Transmittance (τ_o)	0.8
Picture Aspect Ratio H/V (α)	4/3
Photosurface Sensitivity (S)	25 x 10^{-3} A/W
Aperture Correction	none

Sightline Motion

Type	Random Amplitude
Amplitude	25 μrad RMS

Observer

Level of Discrimination:	
Recognition (k_D)	8
Integration Time (t)	0.1 sec

The various system modulation transfer functions (MTFs) and MTF-related quantities are given in Table E-1. The first column in the table is the spatial frequency in lines per picture height. The second and third columns are the MTFs of the Ebsicon and the image intensifier, respectively. The product of the MTFs of the Ebsicon and the intensifier is given in the fourth column. The image motion MTF is calculated from the relation

$$R_{oM}(N) = \exp - \left(\frac{\pi}{\sqrt{2}} \frac{\theta_A}{\phi_v} N \right)^2 , \qquad \text{(E-26)}$$

*Sensor combination used in the 698DF Program.

where θ_A is the RMS amplitude of the random sightline motion and ϕ_v is the vertical field of view. For $\phi_A = 25 \times 10^{-6}$ rad and $\phi_v = 1.5°/57.3°/\text{rad}$,

$$R_{oM}(N) = \exp - (2.12 \times 10^{-3}N)^2 \quad ,$$

which is tabulated in column 5 of Table E-1. Multiplying column 4 times column 5 gives the combined MTF of the Ebsicon, intensifier, and sightline motion, tabulated in column 6. Since these MTFs follow the point of photoelectron noise insertion, they are included in the noise filtering function $\beta(N)$, defined by

$$\beta(N) = \frac{1}{N} \int_0^N \left[R_{oCIM}(N)\right]^2 dN \qquad \text{(E-27)}$$

for this case, R_{oCIM} is squared in column 7 of Table E-1 and is then numerically integrated by means of the trapezoidal rule explained below. Columns 8 and 9 are intermediate calculations using the trapezoidal rule and leading to $\beta(N)$ in column 10.

TABLE E-1. MTFs and MTF-RELATED FACTORS FOR THE ACTIVE TV SYSTEM ASSUMED

N_{TV}	R_{oC}[a] (Ebsicon MTF)	R_{oI}[b] (Intensifier MTF)	R_{oCI}[c] (I-Ebs MTF)	R_{oM}[d] (Motion MTF)	R_{oCIM}[e] (I-Ebs-Motion MTF)	$(R_{oCIM})^2$	Σ	Divided by:	$\beta(N)$
0	1.000	1.000	1.000	1.000	1.000	1.000	1.000	1	1.000
50	0.990	0.975	0.965	0.989	0.954	0.910	1.911	2	0.955
100	0.945	0.941	0.889	0.956	0.850	0.722	1.771	2	0.886
150	0.885	0.900	0.797	0.904	0.720	0.518	2.391	3	0.797
200	0.816	0.858	0.700	0.835	0.585	0.342	2.821	4	0.705
250	0.720	0.810	0.583	0.755	0.440	0.194	3.089	5	0.618
300	0.595	0.758	0.451	0.667	0.301	0.091	3.231	6	0.539
350	0.500	0.702	0.351	0.577	0.203	0.041	3.297	7	0.471
400	0.480	0.650	0.265	0.487	0.129	0.017	3.326	8	0.416
450	0.322	0.600	0.193	0.402	0.078	0.006	3.338	9	0.371
500	0.259	0.555	0.144	0.325	0.047	0.002	3.342	10	0.334
550	0.212	0.510	0.108	0.257	0.028	--	3.343	11	0.304
600	0.173	0.470	0.081	0.198	0.016	--	--	12	0.279
650	0.137	0.430	0.059	0.150	0.009	--	--	13	0.257
700	0.110	0.390	0.043	0.111	0.005	--	--	14	0.239
750	0.086	0.350	0.030	0.080	0.002	--	--	15	0.223
800	0.063	0.320	0.020	0.056	0.001	--	--	16	0.209

[a] Camera tube (Ebsicon) MTF (25/27 mm).

[b] Intensifier MTF (25/25 mm).

[c] $R_{oC} \times R_{oI} = R_{oCI}$.

[d] Motion MTF (25 μrad RMS)

[e] $R_{oCI} \times R_{oM} = R_{oCIM}$.

The general trapezoidal rule for numerical integration is

$$\int_{x_1}^{x_p} y\,dx = \Delta x\left(\frac{y_1}{2} + y_2 + \ldots y_{n-1} + \frac{y_n}{2}\right) \tag{E-28}$$

$$+ (x_p - x_n)\left(\frac{y_n}{2} + \frac{y_p}{3}\right).$$

Then,

$$\frac{1}{N}\int R_o^2(N)dN = \frac{\Delta N}{k\Delta N}\left[\frac{R_o^2(0)}{2} + R_o^2(\Delta N) + R_o^2(2\Delta N) + \ldots \frac{R_o^2(k\Delta N)}{2}\right]$$

$$+ \frac{\Delta N}{k\Delta N}\left[\frac{R_o(k\Delta N) + R_o(k+1)\Delta N}{2}\right] \qquad \text{(E-29)}$$

$$(N = k\Delta N).$$

For example,

$$\beta(50) = \frac{50}{50}\left[\frac{R_o^2(0) + R_o^2(50)}{2}\right]$$

$$\beta(100) = \frac{50}{100}\left[\frac{R_o^2(0)}{2} + R_o^2(50) + \frac{R_o^2(100)}{2}\right]$$

$$\beta(150) = \frac{50}{150}\left[2\beta(100) + \frac{R_o^2(100) + R_o^2(150)}{2}\right]$$

$$\beta(200) = \frac{50}{200}\left[3\beta(150) + \frac{R_o^2(150) + R_o^2(200)}{2}\right].$$

The lens MTF does not enter the noise-filtering function but is a part of the overall system MTF. In column 1 of Table E-2, we again tabulate the spatial frequency N_{TV}. In column 2, we repeat the MTFs of column 6 of Table E-1, which we multiply by the lens MTFs of column 3 of Table E-2 to obtain the overall system MTFs in column 4. Knowing the overall system MTFs, we can calculate the square-wave flux response $R_{sf}(N)$ from the equation

$$R_{sf}(N) = \frac{8}{\pi^2}\sum_{k=1}^{\infty}\frac{R_{oC}\cdot R_{oI}\cdot R_{oM}\cdot R_{oL}(kN)}{k^2}, \qquad \text{(E-30)}$$

where k = 1, 3, 5 ... $R_{sf}(N)$ is given in column 5 of Table E-2. The $\beta(N)$ of column 6 is repeated from column 10 of Table E-1.

TABLE E-2. MTFs and MTF-RELATED FACTORS FOR THE ACTIVE TV SYSTEM ASSUMED (CONTINUED)

N_{TV}	R_{oCIM}	R_{oL} (Lens MTF)	System MTF	$R_{sf}(N)$	$\beta(N)$	Range, km
0	1.000	1.000	1.000	1.000	1.000	0.00
50	0.954	0.962	0.918	0.817	0.955	0.72
100	0.850	0.930	0.791	0.663	0.886	1.43
150	0.720	0.890	0.641	0.524	0.797	2.15
200	0.585	0.855	0.500	0.406	0.705	2.87
250	0.440	0.820	0.361	0.293	0.618	3.58
300	0.301	0.780	0.235	0.190	0.539	4.30
350	0.203	0.742	0.151	0.122	0.471	5.01
400	0.129	0.700	0.090	0.073	0.416	5.73
450	0.078	0.670	0.052	0.042	0.371	6.45
500	0.047	0.630	0.030	0.024	0.334	7.16
550	0.028	0.590	0.017	0.014	0.304	7.88
600	0.016	0.550	0.009	0.007	0.279	8.60
650	0.009	0.510	0.005	0.004	0.257	9.31
700	0.005	0.480	0.002	0.001	0.239	10.00

The basic MTF data are given in terms of the spatial frequency N in lines per picture height, but in using Eq. E-20 we will need the square-wave flux response R_{sf} and the noise-filtering function β as functions of range. The conversion is

performed by means of Eq. E-19. Column 7 of Table E-2 gives the range corresponding to the spatial frequency for the specific scene object. Now, $R_{sf}(N)$ and $\beta(N)$ are updated as functions of range in Fig. E-1. Now, for convenience in calculation, we use Fig. E-1 to create Table E-3, where $R_{sf}(N)$ and $\beta(N)$ are given in even range increments.

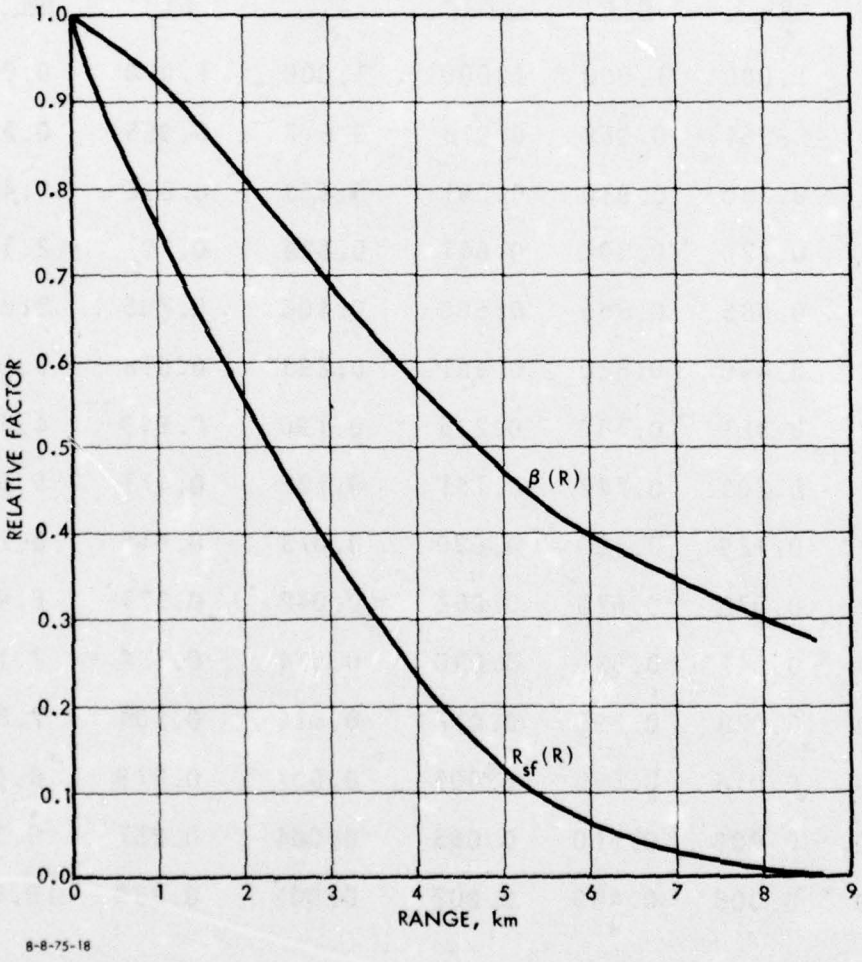


FIGURE E-1. $R_{sf}(R)$ and $\beta(R)$ for Uncompensated 25/25/27-mm I-Zoom-Ebsicon (Program 698DF).

TABLE E-3. SQUARE-WAVE FLUX RESPONSE AND NOISE-FILTERING FACTOR AS FUNCTIONS OF RANGE FOR THE ACTIVE TV SYSTEM ASSUMED[a]

Range, km	$R_{sf}(R)$	$\beta(R)$
0.0	1.000	1.000
0.5	0.873	0.968
1.0	0.760	0.927
1.5	0.657	0.873
2.0	0.555	0.813
2.5	0.464	0.750
3.0	0.380	0.690
3.5	0.305	0.630
4.0	0.237	0.572
4.5	0.175	0.520
5.0	0.130	0.470
5.5	0.090	0.432
6.0	0.062	0.400
6.5	0.042	0.372
7.0	0.030	0.346
7.5	0.020	0.322
8.0	0.010	0.300

[a]These values hold only for the assumed 3 m x 3 m specific scene object and for the recognition case ($k_D = 8$).

By using the system parameters in Table E-3, Eq. E-20 can be written as

$$\frac{SNR_D}{C_I/[(2-C_I)/2]^{\frac{1}{2}}} = \left(\frac{0.1x9x3}{4x8}\right)^{\frac{1}{2}} \frac{R_{sf}(R)}{R^2} \times \frac{10^{-6}m^2}{km^2}$$

$$\times \frac{0.15x57.3}{3} \left(\frac{0.5x0.8x25x10^{-3}x45\tau_{al2}}{1.6x10^{-19}\beta(R)}\right)^{\frac{1}{2}} \quad \text{(E-31)}$$

$$= 1393 \frac{R_{sf}(R)(\tau_{al2})^{\frac{1}{2}}}{R^2[\beta(R)]^{\frac{1}{2}}}$$

The SNR_D that assumes the recognition criterion $k_D = 8$ is calculated for visibility in a vacuum ($\tau_{al2} = 1.0$) and for other visibilities by means of Eqs. E-9, E-10, and Table E-4:*

$$\tau_{al2} = 0.5 \exp(-\sigma R), \quad \text{(E-9)}$$

and

$$\sigma = \frac{3.912}{v} k_h (0.64)^{0.5v^{1/3}}, \text{ assume } k_h = 1.0. \quad \text{(E-10)}$$

---

*As mentioned earlier, Eqs. E-9 and E-10 are used in this discussion in lieu of the LOWTRAN 3 atmospheric transmission model, which was not available to the writer when he wrote this appendix. The atmospheric transmittance at Hannover, Germany, for each hour of January and August 1970 as computed by means of LOWTRAN 3 for ranges of 1 and 3 km and a wavelength of 0.85 μm is shown in Figs. 42 and 43 of the main text.

TABLE E-4. ATMOSPHERIC EXTINCTION COEFFICIENT VERSUS VISIBILITY

Visibility, km	σ, km^{-1}
2.0	1.464
4.0	0.686
6.0	0.435
8.0	0.312
10.0	0.242
15.0	0.150
20.0	0.107

The results of these calculations are shown in Table E-5.

The SNR_D values of Table E-5, to be plotted in Fig. E-2, can be used in a variety of ways. Assuming an optimal display viewing distance, the observer's SNR_D thresholds are as given in Table E-6. The thresholds of Table E-6 must be adjusted by the factor

$$SNR_{DT} = \frac{SNR_D[(2 - C_I)/2]^{\frac{1}{2}}}{C_I} , \qquad \text{(E-32)}$$

as given in Table E-7, before being plotted in Fig. E-2.

In Table E-8, the SNR_{DT} values of Table E-6 are adjusted for various contrasts. These adjusted SNR_{DT} values are then plotted along with the SNR_D curves transposed from Fig. E-2. These thresholds, which imply a 50% probability of recognition, give threshold range by their intersection with the SNR_D curves, as shown in Fig. E-3 and Table E-9.

TABLE E-5. CALCULATED SNR_D VALUES FOR THE ACTIVE TV SYSTEM ASSUMED, RECOGNITION OF TANK TARGET IN FRONTAL ASPECT (BASED ON FOUR-LINE-PAIR CRITERION), FOR VISIBILITIES OF ∞ (VACUUM), 20, 15, 10, 8, 6, 4, AND 2 km

R, km	R_{sf} (N)	β (N)	SNR_D Vacuum	$(\tau_{a12})^{1/2}$ 20 km	SNR_D 20 km	$(\tau_{a12})^{1/2}$ 15 km	SNR_D 15 km	$(\tau_{a12})^{1/2}$ 10 km	SNR_D 10 km
0.0	1.000	1.000	∞	1.000	∞	1.000	∞	1.000	∞
0.5	0.873	0.968	4944	0.688	3400	0.681	3370	0.666	3290
1.0	0.760	0.927	1100	0.670	737	0.656	722	0.626	689
1.5	0.657	0.873	435	0.653	284	0.632	275	0.590	256
2.0	0.555	0.813	215	0.636	137	0.609	131	0.555	119
2.5	0.464	0.750	119.4	0.619	73.9	0.586	70	0.523	62.4
3.0	0.380	0.690	70.8	0.602	42.7	0.565	40	0.492	34.8
3.5	0.305	0.630	43.7	0.587	25.6	0.544	23.8	0.463	20.2
4.0	0.237	0.572	27.3	0.571	15.6	0.524	14.3	0.436	11.9
4.5	0.175	0.520	16.7	0.556	9.3	0.505	8.4	0.410	6.9
5.0	0.130	0.470	10.6	0.541	5.7	0.486	5.2	0.386	4.1
5.5	0.090	0.432	6.31	0.527	3.3	0.468	2.95	0.364	2.29
6.0	0.062	0.400	3.79	0.513	1.9	0.451	1.71	0.342	1.30
6.5	0.042	0.372	2.27	0.500	1.14	0.434	0.99	--	--
7.0	0.030	0.346	1.45	--	--	--	--	--	--
7.5	0.020	0.322	--	--	--	--	--	--	--
8.0	0.010	0.300	--	--	--	--	--	--	--

R, km	SNR_D Vacuum	$(\tau_{a12})^{1/2}$ 8 km	SNR_D 8 km	$(\tau_{a12})^{1/2}$ 6 km	SNR_D 6 km	$(\tau_{a12})^{1/2}$ 4 km	SNR_D 4 km	$(\tau_{a12})^{1/2}$ 2 km	SNR_D 2 km
0.0	∞	1.000	∞	1.000	∞	1.000	∞	1.000	∞
0.5	4944	0.654	3230	0.634	3135	0.596	2945	0.490	2424
1.0	1100	0.605	665	0.569	626	0.502	552	0.340	374
1.5	435	0.560	243	0.510	222	0.423	184	0.236	103
2.0	215	0.518	111	0.458	98.4	0.356	76.6	0.164	35.2
2.5	119.4	0.479	57.2	0.410	49.0	0.300	35.8	0.113	13.5
3.0	70.8	0.443	31.4	0.368	26.1	0.253	17.9	0.079	5.6
3.5	43.7	0.410	17.9	0.330	14.4	0.213	9.30	0.055	2.4
4.0	27.3	0.379	10.3	0.296	8.1	0.179	4.90	0.038	1.03
4.5	16.7	0.350	5.9	0.266	4.4	0.151	2.52	--	--
5.0	10.6	0.324	3.4	0.238	2.5	0.127	1.35	--	--
5.5	6.31	0.300	1.9	0.214	1.3	--	--	--	--
6.0	3.79	0.277	1.1	--	--	---	--	--	--

TABLE E-6. THRESHOLD SIGNAL-TO NOISE RATIOS FOR VARIOUS SPATIAL FREQUENCIES, AT OPTIMAL DISPLAY VIEWING DISTANCE

Spatial Frequency N, TV lines/picture height	SNR_{DT} ($C_I = 1.0$)	Range, km
100	2.65	1.43
200	2.50	2.86
300	2.50	4.30
400	2.30	5.73
500	2.00	7.16
600	1.80	8.60
700	1.55	10.00

TABLE E-7. CONTRAST ADJUSTMENT FACTORS TO BE APPLIED TO SNR_{DT} VALUES OF TABLE E-5

Contrast	$\frac{[(2 - C_I)/2]^{\frac{1}{2}}}{C_I}$
0.1	9.75
0.2	4.74
0.3	3.07
0.4	2.23
0.5	1.73
0.6	1.39
0.7	1.15
0.8	0.968
0.9	0.824
0.99	0.707

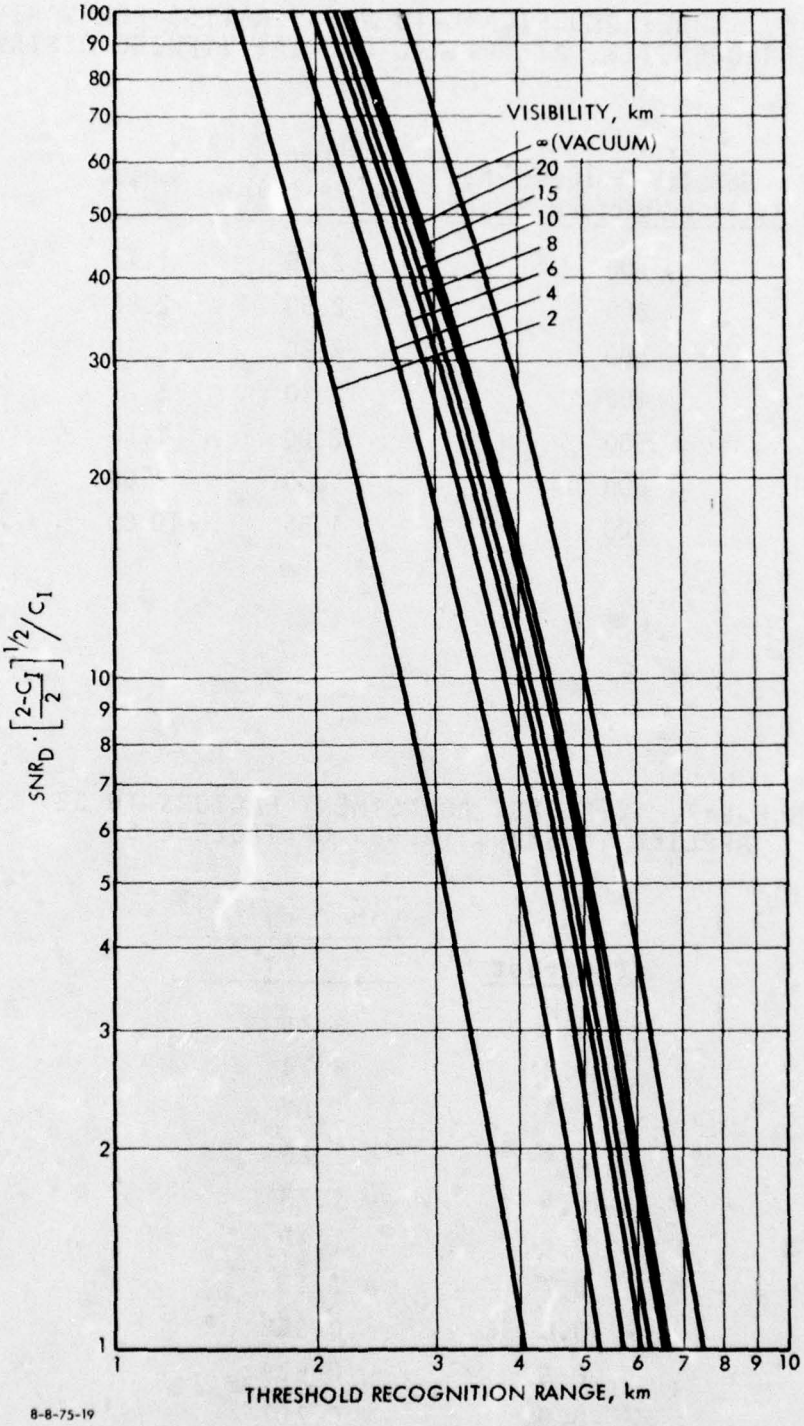


FIGURE E-2. SNR_D (Normalized to the Contrast Term) Needed to Achieve Threshold Recognition Range for Tank in Frontal Aspect at Various Visibilities.

TABLE E-8. OBSERVER SNR_{DT} AS A FUNCTION OF RANGE (ADJUSTED FOR CONTRAST), AT OPTIMAL DISPLAY VIEWING DISTANCE

R, km	SNR_{DT}	C_I=1.0 SNR_{DT}	C_I=0.7 SNR_{DT}	C_I=0.5 SNR_{DT}	C_I=0.3 SNR_{DT}	C_I=0.1 SNR_{DT}
1.43	2.65	1.87	3.05	4.58	8.14	25.83
2.86	2.50	1.77	2.88	4.33	7.68	24.38
4.30	2.50	1.77	2.88	4.33	7.68	24.38
5.73	2.30	1.63	2.05	3.98	7.06	22.43
7.16	2.00	1.41	2.30	3.46	6.14	19.50
8.60	1.80	1.27	2.07	3.11	5.53	17.55
10.00	1.55	1.10	1.78	2.68	4.76	15.10

TABLE E-9. THRESHOLD RANGE, km, FOR 50% PROBABILITY OF RECOGNITION OF TANK IN FRONTAL ASPECT AS FUNCTION OF VISIBILITY AND CONTRAST

	C_I				
Visibility, km	1.0	0.7	0.5	0.3	0.1
∞ (Vacuum)	7.0	6.20	5.95	5.35	4.20
20	6.1	5.70	5.30	4.70	3.55
15	5.9	5.55	5.20	4.60	3.45
10	5.7	5.35	5.00	4.40	3.35
8	5.6	5.20	4.80	4.25	3.25
6	5.3	4.90	4.50	4.05	3.10
4	4.8	4.40	4.10	3.65	2.80
2	3.7	3.40	3.15	2.82	2.20

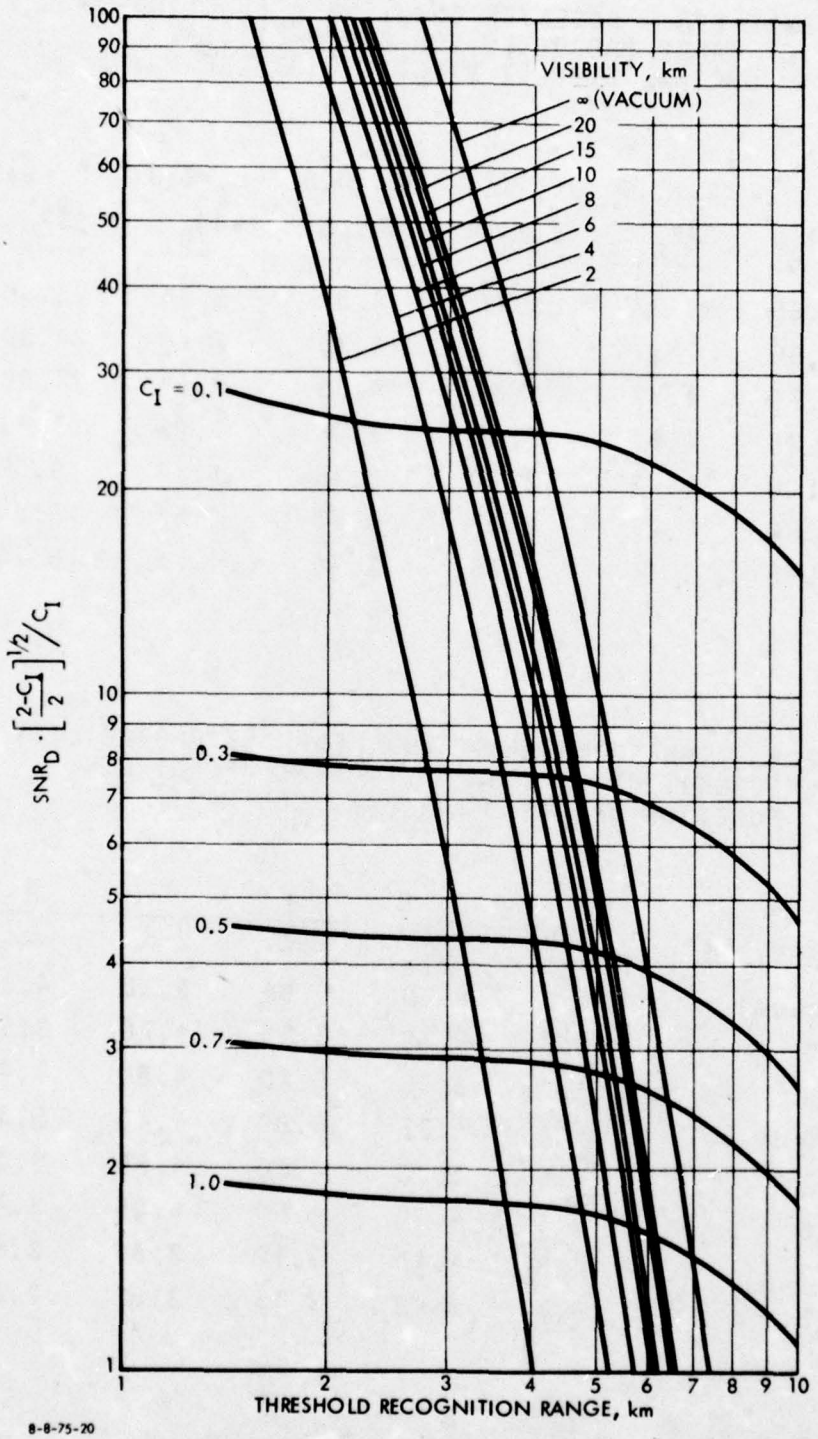


FIGURE E-3. Graphical Calculation of Threshold Recognition Range for Tank in Frontal Aspect at Various Visibilities and Image Contrasts.

The threshold ranges are plotted for various image contrasts in Fig. E-4. An alternative use of the SNR_D curves is to obtain the cumulative probability of recognition versus range by use of the probability factor of Table E-10. This factor multiplies the threshold SNR (for 50% probability). The resulting series of observer SNR_D requirement curves is shown in Fig. E-5, and the cumulative probability-versus-range curves are shown in Fig. E-6.

TABLE E-10. PROBABILITY VERSUS NORMALIZED SNR_D

Probability of Recognition	Normalized SNR_D
0.1	0.53
0.2	0.70
0.3	0.81
0.4	0.91
0.5	1.00
0.6	1.10
0.7	1.19
0.8	1.30
0.9	1.44
0.99	1.82

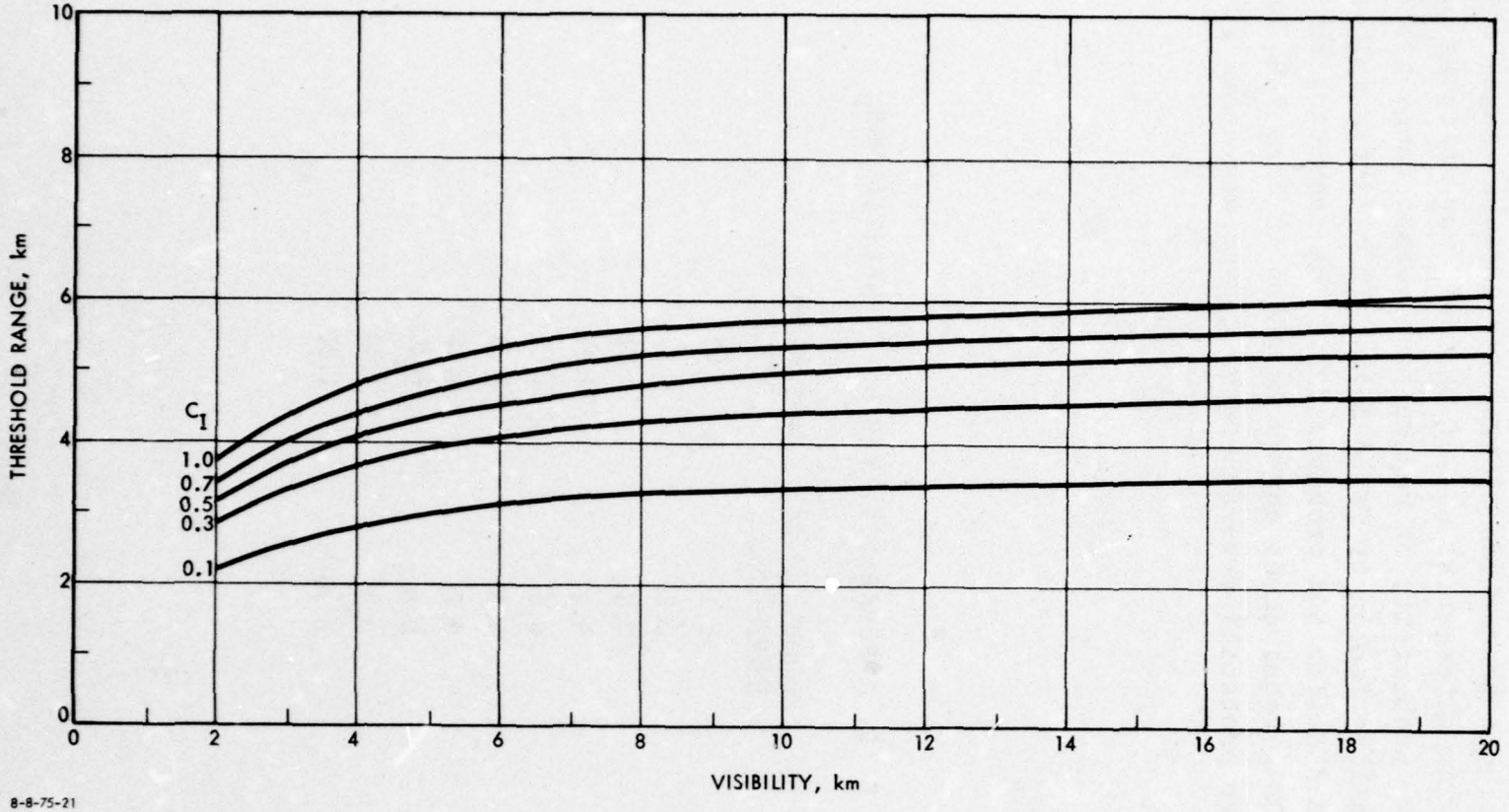


FIGURE E-4. Threshold Recognition Range for Tank in Frontal Aspect versus Visibility for Various Image Contrasts, 25/25/27-mm I-Zoom-Ebsicon, 25-deg FOV, 25-μrad Motion.

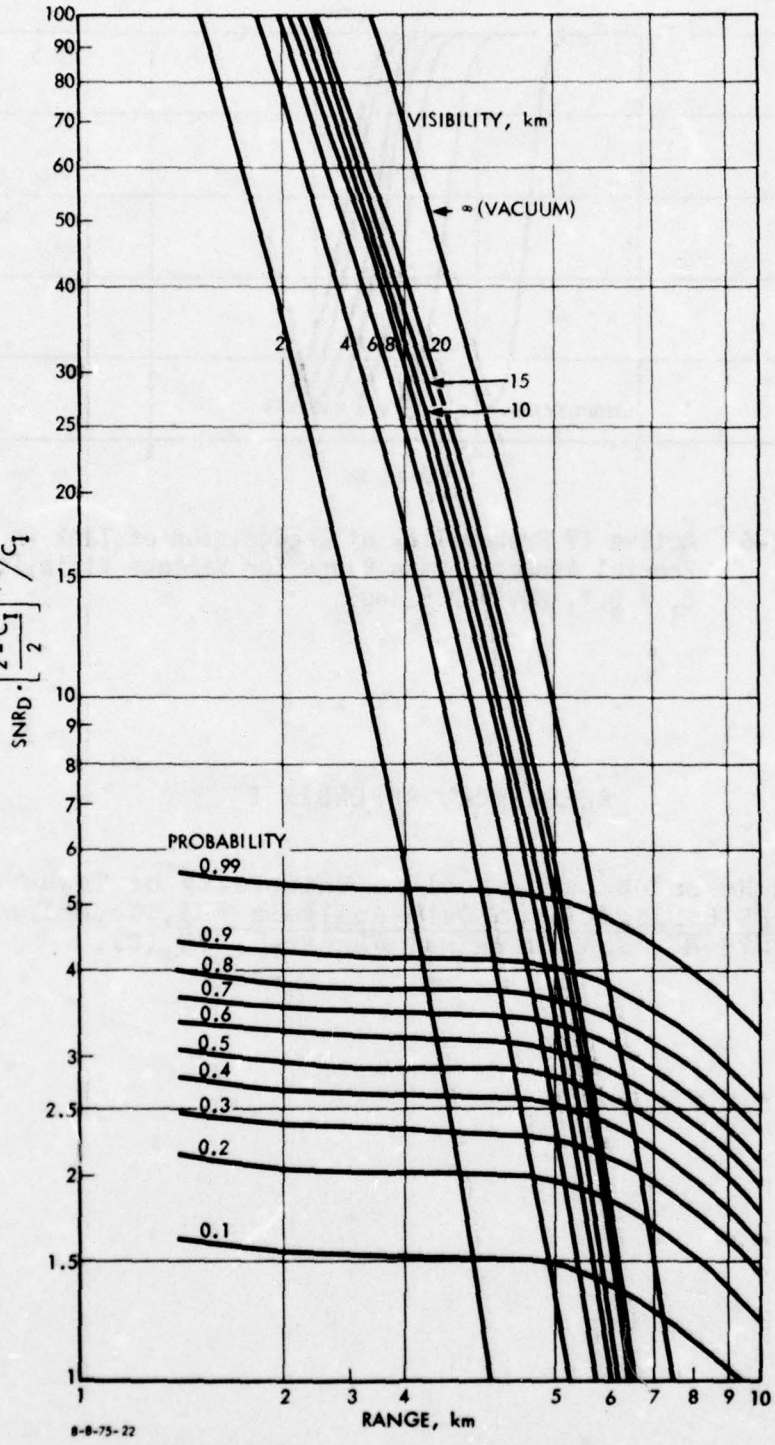


FIGURE E-5. Graphical Calculation of Cumulative Probability of Recognition of Tank in Frontal Aspect at Various Visibilities. Image Contrast = 0.7.

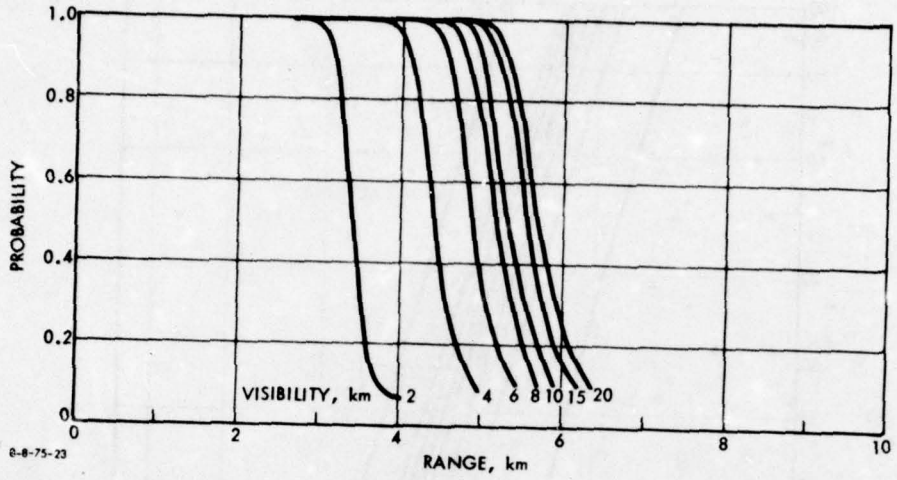


FIGURE E-6. Active TV Probability of Recognition of Tank in Frontal Aspect versus Range for Various Visibilities, C_I = 0.7, FOV = 2.5 deg.

REFERENCE, APPENDIX E

1. Applied Research Laboratories, University of Texas at Austin, ACTV/MAFLIR Flight Test Data Analysis (U), Technical Report AFAL-TR-75-85, J.A. Hawkins, January 1975 (C).

APPENDIX F

CALCULATION OF PROBABILITY OF RECOGNITION OF TANK IN FRONTAL ASPECT, PASSIVE TELEVISION

Frederick A. Rosell

Defense and Electronic Systems Center
Westinghouse Electric Corporation

CONTENTS

A. Range Prediction for Passive TV Systems F-3

B. Equivalent Scene Parameters F-3

C. Scene Illumination versus Irradiance Level F-6

D. Atmospheric Effect on Contrast F-8

E. Display Signal-to-Noise Ratio--Photoelectron and Preamplifier Noise Limited F-8

F. Sample Calculation for a Passive Low-Light-Level TV System F-11

A. RANGE PREDICTION FOR PASSIVE TV SYSTEMS

The equations for passive TV may be more complex because preamplifier noise must sometimes be included in the SNR_D equation, but the calculation procedure is otherwise similar to that used for active TV.

B. EQUIVALENT SCENE PARAMETERS

The passive scene can be very complex, since objects being viewed can be lighted diffusely or from the back, front, or side. Scene objects may throw shadows or be obscured by the shadows of trees or buildings. The combination of direct light and light reflected from the foreground onto a scene object can drastically change the inherent object contrasts and can even cause contrast reversals as a function of the viewing aspect angle. While mathematical description of the contrast of a scene object may be highly complicated, it is common experience that most scene objects can be visually discerned most of the time when the eye's visual acuity and the atmospheric visibility permit.

To avoid undue complexity, it is common to replace the real scene object by a diffuse reflector of contrast equal to some assumed average number related to the difference in reflectivity between the object and the background, i.e.,

$$C_I = \frac{\rho_{max} - \rho_{min}}{\rho_{max}} , \qquad \text{(F-1)}$$

PRECEDING PAGE BLANK-NOT FILMED

where ρ_{max} and ρ_{min} are the reflectivities of either the scene or the object. For convenience in the analysis, contrast is defined as always being positive.

The TV camera tube is operated so as to maintain the output current (at the input to the video preamplifier), corresponding to the scene highlight level, at some constant level I_{op}, if possible. The value of I_{op} is given by:

$$I_{op} = I_{max} - I_{dkm} , \qquad \text{(F-2)}$$

where I_{max} is the maximum signal output current obtainable and I_{dkm} is the maximum dark current expected at the highest tube temperature expected. At very low light levels, scene highlight level may be insufficient to produce I_{op} at the output. In this case, the tube gain is set at its near-maximum value, i.e.,

$$G = G_{max} \text{ for } I_o \leq I_{op}. \qquad \text{(F-3)}$$

I_o equals I_{op} when the highlight scene irradiance E_s is

$$E_{sl} = \frac{4T^2 \, I_{op}}{G_{max} \, SA} , \qquad \text{(F-4)}$$

where E_{sl} is the value of scene irradiance just sufficient to achieve I_{op} using maximum gain G_{max}, T is the lens T/stop, S is the effective photosurface sensitivity to E_s, and A is the effective photosurface area. Scene reflectivity is assumed to be unity for this calculation.

As the scene highlight level increases above E_{s1}, the gain of the camera tube is decreased to maintain the output current at I_{op}. The value of G is then equal to

$$G = \frac{4T^2 I_{op}}{SAE_s} \qquad \begin{matrix} I_o = I_{op} \\ G \leq G_{min} \end{matrix} \tag{F-5}$$

Note the restriction that G be above its minimum value G_{min}. At some point, it will become difficult to reduce gain further because of loss of focus, onset of image derotation, or some other physical phenomenon. The maximum value of E_s equals E_{s2}, which is

$$E_{s2} = \frac{4T^2 I_{op}}{G_{min} SA} . \tag{F-6}$$

After gain has reached its minimum value, the lens T/stop is adjusted to maintain E_s at the constant value E_{s2}.

Thus we define the three operating ranges as

1. Very low light level

$$\begin{matrix} E_s \leq E_{s1} \\ G = G_{max} \end{matrix} \tag{F-7}$$

2. Moderate light level

$$E_{s1} \leq E_s \leq E_{s2} \tag{F-8}$$

$$G = \frac{4T^2 I_{op}}{SAE_s}$$

3. High light level

$$\begin{aligned} E_s &> E_{s2} \\ G &= G_{min} \\ E_s &= E_{s2} \cdot \end{aligned} \tag{F-9}$$

Actually, the third case is trivial, since it is the endpoint of the second case and implies that further increases in scene irradiance level above some point will not increase the image SNR.

C. SCENE ILLUMINANCE VERSUS IRRADIANCE LEVEL

The most common low-light-level television cameras use the S-25 photosurfaces on the image intensifier. The spectral response of the S-25 is shown in Fig. F-1. The spectral response is seen to extend well beyond the visible cutoff of about 0.7 μm. The earth's irradiance level in the spectral band of the S-25 photosurface is hardly ever measured. Instead, photometers with the same response of the eye are used, and the results are reported in terms of photometric units which are inappropriate for physical devices with substantial near-infrared response. However, it may be possible to find a reasonable approximate relationship between the photometric and radiometric quantities which would permit the use of the reported photometric quantities. Such an approximation is given in Appendix G.

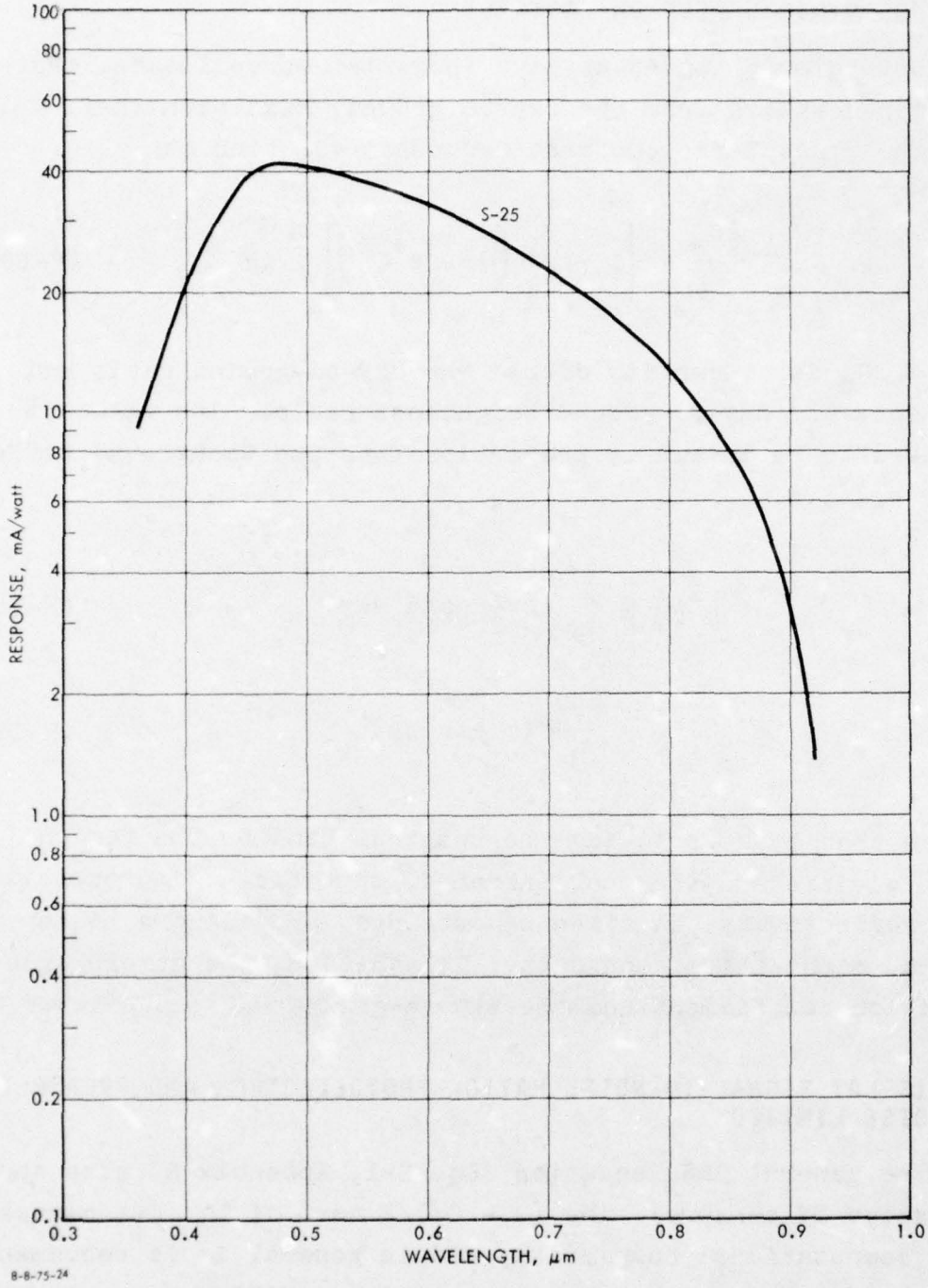


FIGURE F-1. Spectral Response of S-25 Photosurface.

D. ATMOSPHERIC EFFECT ON CONTRAST

For the most important case in aerial surveillance, that of vision downward from the sky to ground, Middleton (Ref. F-1) gives the atmospheric contrast reduction equation as

$$\frac{C_R}{C_o} = \left[1 - \frac{S_k}{G_d}\left(1 - e^{+\sigma \bar{R}}\right)\right]^{-1}, \qquad \text{(F-10)}$$

where S_k/G_d is a quantity dubbed the sky-to-ground ratio and represents the sky-to-ground brightness ratio. Its value is estimated to be inversely proportional to the background reflectivity ρ_b, i.e.,

$$\frac{S_k}{G_d} = \frac{1}{\rho_b} \text{ (overcast sky)} \qquad \text{(F-11)}$$

$$= \frac{0.2}{\rho_b} \text{ (clear sky)} \quad . \qquad \text{(F-12)}$$

Observe that by restricting the spectral band to the far end of the visible and the near infrared, significant increases in scene reflectivity can often be obtained, providing a higher inherent scene-object contrast. In addition, the atmospheric extinction coefficient and the sky-to-ground ratio are lower.

E. DISPLAY SIGNAL-TO-NOISE RATIO--PHOTOELECTRON AND PREAMPLIFIER NOISE LIMITED

The general SNR_D equation (Eq. E-1, Appendix E) also applies to passive TV sensors. The $(2 - C_I)/2$ term of Eq. E-1 causes undue computational complexity, and in general it is recommended that it be replaced by a constant if preamplifier noise is a factor. If C_I is taken to be 0.3, the value of the constant will

be 0.85, which will suffice for practical purposes. Using the specific target contrast concept discussed in connection with the active TV sensor, we can write Eq. E-1 as

$$\frac{SNR_D}{C_I} = \left[\frac{t\, X_o Y_o}{\alpha k_d}\right]^{\frac{1}{2}} \frac{R_{sf}(R)}{R} \frac{F_L}{Y} \frac{G\, i_h}{\left[0.85\, G^2 e\beta(R) i_h + I_p^2/2\Delta f_v\right]^{\frac{1}{2}}} \cdot \quad \text{(F-13)}$$

The input photocurrent i_h is given by

$$i_h = \frac{\rho_{max}\, SAE_h}{4T^2}, \quad \text{(F-14)}$$

which can be inserted into Eq. F-13.

If the sensor gain is high enough at low light levels or if the minimum gain obtainable is not too low at the higher light levels, the sensor is essentially photoelectron noise limited. If the preamplifier noise is PA, and the photoelectron noise is PE, then the sensor is essentially photoelectron noise limited if the ratio

$$\left[\frac{PE^2 + PA^2}{PE^2}\right]^{\frac{1}{2}} \leq 1.1 \quad \text{(F-15)}$$

or if

$$PA^2 + PE^2 \leq 1.21(PA)^2$$

$$PE^2 \geq 4.76(PA)^2. \quad \text{(F-16)}$$

The test then is

$$\left(\frac{2 - C_I}{2}\right) G^2 e\beta(N) i_h \geq \frac{4.76 I_p^2}{2\Delta f_v} \qquad \text{(F-17)}$$

or

$$i_h \geq \frac{4.76\ I_p^2}{2\Delta f_v \left(\frac{2 - C_I}{2}\right) e\beta(N) G^2} . \qquad \text{(F-18)}$$

For sensors with very high gain capability, such as the I-Ebsicon, the sensor is more often photoelectron noise limited than not. The possible exceptions are:

1. When light level, scene contrast, and scene reflectivity are very low
2. When sensor gain is very low and scene light level, reflectivity, and contrast are very high.

In general, the error in assuming that the I-Ebsicon is photoelectron noise limited is small. The result of the assumption is that the range predictions will be slightly optimistic at the very lowest light level and slightly pessimistic at the highest light levels.

Observe that in the photoelectron-noise-limited conditions Eq. E-1 reduces to

$$\frac{SNR_D}{C_I} = \left[\frac{tX_o Y_o}{\alpha k_d}\right]^{\frac{1}{2}} \frac{R_{sf}(R)}{R} \frac{F_L}{R} \frac{1}{2T} \frac{\left[\rho_{max} S\alpha Y^2 E_h\right]^{\frac{1}{2}}}{\left[\left(\frac{2 - C_I}{2}\right) e\beta(R)\right]^{\frac{1}{2}}}, \qquad \text{(F-19)}$$

where we have used Eq. F-14. Reducing further, we get

$$\frac{SNR_D}{C_I/[2 - C_I]^{\frac{1}{2}}} = \left[\frac{t\ X_o Y_o}{k_d}\right]^{\frac{1}{2}} \frac{R_{sf}(R)}{R}\ \frac{D_o}{2}\ \left[\frac{h_{max}\ \tau_o\ S\ E_h}{e\beta(R)}\right]^{\frac{1}{2}}. \qquad \text{(F-20)}$$

F. SAMPLE CALCULATION FOR A PASSIVE LOW-LIGHT-LEVEL TV SYSTEM

The following scene sensor and observer parameters are used for the examples below:

Scene

Highlight reflectivity	0.5
Scene Object Size (X_o, Y_o)	3 x 3 m
Visibility (V)	2,4,6,8,10,15, 20 km
Altitude	Sea Level
Object Contrast	0.5
Light-Level Range	Twilight to Cloudy Starlight
Sky	Overcast
Sky-to-Ground Ratio	2.0

Sensor

Type	25/25/27-mm I-Ebsicon
Field of View	1.5° x 2.0°
Lens Diameter (D_L)	0.2 m
Focal Length (F_L)	573 mm
Transmittance (τ_o)	0.915
Picture Aspect Ratio (H/V)	4/3
Photosurface Sensitivity	2×10^{-4} A/lm
Transmittance of Spectral Filter	0.5
Bandpass	0.6 to 0.8 μm

Sightline Motion

Type	Random Amplitude
Amplitude	25 μrad RMS

Observer

Level of Discrimination:

Recognition (k_D)	8
Integration Time (t)	0.1 sec

The various system MTFs and MTF-related quantities are given in Tables F-1 and F-2. The sensor here is the same as was used in the active TV case, but horizontal aperture correction is applied.

We shall next test to see whether the sensor is photoelectron or preamplifier noise limited, starting with Eq. F-13. If we use the above numerical quantities, we have

$$\frac{SNR_D}{C_I} = \left(\frac{tX_oY_o}{\alpha k_d}\right)^{\frac{1}{2}} \frac{R_{sf}(R)}{R} \frac{F_L}{Y} \frac{G\, i_h'}{[0.85G^2 e\beta(R) i_h + I_p^2/2\Delta f_v]^{\frac{1}{2}}}$$

$$= \frac{R_{sf}(R)}{R} \left[\frac{0.1 \times 3 \times 3 \times 3}{4 \times 8}\right]^{\frac{1}{2}}$$

$$\cdot \frac{(573/15)\, G\, i_h}{[0.85G^2(1.6 \times 10^{-19})\beta(R) i_h + (81 \times 10^{-18})/(18 \times 10^6)]^{\frac{1}{2}}}$$

with aperture correction

$$= \frac{R_{sf}(R)}{R} \frac{11.1\, G\, i_h}{[(1.36 \times 10^{-19})\beta(R) i_h + (4.5 \times 10^{-24})]^{\frac{1}{2}}} \qquad \text{(F-21)}$$

TABLE F-1. MTFs AND MTF-RELATED QUANTITIES, WITH APERTURE CORRECTION, 25/25/27-mm I-EBSICON[a]

N	I-Ebs MTF	Motion MTF, 25 μrad RMS	I-Ebs x Motion MTF	→ $(\ )^2$	$\sum$	Divided by	β(N)
0	1.000	1.000	1.000	1.000	1.000	1	1.000
50	0.988	0.989	0.977	0.955	1.955	2	0.977
100	0.956	0.956	0.914	0.835	1.873	2	0.936
150	0.877	0.904	0.793	0.629	2.604	3	0.868
200	0.853	0.835	0.712	0.507	3.173	4	0.793
250	0.785	0.755	0.593	0.351	3.602	5	0.720
300	0.785	0.667	0.523	0.274	3.914	6	0.652
350	0.746	0.577	0.430	0.185	4.144	7	0.592
400	0.668	0.487	0.325	0.106	4.289	8	0.536
450	0.573	0.402	0.230	0.053	4.369	9	0.485
500	0.456	0.325	0.148	0.022	4.406	10	0.441
550	0.338	0.257	0.087	0.008	4.421	11	0.402
600	0.204	0.198	0.040	0.002	4.426	12	0.369
650	0.100	0.150	0.015	--	--	13	0.340
700	0.050	0.111	0.005	--	--	14	0.316

N	I-Ebs x Motion MTF	Lens MTF	System MTF	$R_{sf}(N)$	Range, km
0	1.000	1.000	1.000	1.000	0.0
50	0.977	0.962	0.940	0.848	0.72
100	0.914	0.930	0.850	0.729	1.43
150	0.793	0.890	0.706	0.586	2.15
200	0.712	0.855	0.609	0.496	2.87
250	0.593	0.820	0.486	0.394	3.58
300	0.523	0.780	0.408	0.331	4.30
350	0.430	0.742	0.319	0.259	5.01
400	0.325	0.700	0.228	0.185	5.73
450	0.230	0.670	0.154	0.125	6.45
500	0.148	0.630	0.093	0.075	7.16
550	0.087	0.590	0.051	0.041	7.88
600	0.040	0.550	0.022	0.018	8.60
650	0.015	0.510	0.008	0.006	9.31
700	0.005	0.480	0.002	--	10.00

[a] Intensifier-camera used in Program 698DF.

TABLE F-2. MTFs and MTF-RELATED FACTORS FOR THE PASSIVE TV SYSTEM ASSUMED

Range, km	$R_{sf}(R)$	$\beta(R)$
0.0	1.000	1.000
0.5	0.890	0.985
1.0	0.790	0.960
1.5	0.700	0.937
2.0	0.620	0.882
2.5	0.540	0.830
3.0	0.470	0.777
3.5	0.410	0.727
4.0	0.360	0.680
4.5	0.305	0.637
5.0	0.255	0.595
5.5	0.210	0.555
6.0	0.165	0.518
6.5	0.125	0.483
7.0	0.090	0.453
7.5	0.060	0.427
8.0	0.035	0.400
8.5	0.020	0.377

Assume that a spectral filter is used that decreases the spectral band to 0.6-0.8 μm, and that the signal current is thereby cut in half:

$$i_h = 0.5\rho_{max} SAE_h / 4T^2. \qquad \text{(F-22)}$$

The lens T/stop is 3, and

$$A = 0.48\left(\frac{25 \text{ mm}}{25.4 \text{ mm}} \text{ in.}\right)^2 \frac{\text{ft}^2}{144}$$

$$= 3.33 \times 10^{-3} \text{ ft}^2,$$

and

$$i_h = \frac{0.5\ \rho_{max}(2 \times 10^{-4})(3.33 \times 10^{-3})E_h}{4 \times 9} \qquad \text{(F-23)}$$

$$= 9.26 \times 10^{-9}\ \rho_{max}\ E_h.^*$$

The sensor gain G is calculated from the relation

$$G = \frac{I_{op}}{(9.26 \times 10^{-4})E_h} = \frac{8 \times 10^{-7}}{(9.26 \times 10^{-4})E_h} \quad \begin{cases} \text{Maximum gain available} = 50{,}000 \\ \text{Minimum gain available} = 10 \end{cases} \qquad \text{(F-24)}$$

and the results are tabulated in Table F-3.

TABLE F-3. SENSOR GAIN AS FUNCTION OF SCENE LIGHT LEVEL

Sky Condition	E_h, fc	Calculated Gain	Useful Gain	i_h (ρ_{max} = 0.5)
Clear Starlight	1×10^{-4}	864,000	50,000	4.65×10^{-13}
1/4 Moon, Overcast	3.16×10^{-4}	272,322	50,000	1.47×10^{-12}
1/4 Moon	1×10^{-3}	86,400	50,000	4.65×10^{-12}
Full Moon, Overcast	3.16×10^{-3}	27,232	27,232	1.47×10^{-11}
Full Moon	1×10^{-2}	8,640	8,611	4.65×10^{-11}
Twilight, Overcast	3.16×10^{-2}	2,723	2,723	1.47×10^{-10}
Twilight	1×10^{-1}	864	864	4.65×10^{-10}

*The quantity E_h is in footcandles, which photometric units, as we have noted, are appropriate for use with the human eye but are inappropriate for use with electrooptical sensors. Lacking nocturnal light levels expressed in radiometric form, an approximate correspondence between photometric and radiometric units may be found, as is discussed in Appendix G. For the S-25 photosurface, the error in using photometric units rather than radiometric units is small. This is by no means the case in general, however, and photometric units must not be used unless the correspondence between photometric and radiometric units has been thoroughly investigated.

Note that when the calculated gain exceeds 50,000, the actual sensor gain will be at its maximum of 50,000. We now write the SNR_D equation for the various scene light levels in the forms

- Twilight
  $G = 864$
  $i_h = 4.65 \times 10^{-10}$

$$\frac{SNR_D}{C_I} = \frac{R_{sf}}{R} \frac{(1.165 \times 10^{-7})\ 38.2}{[(4.72 \times 10^{-23})\beta(N) + (4.5 \times 10^{-24})]^{\frac{1}{2}}}$$

F_L/Y^*

- Overcast Twilight
  $G = 2,723$
  $i_h = 1.47 \times 10^{-10}$

$$\frac{SNR_D}{C_I} = \frac{R_{sf}}{R} \frac{(1.165 \times 10^{-7})\ 38.2}{[(1.48 \times 10^{-22})\beta(N) + (4.5 \times 10^{-24})]^{\frac{1}{2}}}$$

- Full Moon
  $G = 8,611$
  $i_h = 4.65 \times 10^{-11}$

$$\frac{SNR_D}{C_I} = \frac{R_{sf}}{R} \frac{(1.165 \times 10^{-7})\ 38.2}{[(4.69 \times 10^{-22})\beta(N) + (4.5 \times 10^{-24})]^{\frac{1}{2}}}$$

- Overcast Full Moon
  $G = 27,232$
  $i_h = 1.47 \times 10^{-11}$

$$\frac{SNR_D}{C_I} = \frac{R_{sf}}{R} \frac{(1.165 \times 10^{-7})\ 38.2}{[(1.48 \times 10^{-21})\beta(N) + (4.5 \times 10^{-24})]^{\frac{1}{2}}}$$

- 1/4 Moon
  $G = 50,000$
  $i_h = 4.65 \times 10^{-12}$

$$\frac{SNR_D}{C_I} = \frac{R_{sf}}{R} \frac{(6.74 \times 10^{-8})\ 38.2}{[(1.58 \times 10^{-21})\beta(N) + (4.5 \times 10^{-24})]^{\frac{1}{2}}}$$

- Overcast 1/4 Moon
  $G = 50,000$
  $i_h = 1.47 \times 10^{-12}$

$$\frac{SNR_D}{C_I} = \frac{R_{sf}}{R} \frac{(2.13 \times 10^{-8})\ 38.2}{[(5 \times 10^{-22})\beta(N) + (4.5 \times 10^{-24})]^{\frac{1}{2}}}$$

- Clear Starlight
  $G = 50,000$
  $i_h = 4.65 \times 10^{-13}$

$$\frac{SNR_D}{C_I} = \frac{R_{sf}}{R} \frac{(6.74 \times 10^{-9})\ 38.2}{[(1.58 \times 10^{-22})\beta(N) + (4.5 \times 10^{-24})]^{\frac{1}{2}}}$$

---

*The ratio of focal length to picture height $F_L/Y = 38.2$.

As previously observed, the sensor will be predominantly photoelectron noise limited if the ratio of mean square photoelectron noise to preamplifier noise exceeds 5. The ratios of photoelectron noise to preamplifier noise are given in Table F-4 for the above conditions. Observe that we assumed a scene reflectivity of 0.5 in making the above calculations, so we have divided the ratios by 0.5 and multiplied the photoelectron noise by ρ_{max}, the highlight scene reflectivity.

TABLE F-4. RATIOS OF PHOTOELECTRON NOISE TO PREAMPLIFIER NOISE

Twilight	$10.5 \times \beta(N) \times \rho_{max}/0.5$
Overcast Twilight	$32.9 \times \beta(N) \times \rho_{max}/0.5$
Full Moon	$104.2 \times \beta(N) \times \rho_{max}/0.5$
Overcast Full Moon	$329 \times \beta(N) \times \rho_{max}/0.5$
1/4 Moon	$351 \times \beta(N) \times \rho_{max}/0.5$
Overcast 1/4 Moon	$111 \times \beta(N) \times \rho_{max}/0.5$
Clear Starlight	$35.1 \times \beta(N) \times \rho_{max}/0.5$

The average value of the noise-filtering function $\beta(N)$ is 0.5, and thus it can be seen that the sensor is primarily photoelectron noise limited throughout the range of light levels considered.

Using Eq. F-20 and the above parameters, we obtain

$$\frac{SNR_D}{C_I/[(2 - C_I)/2]^{\frac{1}{2}}} = \left[\frac{0.1 \times 9}{8}\right]^{\frac{1}{2}} \frac{R_{sf}(R)}{R} \times 10^{-3}$$

$$\times \frac{0.2}{2} \left[\frac{0.915 \times 0.5 \times 2\times10^{-4} \times 10.76\rho_{max}E_H}{1.6 \times 10^{-19}}\right]^{\frac{1}{2}} \quad \text{(F-25)}$$

$$= \frac{R_{sf}(R)}{R} \times 2631 \times \left[\frac{\rho_{max}E_h}{\beta(R)}\right]^{\frac{1}{2}},$$

where R is in kilometers and E_h is in footcandles. The SNR_D is calculated, tabulated in Table F-5, and plotted in Fig. F-2. We next calculate the atmospheric extinction coefficient* using an average λ of 0.7 μm and

$$\sigma = \frac{3.912}{V} \left[\frac{0.55}{0.70}\right]^{0.5V^{1/3}} , \qquad \text{(F-26)}$$

where V is the visibility, and next we calculate the ratio C_R/C_o from Eq. F-10. The values of σ and C_R/C_o are tabulated in Tables F-6 and F-7. The contrast normalization factor $[(2 - C_I)2]^{\frac{1}{2}}/C_I$ is evaluated by using the values of Table F-7 for C_R/C_o and the value of 0.5 for C_o. Note that C_I equals C_R. The SNR_D thresholds are tabulated in Table F-9 using the SNR_D range dependence and the normalization factors of Table F-8, i.e.,

$$SNR_{DT} = \frac{SNR_{DT}(R)}{C_I/[(2 - C_I)/2]^{\frac{1}{2}}} . \qquad \text{(F-27)}$$

The SNR_{DT} values are plotted for the various visibilities in Fig. F-2. The interactions of the SNR_D and SNR_{DT} curves give the threshold recognition ranges shown in Table F-10 and Fig. F-3.

---

*This appendix was written without benefit of the LOWTRAN 3 atmospheric transmission model, and Eq. F-26 is used in lieu of LOWTRAN 3.

TABLE F-5. SNR_D CALCULATION FOR PASSIVE TV

R, km	$R_{sf}(R)$	$\beta(R)$	Scene Light Level, footcandles equivalent								
			10^{-1}	3.16×10^{-2}	10^{-2}	3.16×10^{-3}	10^{-3}	3.16×10^{-4}	10^{-4}	3.16×10^{-5}	10^{-5}
0.0	1.000	1.000	∞	∞	∞	∞	∞	∞	∞	∞	∞
0.5	0.890	0.985	1055	593	334	188	106	59.3	33.4	18.7	10.6
1.0	0.790	0.960	474	266	150	84.3	47.4	26.7	15.0	8.43	4.74
1.5	0.700	0.937	284	160	89.8	50.5	28.4	16.0	9.0	5.05	2.84
2.0	0.620	0.882	194	109	61.3	34.5	19.4	10.9	6.1	3.4	1.94
2.5	0.540	0.830	140	78.7	44.3	24.9	14.0	7.9	4.4	2.5	1.40
3.0	0.470	0.777	105	59.0	33.2	18.7	10.5	5.9	3.3	1.9	--
3.5	0.410	0.727	80.8	45.5	25.6	14.4	8.10	4.6	2.6	1.1	--
4.0	0.360	0.680	64.2	36.1	20.3	11.4	6.42	3.6	2.0	--	--
4.5	0.305	0.637	50.0	28.1	15.8	8.9	5.0	2.8	1.6	--	--
5.0	0.255	0.595	38.9	21.9	12.3	6.9	3.9	2.2	1.2	--	--
5.5	0.210	0.555	30.1	16.9	9.5	5.35	3.0	1.7	--	--	--
6.0	0.165	0.518	22.5	12.7	7.1	4.0	2.3	1.3	--	--	--
6.5	0.125	0.483	16.8	9.2	5.2	2.9	1.6	--	--	--	--
7.0	0.090	0.453	11.2	6.3	3.5	2.0	1.1	--	--	--	--
7.5	0.060	0.427	7.2	4.0	2.8	1.3	--	--	--	--	--
8.0	0.035	0.400	4.1	2.3	1.3	--	--	--	--	--	--
8.5	0.020	0.377	2.3	1.3	--	--	--	--	--	--	--

TABLE F-6. ATMOSPHERIC EXTINCTION COEFFICIENT

Visibility, km	σ, km^{-1}
2	1.681
4	0.808
6	0.524
8	0.384
10	0.233
15	0.144
20	0.102

TABLE F-7. C_R/C_o VERSUS VISIBILITY

Range, km	C_R/C_o for Visibility, km, of 20	15	10	8	6	4	2
0.5	0.905	0.870	0.802	0.703	0.625	0.501	0.275
1.0	0.823	0.763	0.656	0.516	0.421	0.287	0.103
2.0	0.688	0.600	0.457	0.302	0.212	0.110	0.018
4.0	0.498	0.391	0.245	0.121	0.066	0.020	--
6.0	0.372	0.267	0.141	0.053	0.022	0.004	--
8.0	0.284	0.188	0.084	0.024	0.008	--	--
10.0	0.220	0.134	0.051	0.011	--	--	--

TABLE F-8. CONTRAST NORMALIZATION FACTOR

Range, km	$[(2 - C_I)/2]^{\frac{1}{2}}/C_I$ for Visibility, km, of 20	15	10	8	6	4	2
0.5	1.94	2.03	2.23	2.58	2.94	3.73	7.01
1.0	2.17	2.36	2.79	3.62	4.49	6.71	19.2
2.0	2.41	3.07	4.12	6.37	9.18	17.9	111.9
4.0	3.78	4.86	7.91	16.3	30.1	99.7	--
6.0	4.88	7.24	13.9	37.5	90.7	--	--
8.0	6.78	10.4	23.6	83.1	250	--	--
10.0	8.84	14.7	39.0	182	--	--	--

TABLE F-9. THRESHOLD SIGNAL-TO-NOISE RATIOS

Range, km	SNR_{DT} $C_I = 1$ Vacuum	SNR_{DT} for Visibility, km, of 20	15	10	8	6	4	2
0.5	2.90	5.63	5.89	6.47	7.48	8.53	10.8	20.3
1.0	2.77	6.01	6.54	7.73	10.0	12.4	18.6	53.1
2.0	2.56	6.17	7.86	10.5	16.3	23.5	45.8	286
4.0	2.50	9.45	12.2	19.8	40.8	75.3	250	--
6.0	2.30	11.2	16.7	32.0	86.3	209	--	--
8.0	1.90	12.9	19.8	44.8	158	--	--	--
10.0	1.50	13.3	22.1	58.5	273	--	--	--

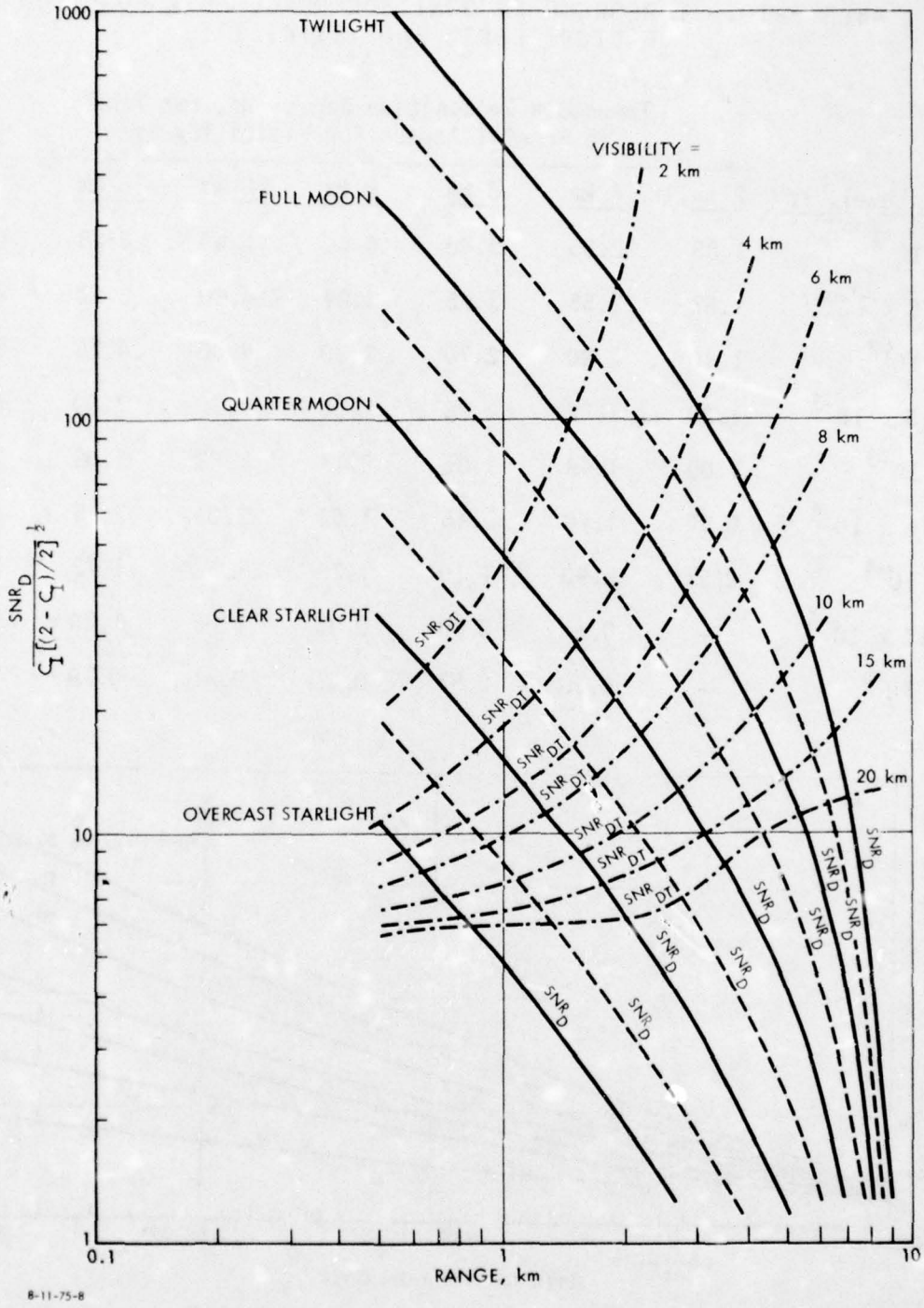


FIGURE F-2. SNR_D versus Range for Various Light Levels, and SNR_{DT} versus Range for Various Light Levels and Visibilities.

TABLE F-10. THRESHOLD RECOGNITION RANGE AS A FUNCTION OF LIGHT LEVEL AND VISIBILITY

Light Level, fc	Threshold Recognition Range, km, for Tank in Frontal Aspect for Visibility of						
	2 km	4 km	6 km	8 km	10 km	15 km	20 km
10^{-1}	1.85	2.95	3.80	4.60	5.60	6.28	6.90
3.16×10^{-2}	1.62	2.55	3.25	3.82	4.80	5.60	6.10
10^{-2}	1.40	2.20	2.75	3.20	4.00	4.75	5.30
3.16×10^{-3}	1.20	1.82	2.28	2.60	3.30	3.90	4.30
10^{-3}	1.00	1.48	1.85	2.13	2.62	3.08	3.40
3.16×10^{-4}	0.81	1.18	1.45	1.68	2.03	2.35	2.75
10^{-4}	0.63	0.90	1.10	1.25	1.50	1.72	2.00
3.16×10^{-5}	--	0.67	0.80	0.91	1.06	1.20	1.30
10^{-5}	--	0.50	0.57	0.62	0.71	0.79	0.83

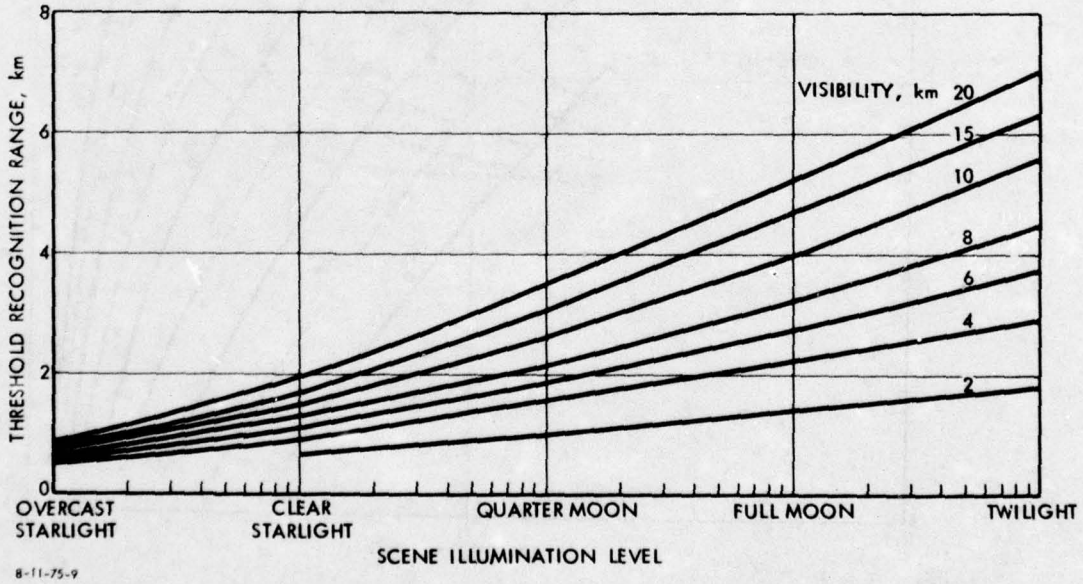


FIGURE F-3. Threshold Recognition Range versus Light Level for Various Visibilities, $C_o = 0.5$, $\rho_{max} = 0.5$, $\lambda_{av} = 0.7$ μm.

APPENDIX G

APPROXIMATE RELATIONSHIP OF PHOTOMETRIC AND RADIOMETRIC QUANTITIES

Frederick A. Rosell

Defense and Electronic Systems Center
Westinghouse Electric Corporation

APPROXIMATE RELATIONSHIP OF PHOTOMETRIC AND RADIOMETRIC QUANTITIES

In converting from photometrics to radiometrics, it will first be worthwhile to review the current methods of analysis using photometric units. The luminous sensitivity of photosurfaces is often measured by using a 2854°K source. A known amount of light measured in footcandles is projected on the photocathode, and the current drawn from the surface is measured. The ratio in amperes/lumen, or, more commonly, in microamperes/lumen, is known as the luminous sensitivity; the luminous sensitivity S can be calculated from the relation

$$S = \frac{\sigma_o \int_\lambda R(\lambda)\, M_{2854°K}(\lambda)\, d\lambda}{680 \int_\lambda y(\lambda)\, M_{2854°K}(\lambda)\, d\lambda} \quad \frac{\text{amperes}}{\text{lumen}}, \qquad \text{(G-1)}$$

where

σ_o is the spectral responsivity of the photosurface at the peak in amperes/watt

$R(\lambda)$ is the relative spectral response of the photosurface

$M_{2854°K}$ is the relative spectral emittance of a 2854°K source

680 is the peak response of the human eye in lumens/watt

$y(\lambda)$ is the relative spectral response of the eye.

The result of performing the calculation using the S-25 surface is 198 μA/lm, which corresponds closely to the value of 200 μA/lm quoted by the manufacturer of the S-25.

PRECEDING PAGE BLANK-NOT FILMED

The illuminance of the earth, or a particular target on it, is either measured with a photometer or calculated, if the spectral irradiance of the source is known, as follows:

$$E_s = 680 \int_{\lambda} y(\lambda) E(\lambda) d\lambda \ \frac{lm}{ft^2} = fc \ , \qquad (G\text{-}2)$$

where the terms are as before, except for $E(\lambda)$, which is the source irradiance in watts/square foot. The results of this calculation for four cases (full moon, 0.3 full moon, 0.1 full moon, and 0.03 full moon, all plus airglow) as a function of the number of air masses between the moon and the irradiated area, are compiled in Tables G-1 through G-4. The number of air masses between the illuminated area and the moon is shown in Fig. G-1, and the spectral distribution for 0.1 full moon plus airglow is shown in Fig. G-2 for various values of air masses.

In making system calculations, it is customary in current practice to use the illuminance calculated by Eq. G-2 together with the photocathode luminous sensitivity as calculated in Eq. G-1 to obtain the photocathode signal current from the relation

$$i_{pc} = \frac{\rho}{4T^2} SAE_s \ , \qquad (G\text{-}3)$$

where ρ is the scene reflectivity (assumed to be independent of wavelength), T is the T/stop of the objective lens, and A is the photocathode area.

The luminous sensitivity of the photosurface, as defined by Eq. G-2, has some utility as an indicator of photosurface quality. A quick conversion from amperes/lumen to amperes/watt can be obtained by noting that the luminous efficiency of tungsten

TABLE G-1. RELATIONSHIP BETWEEN RADIOMETRIC AND PHOTOMETRIC QUANTITIES, FULL MOON PLUS AIRGLOW WITH S-25 PHOTOCATHODE

	1 Air Mass	2 Air Masses	3 Air Masses	4 Air Masses	5 Air Masses	6 Air Masses
Natural Illuminance, fc	1.532×10^{-2}	1.228×10^{-2}	1.004×10^{-2}	8.2×10^{-3}	6.67×10^{-3}	5.42×10^{-3}
Natural Irradiance, W/m^2	1.066×10^{-3}	8.718×10^{-4}	7.309×10^{-4}	6.06×10^{-4}	5.052×10^{-4}	4.246×10^{-4}
Radiant Sensitivity, A/m^2	2.537×10^{-5}	2.042×10^{-5}	1.676×10^{-5}	1.368×10^{-5}	1.113×10^{-5}	9.157×10^{-6}
Radiometric Responsivity, A/W	2.379×10^{-2}	2.343×10^{-2}	2.294×10^{-2}	2.258×10^{-2}	2.203×10^{-2}	2.157×10^{-2}
Luminous Sensitivity, A/lm	1.983×10^{-4}	1.983×10^{-4}	1.983×10^{-4}	1.983×10^{-4}	1.983×10^{-4}	1.983×10^{-4}
Correction Factor, $\frac{i_{pc}\ \text{illuminance basis}}{i_{pc}\ \text{irradiance basis}}$	1.287	1.281	1.277	1.277	1.277	1.261

TABLE G-2. RELATIONSHIP BETWEEN RADIOMETRIC AND PHOTOMETRIC QUANTITIES, 0.3 FULL MOON PLUS AIRGLOW WITH S-25 PHOTOCATHODE

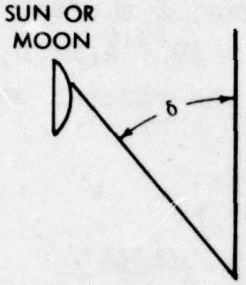
	1 Air Mass	2 Air Masses	3 Air Masses	4 Air Masses	5 Air Masses	6 Air Masses
Natural Illuminance, fc	4.602×10^{-3}	3.696×10^{-3}	3.013×10^{-3}	2.46×10^{-3}	2.007×10^{-3}	1.001×10^{-3}
Natural Irradiance, W/m^2	3.237×10^{-4}	2.624×10^{-4}	2.199×10^{-4}	1.818×10^{-4}	1.525×10^{-4}	1.277×10^{-4}
Radiant Sensitivity, A/m^2	7.663×10^{-6}	6.146×10^{-6}	5.04×10^{-6}	4.106×10^{-6}	3.365×10^{-6}	2.745×10^{-6}
Radiometric Responsivity, A/W	2.367×10^{-2}	2.342×10^{-2}	2.291×10^{-2}	2.259×10^{-2}	2.207×10^{-2}	2.15×10^{-2}
Luminous Sensitivity, A/lm	1.983×10^{-4}	1.983×10^{-4}	1.983×10^{-4}	1.983×10^{-4}	1.983×10^{-4}	1.983×10^{-4}
Correction Factor, $\frac{i_{pc}\ \text{illuminance basis}}{i_{pc}\ \text{irradiance basis}}$	1.279	1.281	1.274	1.277	1.271	1.264

TABLE G-3. RELATIONSHIP BETWEEN RADIOMETRIC AND PHOTOMETRIC QUANTITIES, 0.1 FULL MOON PLUS AIRGLOW WITH S-25 PHOTOCATHODE

	1 Air Mass	2 Air Masses	3 Air Masses	4 Air Masses	5 Air Masses	6 Air Masses
Natural Illuminance, fc	1.539×10^{-3}	1.22×10^{-3}	1.011×10^{-3}	8.25×10^{-4}	6.742×10^{-4}	5.402×10^{-4}
Natural Irradiance, W/m^2	1.087×10^{-4}	8.82×10^{-5}	7.408×10^{-5}	6.151×10^{-5}	5.151×10^{-5}	4.345×10^{-5}
Radiant Sensitivity, A/m^2	2.567×10^{-6}	2.061×10^{-6}	1.693×10^{-6}	1.382×10^{-6}	1.129×10^{-6}	9.327×10^{-7}
Radiometric Responsivity, A/W	2.363×10^{-2}	2.336×10^{-2}	2.285×10^{-2}	2.246×10^{-2}	2.192×10^{-2}	2.147×10^{-2}
Luminous Sensitivity, A/lm	1.983×10^{-4}	1.983×10^{-4}	1.983×10^{-4}	1.983×10^{-3}	1.983×10^{-3}	1.983×10^{-3}
Correction Factor, $\frac{i_{pc}\ \text{illuminance basis}}{i_{pc}\ \text{irradiance basis}}$	1.278	1.261	1.273	1.274	1.272	1.234

TABLE G-4. RELATIONSHIP BETWEEN RADIOMETRIC AND PHOTOMETRIC QUANTITIES, 0.03 FULL MOON PLUS AIRGLOW WITH S-25 PHOTOCATHODE

	1 Air Mass	2 Air Masses	3 Air Masses	4 Air Masses	5 Air Masses	6 Air Masses
Natural Illuminance, fc	4.672×10^{-4}	3.766×10^{-4}	3.089×10^{-4}	2.536×10^{-4}	2.078×10^{-4}	1.7×10^{-4}
Natural Irradiance, W/m^2	3.336×10^{-5}	2.724×10^{-5}	2.3×10^{-5}	1.926×10^{-5}	1.623×10^{-5}	1.381×10^{-5}
Radiant Sensitivity, A/m^2	7.832×10^{-7}	6.317×10^{-7}	5.211×10^{-7}	4.289×10^{-7}	3.521×10^{-7}	2.928×10^{-7}
Radiometric Responsivity, A/W	2.347×10^{-2}	2.319×10^{-2}	2.266×10^{-2}	2.227×10^{-2}	2.169×10^{-2}	2.12×10^{-2}
Luminous Sensitivity, A/lm	1.983×10^{-4}	1.983×10^{-4}	1.983×10^{-4}	1.983×10^{-4}	1.983×10^{-4}	1.983×10^{-4}
Correction Factor, $\frac{i_{pc}\ \text{illuminance basis}}{i_{pc}\ \text{irradiance basis}}$	1.2716	1.2713	1.2635	1.2604	1.2479	1.282



OPTICAL AIR MASS	δ, deg
m = 1	0
m = 2	60.0
m = 3	70.5
m = 4	75.5
m = 5	78.5

8-8-75-25

P = 760 mm PRESSURE
W = 2.0/cm WATER VAPOR*
D = 300 DUST PARTICLES/cm^3
OZONE = 0.28 atm-cm

*Per unit of optical air mass

FIGURE G-1. Air Mass versus Source Declination.

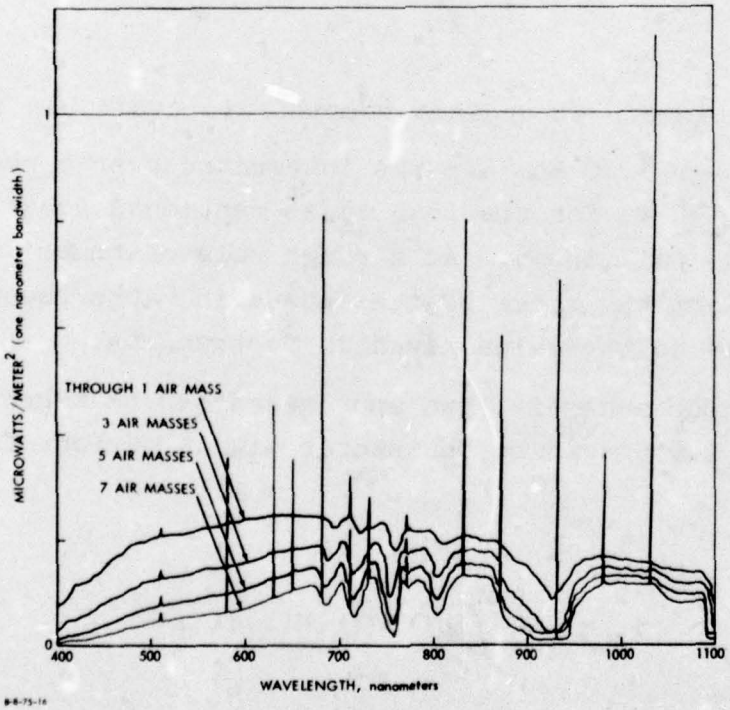


FIGURE G-2. Irradiance from 0.1 x Full Moon plus Airglow.

at 2854°K is about 20 lm/W. Thus, a surface of luminous sensitivity 2 x 10^{-4} A/lm becomes 4 x 10^{-3} A/W in radiometric terms. Alternatively, one can compute the radiant sensitivity P_R from the relation

$$P_R = \frac{\sigma_o \int_\lambda R(\lambda)\, W_{2854°K}(\lambda)d\lambda}{\int_\lambda W_{2854°K}(\lambda)d\lambda} \quad \frac{\text{amperes}}{\text{watt}} \; . \qquad \text{(G-4)}$$

The illuminance of the earth by natural radiant sources is quite commonly known, and it would be desirable to develop radiometric equivalents such as

$$E_T = \int_\lambda E(\lambda)d\lambda \; . \qquad \text{(G-5)}$$

Tables for a number of radiant sources are available in Ref. 1.

The integral of Eq. G-5 was integrated over a spectral band of 0.35 to 0.94 μm for the four cases mentioned above (1.0, 0.3, 0.1, and 0.03 full moon). As a rough rule of thumb, the natural irradiance from the three sources above in watts/square meter is about 1/14 of the value given in footcandles.

For sensor analysis, two approaches can be taken. The most direct is to compute the sensor signal current from the equation

$$i_S = \frac{A\sigma}{4T^2} \int \rho(\lambda)R(\lambda)H(\lambda)d\lambda \; . \qquad \text{(G-6)}$$

The value of this integral in the form of $4T^2\, i_S/A$ is provided for the sensors in Tables G-1 through G-4.

An alternate method corresponding to that used in current psychometric calculations is to define a specific radiant sensitivity similar to the radiant sensitivity term of Eq. G-4 as

$$\sigma = \frac{\sigma_o \int R(\lambda)H(\lambda)d\lambda}{\int H(\lambda)d\lambda} . \qquad \text{(G-7)}$$

This term is also compiled in Tables G-1 through G-4. This quantity has some use when viewing objects of neutral reflectivity; i.e., reflectivity which is constant with wavelength. In this event, one can calculate the signal current from the simple equation

$$i_S = \frac{\rho}{4T^2} [\sigma \cdot A \cdot H_T] = \sigma A H_{pc} , \qquad \text{(G-8)}$$

which compares directly with Eq. G-3.

Now it is of interest to compare the results obtained using Eq. G-3 with those obtained using Eq. G-8 in the form

$$\frac{i_S \text{ (illuminance basis)}}{i_S \text{ (irradiance basis)}} = \frac{SAE_S}{\sigma A H_T} , \qquad \text{(G-9)}$$

as shown in Tables G-1 through G-4. This ratio for the specific photosurfaces involved, and assuming neutral reflectivity, is very nearly constant, equal to about 1.25 for all three sources assumed. This result, as mentioned above, is pure happenstance, although it is perhaps comforting to know that most of the rough first-order calculations made using photometric terms are very nearly correct (optimistic by about 25%).

In the more general aerial reconnaissance case, spectral filters are used to enhance scene object contrast and new relations between the radiometric and photometric measures will be required. The procedure above should apply, however.

REFERENCE, APPENDIX G

1. L.M. Biberman, "Luminance, Radiance, and Temperature," Chapter 2 in L.M. Biberman and S. Nudelman, eds., Photoelectronic Imaging Devices, Vol. 1, Physical Processes and Methods of Analysis, Plenum Press, New York, 1971, pp. 9-38.

APPENDIX H

EFFECTS OF FLIGHT VIBRATION, AIR TURBULENCE, ACCELERATION, VIEWING DISTANCE, AND IMAGE SIZE ON THE PERFORMANCE OF AIRBORNE OBSERVERS AND THUS ON THE REQUIRED THRESHOLD SIGNAL-TO-NOISE RATIO AT THE DISPLAY

Frederick A. Rosell and Robert H. Willson

Defense and Electronic Systems Center
Westinghouse Electric Corporation

EFFECTS OF FLIGHT VIBRATION, AIR TURBULENCE, ACCELERATION, VIEWING DISTANCE, AND IMAGE SIZE ON THE PERFORMANCE OF AIRBORNE OBSERVERS AND THUS ON THE REQUIRED THRESHOLD SIGNAL-TO-NOISE RATIO AT THE DISPLAY

Early in Chapter IV, we discussed the values of SNR_D for the bars of an equivalent bar pattern as computed for favorable field-test and laboratory conditions. It is to be expected that seeing small images would be more difficult in a vibrating aircraft buffeted by air turbulence than in a laboratory, just as reading a newspaper on a moving bus is more difficult on a rough road than on a smooth one. Here we shall briefly consider some of the effects of flight on perception of electrooptically displayed images (squares and bar patterns).

The value of threshold SNR_D is relatively constant over a broad range of image sizes and then grows rapidly for sizes either much larger or much smaller (Fig. H-1). The smaller images are smeared or blurred by the modulation transfer function (MTF) of the eye, and the reduced contrast of those images necessitates a larger SNR_D. For the larger images, the limitations of the eye as a spatial integrator come into play, again requiring compensation in the form of SNR_D. The effects are discussed more completely in Refs. 1-9.

The threshold SNR_D, which by definition corresponds to a 50% probability of detection, is plotted in Fig. H-1. Note the increase in SNR_D needed for a 2 x 2-line square. This square subtends about 1 mrad at the eye. Thus, the ability of the observer to detect images subtending less than about 1 mrad will be limited by the MTF of the observer's eye. The threshold signal-to-noise ratios at the display (SNR_{DT}) that are required for various square sizes are summarized in Table H-1 for various

PRECEDING PAGE BLANK-NOT FILMED

squares at a viewing-distance-to-display-height ratio (D_V/D_H) of 3.5. If the viewing distance is doubled using the same display, the SNR_{DT} applying to a 4 x 4-line square becomes that for a 2 x 2 square, as illustrated in Table H-1.

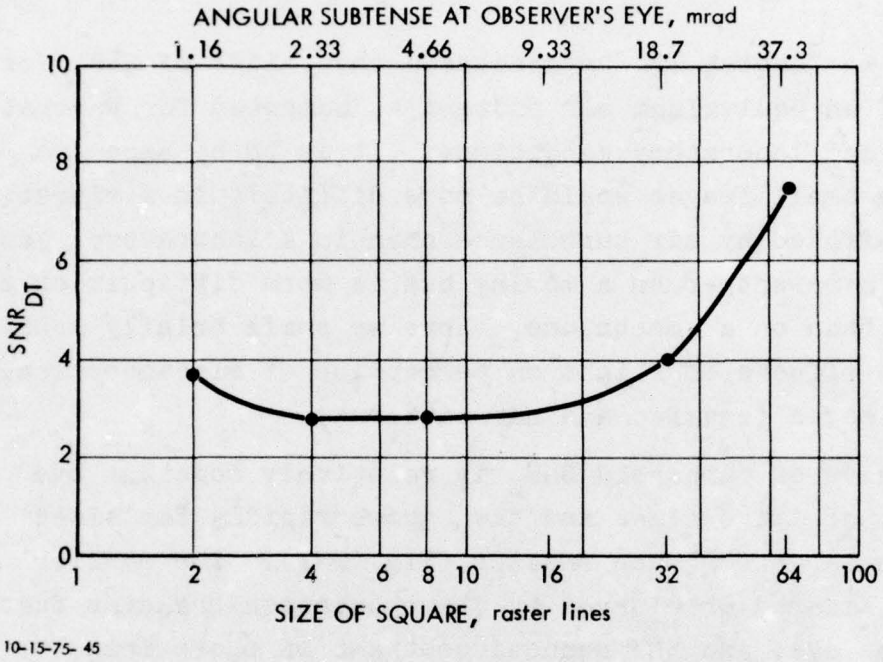


FIGURE H-1. SNR_{DT} versus Size of Square Image. $D_V/D_H = 3.5$.

It is clear the factor of 2 in D_V/D_H corresponds to a factor of 2 in viewing angle. Thus, the 4 x 4 square at $D_V/D_H = 7$ appears to the eye as identical to a 2 x 2 square at $D_V/D_H = 3.5$. The SNR_{DT} is therefore identically 3.7 for both cases.

The primary effect of the viewing-distance-to-display-height ratio is to change the observer threshold somewhat when the observer is comfortably viewing a stationary display. The change is not large for square images which subtend angles from 1 to 15 mrad at the observer's eye. In an environment of severe vibration, one would expect the detectability of small images to be degraded more than that of larger images.

TABLE H-1. SNR_{DT} VERSUS SIZE OF SQUARE IMAGE FOR TWO VALUES OF D_V/D_H

Image Size, raster lines	SNR_{DT} for $D_V/D_H = 3.5$	SNR_{DT} for $D_V/D_H = 7.0$
2 x 2	3.7	-
4 x 4	2.8	3.7
8 x 8	2.8	2.8
16 x 16	3.3	2.8
32 x 32	4.0	3.3
64 x 64	7.5	4.0

To study such effects, four flights were flown in early spring 1975, and a total of 1,928 data points were taken in conditions of straight-and-level flight, air turbulence, 2.5g turns, and 1.5g turns. Figure H-2 illustrates the placement of observers and displays.

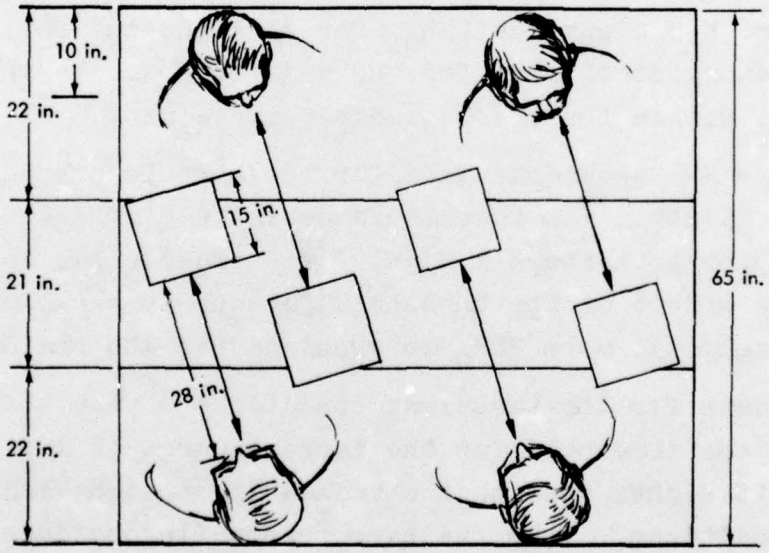


FIGURE H-2. Layout of Observer's Compartment.

Table H-2 shows the numbers of observations on square images made in various conditions during each of the four flights.

TABLE H-2. NUMBERS OF OBSERVATIONS TAKEN EACH FLIGHT FOR VARIOUS CONDITIONS, SQUARE IMAGES

Flight No.	Condition			
	Straight & Level Flight	Air Turbulence	2.5g Turns	1.5g Turns
1	400	40	32	20
2	324	28	48	--
3	60	400	56	--
4	60	400	60	--

An analysis of the data from the first flight indicates (a) no noticeable effect due to 1.5g turns, (b) only a slight effect (if any) due to 2.5g turns, and (c) a definite effect due to air turbulence. Data from straight-and-level flight were virtually identical to laboratory data.

Figure H-3 shows the SNR_{DT} for straight-and-level flight and laboratory conditions for the same observers. The flight values are within 10% of the laboratory values.

Figure H-4 shows the data for the turbulent conditions of the third flight. The turbulence definitely affected the threshold for both the 2 x 2 and 4 x 4 squares but apparently had little effect on the threshold for the larger squares. Approximately 33% more SNR_D is required for the smaller squares.

The data for the turbulent conditions of the third flight show that the threshold for the large squares (8 x 8 and 16 x 16) is only 14% higher than that obtained in straight-and-level flight conditions. Thus, we have reasonable confidence that turbulence of the type encountered has little effect on larger squares.

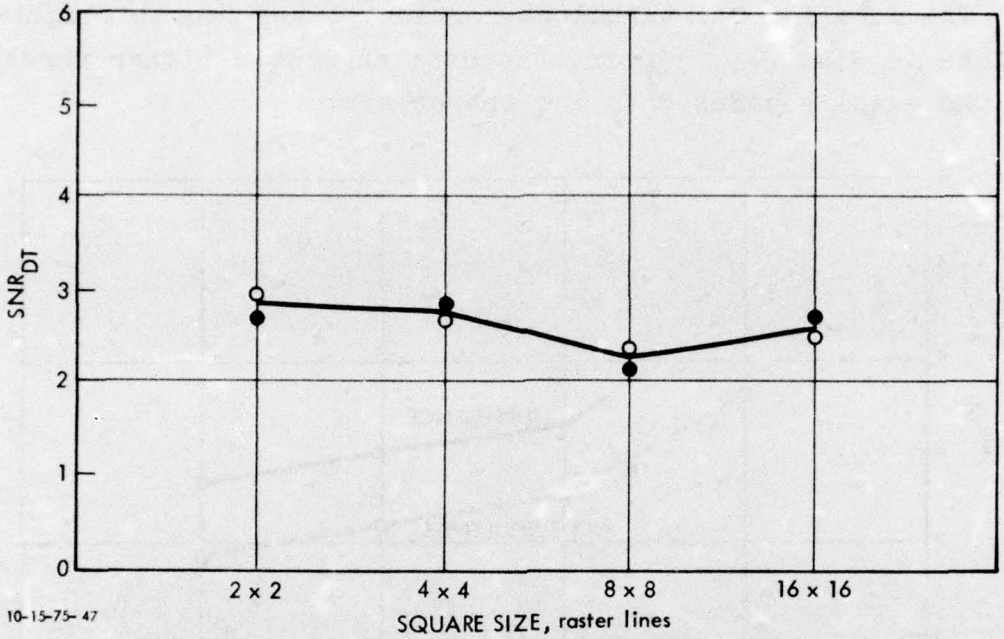


FIGURE H-3. SNR_{DT} as a Function of Square Size for Straight-and-Level Flight (o) and Laboratory Conditions (•).

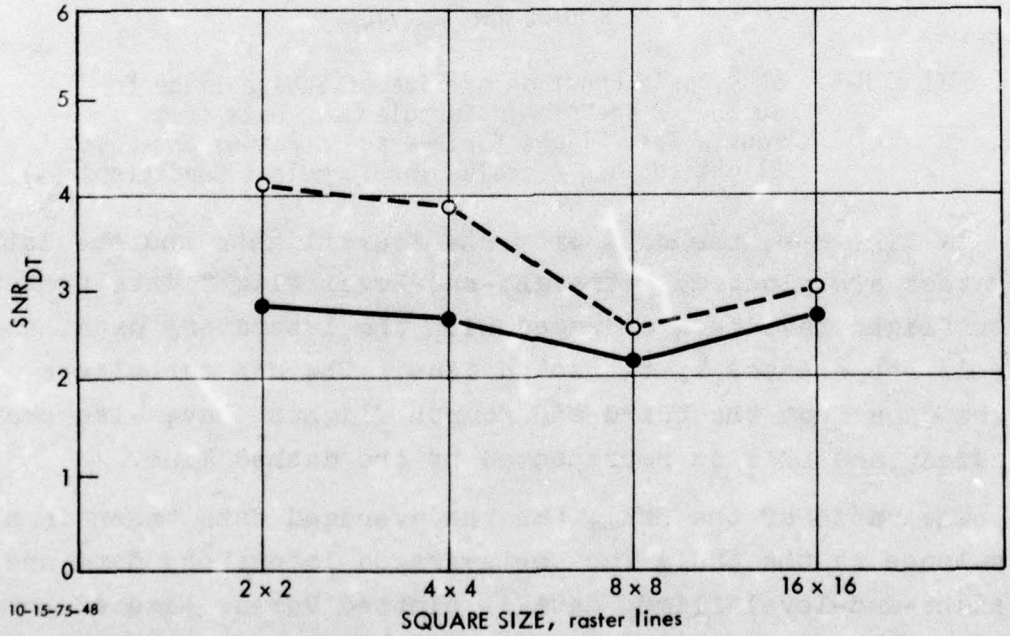


FIGURE H-4. SNR_{DT} as a Function of Size of Square Image for ±0.2g, 1 sec of Air Turbulence. Data from Third Test Flight (o) and Average Straight-and-Level Flight (•).

The data for the turbulent portion of the fourth flight are plotted in Fig. H-5. Again, the data suggest a higher threshold for the small squares than for the others.

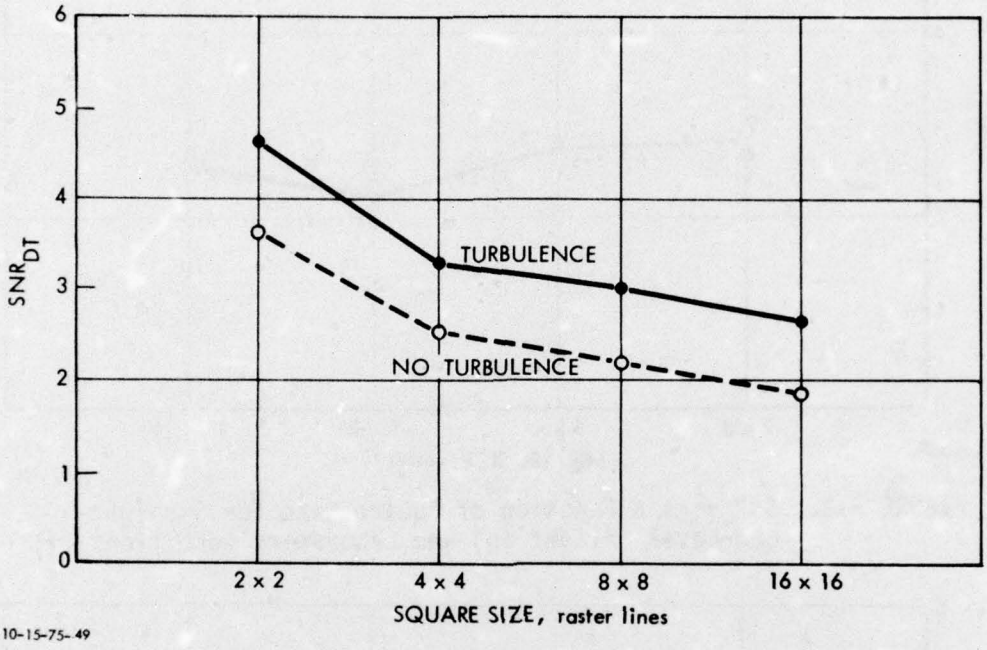


FIGURE H-5. SNR_{DT} as a Function of Size of Square Image for ±0.35g, 2 sec of Air Turbulence. Data from Fourth Test Flight for Average Straight-and-Level Flight (o) and Rescaled for Turbulent Conditions (•).

In Fig. H-6, the data from the four flights and the laboratory test are plotted. Straight-and-level flight data from the first flight have been averaged with the laboratory data, and this is represented by the solid line. The air turbulence flight data from the third and fourth flights have also been averaged, and this is represented by the dashed line.

The ratio of the SNR_{DT} for the averaged data taken in air turbulence to the SNR_{DT} for the averaged laboratory data and straight-and-level flight data is plotted versus size of square image in Fig. H-7 and represents the effect of the average air turbulence in the experiment on image size requirements.

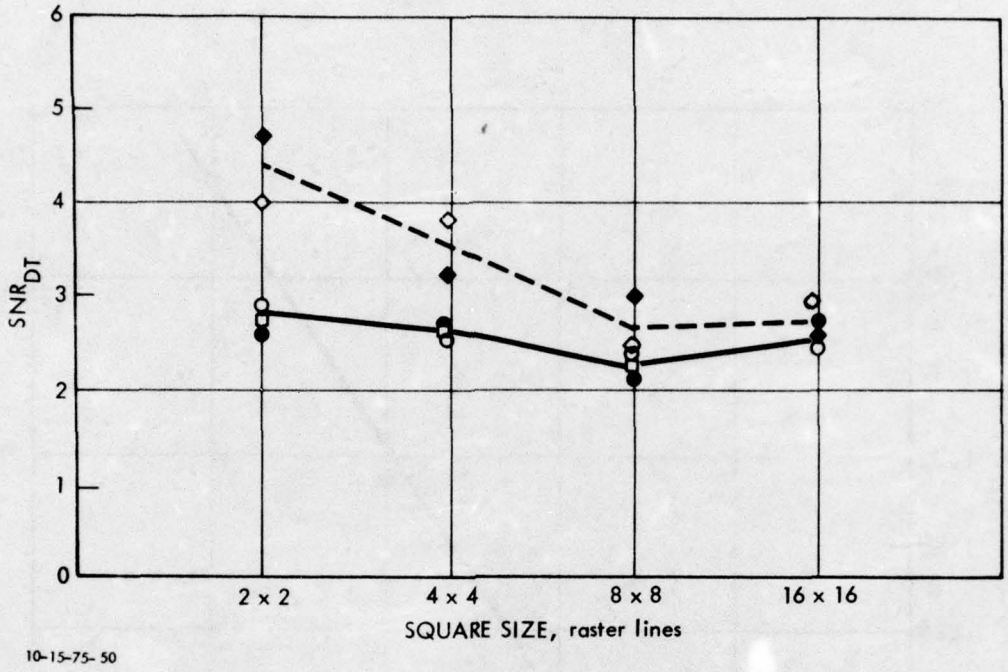


FIGURE H-6. SNR_{DT} as a Function of Size of Square Image for the Four Test Flights and Laboratory Conditions: Laboratory (•); Straight-and-Level Flight, Flight No. 1 (o); Straight-and-Level Flight, Flight No. 2 (Scaled) (▫); Air Turbulence, Flight No. 3 (◇); and Air Turbulence, Flight No. 4 (Scaled) (◆).

It is interesting to note that, for the average air turbulence represented by the experiment, an experimental relationship between the ratio and the square size is suggested by the data of Fig. H-7. This is analogous to the effect due to random motion of the input photocathode of an electrooptical integrating sensor.

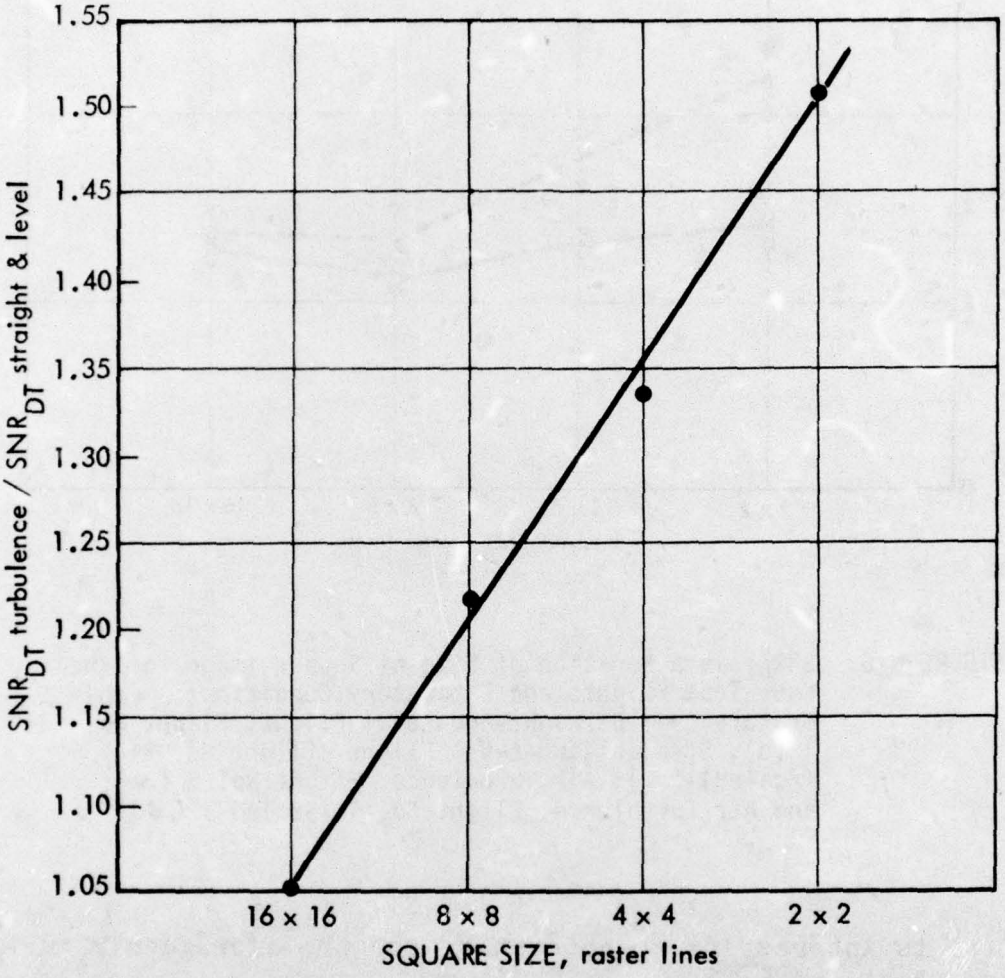


FIGURE H-7. Ratio of SNR_{DT} for Average of Data Taken on Flights in Air Turbulence to SNR_{DT} for Average of Data Taken on Straight-and-Level Flights and in the Laboratory versus Size of Square Image. Note that about 50% more signal is required for the 2x2 image than for the 16x16 image.

In general, the observers *believed* that turbulence made it more difficult to detect the squares (much more work was required to search out the four quadrants). Also, it *appeared* that the squares were broken up by the turbulence and were therefore more difficult to see. The same amount of air turbulence had less effect on bar-pattern recognition than on square detection.

The observers *believed* that they fatigued after taking 60 data points or so, but the data do not show effects of this fatigue.

Figures H-8 through H-12 show the effects of turbulent flight upon the SNR_{DT} for bar patterns. As is explained in Refs. 1-9, the data on rectangles apply well to detection of isolated (nonperiodic) imagery and could apply to finding a large ship against a calm sea.

For higher order tasks, such as detection in a cluttered background, recognition, or identification, the periodic models apply, and equivalent bar patterns adjusted for the aspect ratios of the objects to be seen are the appropriate test objects or models (Refs. 1-9).

Thus, the data in Figs. H-3 through H-7 show the effects of flight-condition degradation on the incremental SNR_{DT} for the non-periodic simple detection case, and the data in Figs H-8 through H-12 show the increments in SNR_{DT} for bar patterns, and thus the typical incremental effects for recognition or identification.

It is clear from the limited data obtained in the flight tests just discussed that conditions of air turbulence will degrade pilot perception of a displayed image or, conversely, will increase the SNR_{DT} required.

Such factors have <u>not</u> been taken into account in our predictions of ranges at which electrooptical sensors can be used. When such factors are more completely documented, they must be considered in the planning and evaluation of imaging sensor systems.

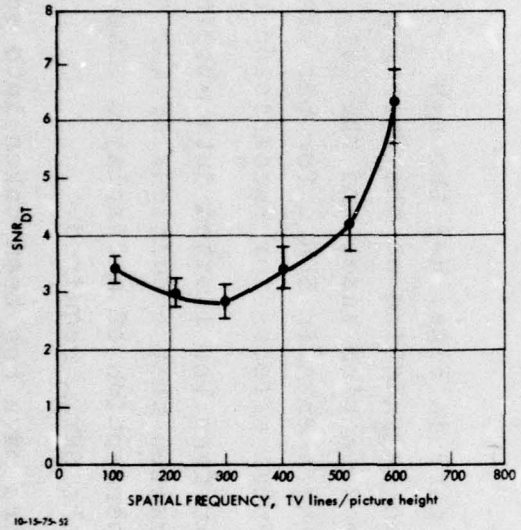


FIGURE H-8. Average SNR$_{DT}$ for Bar-Pattern Recognition in Straight-and-Level Flight as a Function of Spatial Frequency, ±1σ Limits.

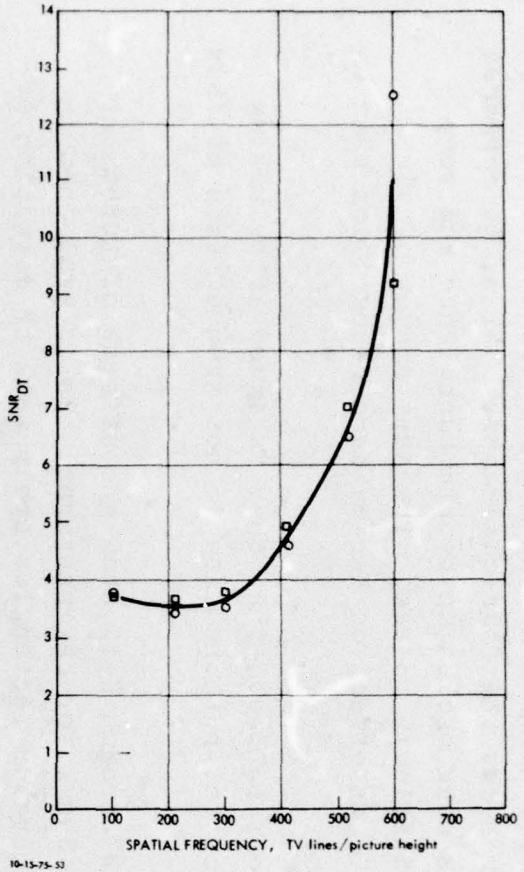


FIGURE H-9. SNR$_{DT}$ for Bar-Pattern Recognition in Air Turbulence as a Function of Spatial Frequency: Method of Limits, Flight No. 6 (o); Random dB, Flight No. 7 (□); and Average (——).

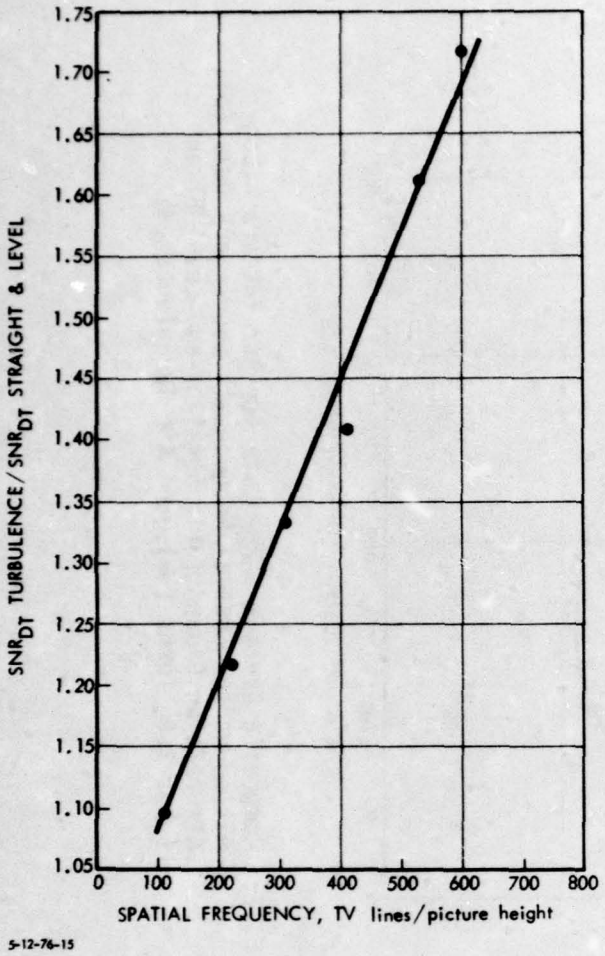


FIGURE H-10. Ratio of SNR_{DT} in Air Turbulence to SNR_{DT} in Straight-and-Level Flight versus Spatial Frequency, Bar-Pattern Recognition.

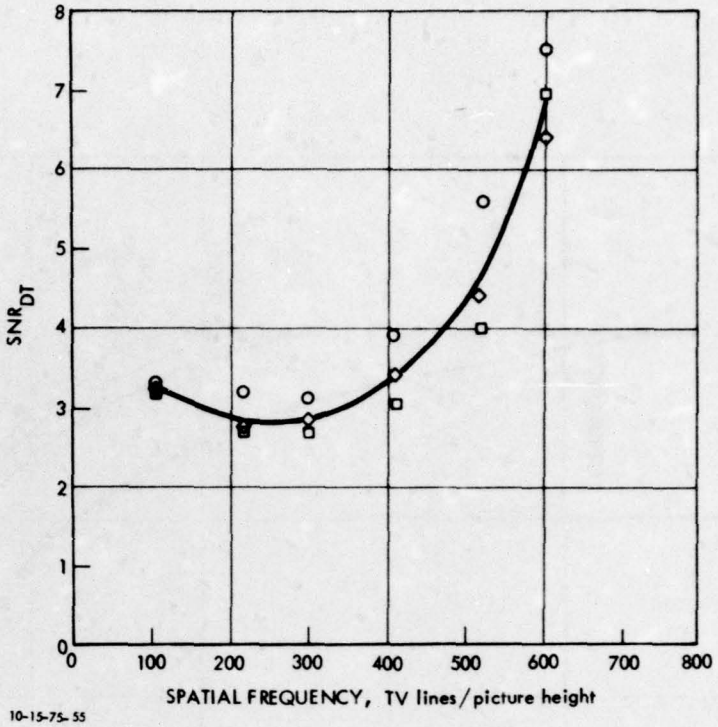


FIGURE H-11. SNR_{DT} as a Function of Spatial Frequency During 2.5g Steep Turns, Bar-Pattern Recognition: Random dB, Flight No. 7 (o); Method of Limits, Flight Nos. 5, 6, 8 (□); Random dB, Flight No. 8 (◇); and Composite Average (—).

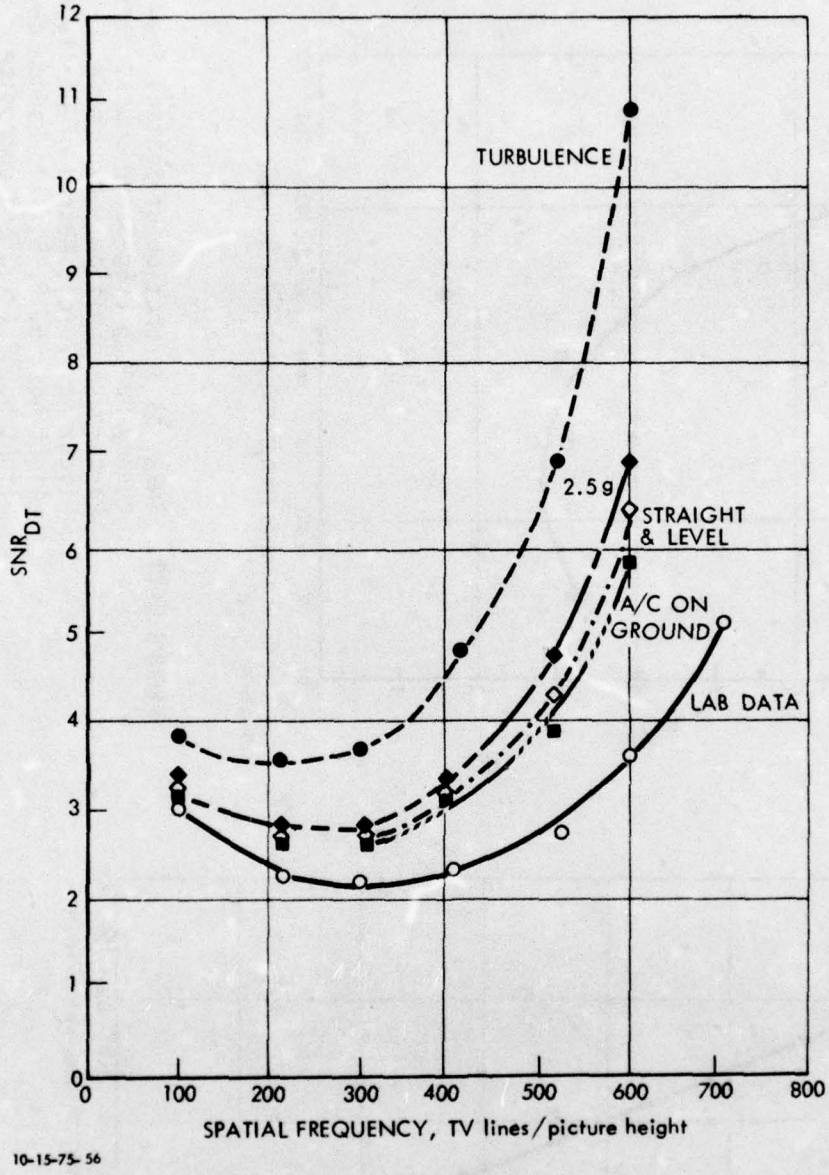


FIGURE H-12. Composite Average SNR_{DT} Data for Bar-Pattern Recognition versus Spatial Frequency: Laboratory Data (o); Aircraft on Ground (■); Straight-and-Level Flight (◇); 2.5g Turns (◆); and Air Turbulence (●).

If the values of SNR_D are very large or very small, air turbulence will apparently have little effect on pilot performance. If he cannot find the target image or can do so only with great difficulty, his performance will be somewhat worse than poor. If the target is large, clear, and bright, its image will be somewhat less than clear but still large and bright, and the probability of detection should not decrease appreciably. When, however, the signal-to-noise ratio is somewhere near the values required for, say, 40-80% detection probability in a laboratory environment, it is to be expected that air turbulence would have a strong adverse effect on detection probability.

Such factors must be considered in reviewing the data in this volume and the other volumes in this series.

REFERENCES, APPENDIX H

1. F.A. Rosell, "The Limiting Resolution of Low-Light-Level Imaging Sensors," Chapter 14 in L.M. Biberman and S. Nudelman, eds., Photoelectronic Imaging Devices, Vol. 1, Physical Processes and Methods of Analysis, Plenum Press, New York, 1971, pp. 307-309.

2. F.A. Rosell and R.H. Willson, "Recent Psychophysical Experiments and the Display Signal-to-Noise Ratio Concept," Chapter 5 in L.M. Biberman, ed., Perception of Displayed Information, Plenum Press, New York, 1973, pp. 175-232.

3. Defense and Electronic Systems Center, Westinghouse Electric Corporation, Recent Psychophysical Experiments and the Display Signal-to-Noise Ratio Concept, Report ADTM 110, F.A. Rosell and R.H. Willson, 7 September 1972.

4. Systems Development Division, Defense and Electronic Systems Center, Westinghouse Electric Corporation, Performance Synthesis of Electro-Optical Sensors, Report AFAL-TR-74-104, F.A. Rosell and R.H. Willson, April 1974.

5. A.D. Schnitzler, "Analysis of Noise-Required Contrast and Modulation in Image-Detecting and Display Systems," Chapter 4 in L.M. Biberman, ed., Perception of Displayed Information, Plenum Press, New York, 1973, pp. 119-166.

6. Institute for Defense Analyses, Low-Light-Level Devices: A Designers' Manual, IDA Report R-169, L.M. Biberman et al., August 1971. (NTIS AD735006)

7. Aerospace Applications Studies Committee, Advisory Group for Aerospace Research and Development, North Atlantic Treaty Organization, Study No. 5 on Night Vision Devices for Fast Combat Aircraft (U), AGARD Report No. 73, Vol. I, January 1976, and Vols. II and III, December 1975 (NATO SECRET).

8. Electro-Optical Systems, Xerox Corporation, E/O Sensor Performance Analysis and Synthesis (TV/IR Comparison Study), Report AFAL-TR-72-374, R.L. Sendall and F.A. Rosell, April 1973.

9. L.M. Biberman, "Luminance, Radiance, and Temperature," Chapter 2 in L.M. Biberman and S. Nudelman, eds., Photo-electronic Imaging Devices, Vol. 1, Physical Processes and Methods of Analysis, Plenum Press, New York, 1971, pp. 9-38.